Determination of the τ-lepton reconstruction and identification efficiency using $\mathrm{Z} \rightarrow \tau\tau$ events in first data at ATLAS

Dissertation
zur Erlangung des Doktorgrades
des Department Physik
der Universität Hamburg

vorgelegt von
Diplom-Physiker Gordon Fischer
aus Prenzlau

Hamburg
Mai 2011

Gutachter der Dissertation:	Dr. Philip Bechtle Prof. Dr. Johannes Haller
Gutachter der Disputation:	Dr. Philip Bechtle Prof. Dr. Peter Schleper
Datum der Disputation:	15.06.2011
Vorsitzender des Prüfungsausschusses:	Dr. Georg Steinbrück
Vorsitzender des Promotionsausschusses:	Prof. Dr. Peter Hauschildt
Leiter des Departments Physik:	Prof. Dr. Daniela Pfannkuche
Dekan der MIN-Fakultät:	Prof. Dr. Heinrich Graener

Einer dem Dunklen Hawking auf dunklem Thron.
Im Lande CERN, wo die Schatten drohn.
Ein Ring, sie zu knechten, sie alle zu finden.
Ins Schwarze Loch zu treiben und ewig zu binden
Im Lande CERN, wo die Schatten drohn.

Abstract

The Large Hadron Collider (LHC) at CERN started operation in November 2009. At the same time the ATLAS experiment started data taking. Since this time a large number of Z-bosons is produced. An important decay channel of the Z-boson is the decay into two τ-leptons. The large mass of the τ-lepton allows the decay into pions or kaons. In many models considering new physics the τ-lepton is an important final state. The LHC is a proton-proton collider and for that reason, the hadronic τ-lepton decay is difficult to distinguish from QCD multi-jet background. For the selection of hadronically decaying τ-leptons, reconstruction and identification algorithms were developed in order to suppress this background. In order to measure the Z-boson production cross section or possible new particles decaying into τ-leptons, the estimation of the τ-lepton reconstruction and identification efficiency is required. Furthermore, for detector calibration the Z-boson as well as the τ-lepton are helpful probes.

In this thesis two methods are discussed which provide an estimation of τ-lepton reconstruction and identification efficiencies from data. The full selection of $Z \rightarrow \tau\tau$ events including data-driven techniques for background extraction is discussed. The semi-leptonic $Z \rightarrow \tau\tau$ channel promises a good QCD multi-jet suppression because of the selected additional lepton. For that reason also the leptonically decaying τ-lepton is discussed. The Z-boson production cross section can be calculated with the estimated efficiencies.

Zusammenfassung

Seit November 2009 läuft der Large Hadron Collider (LHC) am CERN. Zur selben Zeit hat das ATLAS Experiment seinen Betrieb aufgenommen. Seit dieser Zeit wurde eine große Anzahl von Z Bosonen produziert. Ein wichtiger Zerfallskanal des Z Bosons ist der Zerfall in zwei τ-Leptonen. Das τ-Lepton kann leptonisch in ein Elektron oder ein Myon zerfallen aber aufgrund seiner großen Masse auch in leichte Hadronen wie z.B. das Pion. In vielen Modellen, die neue Physik beschreiben, wird das τ-Lepton als wesentlicher Endzustand zerfallender neuer Teilchen gehandelt.

Der LHC ist ein Proton Proton Beschleuniger was zur Folge hat, dass Z Boson Zerfälle von QCD Jets hoher Multiplizität überlagert werden, was die Selektion von τ-Leptonen sehr schwierig gestaltet. Für eine optimierte Selektion hadronisch zerfallender τ-Leptonen wurden verschiedene Rekonstruktions- und Identifikationsalgorithmen entwickelt, deren hauptsächliche Aufgabe die Unterdrückung von Untergrundereignissen ist. Um Produktionswirkungsquerschnitte von Z Bosonen zu messen, ist die Rekonstruktions- und Identifikationseffizienz unabdingbar. Weiterhin eignen sich das Z Boson und das τ-Lepton hervorragend für die Detektorkalibrierung.

In dieser Arbeit werden Analysen entwickelt und diskutiert, die das Signal vom Untergrund trennen sollen. Weiterhin werden zwei Methoden zur Bestimmung der Rekonstruktions- und Identifikationseffizienz von τ-Leptonen vorgestellt. Zum Schluss wird der Wirkungsquerschnitt für Z Bosonen ermittelt.

Contents

Chapter 1

Introduction

'We have found events of the form $e^+ + e^- \to e^\pm + \mu^\pm$ *+missing energy, in which no other charged particles or photons are detected. Most of these events are detected at or above a centre-of-mass energy of 4 GeV. The missing-energy and missing-momentum spectra require that at least two additional particles be produced in each event. We have no conventional explanation for these events.'*

Starting with these four sentences a paper was published which firstly describes the τ-lepton, discovered in 1975 by Martin Perl and his collaborators [1]. Nowadays, the τ-lepton plays an important role for discovering new physics like the Higgs boson or supersymmetric particles. For that reason investigations of τ-leptons have a high priority at the LHC. Furthermore, the Z-boson is a 'standard candle' in the description of the Standard Model. The process $Z \to \tau\tau$ is well understood. For that reason it can be used for detector calibration and optimisation.

The Standard Model of particles describes very successful the fundamental constituents of matter and their interactions. But experiments as well as theoretical predictions showed that this statement is only true for a certain energy range. Cosmological aspects as well as results from collider experiments forces the searches for new physics in unknown energy regions. This will be done at the Large Hadron Collider (LHC). Theoretical inconsistencies (e.g. the Standard Model does not contain general relativity or dark matter) are also a motivation to cover higher energy regions. Independent from phenomena which restrict extensions of the Standard Model, also the last element for the completeness of the existing model, the Higgs boson, is not discovered yet.

In order to solve such problems, in the late eighties the LHC was designed to reach new energy regions. At this time the Large Electron Positron Collider (LEP) was in this starting phase and the Electron Proton Collider (HERA) at DESY started few years later with new experiments investigating the structure of the proton. The Fermi-Lab has started a proton-antiproton collider, the TEVATRON. LEP was a precision experiment and has measured the Z-boson mass peak very precisely. The structure functions of the proton were investigated at the HERA collider. TEVATRON will operate until the end of 2011 and has set limits on the Higgs masses.

All these experiments are quite important for the developing of the LHC. Current results (spring 2011) indicates that it is most probable that the low mass Higgs can be localised close above the lower limit of 114 GeV given by the LEP experiments. The fact that this mass is in the order of the Z-boson mass and the fact that the low mass Higgs-boson preferably couples to τ-leptons, makes the Z $\rightarrow \tau\tau$ channel very interesting and important.

This thesis is separated into two parts. The first part includes general comments on the Standard Model physics as well as experimental requirements. The second part discusses the Z-boson and τ-lepton specific issues.

Part I Chapter 2 gives a general theoretical introduction in the Standard Model and discusses supersymmetric extensions. Chapter 3 discusses the experimental environment, the LHC and the ATLAS detector, and shows first results from detector performance studies with real data. Chapter 4 gives an overview of the Monte Carlo simulation, the data taking and the full trigger performance. A discussion of tools required by the monitoring of the trigger system are also considered. The tau trigger properties as well as trigger studies with first data are also covered in this chapter.

Part II Chapter 5 is reserved for a detailed discussion of the Z-boson and τ-lepton related properties. The production of Z-bosons at proton proton collide-rs including first measurements of the transverse momenta of the Z-boson will be discussed in the first part. The τ-lepton and its decay modes are also covered. Finally, the role of the Z-boson and the τ-lepton in context of possible extensions of the Standard Model is discussed. Chapter 6 deals with the full electron, muon and τ-lepton reconstruction and identification. Variables, useful for QCD multi-jet suppression are introduced. The current cut based identification variables are discussed. This chapter closes with a short overview about the τ-lepton fake rates which describe the probability that a jet fakes a hadronically decaying τ-lepton. Chapter 7 introduces the full semileptonic $Z \rightarrow \tau\tau$ visible mass analysis including background suppression. Chapter 8 discussed two methods for τ-lepton reconstruction and identification efficiency measurements from data. The main part of this thesis closes with a summary and an outlook. The appendix contains further figures useful for a better understanding of the introduced analysis and methods.

Chapter 2

Theoretical aspects

This chapter introduces the Standard Model (SM) of particle physics with a detailed discussion of the different interactions, particle content, limits and extensions. The SM describes the unification of the electromagnetic and the weak interaction to the electro-weak interaction and connection with the strong interaction.

In the SM all elementary particles and their properties are summarised and ordered into gauge bosons and fermions creating the matter. Tables 2.1 and 2.2 summarise all known fermions (half-integer spin) and bosons (integer spin) [2].

2.1 The interactions in the Standard Model

The strong interaction

Strong forces (also known as nuclear forces) are studied since 1930. Yukawa [3] has described these effects by an interaction of nucleis mediated by pions. The strong interaction is mediated by colour charges, described as $\mathrm{g_s}$, $\frac{\lambda^{\mathrm{i}}}{2}$ with $\lambda^{\mathrm{i}}(\mathrm{i}=1,2,....8)$ denoting the Gell-Mann matrices. The quarks are bound inside hadrons through strong interactions mediated by gluons. The underlying symmetry is the $\mathrm{SU(3)_C}$[1)] gauge group which is non-abelian and the theory is called `quantum chromo-dynamic` (QCD). Gluons are massless and carry a charge, which results in a self-interaction.

The Lagrangian for the strong interaction (QCD) is

$$\mathcal{L}_{\mathrm{QCD}}(\mathrm{q},\mathrm{A}) = \bar{\mathrm{q}}\left(\mathrm{i}\gamma^{\mu}\mathrm{D}_{\mu} - \mathrm{m}\right)\mathrm{q} - \frac{1}{4}\mathrm{F}^{\mathrm{a}}_{\mu\nu}\mathrm{F}^{\mu\nu}_{\mathrm{a}} = \bar{\mathrm{q}}(\mathrm{i}\gamma^{\mu}\partial_{\mu} - \mathrm{m})\mathrm{q} + \mathrm{g}\bar{\mathrm{q}}\gamma^{\mu}\mathrm{T_a}\mathrm{q}\mathrm{A}^{\mathrm{a}}_{\mu} - \frac{1}{4}\mathrm{F}^{\mathrm{a}}_{\mu\nu}\mathrm{F}^{\mu\nu}_{\mathrm{a}} \tag{2.1}$$

with $\bar{\mathrm{q}}(\mathrm{i}\gamma^{\mu}\partial_{\mu} - \mathrm{m})\mathrm{q}$ describing the kinematic term of the quarks. The second term $\mathrm{g}\bar{\mathrm{q}}\gamma^{\mu}\mathrm{T_a}\mathrm{q}\mathrm{A}^{\mathrm{a}}_{\mu}$ describes the interaction between quarks and gluons and the last term $\frac{1}{4}F^{a}_{\mu\nu}F^{\mu\nu}_{a}$ describes the interaction of the gluon-fields (3-gluon and 4-gluon interaction).

[1)] C denotes the colour structure.

First generation			
Particle	**Q**	I_3	**Mass**
u	+2/3	+1/2	$1.5 \sim 5$ MeV
d	-1/3	-1/2	$3 \sim 9$ MeV
Second generation			
Particle	**Q**	I_3	**Mass**
c	+2/3	0	$1.47 \sim 1.83$ GeV
s	-1/3	0	$60 \sim 170$ MeV
Third generation			
Particle	**Q**	I_3	**Mass**
t	+2/3	0	$174.3 \pm 3.2 \pm 4.0$ GeV
b	-1/3	0	$4.6 \sim 5.1$ GeV

Table 2.1: *Quarks in the Standard Model separated into the three generations. The electric charge and the third component of the isospin are denoted Q and I_3.*

First generation					
Particle	**Q**	L_e	L_μ	L_τ	**Mass**
e	-1	+1	0	0	$\simeq 0.511$ MeV
ν_e	0	+1	0	0	< 3 eV
Second generation					
Particle	**Q**	L_e	L_μ	L_τ	**Mass**
μ	-1	0	+1	0	$\simeq 105.66$ MeV
ν_μ	0	0	+1	0	< 0.19 MeV
Third generation					
Particle	**Q**	L_e	L_μ	L_τ	**Mass**
τ	-1	0	0	+1	$\simeq 1777.0$ MeV
ν_τ	0	0	0	+1	< 18.2 MeV

Table 2.2: *Leptons in the Standard Model separated into the three generations. The electric charge is denoted Q. The lepton quantum numbers are L_e, L_μ, and L_τ.*

The weak interaction and the electro-weak unification

The weak interaction was first discovered in the β-decay of nuclei [4]. The free neutron has a relative life time ($\sim 900\,\mathrm{s}$) before it decays via the β-decay

$$\mathrm{n} \rightarrow \mathrm{p} + \mathrm{e}^{-} + \bar{\nu} \tag{2.2}$$

into a proton, an electron and an anti-neutrino.

Enrico Fermi has described the β-decay in a more general theoretical context [5]. He introduced a weak coupling constant G which is much smaller than the electromagnetic coupling constant e. Contrary to the electromagnetic case, Fermi assumed that for the weak interaction the interacting partners couple in a four fermion interaction without a mediating propagator term. The description of the weak interaction with the four fermion interaction (see Eq. 2.2) cannot be correct due to the fact that for a point like interaction the total cross section becomes proportional to the maximum of the mediated momentum. For a certain energy the cross section becomes larger than the so called `unitary limit`. For cross sections larger than the unitary limit the interaction probability becomes $\mathcal{P} > 1$. Gauge bosons (like the W-bosons) which mediate the weak interaction can avoid such a problem. The propagator term becomes

$$\frac{1}{\mathrm{q}^2} \rightarrow \frac{1}{(\mathrm{M}_\mathrm{W}^2 - \mathrm{q}^2)}. \tag{2.3}$$

In field theories interactions of particles are described by using a `current`. For example, the radiative process $\mathrm{p} \rightarrow \mathrm{p} + \gamma$ will be expressed via a propagator (photon) and the electromagnetic current of the proton. The W-bosons are charged ($\mathrm{W}^{\pm}$) and therefore they change the charge of the fermions. For that reason these currents are called `charged currents`. The `neutral currents` are mediated by neutral Z-bosons.

The general Hamiltonian for the β-decay can be expressed as

$$\mathrm{H}_\mathrm{w} = \Sigma \frac{\mathrm{G}_\mathrm{i}}{2} \left[\bar{\psi}_\mathrm{p} \mathrm{O}_\mathrm{i} \psi_\mathrm{n}\right] \left[\bar{\psi}_\mathrm{e} \mathrm{O}_\mathrm{i} (1 + \mathrm{c}_\mathrm{i} \gamma_5) \psi_\nu\right] + \mathrm{h.c} \tag{2.4}$$

with G_i as the coupling constant.

The Hamiltonian H_w must be independent from the chosen coordinate system. Due to the parity violation, H_w must include `pseudo-scalars` because they change the sign under parity transformation. The mathematical construct allows the combination of different current-current structures. For example, the vector-vector structure describes electromagnetic processes but is not enough to describe the weak interaction. H_w must be a scalar or pseudo-scalar in order to describe parity violation.

The interactions can be mathematically derived from symmetry groups. The underlying symmetry group is the

$$\mathrm{SU}(2)_\mathrm{L} \otimes \mathrm{U}(1)_\mathrm{Y} \tag{2.5}$$

with $\mathrm{SU}(2)_\mathrm{L}$ describing the weak interaction related to the weak isospin T_3 and $\mathrm{U}(1)_\mathrm{Y}$ the electromagnetic interaction related to the hyper-charge $\mathrm{Y} = 2(\mathrm{Q} - \mathrm{T}_3)$ with the electric charge Q. The SM describes the unification $\mathrm{SU}(2)_\mathrm{L} \otimes \mathrm{U}(1)_\mathrm{Y}$ introducing four gauge fields

	I_{3L}	Y_L
$\psi_{\nu_e L}$	+1/2	-1
ψ_{eL}	-1/2	-1
ψ_{eR}	0	-2
ψ_{uL}	+1/2	+1/3
ψ_{dL}	-1/2	+1/3
ψ_{uR}	0	+4/3
ψ_{dR}	0	-2/3

Table 2.3: *I_{3L} and Y_L for the first generation charged fermion fields.*

W^1, W^2, and W^3 for the weak and B^0 for the electromagnetic interaction. The denotation $SU(2)_L$ refers to the fact that electro-weak interactions only affect left-handed particles. Table 2.3 summarises all fields of the first family. A doublet of a left-handed neutrino and an electron transforms under $SU(2)_L$ as a doublet, as well as for left-handed `up` and `down` quarks. In addition one right-handed electron defined as a $SU(2)_L$ singlet which is required by the electromagnetic interaction, and two right-handed `up` and `down` quarks defined as $SU(2)_L$ singlets are defined. In Eq. 2.6 the gauge bosons of the electro-weak interaction are shown as a combination of the individual gauge fields described before

$$\begin{aligned} \mid \gamma\rangle &= \cos\Theta_W \mid B^0 > +\sin\Theta_W \mid W^0\rangle \\ \mid Z\rangle &= \text{-}\sin\Theta_W \mid B^0 > +\cos\Theta_W \mid W^0\rangle \\ \mid W^{\pm}\rangle &= \frac{1}{\sqrt{2}}(\mid W^1\rangle + i \mid W^2\rangle) \end{aligned} \tag{2.6}$$

with the `Weinberg angle` Θ_W which describes the rotation of the Z-boson field relative to the W^0-field. The γ field is perpendicular to the Z-boson field.

The Lagrangian for the electro-weak unification can be expressed as

$$\mathcal{L} = \frac{g}{\sqrt{2}}(J^-_\mu W^+_\mu + J^+_\mu W^-_\mu) + \frac{g}{\cos\Theta_W}(J^{(3)}_\mu - \sin^2\Theta_W J^{e.m.}_\mu)Z_\mu + g\sin\Theta_W J^{e.m.}_\mu A_\mu. \tag{2.7}$$

The first term on the right hand side describes the charged weak current, the second term describes the neutral weak current and the last term describes the electromagnetic current.

The Grand Unified Theory

The Grand Unified Theory (GUT) is the unification of the electro-weak and strong interaction at higher energies. The underlying symmetry group has to contain

$$SU(3)_C \otimes SU(2)_T \otimes U(1)_Y \tag{2.8}$$

as a sub-group. Only one coupling exists. Moreover, the gauge group must admit complex representations, since SU(3) and SU(2) are complex. Typical groups are the SU(5) or the SO(10). As well known, the current couplings for the three interactions differ at currently experimentally achievable energies, the unification is only allowed at higher energies. The

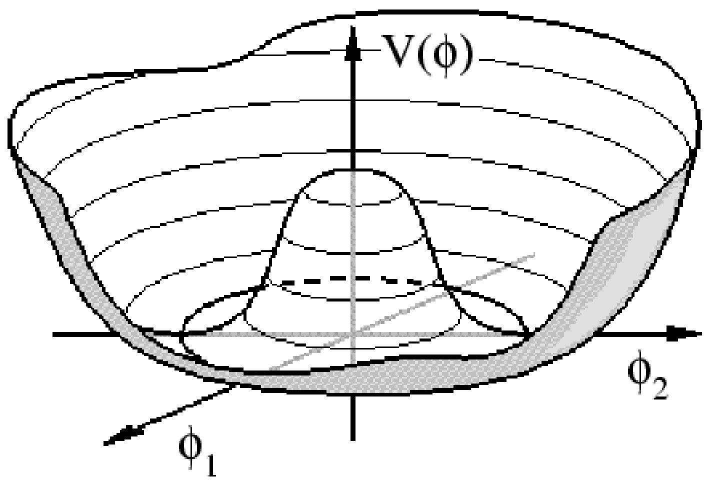

Figure 2.1: *The Higgs potential. The rotational symmetry is broken.*

corresponding symmetry must be broken.

2.2 The Higgs Mechanism

The Standard Model works for massless particles. Experiments showed that the fermions and the weak gauge bosons must have a mass. But simple mass terms would break the local gauge invariance.

In order to introduce the mass terms without breaking the local gauge invariance a new mechanism is introduced. The particles interact with a scalar field, the Higgs field. The corresponding mechanism, the Higgs mechanism [6, 7], bases on spontaneous symmetry breaking. The Higgs field is a complex scalar doublet

$$\phi = \frac{1}{\sqrt{2}} \begin{pmatrix} \phi_1 + \mathrm{i}\phi_2 \\ \phi_3 + \mathrm{i}\phi_4 \end{pmatrix} = \begin{pmatrix} \phi^+ \\ \phi^0 \end{pmatrix} \tag{2.9}$$

with four degrees of freedom.

The $\mathrm{SU(2)_L}$ potential is

$$\mathrm{V}(\phi) = \mu^2 \phi^\dagger \phi + \lambda(\phi^\dagger \phi)^2. \tag{2.10}$$

To ensure the relation $\mathrm{V} \to \infty$ when $\phi \to \infty$ the real parameter λ has to be positive definite. The minimum of the potential is

$$|\phi_0| = \sqrt{\frac{-\mu^2}{\lambda}} = \nu. \tag{2.11}$$

For $\mu^2 = 0$, the minimum of the potential becomes 0. For negative values of μ^2 the minimum of the potential is not longer 0:

$$|\phi_0| \neq 0. \tag{2.12}$$

The potential V is symmetric in $\mathrm{SU(2)_L}$ but every ground state breaks this symmetry.

This is known as spontaneous symmetry breaking. The potential is shown in Fig. 2.1.

Goldstone bosons An expansion around the minimum

$$\phi = \frac{1}{\sqrt{2}} \begin{pmatrix} \xi_1(\mathrm{x}) + \mathrm{i}\xi_2(\mathrm{x}) \\ \nu + \mathrm{h}(\mathrm{x}) + \mathrm{i}\xi_3(\mathrm{x}) \end{pmatrix} \tag{2.13}$$

with $\phi_1 = \phi_2 = \phi_4 = 0$ and $\xi_1(\mathrm{x}), \xi_2(\mathrm{x}), \xi_3(\mathrm{x})$, and $\mathrm{h}(\mathrm{x})$ being real scalar fields results in a mass term $\mathrm{m_h} = \sqrt{2}\mu$ for the field h. The parameter $\xi_1(\mathrm{x}), \xi_2(\mathrm{x}), \mathrm{and}\xi_3(\mathrm{x})$ are still massless and are known as Goldstone bosons.

For a local gauge invariance, $\xi_1(\mathrm{x}), \xi_2(\mathrm{x})$, and $\xi_3(\mathrm{x})$ create mass terms by coupling to the gauge bosons. Since the photon is massless, the ground state is chosen in order to define following masses:

$$\mathrm{m_w} = 1/2\mathrm{g}\nu \tag{2.14}$$

$$\mathrm{m_z} = 1/2\nu\sqrt{\mathrm{g}^2 + (\mathrm{g}')^2} \tag{2.15}$$

$$\mathrm{m}_\gamma = 0 \tag{2.16}$$

with g and g′ as the coupling constants required by the $\mathrm{SU(2)_L \times U(1)_Y}$ theory.

With the relations

$$\mathrm{e} = \mathrm{g}\sin\theta_\mathrm{w} = \mathrm{g}'\cos\theta_\mathrm{W} \tag{2.17}$$

and

$$\mathrm{m_w} = \mathrm{m_z}\cos\theta_\mathrm{w} \tag{2.18}$$

the vacuum expectation value can be estimated to

$$\langle \mathrm{H} \rangle \simeq 246\,\mathrm{GeV}. \tag{2.19}$$

2.3 The limits of the Standard Model

The limits and open questions of the Standard Model are:

- Why are the electric charges of the electron and the proton (exactly) balanced?
- Why exist exact three (lepton and quark) families?
- Why are the gauge interactions so different in their strength?
- Why is the electro-weak symmetry broken at $\langle H \rangle = 246\,\mathrm{GeV}$?
- 18 free parameters have to be measured.
- No unification of coupling constants can be reached at higher energies.

- Where comes the matter-antimatter asymmetry from?
- The Standard Model only describes about 4 % of the matter in the universe. What about the missing 96% (dark matter, dark energy)?

To answer all these questions, experiments at higher energies as the current energies must be designed and realised. Beside the discovery of the Higgs boson, one motivation to build the Large Hadron Collider was to solve those problems. The most studied candidate is the `supersymmetric` model which will be described in the following.

2.4 Supersymmetry

Supersymmetry (SUSY) [8] introduces a new symmetry between fermions and bosons. The model which has a minimal modification of the existing Standard Model is the Minimal Supersymmetric Standard Model (MSSM).

Particles in the SM	**SUSY partner**
$\gamma, \mathrm{Z}^0, \mathrm{h}^0, \mathrm{H}^0$	$\tilde{\chi}_1^0, \tilde{\chi}_1^0, \tilde{\chi}_1^0, \tilde{\chi}_1^0$
$\mathrm{W}^\pm, \mathrm{H}^\pm$	$\tilde{\chi}_1^\pm, \tilde{\chi}_2^\pm$
$\mathrm{e}^\pm, \nu_\mathrm{e}, \mu^\pm, \nu_\mu, \nu_\tau$	$\tilde{\mathrm{e}}_\mathrm{R}^\pm, \tilde{\mathrm{e}}_\mathrm{L}^\pm, \tilde{\nu}_\mathrm{e}, \tilde{\nu}_\mu, \tilde{\mu}_\mathrm{R}^\pm, \tilde{\mu}_\mathrm{L}^\pm, \tilde{\nu}_\tau$
$\tau^\pm$	$\tilde{\tau}_1, \tilde{\tau}_2$
u,d,s,c	$\tilde{\mathrm{u}}_\mathrm{R}, \tilde{\mathrm{u}}_\mathrm{L}, \tilde{\mathrm{d}}_\mathrm{R}, \tilde{\mathrm{d}}_\mathrm{L}, \tilde{\mathrm{s}}_\mathrm{R}, \tilde{\mathrm{s}}_\mathrm{L}, \tilde{\mathrm{c}}_\mathrm{R}, \tilde{\mathrm{c}}_\mathrm{L}$
b	$\tilde{\mathrm{b}}_1, \tilde{\mathrm{b}}_2$
t	$\tilde{\mathrm{t}}_1, \tilde{\mathrm{t}}_2$

Table 2.4: *SM particles and their supersymmetric partners.*

In Tab. 2.4 the known particles in the SM and the corresponding particles in the MSSM are summarised.

Furthermore, it is necessary to enlarge the Higgs spectrum in the MSSM to avoid anomalies. This is required in order to provide masses for all fermions without violating SUSY. A second complex scalar Higgs doublet has to be introduced which increases the number of degree of freedoms up to 8. For that reason, the MSSM requires five (3 neutral and 2 charged) Higgs bosons.

Furthermore, an additional quantum number can be defined, the `R-parity`

$$\mathrm{R} = (-1)^{3(\mathrm{B}-\mathrm{L})+2\mathrm{s}} \tag{2.20}$$

with the baryon number B, the lepton number L, and the spin s. The SM particles have $\mathrm{R} = 1$, contrary to the super-partners which have $\mathrm{R} = -1$. If R-parity is conserved, supersymmetric particles can only be produced in pairs, which has the consequence that the lightest supersymmetric particle (LSP) is stable. One prediction from the MSSM is that the mass for the lightest Higgs boson (h^0) has an upper limit. The current value is about $\mathrm{M}_{\mathrm{h}^0} < 135\,\mathrm{GeV}$ which can be tested at the LHC. It is important to know that the mass limit of the lightest Higgs boson could be nearby the mass of the Z-boson ($\mathrm{M}_\mathrm{Z} = 91.4\,\mathrm{GeV}$)

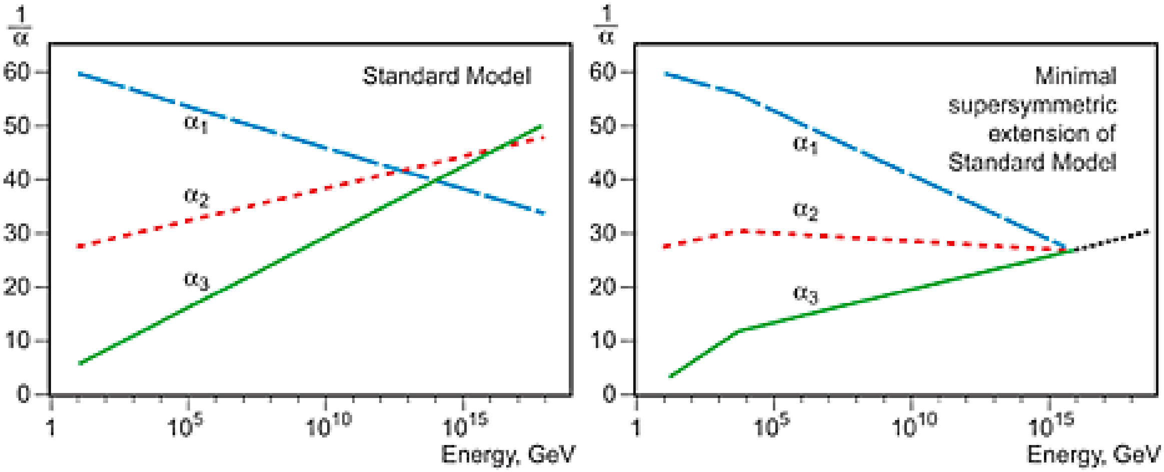

Figure 2.2: *The unification of the three interactions of the SM (left) and for the supersymmetric extension (right).*

which forces the understanding of the Z-boson measurement at LHC. In addition to solve the Hierarchy problem the masses of the super-symmetric particles should be in the order of 1 TeV (the electro-weak scale). Instead of 18 free parameters in the SM, the MSSM involves more than 100 free parameters, which have to be measured in order to avoid conflicts with experimental results. A famous prediction of the MSSM is the supersymmetric grand unification. The MSSM can unify the three couplings which is not possible in the current SM description. Figure 2.2 shows the unification of the three interactions within the Standard Model and the MSSM.

SUSY is broken in a hidden sector and the breaking is mediated by a `messenger`.

Chapter 3

The Large Hadron Collider and the ATLAS detector

This chapter describes the experimental environment at CERN (Geneva). It starts with a brief introduction of the Large Hadron Collider (LHC) in Sec. 3.1 followed by a discussion of the ATLAS Detector in Sec. 3.2.

3.1 The Large Hadron Collider

The LHC [10] is situated in a tunnel with a circumstance of 27 km. About 1200 superconducting dipole magnets providing a magnetic field of 8.5 T. The LHC is designed for a centre-of-mass energy of 14 TeV but the current value is

$$\sqrt{\mathrm{s}} = 7\,\mathrm{TeV}. \tag{3.1}$$

Figure 3.1 shows the LHC and its experiments. The process of proton accelerating at LHC is separated into different steps:

- Atoms are separated into protons and electrons by an electromagnetic field.
- In the Proton Synchrotron and the Super Proton Synchrotron (PS and SPS) the protons reach an energy of about 450 GeV.
- Finally, the radio frequency cavities of the LHC accelerate the protons up to 3.5 TeV.

Figure 3.2 shows the expected cross sections at the LHC at design luminosity and design centre-of-mass energy. Table 3.1 summarises important technical parameters of the LHC [10]. The luminosity is defined as

$$\mathcal{L} = \frac{N^2 f k}{4\pi\sigma_T^2} \tag{3.2}$$

with the number of bunches in the ring k, the bunch width σ_T, the circulation frequency f,

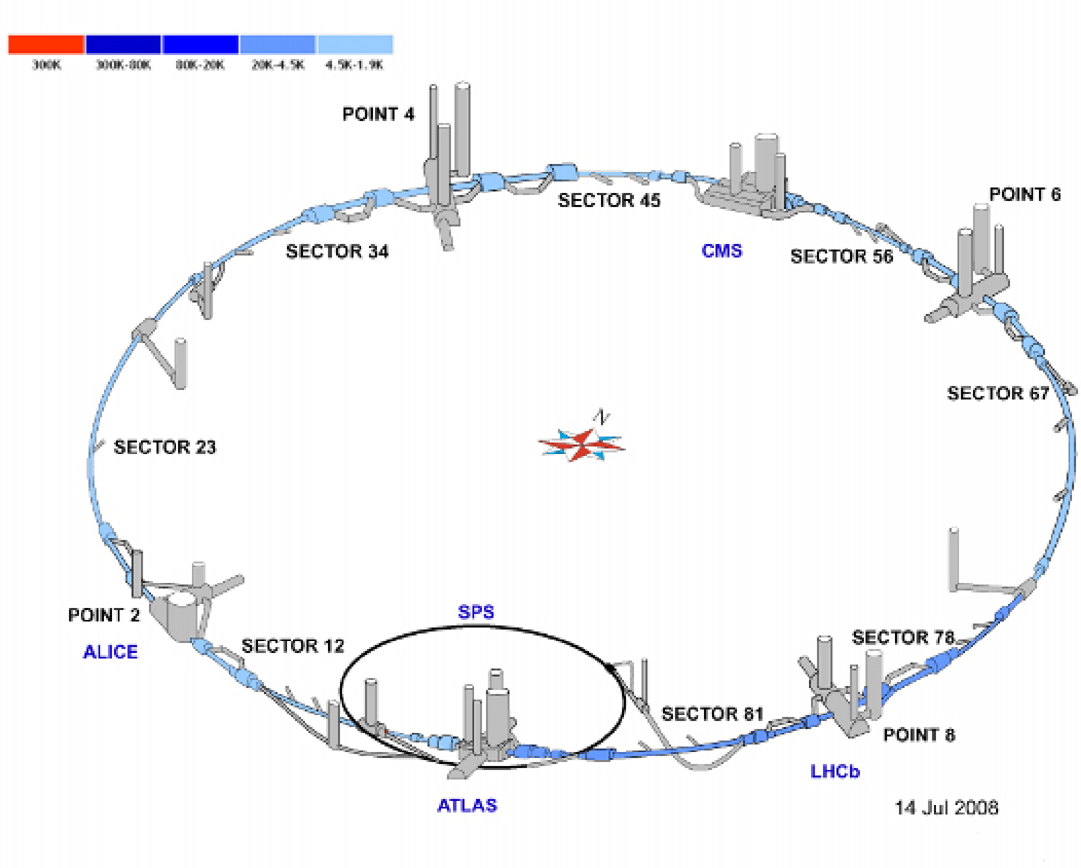

Figure 3.1: *The LHC ring with the four experiments ATLAS, CMS, ALICE, and LHCb [9].*

and the number of protons per bunch N. The design value is

$$\mathcal{L} = 10^{34}\mathrm{cm}^{-2}\mathrm{s}^{-1}. \tag{3.3}$$

The current value is smaller for the data used for this analysis is

$$\mathcal{L} = 10^{32}\mathrm{cm}^{-2}\mathrm{s}^{-1}. \tag{3.4}$$

The two anti parallel beams are crossed at four points where the main detectors are situated:

- **ALICE** (A Large Ion Collider Experiment)
  - Designed for heavy-ion collisions to investigate the earliest states of the universe (quark gluon plasma)
- **LHCb**
  - A symmetric detector (forward spectrometer) designed for B-physics to investigated CP violation

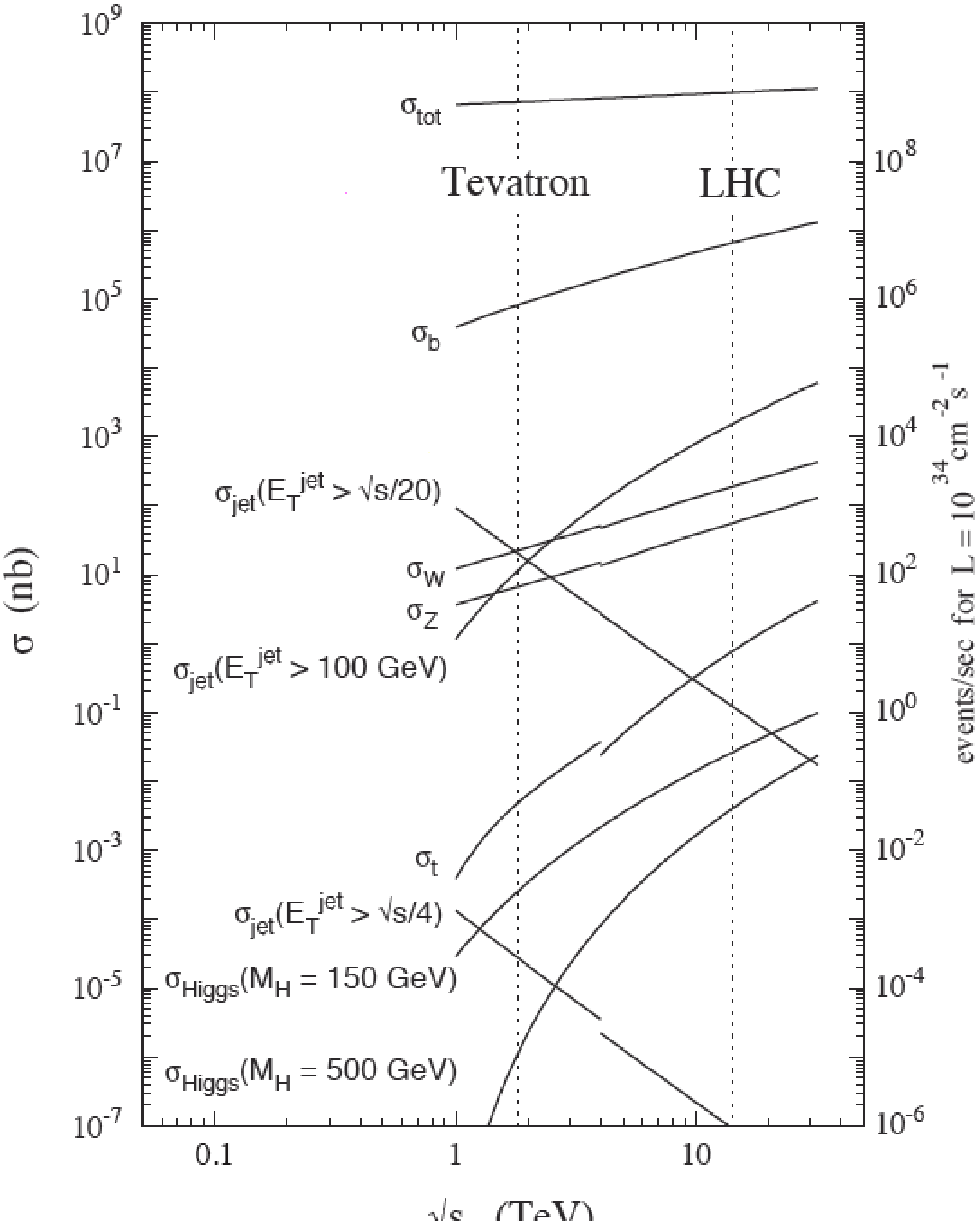

Figure 3.2: *The expected cross sections for several processes at the LHC. For all processes (except the jet production with higher E_T correlated with the centre-of-mass energy $\sigma_{jet}(E_T^{jet} > \sqrt{s}/20$ and $\sigma_{jet}(E_T^{jet} > \sqrt{s}/4)$ the cross section increases.*

Bunch width	15.9 μm
Bunch length	7.6 cm
Number of bunches	2800
Circulation frequency	11.25 kHz
Bunch crossing	$\sim$ 30 ns
Number protons per bunch	1.15×10^{11}

Table 3.1: *Parameters of the LHC storage ring [10].*

- **CMS** (Compact Muon Solenoid)
  - A multi-purpose detector which uses different technologies compared with ATLAS. Optimised for Higgs searches and supersymmetry studies.
- **ATLAS**
  - Also a multi-purpose detector which will be discussed in the next section.

3.2 The ATLAS detector

Figure 3.3 shows a picture of the ATLAS detector. ATLAS is a multi-purpose experiment and is optimised for the measurement of new physics [11]. ATLAS uses the right-handed Cartesian coordinate system [12]. From the interaction point, the positive x-axis is horizontal and points towards the middle of the LHC ring. The positive y-axis is perpendicular pointing up and the z-axis is aligned with the beam direction. The azimuthal angle ϕ is perpendicular to the beam embedded in the (x,y) plane.

Three variables, the `rapidity y`, the `pseudo-rapidity (for high energies)` η, and ΔR define the basic geometry of the detector:

$$\mathrm{y} = \frac{1}{2} \ln \frac{\mathrm{E} + \mathrm{p_z}}{\mathrm{E} - \mathrm{p_z}} \tag{3.5}$$

$$\eta = \frac{1}{2} \ln \frac{1 + \cos\Theta}{1 - \cos\Theta} = -\ln(\tan\Theta/2) \tag{3.6}$$

$$\Delta\mathrm{R} = \sqrt{(\Delta\eta)^2 + (\Delta\phi)^2} \tag{3.7}$$

with the polar angle Θ and the momentum along the beam line $\mathrm{p_z}$. The advantage of the (pseudo) rapidity is the invariance [1)] under Lorentz transformation.

3.2.1 The inner detector

A cross section of the inner detector is shown in Fig. 3.5. It shows the geometry and the position of all sub detector components with respect to the pseudo rapidity η.

[1)] Note that under Lorentz transformation the pseudo rapidity is constant plus an additional constant.

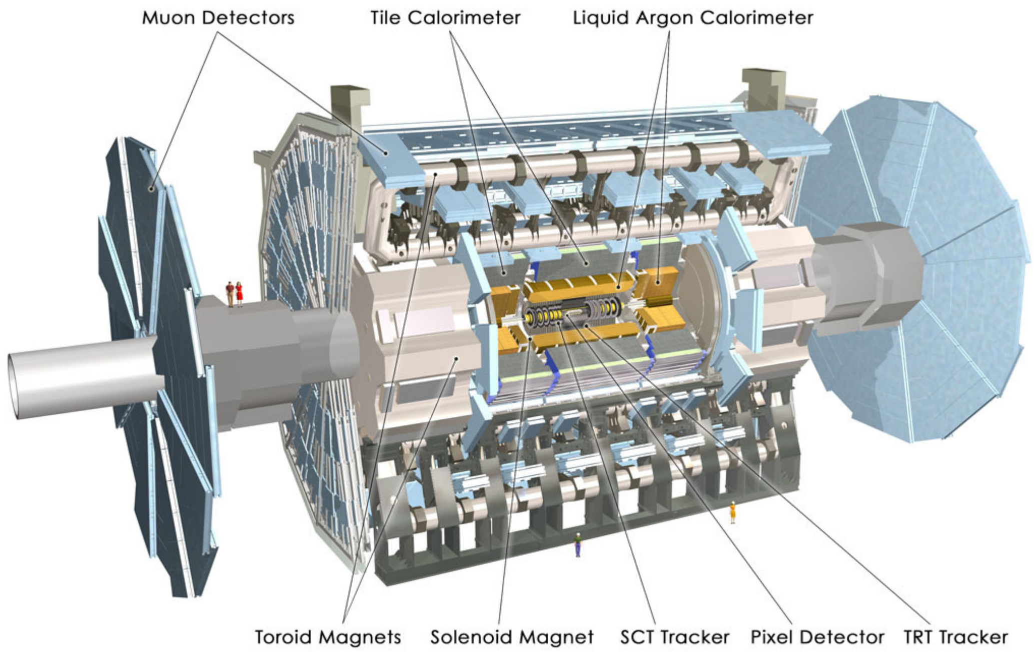

Figure 3.3: *The ATLAS detector [13].*

The inner detector (ID) shown in Fig. 3.4 has been designed to reconstruct charged particles [14, 15]. The focus is on their tracks and vertices. Furthermore, the momentum and the charge can be measured. The complete inner detector is operated in a 2 T magnetic field.

The tracking of particles is enabled in a range of $|\eta| < 2.5$ from the interaction point. The ID is situated in a cylinder with about 7 m length and 1.15 m in diameter. The magnetic field is generated by a solenoid and is directed along the beam axis which bents the trajectories in the transverse direction. The tracking system consists of three different components, which are all divided into a barrel and two end-caps.

The first (inner) component is the `pixel detector`, which provides precise measurements of the charged particle tracks. It has to be as close as possible to the interaction point to provide secondary vertices measurement. The pixel detector elements are mounted on three support structures at about 4 cm, 11 cm and 14 cm from the interaction point and provides about 10^8 read out channels. Since the detector has such high-granularity, it is capable to identify the products of short lived particles like the τ-lepton.

The second component is the `silicon micro-strip detector` (SCT), designed for momentum measurement and determination of vertex positions. Although the underlying technology is the same as for the pixel detector, the design is different. The SCT needs less material as the pixel, because the density of tracks decreases with larger radii. Therefore, the number of read-out channels is smaller compared with the pixel detector. The width of the strips, which are mounted in four cylindrical surfaces in the barrel, is about 80 μm. The end-caps strips are mounted in nine discs.

The last component is the `transition radiation tracker` (TRT) which is a multi-

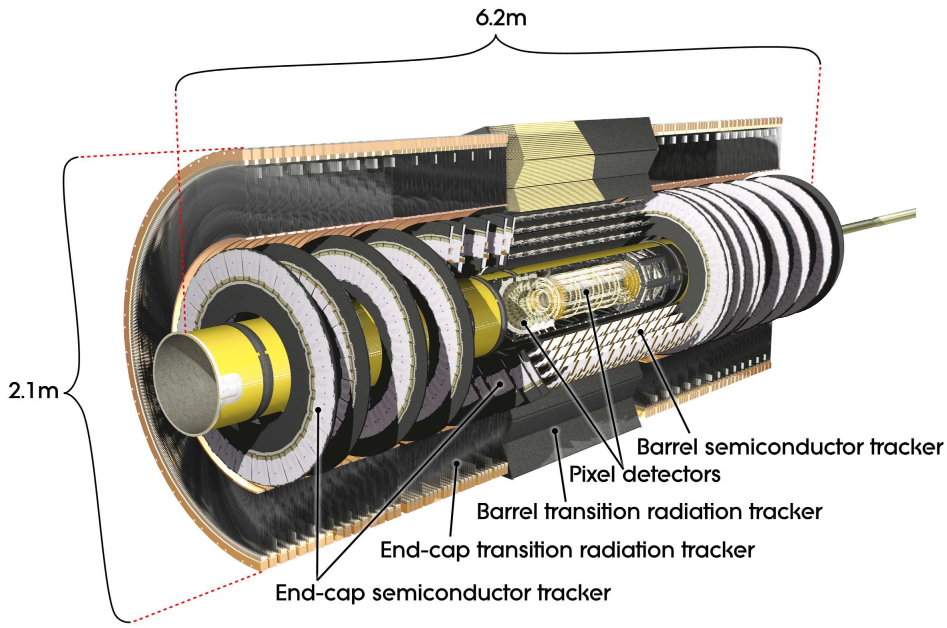

Figure 3.4: *The inner detector [13].*

wire proportional chamber [16]. It uses thin independent drift tubes (straws), mainly for electron detection. The TRT covers the outer area of the inner detector (radii between 56 cm and 107 cm) in a range of $|\eta| < 2.5$. The barrel part consists of straw layers parallel to the beam axis in a rotational symmetry. About 350000 individual straws provide high granularity.

3.2.2 The calorimeter system

The electromagnetic calorimeter The part which encloses the inner detector is the electromagnetic calorimeter (ECAL). The ECAL is able to reconstruct the energy deposits from electrons and photons. It uses a sampling technique with liquid argon as active material and lead plate absorbers [17, 18].

The length of the barrel part is about 6.8 m divided into two half-barrels separated by a gap (for service structures and cabling). The accordion structure allows to cover the full ϕ range. Three samplings with different $\Delta\eta \times \Delta\phi$ segmentation getting coarser with larger distance to the interaction point. The end-caps are separated into an inner wheel ($|\eta| < 2.5$) and an outer wheel ($|\eta| < 3.5$). The thickness of the absorbers remains constant while the amplitude of the accordion structure increases with the radius.

Figure 3.7 shows the three samplings of the central region ($\eta < 2.5$)

- The first sampling has a very high granularity in η ($\eta \times \phi = 0.0031 \times 0.098$) and a thickness of $4.3\,\mathrm{X}_0$ with X_0 as the radiation length. The first sampling ensures a separation in γ and π^0.

- The second sampling is separated into squared towers ($\eta \times \phi = 0.0245 \times 0.0245$) and

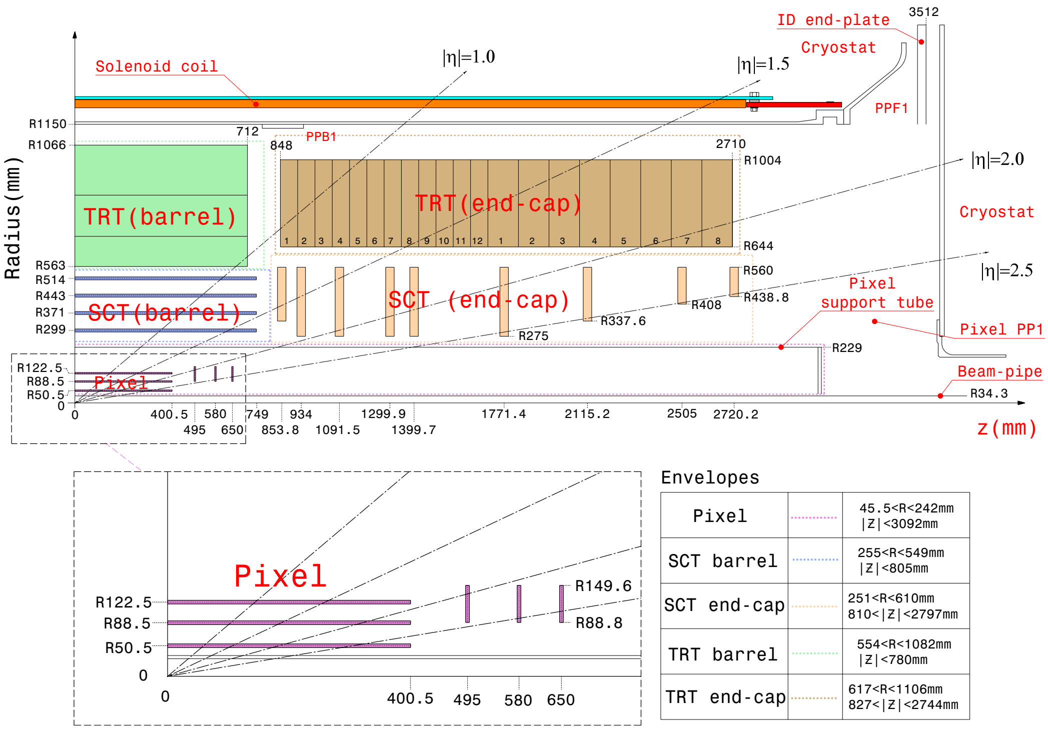

Pixel		45.5<R<242mm |Z|<3092mm
SCT barrel		255<R<549mm |Z|<805mm
SCT end-cap		251<R<610mm 810<|Z|<2797mm
TRT barrel		554<R<1082mm |Z|<780mm
TRT end-cap		617<R<1106mm 827<|Z|<2744mm

Figure 3.5: *Cross section of the inner detector [13].*

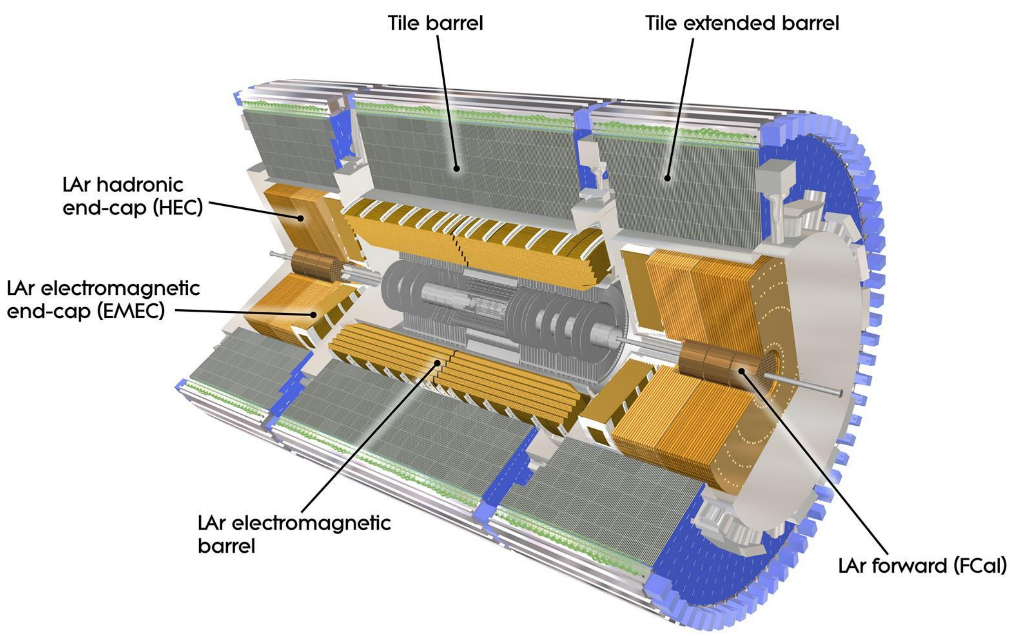

Figure 3.6: *The calorimeter system [13].*

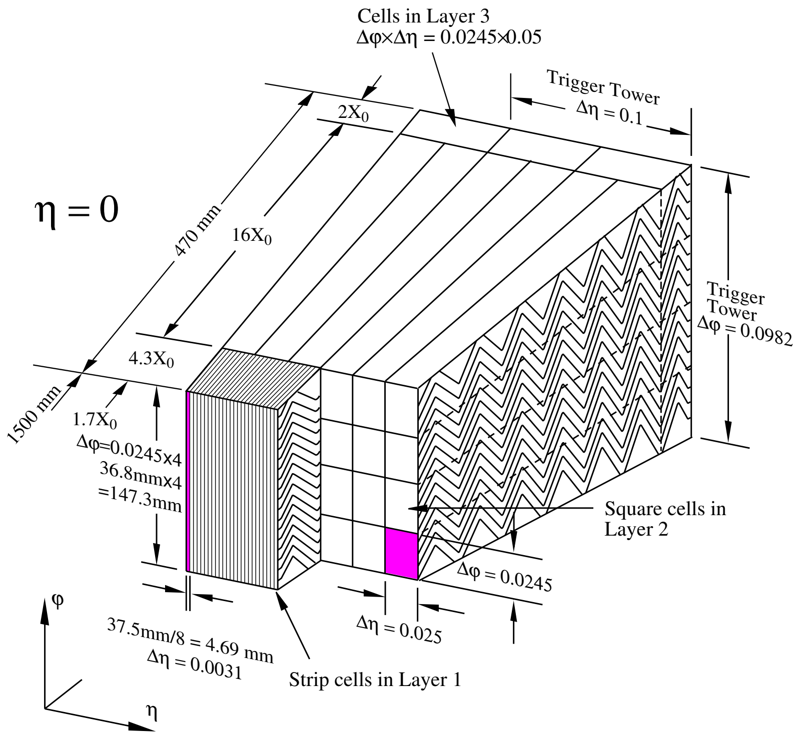

Figure 3.7: *Sketch of a barrel module where the different layers are clearly visible with the ganging of electrodes in ϕ. The granularity in η and ϕ of the cells of each of the three layers and of the trigger towers is also shown [13].*

has a thickness of about $16\,X_0$. In the second sampling most of the electromagnetic energy is deposit.

- The third sampling has a granularity of $\eta \times \phi = 0.05 \times 0.0245$ and a thickness of $2\,X_0$. The third sampling records shower which leaks out of the electromagnetic calorimeter.

The hadronic calorimeter The hadronic calorimeter (HCAL) [19] covers a range up to $|\eta| < 4.9$ and is divided into two parts, `the barrel calorimeter` and the `end-cap calorimeter`. The barrel calorimeter is a sampling calorimeter operating in a range of $|\eta| < 1.6$. The active material are scintillator tiles while the absorber material is iron. The thickness is about 10 interaction lengths (10 λ) which is required by the size of the hadronic showers. The energy resolution is about 50 % $\sqrt{(E)}$ $\otimes$3% [20]. The end-cap calorimeter covers the region within $1.5 < |\eta| < 3.2$ and uses liquid argon as active and copper as absorber material. The end-cap section is thicker ($\sim$ 12 λ) because for larger rapidity the hadron shower containment has to be more efficient.

The tile calorimeter is a sampling calorimeter in the barrel region. The absorber material is iron whereas the detector or active material are scintillating tiles. The structure of the tiles which are placed radially is periodic along the z-axis. The tile calorimeter is build of one central barrel and two extended barrels.

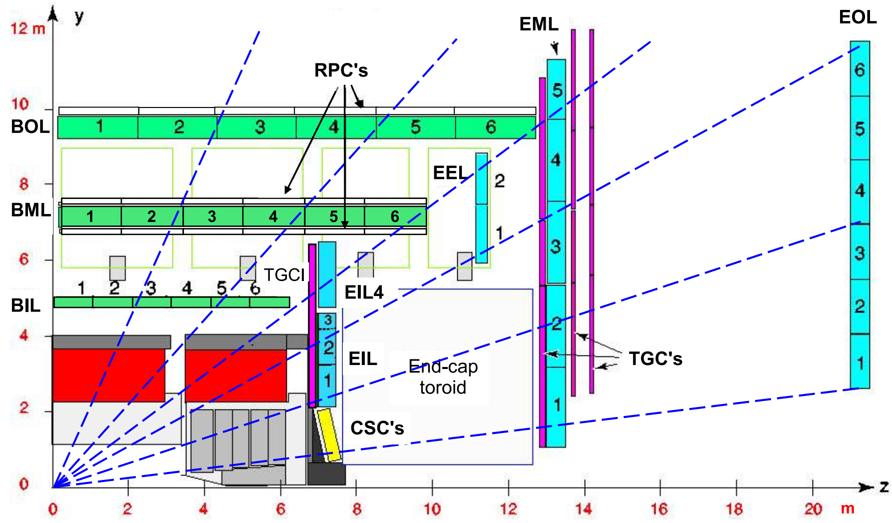

Figure 3.8: *Cross-section of the muon system in a plane containing the beam axis (bending plane). Infinite-momentum muons would propagate along straight trajectories which are illustrated by the dashed lines and typically traverse three muon stations [13].*

The forward calorimeter A `forward calorimeter` (FCAL) has been build at a distance of 4.7 m from the interaction point in order to cover the region $3.1 < |\eta| < 4.9$. The FCAL is also a liquid argon calorimeter and contains copper absorbers. The FCAL has to work with a high level of radiation. In ATLAS, the FCAL is integrated into the end-cap cryostat. The FCAL consists of three sections. One is made of copper and the other two are made of tungsten.

In general the calorimeter has to provide the trigger with event information and in addition it has to measure the energy and direction of jets (the hadronic calorimeter) and the energy and direction of electrons and photons (the electromagnetic calorimeter). A separation of electrons, photons and hadronic tau decays from jets is also required. Figure 3.6 shows all components of the calorimeter system.

3.2.3 The muon spectrometer

Muons are minimal ionising particles, they cannot captured by the calorimeter system. A strong magnetic field orthogonal to the trajectory of the muon bends the muons and the track can be measured. This requires that the muon system is the outermost part of the ATLAS detector [21]. A cross section of the muon system is shown in Fig. 3.8. The magnetic deflection of the muon trajectories in the toroid magnet allows to measure muon properties.

`Monitored Drift Tubes` (MDT) provide an excellent single wire resolution ($\sim 80\,\mu$m) which makes them suitable for track measurement. MDTs are build of aluminium drift tubes of 3 cm diameter with different lengths (0.7–6) m. The `Cathode Strip Chambers` (CSC), have a high granularity and provide measurements at large η, that means near the beam line. The last part, the `Resistive Plate Chambers` (RPC) in the barrel region and the

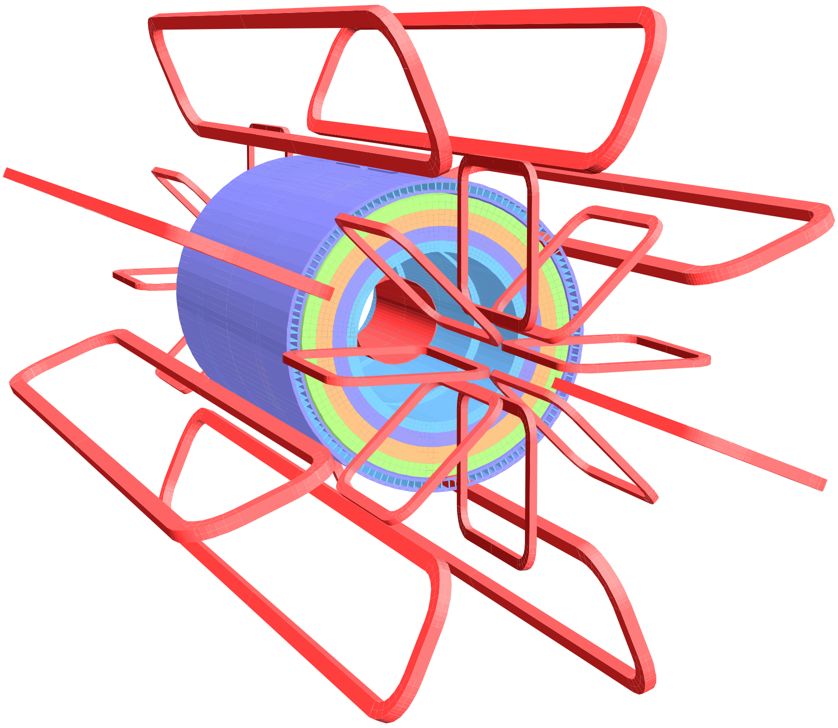

Figure 3.9: *Geometry of magnet windings and tile calorimeter steel. The eight barrel toroid coils, with the end-cap coils interleaved are visible. The solenoid winding lies inside the calorimeter volume. The tile calorimeter is modelled by four layers with different magnetic properties, plus an outside return yoke. For the sake of clarity the forward shielding disk is not displayed [13].*

`Thin Gap Chambers` (TGC) in the end-cap region, supply the Level 1 trigger (see Chapt. 4) with important information. Due to the (expected) bunch crossing of about 25 ns, they must have a better timing resolution as the bunch crossing gap. In addition, RPC and TGC also provide the MDT with further measurements, like the second coordinate of the tracks.

3.2.4 The magnetic field

Figure 3.9 shows the geometry of the magnet windings and tile calorimeter steel. The magnet system in ATLAS is divided into four parts (one solenoid and three toroids). The solenoids provide a magnetic field of 2 T and bends the particle tracks in the inner detector system. The barrel toroid provides a magnetic field of 0.5 T while the end-cap provides 1 T. The toroidal field is required in order to measure the momenta of muons passing the muon spectrometer.

3.3 Detector performance with collision data

Sub detector	Designed resolution	Measured resolution
Inner det.	$\sigma_{\mathrm{p_T}}/\mathrm{p_T} = 0.05\,\%\mathrm{p_T} \otimes 1\,\%$	$\sigma_{\mathrm{p_T}}/\mathrm{p_T} = (4.83 \pm 0.16) \times 10^{-4}\mathrm{GeV}^{-1} \times \mathrm{p_T}$
ECAL	$\sigma_{\mathrm{E}}/\mathrm{E}10\,\%/\sqrt{\mathrm{E}} \otimes 0.7\,\%$	$\sigma_{\mathrm{E}}/\mathrm{E}\ 1\,\%/\sqrt{\mathrm{E}} \otimes 0.7\,\%$
HCAL	$\sigma_{\mathrm{E}}/\mathrm{E}50\,\%/\sqrt{\mathrm{E}} \otimes 3\,\%$	$\sigma_{\mathrm{E}}/\mathrm{E} = 50\,\%[20-30]\,\mathrm{GeV}$
FCAL	$\sigma_{\mathrm{E}}/\mathrm{E}100\,\%/\sqrt{\mathrm{E}} \otimes 10\,\%$	$\sigma_{\mathrm{E}}/\mathrm{E} = 50\,\%[20-30]\,\mathrm{GeV}$
Muon spectr.	$\sigma_{\mathrm{p_T}}/\mathrm{p_T} = 10\,\%$	$\sigma_{\mathrm{p_T}}/\mathrm{p_T} = [4-5]\,\%$

Table 3.2: *Resolution of the detector components [22, 23, 24].*

Sub-detector	Number of channels	Operational fraction
Pixels	80 M	97.2 %
SCT silicon strips	6.3 M	99.2 %
TRT transition radiation tracker	350 k	97.5 %
LAr EM calorimeter	170 k	99.9 %
Tile calorimeter	9800	98.8 %
Hadronic end-cap LAr calorimeter	5600	99.8 %
Forward LAr calorimeter	3500	99.9 %
LVL1 calo trigger	7160	99.9 %
LVL1 muon RPC trigger	370 k	99.5 %
LVL1 muon TGC trigger	320 k	100 %
MDT muon drift tubes	350 k	99.8 %
cathode strip chambers	31 k	98.5 %
RPC barrel muon chambers	370 k	97.0 %
TGC end-cap muon chambers	320 k	99.1 %

Table 3.3: *Operational fraction in 2010 data taking [25].*

Table 3.2 compares the expected resolution for the different sub detectors with measured resolutions using $\sqrt{s} = 7\,\mathrm{TeV}$ data and Tab. 3.3 shows the ATLAS detector status for the 2010 data taking at $\sqrt{\mathrm{s}} = 7\,\mathrm{TeV}$.

Figure 3.10 shows the residuals (defined as the measured hit position minus the expected hit position from the track extrapolation) for the detector alignment reconstructed in LHC minimum bias events at $\sqrt{\mathrm{s}} = 7\,\mathrm{TeV}$. Full blue circles show the real data residuals after the detector alignment, and the open red circles show the residuals using MC with a perfectly aligned detector (normalised to the number of entries in the data distribution). The local x coordinate of the pixels is along the most precise pixel direction [25].

Figure 3.11 shows the relative alignment of the electromagnetic calorimeter and the inner detector to the cluster-track matching variables in the electron and photon reconstruction and identification [26]. Electron candidates which passing the medium offline identification criteria and fulfil $\mathrm{p_T} > 20\,\mathrm{GeV}$, $|\eta| < 2.47$ are selected. In addition, only events compatible with the production of W or Z boson are accepted ($\mathrm{m_T} > 40\,\mathrm{GeV}$ for one electron or $\mathrm{m_{ee}}$ in the range of [66,116] GeV for two electrons are considered). The distributions show the

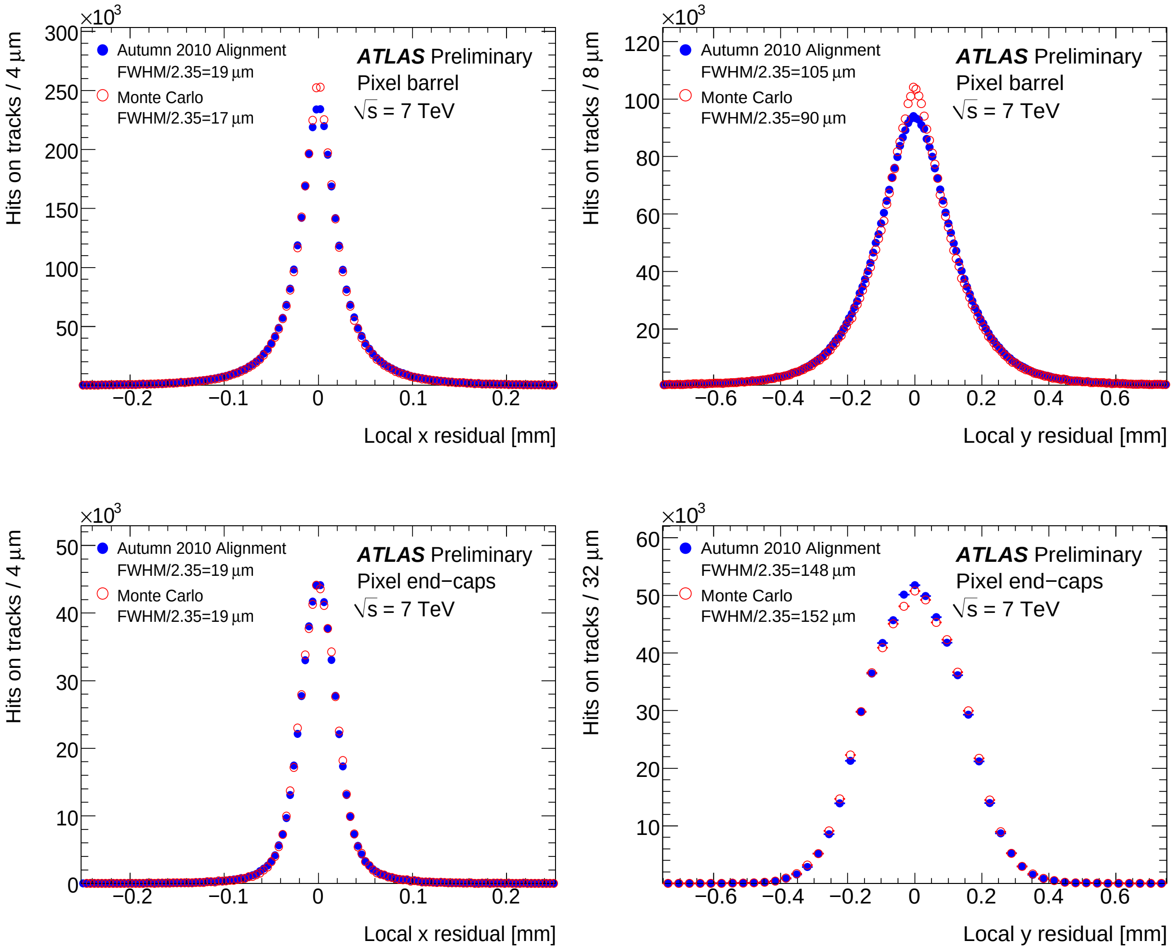

Figure 3.10: *Distribution of the local x unbiased residuals of the pixel end-cap modules [25].*

difference between the cluster pseudo-rapidity, determined from the first sampling of the electromagnetic calorimeter, and the pseudo-rapidity of the inner detector track extrapolated intersection at the entrance of that sampling. The black distribution is before and the red after the inter alignment of the electromagnetic calorimeter and the inner detector. The two-peak structure visible for $|\eta| > 1.52$ is due to the end-cap transverse displacement of the order of 5 mm corrected by the alignment procedure (see top-left plot in Fig. 3.11). The distributions of the difference between the cluster azimuth, determined from the second sampling of the electromagnetic calorimeter, and the azimuth of the inner detector track extrapolated intersection at the entrance of that sampling are shown in Fig. 3.12. Figure 3.13 shows the invariant $m_{\mu\mu}$ system for the inner detector and the combined performance.

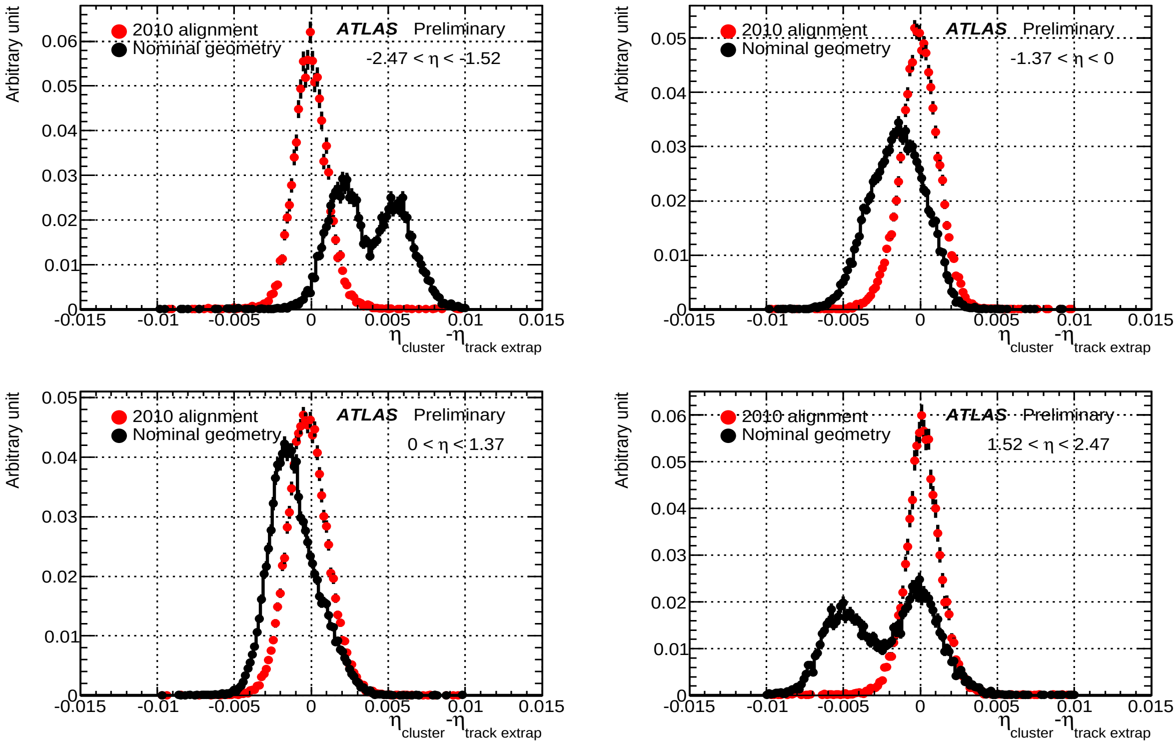

Figure 3.11: *Distributions for η for the second sampling in the electromagnetic calorimeter [26].*

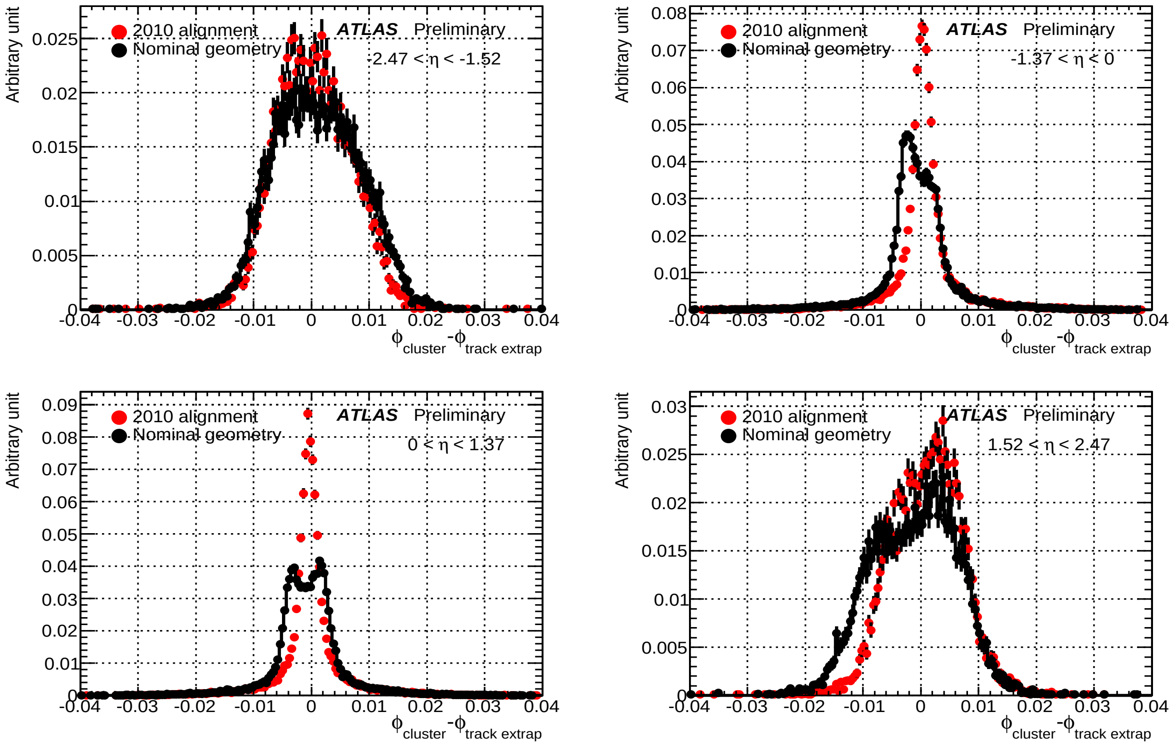

Figure 3.12: *Distributions for ϕ for the second sampling in the electromagnetic calorimeter [26].*

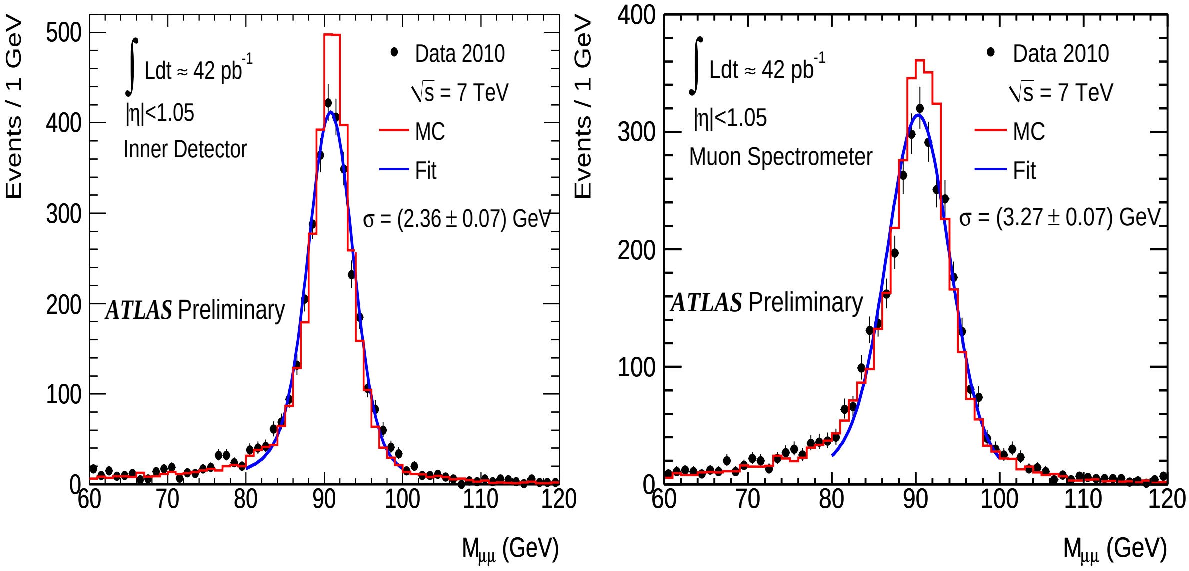

Figure 3.13: *The di-muon invariant mass distribution for oppositely charged muon pairs with transverse momentum above 20 GeV for the inner detector (a) and for the combined performance (b) [25].*

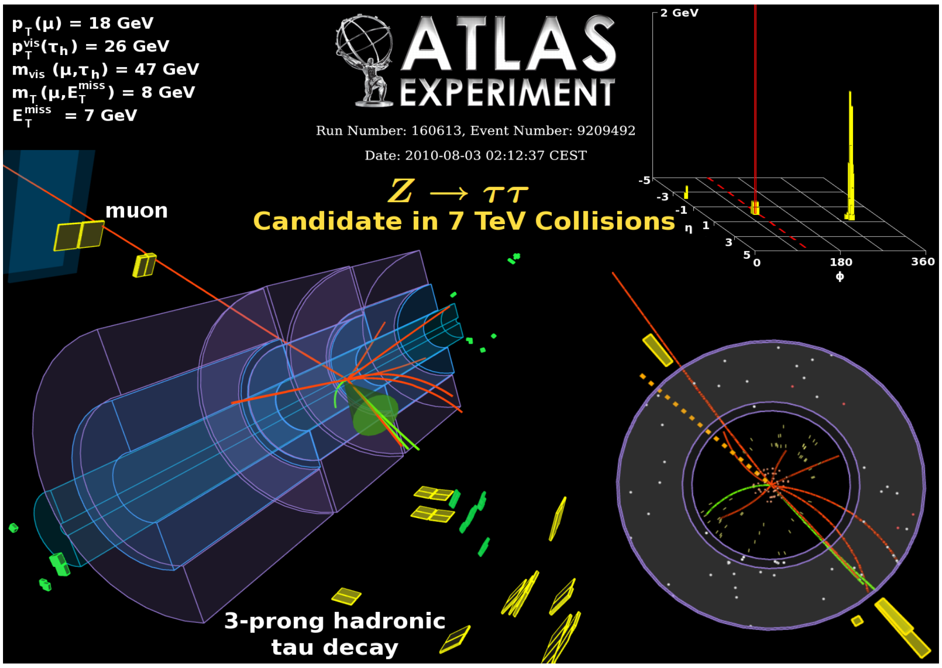

Figure 3.14: *The first* Z $\rightarrow \tau\tau$ *event candidate [25].*

The properties of these event are:

- $p_T(\mu) = 18\,\mathrm{GeV}$ and $p_T^{vis}(\tau) = 26\,\mathrm{GeV}$
- $m^{vis} = 47\,\mathrm{GeV}$ and $m_T(\mu, E_T^{miss}) = 8\,\mathrm{GeV}$ and $E_T^{miss} = 7\,\mathrm{GeV}$.

Chapter 4

Data taking and trigger performance at ATLAS

This chapter discusses the data taking at the ATLAS detector including the trigger system as well as the Monte Carlo production required for pre- and comparison studies.

4.1 Monte Carlo generation and detector simulation

To understand and interpret the collected events it is necessary to simulate physical processes with detailed theoretical knowledge and calculations. The response of the detector to the event has to be simulated as well. The challenge is the implementation of all different effects from the sub-detector components. Different Monte Carlo generators [27, 28] are used to simulate several theoretical event models. The general structure of a Monte Carlo production [29] is shown in Fig. 4.1.

The different steps are:

- hard scattering processes described in the SM
- underlying (minimum bias) events
- initial and final state parton (QCD) radiation
- fragmentation of partons into the observed hadrons
- decay simulation.

The generator used for the presented analysis is `PYTHIA` [30] which is a multipurpose generator and provides all sub processes as shown in Fig. 4.1. Almost all SM (and few SUSY) models are provided in the leading order. Another important generators are `HERWIG` [31], `Alpgen` [32] and `MC@NLO` [33].

The next step is the simulation of the interaction of particles with (detector) matter. ATLAS uses the `GEANT4`[1)] [34] simulation which provides several important features. It can be used for the design of a new detector, for the interaction of an existing detector with

[1)] GEANT means **GE**ometry **AN**d **T**racking.

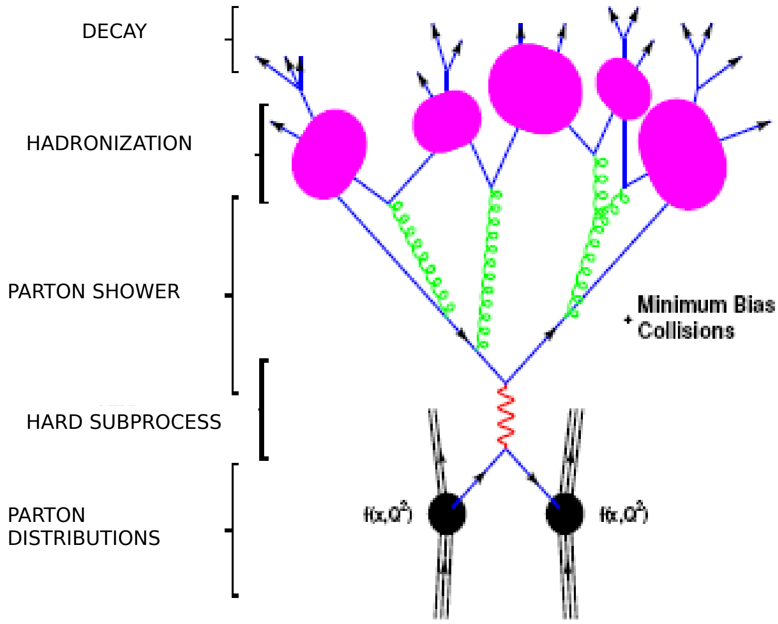

Figure 4.1: *The different steps of MC production.*

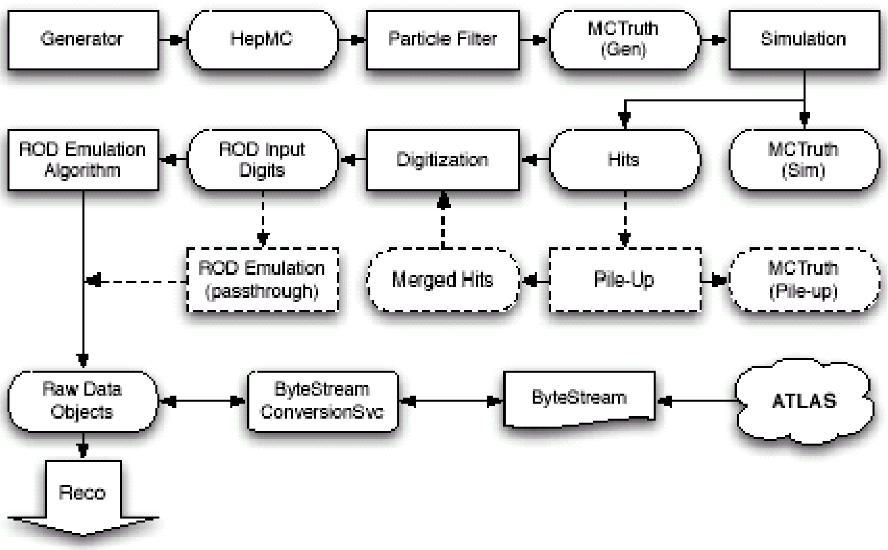

Figure 4.2: *The ATLAS simulation chain.*

particles, and can also be used for trigger cross checks. Different detector geometries can be approved. The full simulation chain in ATLAS is shown in Fig. 4.2.

4.2 Data taking at ATLAS

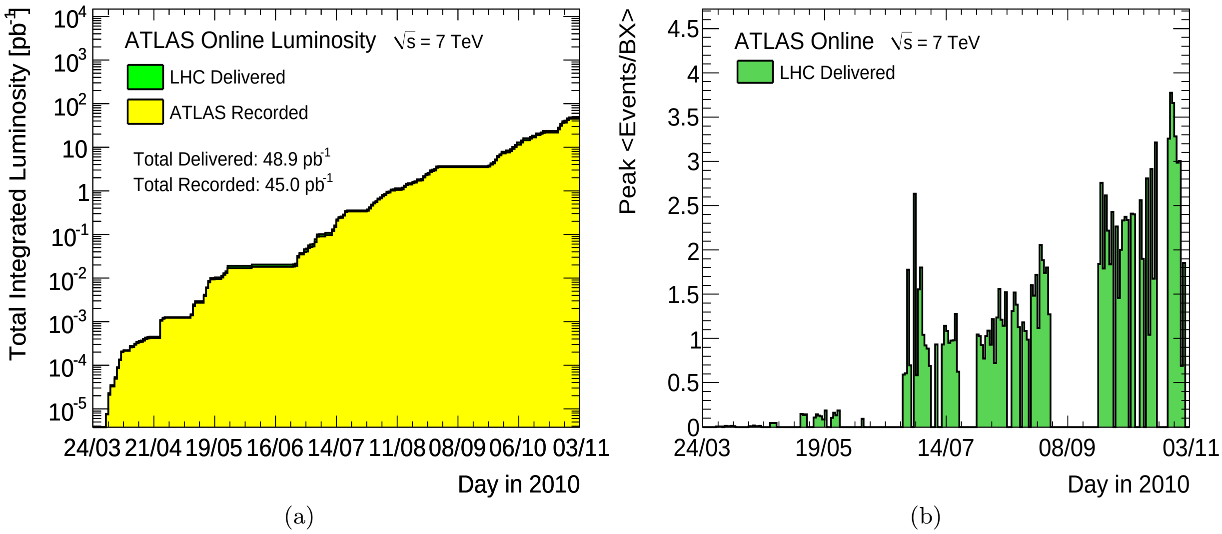

Figure 4.3: *Total integrated luminosity (a). The Number of interactions per bunch crossing (b) [35].*

From March 2010 up to November 2011 LHC runs in very good performance. LHC produces data with a total integrated luminosity of 48.9 pb$^-$1. ATLAS has recorded 45.0 pb$^-$1 (see Fig. 4.3) which corresponds to a data taking efficiency of about 93 %.

The data are stored in different data formats to cover different individual analysis goals [36]:

- **RAW:** contains events coming from the last trigger level. The event size is about 1.6 MB.

- **ESD (Event Summary Data):** contains events after the reconstruction process with sufficient content for data analysis. The event size is in the order of (0.5–1) MB.

- **AOD (Analysis Object Data):** derived from ESD with smaller event size compared with the previous formats.

- **DPD (Derived Physics Data):** is separated in three levels. The primary (D1PD) is divided into the performance and the physics DPD. The secondary (D2PD) contains are written in POOL format and is more specific. The tertiary (D3PD) is the data format used for this analysis and is a collection of ROOT [37] files.

4.3 The ATLAS trigger

4.4 The general trigger structure

In this section a general overview of the ATLAS trigger and data acquisition system (DAQ) will be given [38]. The ATLAS trigger and DAQ system is responsible for the selection of interesting events and it is based on three levels of online event selection.

All parameters used in this chapter are collected here:

- **Central Trigger Processor (CTP):**
  - Generates the LVL1 accept.
- **Chain:**
  - Is build of signatures with the requirement of one signature per decision step and per chain. The chain can only splitting at the interface of two trigger levels.
- **Detector Control System (DCS):**
  - DAQ system which comprises the control of the sub-detectors and common infrastructure of the experiment. It provides the communication between the ATLAS experiment and the CERN as well as the LHC.
- **LVL1 Accept:**
  - A signal produced by the Central Trigger Processor when an event has met the LVL1 trigger criteria.
- **Read-Out Buffer (ROB):**
  - Receives data from one Read Out Link which is the physical link between ROD and ROS through which the data are sent.
- **Read-Out Driver (ROD):**
  - Is part of the electronics and gathers data from the derandomisers and builds ROD fragments to be send to the RoIB.
- **Region of Interest (RoI):**
  - RoI are directions in the detector which are identified in LVL1. Two types exist:
    -Primary RoI: these RoIs are originating directly in LVL1
    -Secondary RoI: these types do not correspond to the LVL1 trigger but might be used for HLT steering. An example is the minimum bias trigger which comes directly from the **CTP**.
- **Region of Interest Builder (RoIB):**
  - Combines RoI information from different parts of LVL1 and forwards it to a LVL2 supervisor.

- **Read-Out Sub-system (ROS):**
  - The ROS is part of ATLAS Data Flow systems and accepts data from the read out drivers (ROD) stores them and makes them available to LVL2 and EF.
- **Signature:**
  - Is a logical combination of different TE via AND (and sometimes NOT). This combination follows from the fact that separate single TE would lead to too high rates.
- **Data Acquisition System (TDAQ):**
  - Is the abbreviation for the complete ATLAS trigger project.
- **Trigger Element (TE):**
  - Is used for communication between the trigger steering and configuration. It is an entity corresponding to physical objects like muon or electron and so on.

In Fig. 4.4 the different functional elements are presented. The trigger part is divided into the level 1 (LVL1), the level 2 (LVL2) and the event filter (EF) conflated to the high level trigger (HLT). The movement of data between the different processing nodes is provided by the data flow system. During the LVL1 decision the complete event data is kept in pipeline memories which are placed in the detector front-end electronics. If an event is accepted by the LVL1 selection the data for this event will be transferred to the readout buffers (ROBs). Furthermore, the LVL1 trigger system produces information which includes positions of interesting objects in form of η and the azimuthal angle ϕ. The results of the LVL2 decision are send to the data flow manager (DFM) which is part of the event builder (EB). In the event builder, the event will be assembled. The event filter (EF) has access to the full event information.

4.5 LVL1 trigger

The ATLAS trigger is based on physical objects like muons, electrons or jets which are identified already in LVL1 [39]. It uses the concept of `Region of Interests` (RoI) which are defined as regions (defined in η and ϕ) of detector areas where a certain activity above a given threshold can be observed. The nomenclature is that the capitals describe the physical object and the number defines the required transverse momentum. For example, `EM20` defines an electromagnetic cluster in the calorimeter with an p_T larger than 20 GeV. A RoI delivers the (η, ϕ) information and the required energy thresholds of these physical objects and seeds the trigger algorithms on the HLT [40].

The LVL1 trigger is a hardware based system which has to reduce the event rate from 40 MHz to about 75 kHz. The latency therefore is about 2.5 μs. The main parts of LVL1 are the calorimeter trigger and the muon trigger. The tracking trigger is not available in LVL1 because it is not possible to handle the huge number of tracks per event at energies of

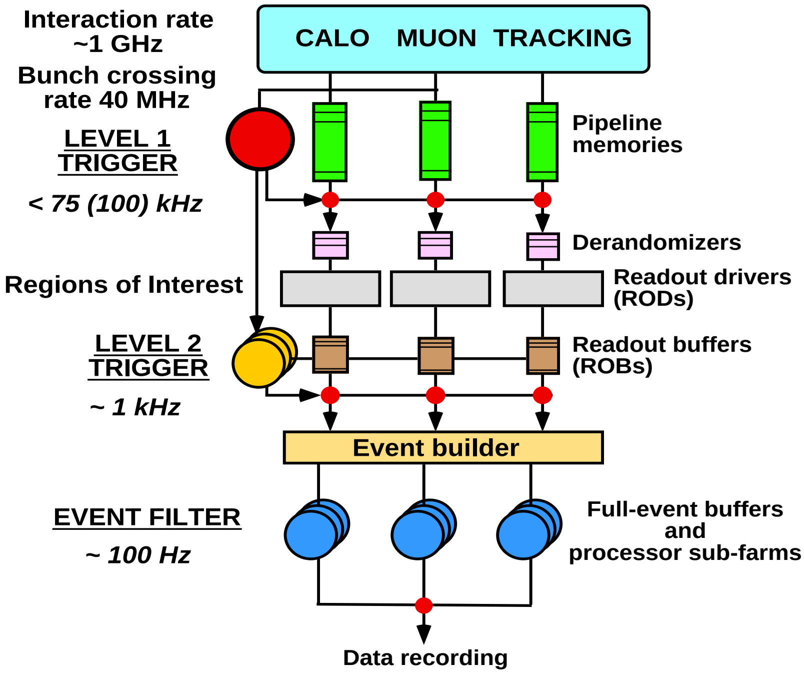

Figure 4.4: *The ATLAS trigger and data acquisition system (DAQ).*

7 TeV in the given time of 2.5 μs. In the following the calorimeter trigger, the muon trigger as well as the central trigger processor (CTP) are briefly discussed.

The calorimeter trigger

The calorimeter trigger uses a pre-processor followed by a jet/energy sum processor and a cluster processor. About 7200 relatively-coarse granularity trigger towers are separated in electromagnetic and hadronic towers. For electron/photon identification a sliding window algorithm sums all neighbouring trigger towers and finds the maximum tower in a $\Delta\eta \times \Delta\phi$ region of 0.2×0.2. A tau/hadron identification is also available using the same inputs. The jet trigger algorithm uses a granularity of $\Delta\eta \times \Delta\phi \simeq 0.2 \times 0.2$ and sums over electromagnetic and hadronic calorimeters.

The muon trigger

The muon trigger uses only the resistive plate chambers (RPC) and the thin gap chambers (TGC) information. The algorithms require a coincidence of hits in different layers. Low p_T muons are selected by requiring three hits in the four inner layers while for high p_T muons one requires an additional hit in the outer station [39].

The central trigger processor

The central trigger processor (CTP) (Fig. 4.5) receives information from the calorimeter trigger and the muon trigger and provides the final `LVL1 accept` [41]. Furthermore, it pro-

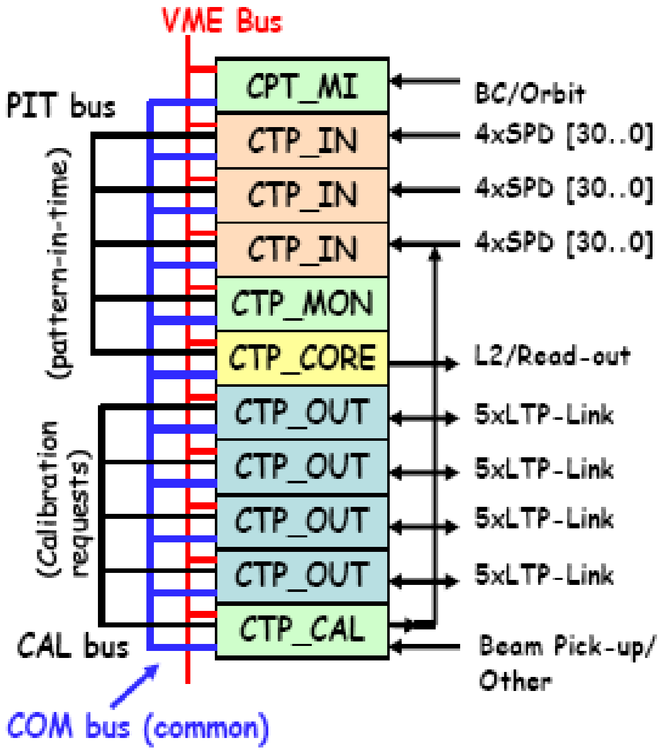

Figure 4.5: *The Central Trigger Processor modules.*

cesses trigger summary information for the LVL2 trigger and the data acquisition system and provides information for the monitoring of the trigger, detector and beam conditions. The CTP includes in addition internal triggers (e.g. random triggers or minimum bias triggers). The trigger information consists of multiplicities for electrons/photons, taus/hadrons etc.. The CTP sends also the RoI information to the RoIB and event data to the `read out system` (ROS). The LVL1 trigger produces 256 LVL1 `trigger items`. A trigger item is a logical combination of different RoIs. The LVL1 configuration sets the conditions for the event selection. Within the CTP the required number of fulfilled RoIs is checked by comparing this number with the required multiplicity from the trigger configuration. These multiplicity N is the number of RoIs of a certain type provided by the muon or calorimeter system. If the calorimeter or muon chambers delivers the required number of RoIs then the event gets the LVL1 accept and passes through the next trigger level.

Different `cores` build the CTP, the `CTPCORE`, the central board, combines trigger information to trigger items and forms the `LVL1 accept` (L1A). Three `CTPINs` handle the information from the subsystems. The `CTPMON` module monitors the trigger information on bunch to bunch basis. In addition, the CTP is composed of several `CTPOUTs` and one `CTPCAL` for calibration tasks. A CTPIN module is constructed of four connectors (CON) with 31+1 inputs (trigger input BITs). The total number of these BITs is 372 for three

CTPINs. To synchronise the data-flow so called `Pattern in Time` (PIT) are defined with the total number of 160.

The challenge is the assignment of 372 BITs to 160 PITs. Since the cabling should be fixed, the assignment has to be flexible depending from the trigger menu. This is realised with a `switch matrix`. A `trigger menu compiler` (TMC) reads in a defined trigger menu and creates output files in form of look-up tables (LUT) and contant addressable memories (CAM) via the switch matrix. The hardware is able to read in these files which a stored in a database. In general, all trigger conditions are stored in this database which is defined as a relational database (RDB). All information for each individual `run` are summarised here. This includes all required `items, signatures` and `trigger elements` as well as all temporary conditions like `prescale` or `pass through factors`.

The RDB can be steered via a graphical user interface (GUI) and is a collection of tables connected via `keys`. As described before, the challenge is the assignment of all counters (which simply counts how often a certain threshold is activated) to the correct names. For each trigger menu the counter to threshold relation can be different. In addition each CTPIN board and each CON has its own numeration. Therefore an identification string defines the CON and the CTPIN board (SLOT). The second problem is the PIT assignment, that means the threshold-BIT to PIT relation. Since a threshold can overlay more than one BIT, it is assigned to several PITs. To realise such conditions, two more tables are stored into the RDB. The first table contains the counter information, the second the PIT mapping.

The RDB to trigger connection is realised by the definition of `loader classes`. Almost each table has its own loader class. The loader class configures the information in the RDB (e.g. LUT or CAM) to make it readable for the trigger modules.

The PIT to threshold assignment: As mentioned before, a single threshold can overlay several BITs (e.g. MU6 at BIT 0 and 1, 2MU8 at BIT 2,3, and 4). Each BIT will be labelled with a PIT, via the class `PitAssignment`.

This can be checked with the help of the TDAQ-GUI [38]. To optimise the performance of the RDB to trigger connection it is useful to read out information directly from the database without creating text files. This is realised via the class `GetFiles` which is used by the CTPIN and CTPCORE modules.

4.6 The high level trigger

After LVL1 processing the information is send to the HLT which is divided into the LVL2 and the EF. The HLT has access to all sub-detectors at full granularity and is (contrary to the LVL1 trigger) a software based system. The main difference between the LVL2 and the EF is the complexity of the algorithms interpreting the raw data. The LVL2 and the EF share the principle of seeded algorithms from the preceding trigger level. Although the EF has access to the whole event, it actually uses only the LVL2 result to seed the algorithms.

4.6.1 LVL2 trigger

The LVL2 receives the output from LVL1 in form of RoIs from the calorimeter or muon trigger and also event information from the CTP. LVL2 has to reduce the incoming rate from 75 kHz to about 1 kHz. The LVL2 is asynchronous and therefore almost dead time free, because every event is processed at the next free farm node which avoids tailback of data. The processing time at LVL2 is about 10 ms. All algorithms at LVL2 have access only to the detector information of the corresponding RoIs. During the decision, the whole event is stored in Read Out Buffers (ROB).

If an event is accepted by the LVL1, different parts of the LVL1 trigger send information like RoIs or passed thresholds. As mentioned previously, the RoIs Builder (RoIB) combines these fragments and sets it in the LVL2 supervisor (L2SV) which supervises the data flow through the trigger. The L2SV itself is a small group of about 10 processors. The LVL2 processing unit (L2PU) communicates with the L2SV from which it receives the RoI information.

4.6.2 Event filter trigger

On event filter level, algorithms which are comparable with the offline reconstruction software have access to the full event information. After the LVL2 acceptance, the corresponding event goes to the event builder which assembles the full ATLAS event and sends it to the event filter. In principle, the event filter trigger works very similar to the LVL2 trigger and reduces the rate from 1 kHz to about 0.1 kHz. The event filter has two main entities, the event handler (EH) and the event filter supervisor (EFS). The first performs the activities related to the event selection. The second is responsible for the configuration, initialisation and error handling of the event filter.

The events are selected and classified within the event selection software (ESS). Possible candidates like electrons or jets are reconstructed from event data by using a particular set of HLT algorithms. An event is selected if at least one of the reconstructed objects satisfies the corresponding trigger chain which contains the physical objects. From the event selection point of view there is no precise boundary between LVL2 trigger and the event filter trigger.

The data flow through the trigger system decreases during the run because of the decreasing luminosity. The ATLAS trigger has to keep the rate constant. The current strategy is the possible changing of the prescale and pass through factors within a run. It is useful to define a time interval where this changes are activated. Therefore the luminosity block is chosen which is a time period in an order of one minute.

The luminosity block is the time which is needed to collect enough data to determine the dead time and prescale corrected luminosity. The length of this time interval is set by the luminosity block supervisor. Furthermore, a luminosity block number is defined as a number which uniquely tags a luminosity block within a run. ATLAS has constraints on the length of a luminosity block. It is possible to change the prescale and pass through factors within a luminosity block. These new factors will be valid in the next luminosity block. This guarantees the stability because a decreased prescale factor keeps the rate constant.

4.7 Monitoring of the trigger system

The ATLAS trigger and data acquisition system is highly complex and requires an efficient monitoring system [42]. One important issue is the correct reading of a menu configured in the database (RDB). Each menu in the database has a unique key, the `supermaster key` (SMK). This allows a fast access to the trigger information in the menu. As described before, due to the decreasing luminosity, the prescale factors have to be adapted to guarantee a efficient usage of the band width.

A `prescale key` (PSK) is defined for each individual sub-menu including different prescale conditions. It is for both cases (the online and the offline trigger performance) important to monitor the correct key information in the trigger menu and in the event information provided by the trigger. For the online case it is important (e.g. to avoid data loss due to wrong prescale keys) and in the offline reconstruction (e.g. for cross section measurements, to rescale the number of objects to the correct prescale factor).

4.7.1 General aspects of trigger monitoring

All trigger performances are realised within the global ATLAS data quality monitoring (DQM). The trigger steering provides about 2500 histograms containing variables like event rates, error codes, timing information, physics parameters etc.. A data quality flag (DQ) is stored for each sub-detector or trigger (also for the τ-lepton selection) to provide different information concerning the performance.

The consistency checks for the different keys as described above are implemented in the trigger steering code. For the online analyis a instantaneous information is required. For the offline reconstruction, the user can cross check this by request. In order to have access to this information a monitoring tool is provided which will be discussed in the following.

Offline check

The offline check runs with the official standard reconstruction and reads out COOL [43] information automatically. The keys in COOL and for the event information have to be checked in order to make sure that the correct menu is also performed during data taking. For a mismatch of keys from COOL and event information, histograms are filled providing the information which key causes the problem. In addition, a text file is written including more detailed information like the corresponding luminosity block, bunch crossing ID as well as run and event number.

Figures 4.6 and 4.7 show the performance of the consistency checks. The nine variables on the x-axis are:

- SMK DB Null or SMK BS Null: filled if the supermaster key stored in the trigger configuration data base (DB) or from read out of the event (byte stream, BS) is zero.
- SMK Inconsistent: filled if the supermaster key is different for DB and BS.
- HLT Prescale DB Null or HLT Prescale BS Null: filled if the prescale key stored in the trigger. configuration data base (DB) or from read out of the event (BS) is zero

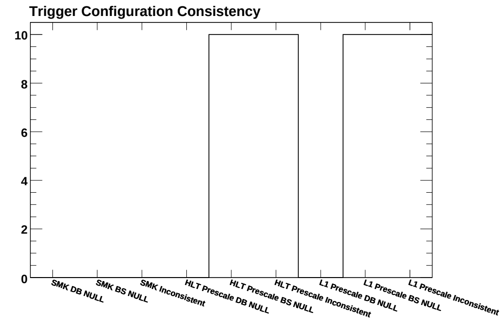

Figure 4.6: *The plot shows the consistency checks for LVL2 for a test file in order to check the performance of the code.*

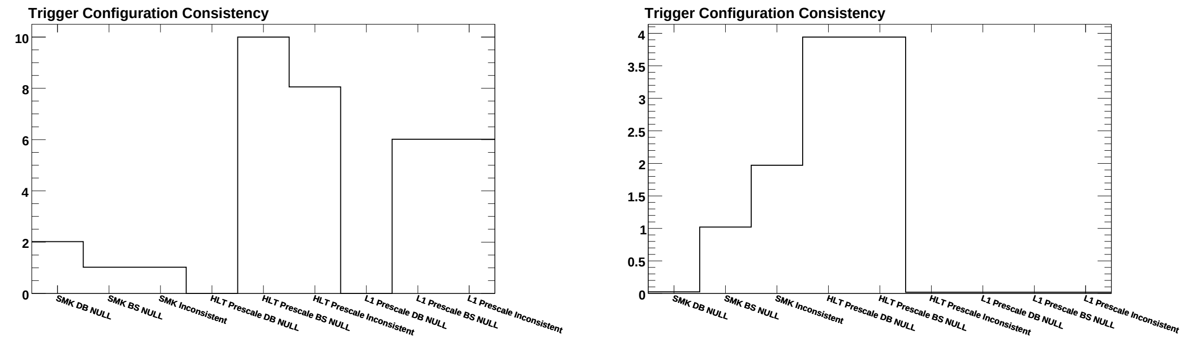

Figure 4.7: *The plots show the consistency checks for LVL2 (left) and EF (right) for a test file in order to check the performance of the code. The interpretation of these distributions are discussed in the text.*

separated into LVL2 and the Event Filter.

- HLT Prescale Inconsistent: filled if the prescale key is different for DB and BS.
- L1 Prescale DB Null or L1 Prescale BS Null: filled if the prescale key stored in the trigger configuration. data base (DB) or from read out of the event (BS) is zero on LVL1.
- L1 Prescale Inconsistent: filled if the LVL1 prescale key is different for DB and BS .

The histogram in Fig. 4.6 has entries in the 'HLT Prescale BS Null' bin and the 'HLT Prescale Inconsistent' bin. This figures out, that the prescale factors are not (or wrongly) defined in the event read out. Although the trigger data base has defined these factors. For that reason the prescale key is inconsistent.

For the two histograms in Fig. 4.7 the situation is more complex. Figure 4.7(a) shows the performance for LVL2. For two events the supermaster key is not defined in the data base. The byte stream includes one event which has no defined supermaster key. The one entry in the third bin is related to the fact, that one event has no defined supermaster key stored in the data base and the byte stream. If the two events in the first bin and the one event in the second bin are not the same, the third bin ('SMK Inconsistent') gets three entries. All further bins are defined with the same logic. In Fig. 4.7(b) it can be seen that the 'SMK BS NULL' bin has one entry while the 'SMK Inconsistent' bin has two entries. In this case each event has a defined supermaster key stored in the data base and also (except for the event which causes the entry in the second bin a defined supermaster key written into the byte stream. The second entry in the third bin points out that for one event the supermaster key stored in the data base and stored in the byte stream is not the same, although both keys are defined.

Online check

The online check is implemented within the code which runs the trigger configuration. The information from the online check will be send to the online histogram presenter (OHP). Furthermore, a cross check if all processors work is provided. The OHP receives the same histograms as used for the offline monitoring.

4.8 The Tau trigger

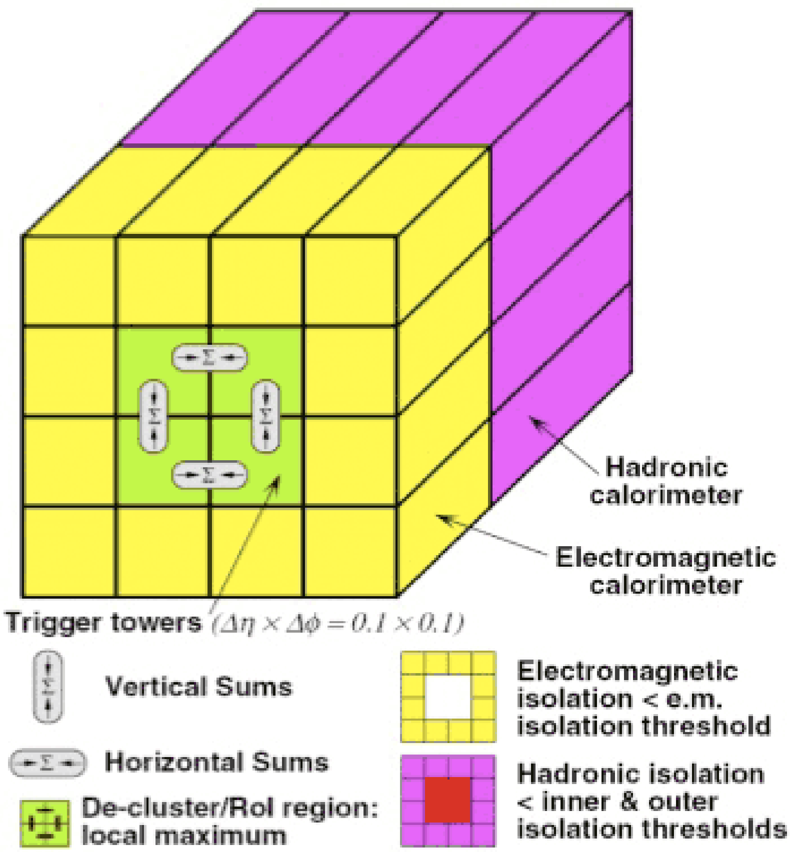

Figure 4.8: *The ATLAS Level 1 tau trigger.*

For the semi-leptonic $Z \to \tau\tau$ decay the lepton trigger is used. This promises a better performance since leptons are easier to trigger than taus. Nevertheless, the tau trigger will be shortly described. The `LVL1` tau trigger selection [44] uses electromagnetic and hadronic calorimeter information using trigger towers which provides the RoI. The centre of the RoI defines the position of the tau candidate. The transverse energy E_T is defined from the two most energetic neighbouring towers in the electromagnetic calorimeter and the full core of the hadronic calorimeter. The `LVL2` selection uses the second sampling layer in the electromagnetic calorimeter to refine the LVL1 position. Finally, the total energy of all layers in the electromagnetic and hadronic calorimeter is computed. The shape variable `EMRadius` (see Chapt. 6) is calculated with respect to the refined LVL2 position and is defined as

$$(\Delta \mathrm{R})^2 = (\Delta\eta)^2 + (\Delta\phi)^2 \tag{4.1}$$

in a region of size 0.6 × 0.6 [45]. It is shown in [45] that the separation of taus and QCD jets is quit difficult at low E_T regions while it becomes better for higher E_T. The `EMRadius` together with the total transverse energy are the basis of the LVL2 (calorimeter) selection. The event filter selection is based on offline tau algorithms [46]. Topological clusters (using cell information within RoI of 0.8 × 0.8) around the LVL2 direction are used. All clusters within such a RoI are collected to a jet. A jet calibration (tau specific) and the position of the tau candidate as well as the transverse energy and a number of shower shape variables are provided by the event filer selection. The most important tau signatures are summarised in Tab. 4.1 [45].

single tau signatures	**comment**
`tau12`,`tau16i`,`tau20i`,`tau29i`,`tau38i`, `tau50`, `tau84`	all single tau triggers, lower tau signatures have to be prescaled due to the QCD background. Only high transverse energy signatures can be run standalone
combined trigger	**comment**
tau+missingE_T	required for $W \to \tau\nu$ at low luminosity
tau+ℓ (+jets)	for events with two taus in the final state (e.g. Z or H^0)
tau+tau (+jets)	selects events with two taus decaying hadronically. Useful for Higgs boson or Z' searches
tau+jets, tau+b-jets	alternative trigger for $t\bar{t}$ studies

Table 4.1: *Trigger signatures for the tau selection referred to `tauXXi` where `tau` is the particle, `XX` the transverse energy threshold, and `i` the isolation criteria.*

4.8.1 Tau trigger performance for $\sqrt{s} = 7\,\mathrm{TeV}$ data

The performance of the tau trigger was checked during 2010 collision data. Figures 4.9 and 4.10 show few variables studied in order to optimise the trigger conditions.

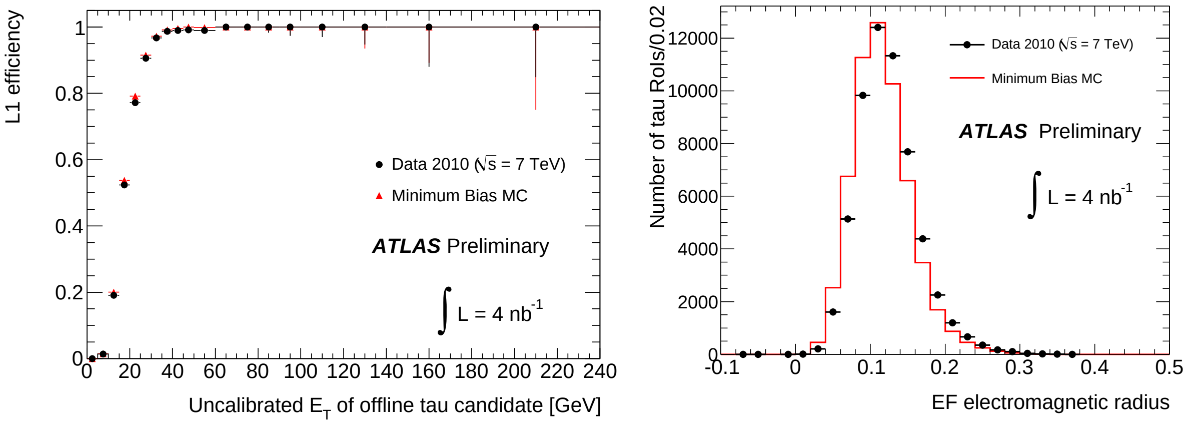

Figure 4.9: *Fraction of the offline tau candidates matched to a L1 trigger object with $E_T > 5\,GeV$ as a function of the E_T of the offline tau candidate. The small differences at low E_T can be attributed to inefficiencies in the forward region of the detector (a). Comparison of the tau candidate EM radius distribution at EF for 7 TeV data and MB MC. MC has been normalised to the number of entries of the data histogram. The shift of the peak has also been observed in the corresponding variable reconstructed offline and can be attributed to the insufficient tuning of MC to 7 TeV collision data. The systematic effects include the description of the hadronic shower, the underlying event and detector material (b) [25].*

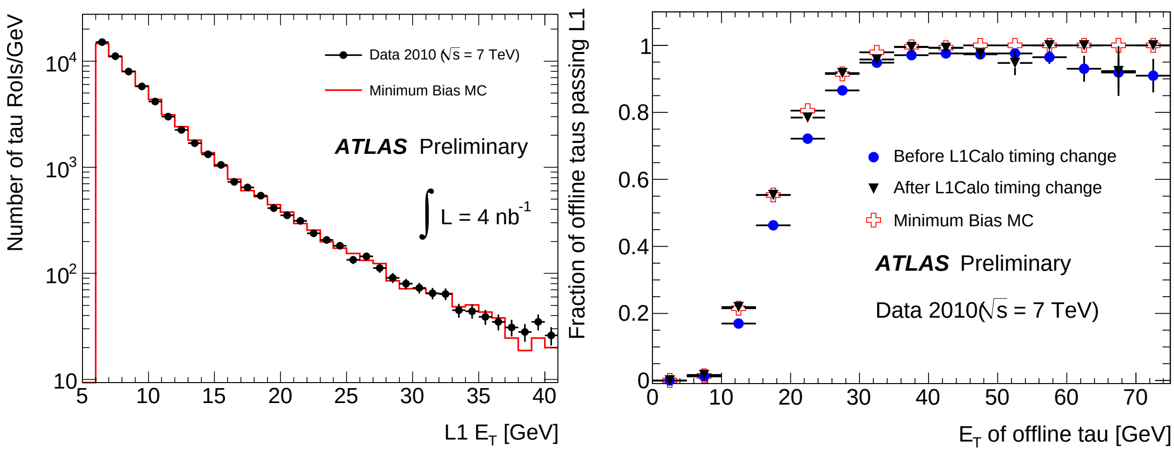

Figure 4.10: *Comparison of the L1 tau candidate ET distribution for 7 TeV data and MB MC. The cut off at 6 GeV corresponds to the L1_TAU5 threshold. The Monte Carlo has been normalised to the number of entries of the data histogram (a). Fraction of the offline tau candidates matched to a L1 trigger object with $E_T > 5\,GeV$ as a function of the E_T of the offline τ-lepton candidate (b) [25].*

Chapter 5

General aspects of the $\mathrm{pp} \rightarrow \mathrm{Z} + \mathrm{X} \rightarrow \tau\tau$ analysis

This chapter describes the process $\mathrm{pp} \rightarrow \mathrm{Z} + \mathrm{X} \rightarrow \tau\tau$ with all contributing particles in more detail. For simplification in the following the process $\mathrm{pp} \rightarrow \mathrm{Z} + \mathrm{X} \rightarrow \tau\tau$ will be denoted as $\mathrm{pp} \rightarrow \mathrm{Z} \rightarrow \tau\tau$ or $\mathrm{Z} \rightarrow \tau\tau$. The discussion starts with an overview of the Z-boson production followed by general remarks for the Z-boson as well as for the τ-lepton.

5.1 Z-boson production at a proton-proton collider

5.1.1 Topology of proton proton collisions

To describe the production theoretically it is necessary to define the structure function of the proton. Since protons collide at the LHC these functions become important in order to estimate the energy range of the produced particles. The structure functions describe the content of the proton. It is build up of partons which are the valence quarks u and d, the gluons and the sea-quarks (quark-antiquark pairs).

The proton was investigated at DESY in Hamburg. The accelerator HERA collides electrons and protons and the to investigate the inner structure of the proton (see Fig. 5.1). The full proton momentum will be separated in parton momenta $\mathrm{p}_{\mathrm{parton}} = \mathrm{x}_{\mathrm{Bjoerken}} \cdot \mathrm{p}_{\mathrm{proton}}$.

A short overview of the Z-boson production at the LHC will be given. In general, at hadron colliders, the massive electro-weak bosons (W and Z) will be produced mostly in $\mathrm{q}\bar{\mathrm{q}}$ annihilation. A hadronic cross section is defined as a product of hard scattering cross sections and non-perturbative parton distribution functions (PDF). The hard scattering cross sections are known up to orders of α_{s}^2 for observables depending on the same energy scale and orders of α_{s} for observables depending on different energy scales [49]. The `total cross section` in pertubative QCD can be expressed as:

$$\sigma_{\mathrm{tot}}(\mathrm{pp} \rightarrow (\mathrm{Z} \rightarrow \ell\ell)\mathrm{X}) = \sum_{\mathrm{a,b=q,\bar{q},g}} \int \mathrm{dx_1 dx_2 f_{a/p}(x_1}, \mu)\mathrm{f_{b/p}(x_2}, \mu)\hat{\sigma}_{\mathrm{tot}}(\mathrm{ab} \rightarrow (\mathrm{V} \rightarrow \ell\ell)\mathrm{X}) \tag{5.1}$$

where $\hat{\sigma}_{\mathrm{tot}}$ is the hard scattering cross section and $\mathrm{f_{a/p}}$ and $\mathrm{f_{b/p}}$ are the parton distributions

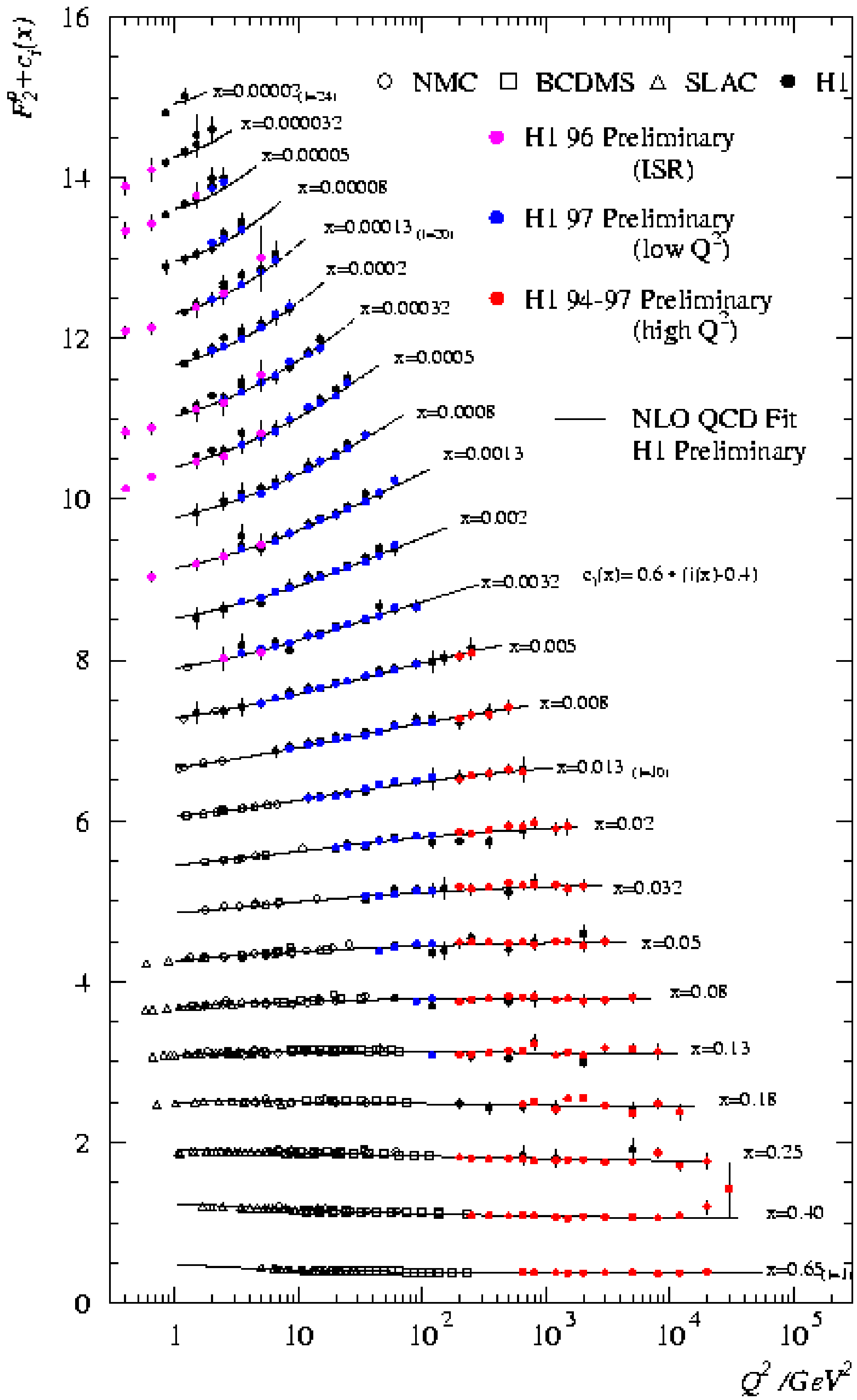

Figure 5.1: *Structure function obtained from H1 at DESY [47].*

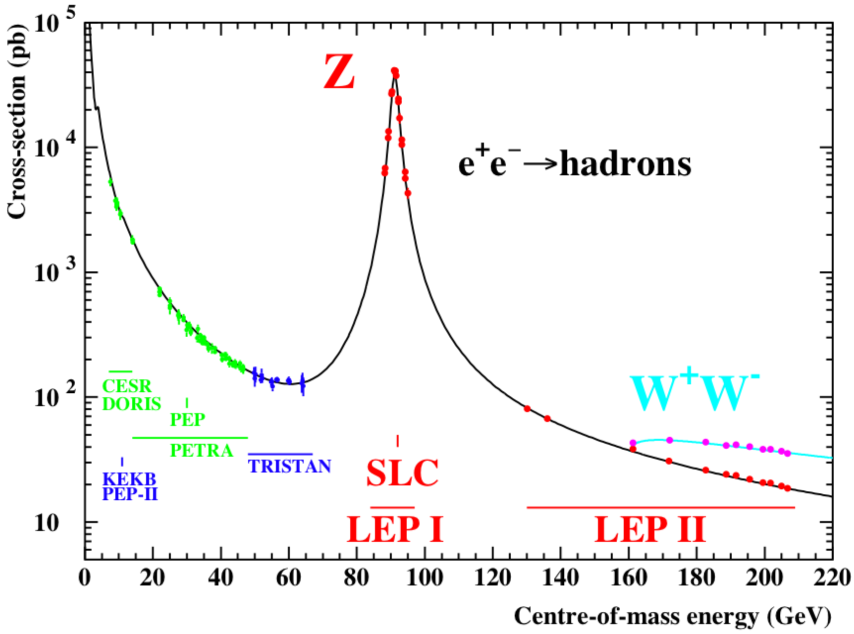

Figure 5.2: *The cross section versus the centre-of-mass energy at LEP.It shows the resonance peak at $\sqrt{s}$ = 91.2 GeV for $e^+e^- \rightarrow q\bar{q}$. Measured values from different experiments are also drawn [48].*

for the protons. The factorisation scale is denoted as μ. The integration is over the momentum fractions x_1 and x_2 and the sum is over the parton flavour. In Chapt. 3 the total cross section is shown in Fig. 3.2. For the total Z-boson cross section in proton-proton collisions (at centre-of-mass energies $\sqrt{s} = 7\,\mathrm{TeV}$) the $u\bar{u}$ annihilation is dominant [50]. The relation is $u\bar{u} \sim d\bar{d} \gg s\bar{s} \gg c\bar{c}$.

5.2 The physics of the Z-boson

Figures 5.3 and 5.4 show the measured p_T distributions for Z-bosons obtained from first ATLAS data at $\sqrt{s} = 7\,\mathrm{TeV}$ [51]. The transverse momentum was obtained from the measurements in the $Z \rightarrow ee$ and $Z \rightarrow \mu\mu$ channel respectively. The $Z/\gamma^\star$ momentum is measured from lepton transverse momenta. The Z-boson p_T spectrum is found to be well described by Monte Carlo descriptions.

The Z-boson is responsible for the neutral current predicted by Sheldon Glashow, Abdus Salam and Steven Weinberg in 1961 [52, 53, 54] in the context of the electro-weak unification. The first direct evidence appeared 1983 at the super proton synchrotron (SPS) detectors UA1 and UA2 [55, 56, 57]. Its properties were most precisely determined by the LEP detectors OPAL and L3 [48] in $e^+e^- \rightarrow f\bar{f}$ processes.[1)] This was a milestone in the confirmation of the Standard Model (SM). Precision measurements at centre-of-mass energies $\sqrt{s} = M_Z$ allow to measure many aspects of electro-weak unification very exactly. (e.g. forward-backward asymmetry, electro-weak radiative corrections). Figure 5.2 (with the centre-of-mass energy

[1)] The $W^\pm$ bosons were observed at Tevatron and LEP2.

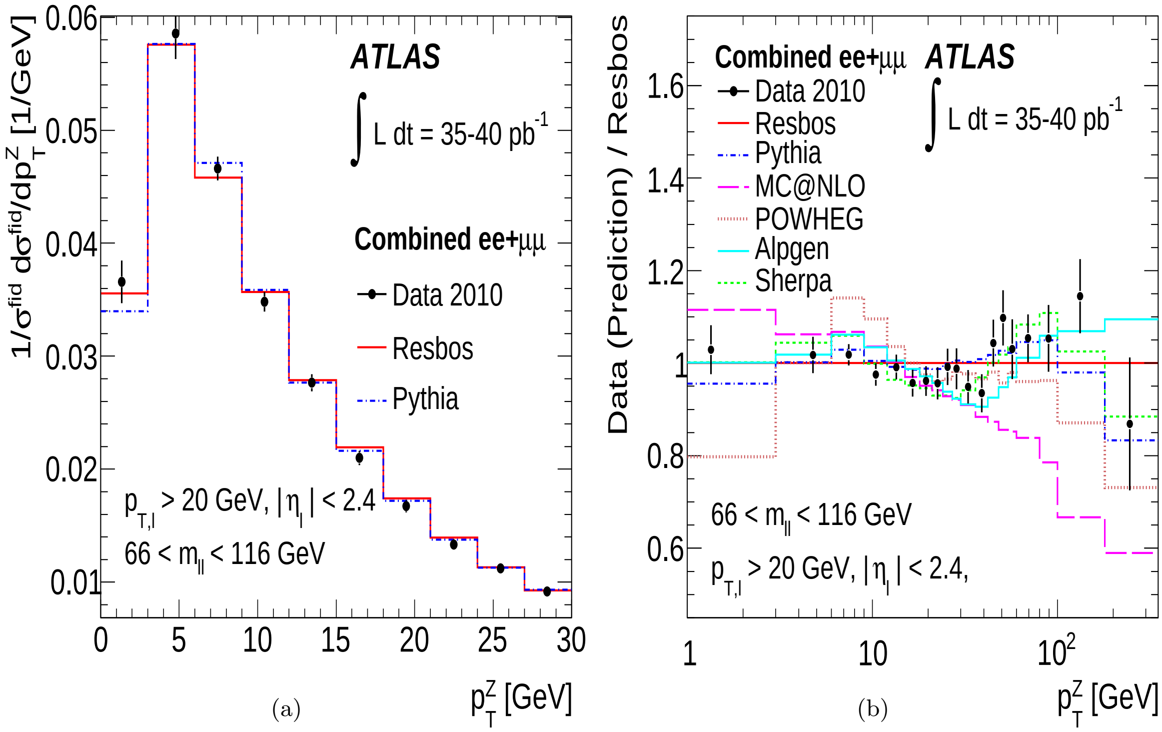

Figure 5.3: *The measured p_T distribution for the Z-boson at ATLAS (a) and a comparison of different MC generators (b) [51].*

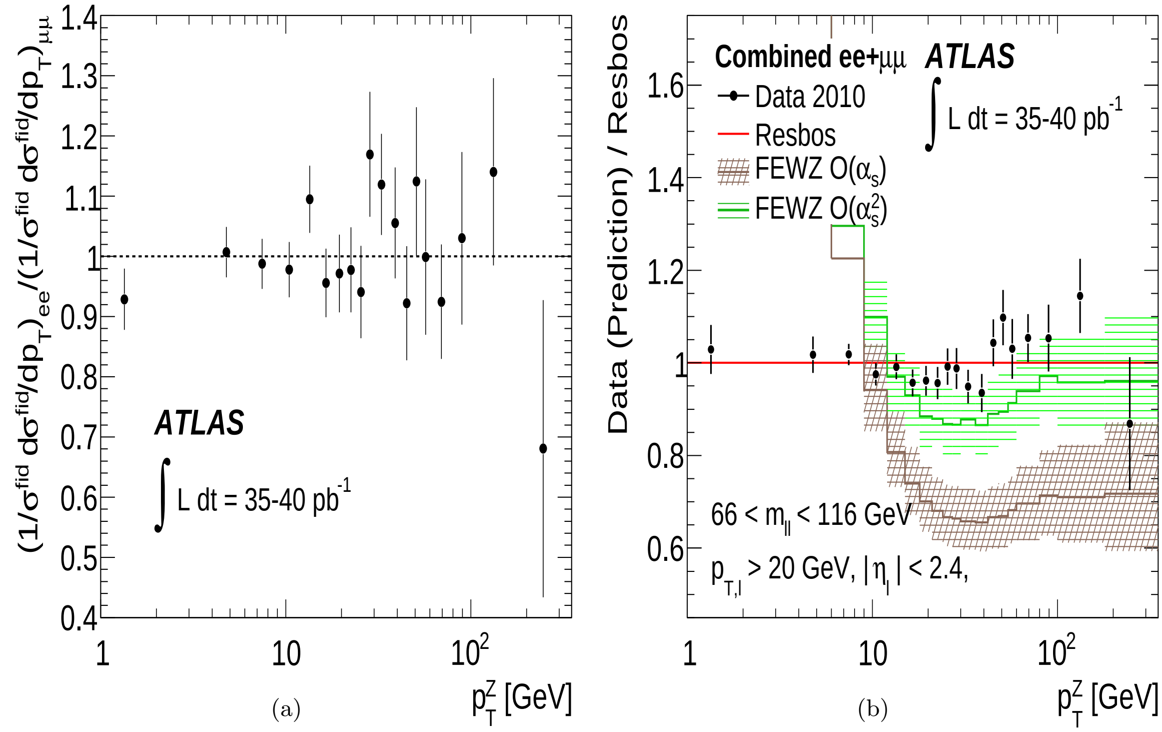

Figure 5.4: *Comparison of ee and $\mu\mu$ channel (a) and and a comparison of different MC generators (b) [51].*

Z decay width	Experiment [MeV]	SM prediction [MeV]
$\Gamma_{e^+e^-}$	83.0 ± 0.5	83.52–83.78
$\Gamma_{\mu^+\mu^-}$	83.8 ± 0.8	83.52–83.78
$\Gamma_{\tau^+\tau^-}$	83.3 ± 1.0	83.52–83.78
Γ_{had}	1740 ± 9	1731–1742
$\Gamma_{had}/\Gamma_{lep}$	20.92 ± 0.11	20.71–20.84
Γ_{inv}	496.2 ± 8.8	496–497
Γ_{tot}	2487 ± 10	2484–2496

Table 5.1: *Different Z-boson decay widths for LEP data. For the SM prediction the mass of the top quark is assumed to be* $\mathrm{m_{top}} = 150\,\mathrm{GeV}$ *and the value of* $\alpha_\mathrm{s}(\mathrm{M_Z})$ *is assumed to be 0.118. Furthermore, the band of predicted values corresponds to the Higgs mass range of* $50\,\mathrm{GeV} \leq \mathrm{M_H} \leq 1000\,\mathrm{GeV}$ *[48].*

at the x-axis versus the cross section at the y-axis) shows the different resonances in e^+e^- collisions at LEP [48]. The total cross section for $e^+e^- \rightarrow f\bar{f}$ depends on the different inter-mediating processes. It is the sum of the Z mediated term, the γ mediated term, and the interference term and can be written as

$$\sigma(\mathrm{e^+e^-} \rightarrow \mathrm{f\bar{f}}) = \sigma(\mathrm{Z}) + \sigma(\gamma) + \sigma(\mathrm{Z}, \gamma). \tag{5.2}$$

Since the Z-boson is a resonance it decays instantaneously with a lifetime $\tau_\mathrm{Z} \approx 3 \times 10^{-25}\,\mathrm{s}$. The decay of the Z-boson can be expressed as

$$\Gamma_{\mathrm{Z}\rightarrow\mathrm{f\bar{f}}} = \delta_{\mathrm{QCD}} \mathrm{N_c} \frac{\mathrm{G}_\mu \mathrm{M_Z^3}}{6\pi\sqrt{2}} (\mathrm{g_V^2} + \mathrm{g_A^2}) \tag{5.3}$$

with the QCD radiative correction δ_{QCD}. $\mathrm{N_c}$ describes the colour flavours, G_μ is the `Fermi constant`, $\mathrm{M_Z}$ the mass of the Z-boson and $\mathrm{g_V}$ and $\mathrm{g_A}$ describe couplings of the vector and axial vector currents.

Table 5.1 shows the different decay widths for all possible Z-boson decays measured at LEP [48]. It shows an agreement between experiments and SM predictions. Two examples show the importance of the Z-boson measurements at LEP in context of the Standard Model: the angular and polarisation asymmetries due to parity violation and the number of light neutrino generations.

Asymmetries in the Z-boson environment can be separated into the longitudinal polarisation asymmetry, the unplaced forward-backward asymmetry, and the polarised forward-backward asymmetry [58]. The first asymmetry, the longitudinal polarisation asymmetry can be expressed as

$$\mathrm{A_{LR}} = \frac{\sigma_{\mathrm{e_L^-}} - \sigma_{\mathrm{e_R^-}}}{\sigma_{\mathrm{e_L^-}} + \sigma_{\mathrm{e_R^-}}} \tag{5.4}$$

where σ denotes the total cross sections for the $\mathrm{Z} \rightarrow \mu^-\mu^+$ production, obtained with a sum over the possible positron polarisations. The second is the unplaced forward-backward asymmetry which refers to the relative distance between the negative charged fermions f^-

travelling forward or backward relative to the incident e^- direction

$$\mathrm{A_{FB}} = \frac{\sigma_\mathrm{F} - \sigma_\mathrm{B}}{\sigma_\mathrm{F} + \sigma_\mathrm{B}}. \tag{5.5}$$

The forward region is defined as the region were $0 < \cos\Theta \leqslant 1$ and the backward region is defined as $-1 < \cos\Theta \leqslant 0$, with the angle Θ between the incoming electron and the outgoing negative fermion. The last asymmetry is the polarised forward-backward asymmetry which can be expressed as

$$\mathrm{A_{FB}^{pol}} = \frac{(\sigma_{\mathrm{e_L^-f_F}} - \sigma_{\mathrm{e_R^-f_F}}) - (\sigma_{\mathrm{e_L^-f_B}} - \sigma_{\mathrm{e_R^-f_B}})}{\sigma_{\mathrm{e_L^-f_F}} + \sigma_{\mathrm{e_R^-f_F}} + \sigma_{\mathrm{e_L^-f_B}} + \sigma_{\mathrm{e_R^-f_B}}}, \tag{5.6}$$

with $\mathrm{f_F}$ and $\mathrm{f_B}$ indicating forward and backward outgoing fermions.

The second consequence is the determination of the number of the light neutrino generations using LEP data [59]. The most straightforward method is to compare the total measured Z-boson width Γ_tot with the SM prediction:

$$\Gamma_\mathrm{tot}^\mathrm{SM} = 3\Gamma_{\nu\nu} + \Gamma_\mathrm{lep} + \Gamma_\mathrm{had}. \tag{5.7}$$

The number of light neutrino generations is therefore

$$\mathrm{N}_\nu = \frac{\Gamma_\mathrm{inv}}{\Gamma_\nu} \tag{5.8}$$

with the assumption that all decay channels contributing to Γ_inv containing $\nu\bar{\nu}$ pairs.

5.3 Physics of the τ-lepton

The τ-lepton (discovered in 1975 by Martin Perl and his collaborators [1]) has the same properties as the electron but a mass which is about 3480 times larger (see Tab. 2.2). Because of the large mass of 1.777 GeV it is the only lepton which can decay hadronically. Pions with a mass of about 140 MeV or kaons with a mass of about 500 MeV are the decay products in case of the hadronic decay. All possible decays of the τ^--lepton are summarised in Tab. 5.2. For analysing the hadronic τ-lepton decays a normalisation to the electron final state of the τ-lepton decay is applied:

$$\mathrm{R}_\tau = \frac{\Gamma(\tau^- \rightarrow \nu_\tau + \mathrm{hadrons})}{\Gamma(\tau^- \rightarrow \nu_\tau \mathrm{e}^- \bar{\nu}_\mathrm{e})}. \tag{5.9}$$

The τ-lepton decay into hadrons proceeds through the processes $\tau^- \rightarrow \nu_\tau \mathrm{d\bar{u}}$ or $\tau^- \rightarrow \nu_\tau \mathrm{s\bar{u}}$. The ratio can be roughly estimated due to the effect that the coupling to a virtual W only differs by a factor in the CKM matrices

$$R_\tau \simeq 3\ (\mid V_{ud} \mid^2 + \mid V_{us} \mid^2). \tag{5.10}$$

Decay	**probability** [%]
$\tau^- \to \mu^- \bar{\nu}_\mu \nu_\tau$	17.36 ± 0.05
$\tau^- \to e^- \bar{\nu}_e \nu_\tau$	17.84 ± 0.05
$\tau^- \to \pi^- \pi^0 \nu_\tau$	25.50 ± 0.10
$\tau^- \to \pi^- \nu_\tau$	10.90 ± 0.07
$\tau^- \to \pi^- \pi^+ \pi^- \nu_\tau$	9.33 ± 0.08
$\tau^- \to \pi^- \pi^+ \pi^- \pi^0 \nu_\tau$	4.59 ± 0.07
$\tau^- \to K^- \nu_\tau$	6.91 ± 0.23
$\tau^- \to K^- \pi^0 \nu_\tau$	4.52 ± 0.27

Table 5.2: *Possible decay-modes of the τ^--lepton.*

5.3.1 Inclusive decays

The mass of the τ-lepton is lighter than any charmed state. For that reason hadronically decaying taus must involve the weak quark current. A simply estimate of the branching ratio for the hadronic decay and the leptonic decay yields

$$\frac{\Gamma_{\mathrm{had.}}}{\Gamma_{\mathrm{lep.}}} \simeq \mathrm{N_c} \frac{|\ \mathrm{V_{ud}}\ |^2 + |\ \mathrm{V_{us}}\ |^2}{2} \to 1.5 \tag{5.11}$$

with the number of quark colour degrees of freedom $\mathrm{N_c}$. The experimental value is about 1.85±0.02 due to additional effects like electro-weak and QCD perturbative corrections.

5.3.2 Exclusive leptonic decays

The τ-lepton is a good candidate to check the `lepton universality`, that means the fact, that the three leptons (electron, muon, τ-lepton) have the same properties (spin, charge etc.) except the different masses. In particular, the weak coupling is expected to be identical. The theoretically expected ratio of leptonic decays is

$$\frac{\Gamma_{\tau \to \mu \nu_\mu \bar{\nu}_\tau}}{\Gamma_{\tau \to \mathrm{e} \nu_\mathrm{e} \bar{\nu}_\tau}} \simeq 0.973. \tag{5.12}$$

The branching ratio of the decay into muons is slightly smaller because of the relative phase space suppression compared with the electron branching ratio. This is also experimentally confirmed (see Tab. 5.2). Another important consequence of lepton universality is the observation that the rates for $\tau \to \mathrm{e}\bar{\nu}_\mathrm{e}\nu_\tau$ and $\mu \to \mathrm{e}\bar{\nu}_\mathrm{e}\nu_\tau$ must have the same value. This can be used to determine the τ-lepton lifetime τ_τ theoretically

$$\begin{aligned} \tau_\tau^{\mathrm{theor.}} &= (2.942 \pm 0.062) \times 10^{-13}\,\mathrm{s} \\ \tau_\tau^{\mathrm{expt.}} &= (2.95 \pm 0.03) \times 10^{-13}\,\mathrm{s}. \end{aligned} \tag{5.13}$$

5.3.3 Exclusive hadronic decays

The identification of τ-leptons (see Chapt. 6) is related only to the hadronically decaying τ-leptons. Hadronic final states are complex due to the large number of modes. In general, the weak current can be separated into the pure leptonic and the pure hadronic part

$$J^{\mu}_{\mathrm{weak}} = J^{\mu}_{\mathrm{lept.}} + J^{\mu}_{\mathrm{hadr.}}. \tag{5.14}$$

That means the matrix element can be expressed as

$$M_{\mathrm{semilept.}} = \frac{G_{\mu}}{\sqrt{2}} L^{\mu} H_{\mu} \tag{5.15}$$

with the Fermi coupling constant G_{μ}, the leptonic current L^{μ} and the hadronic current H_{μ}. The ratio R_{τ} defines the partial decay width of the τ-lepton into hadrons normalised to the partial decay width of the τ-lepton into electrons [60]:

$$R_{\tau} = \frac{\Gamma(\tau \rightarrow \bar{u}d) + \Gamma(\tau \rightarrow \bar{u}s)}{\Gamma(\tau \rightarrow e)}. \tag{5.16}$$

The numerator has two contributions, the decay into the final state ūd (non-strange, $\sim \cos^2 \Theta_C$) and the decay into ūs (strange, $\sim \sin^2 \Theta_C$) with the quark-mixing angle Θ_C (Cabibbo-angle, [61]). The leptonic current is given by

$$L^{\mu} = \bar{u}(\ell', s')\gamma_{\mu}(g_V - g_A\gamma_{\mu})u(\ell, s) \tag{5.17}$$

with $g_V = g_A = 1$ defined in the Standard Model. The hadronic current can be expressed in terms of vector and axial-vector current [62]:

$$H_{\mu} = \langle h(q) \mid V^{\mu}(0) - A^{\mu}(0) \mid 0 \rangle \tag{5.18}$$

with h(q) describing the hadrons. The hadronic current depends on the number of final state mesons. The first case, the one meson final state (pion or kaon) proceeds only through the axial vector current.

- **One meson decay**
  - The simplest decay mode into one pion π or kaon K can be well described by the decay constants f_{π} and f_K:

$$\langle (\pi(q), K(q)) \mid A^{\mu}(0) \mid 0 \rangle = i\sqrt{2} f_{(\pi,K)} q^{\mu}. \tag{5.19}$$

  - The branching ratios for the one meson decay can be determined using the τ-lepton lifetime τ_{τ} [63, 64] and are summarised in Tab. 5.2.
- **Two mesons decay**
  - The matrix element for the two meson decay can be written as

$$\langle (h_1(q_1)h_2(q_2)) \mid V^{\mu}(0) \mid 0 \rangle = \left[(q_1 - q_2)_{\nu} T^{\nu\mu} F^{h_1 h_2} + (q_1 + q_2)^{\mu} F_4^{h_1 h_2} \right] \tag{5.20}$$

  with the transverse projector $T^{\nu\mu}$ and the form factor F_4, which describes the two mesons h_1 and h_2 in an s wave.

  - The form factor $F^{h_1 h_2}$ can be obtained from the conserved vector current theorem [65, 66]. A typical process is $\tau^- \to \rho^- \ \nu \to \pi^0 \ \pi^- \ \nu$ via the ρ-resonance. One has to distinguish `Cabbibo suppressed` and `Cabbibo allowed` processes [67]. For example the final state $K^-\pi^0\nu_\tau$ is suppressed (the hadronic matrix element is dominated by $K^\star$.) The matrix element for the Cabbibo allowed process K^0K^- is dominated by the high energy tail of the ρ-resonance. The branching ratios can be obtained from Tab. 5.2.

- **Three mesons decay**
  - The structure of the matrix elements for three meson final states is much more complex as for the one or two meson case. The three meson mode can be expressed as

$$\langle (h_1(q_1)h_2(q_2)h_3(q_3)) \mid V^\mu(0) - A^\mu(0) \mid 0 \rangle \,, \tag{5.21}$$

    which allows for decay modes involving a kaon vector and axial vector contributions [68, 69].
  - A more detailed description using form factors can be found in [70, 71, 72].
  - The corresponding branching ratios can also be found in Tab. 5.2.

5.3.4 The τ-neutrino

Since the τ-neutrino is connected to all decay modes it will be shortly discussed. The first observation of the τ-neutrino was announced in July 2000 by the DONuT collaboration at Fermilab [73]. For this experiment, the Tevatron accelerated protons to produce τ-neutrinos via the decay of charmed mesons. The resulting particles passed through a number of magnets as well as iron and concrete blocks. In 2010 also the first τ-neutrino was observed at the OPERA experiment (Grand Sasso) [74]. The current upper mass limit is about 18.2 MeV [75].

5.3.5 Spin polarisation

Another central aspect of τ-lepton physics is the spin correlation of both charged τ-lepton states. It appears that the spins of the τ^--lepton and the τ^+-lepton are strongly correlated [76]. Experimentally, it was shown that the spins tend to be parallel and aligned with τ^--lepton and the τ^+-lepton momenta. A precise spin analysis is possible with the $\tau^- \to \pi^-\nu_\tau$ decay whereas the pion will be emitted almost in the direction of the spin of the τ-lepton which can be described by

$$\frac{d\Gamma}{d\cos\Theta} = \Gamma\frac{1 + P\cos\Theta}{2}, \tag{5.22}$$

where Θ describes the angle between the momentum of the outgoing pion and the spin quantisation axis of the τ-lepton. The polarisation of the τ-lepton along the quantisation axis is denoted as P. The measurement of the Z^0 resonance allows for a precise determination of the weak mixing angle Θ_W [77]. The polarisation is predicted as

$$P = -2(1 - 4\sin^2\Theta_W). \tag{5.23}$$

The measured polarisation is $P = -0.13 \pm 0.03$ which yields $\sin^2\Theta_W = 0.233 \pm 0.004$. Since the spin of the τ-lepton is measurable with a large sensitivity these can be used for the construction of a large number of CP violating variables. In addition and important for physics at LHC is the possibility to identify new heavy particles via their decay into τ-leptons. For example a charged Higgs boson would decay in a purely right-handed τ-lepton.

5.4 The contribution of the Z-boson and the τ-lepton in context of the Standard Model

The decay Z $\rightarrow \tau\tau$ plays an important role in many aspects of the physics within and beyond the Standard Model (SM). The Z-boson mass is nearby the mass of the predicted low mass Higgs boson and therefore an important background process for this energy region. Also for other new particles like a Z′ it is quite important to understand the Z-boson production and decay at the LHC. The τ-lepton is the final state for many processes expected for new physics and also connected with the Higgs mechanism (see Chapt. 2).

5.4.1 The τ-lepton as the final state for the Higgs boson

The Higgs boson production in proton-proton interactions can be subdivided into four scenarios:

- Gluon fusion ($\sigma \sim$ [20–60] pb): is proportional to the Yukawa coupling and has the largest production rate.
- Weak boson fusion ($\sigma \sim$ [3–5)] pb)
- Higgs strahlung ($\sigma \sim$ [0.2–3] pb): has the same coupling as in weak boson fusion.
- $t\bar{t}(b\bar{b})$ associated production ($\sigma \sim$ [0.2–3] pb): is proportional to the heavy quark coupling.

The most important Higgs decays are:

- H $\rightarrow \gamma\gamma$: which has a large background from pp $\rightarrow \gamma\gamma$.
- H $\rightarrow$ ZZ $\rightarrow \ell^+\ell^-\ell^+\ell^-$: known as the `golden channel` for $2\,m_Z < m_H < 600$ GeV. The main background is $pp \rightarrow ZZ$.
- H $\rightarrow$ ZZ $\rightarrow \ell^+\ell^-\nu\nu$: is known as the `silver channel` and becomes important for $m_H > 800$ GeV.
- H $\rightarrow$ WW $\rightarrow \ell^+\nu\ell^-\nu$: important for $m_H > 2m_W$ but difficult to distinguish signal from background processes.

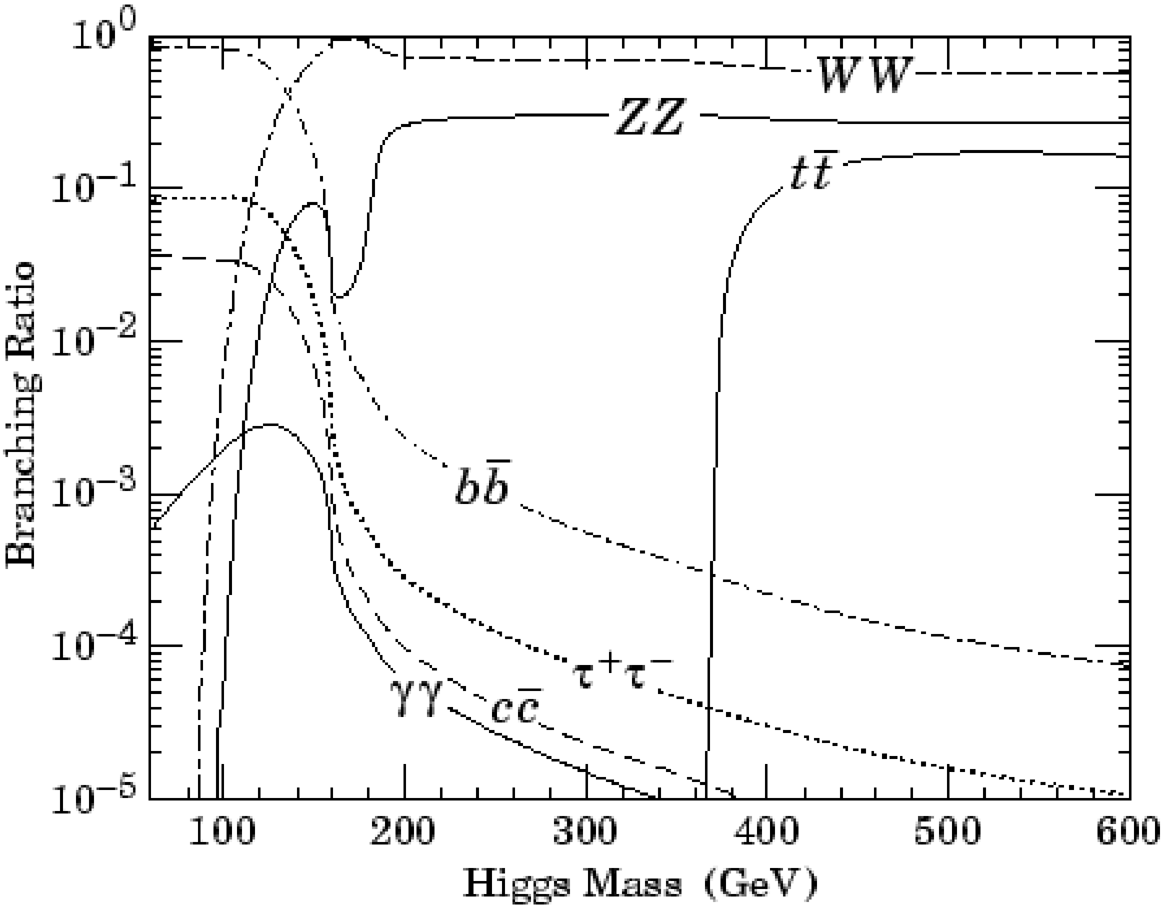

Figure 5.5: *The branching ratios for the expected Higgs decays depending on the Higgs mass. In general, the Higgs decays primarily into heavy particles (third generation). Although the relation $BR_{H\to b\bar{b}} > BR_{H\to\tau\tau}$ is realised, the decay into τ leptons is more important due to the challenging $b\bar{b}$ selection at the LHC.*

- $\mathrm{Ht\bar{t}} \to \mathrm{t\bar{t}b\bar{b}}$: is important for $120\,\mathrm{GeV} < \mathrm{m_H} < 130\,\mathrm{GeV}$.

In general (as shown in Fig. 5.5) the Higgs couplings are proportional to the particle masses. The decay channels for the low mass Higgs are almost the $\mathrm{b\bar{b}}$ and $\tau^-\tau^+$ final states. Since b-quarks are complicated to measure at the LHC, the $(\tau^-\tau^+)$ final state is the most important low mass Higgs decay channel.

5.4.2 The τ-lepton as the final state for supersymmetric scenarios

More essential as for Higgs physics, the τ-leptons are important in the investigation of SUSY models. Due to the SUSY breaking, left-right sfermion mixing occurs (this follows the $\mathrm{SU(2)_L}$ doublet and right handed singlet structure). The sfermion mass eigenstates are mixtures of left- and right handed components and the mixing matrix can be written as:

$$\mathcal{M}^2_{\tilde{\tau}} = \begin{pmatrix} m^2_{\tilde{\tau}_L} & -m_\tau(A_\tau + \mu\tan\beta) \\ -m_\tau(A_\tau + \mu\tan\beta) & m^2_{\tilde{\tau}_R} \end{pmatrix}, \tag{5.24}$$

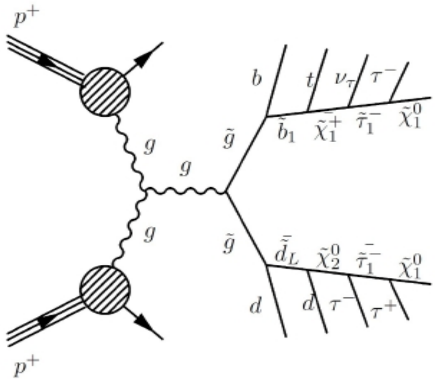

Figure 5.6: *Typical SUSY decay chain including $\tilde{\tau}$ and τ-leptons.*

with the ratio of the vacuum expectation values $\tan\beta$ and the sign of the Higgsino mixing parameter μ . The parameter A_τ expresses the soft SUSY-breaking trilinear scalar coupling. If A_τ, μ or $\tan\beta$ are large, the off-diagonal elements become important. The mass eigenstates can be expressed as

$$\begin{pmatrix} \tilde{\tau}_1 \\ \tilde{\tau}_2 \end{pmatrix} = \begin{pmatrix} \cos\theta_\tau & \sin\theta_\tau \\ -\sin\theta_\tau & \cos\theta_\tau \end{pmatrix} \begin{pmatrix} \tilde{\tau}_L \\ \tilde{\tau}_R \end{pmatrix}. \tag{5.25}$$

In many SUSY models the first and second generation sfermions have large masses. For the third generation (due to the large τ-lepton mass) the mixing of left- and right handed eigenstates becomes more important. For that reason the mass eigenstates become a mixture of left- and right handed contributions.

The sfermion partners of the τ-lepton are the $\tilde{\tau}_1$ and the $\tilde{\tau}_2$. For the mixture described above the mass for one $\tilde{\tau}$ becomes smaller while for the other $\tilde{\tau}$ the mass becomes larger. The lighter $\tilde{\tau}$ is lighter than the other sleptons.

Chapter 6

Tau lepton reconstruction and identification

Tau leptons within a momentum range of 10 GeV up to 500 GeV are interesting for a variety of different studies at the LHC [78]. The lower momentum range is related to known Standard Model processes involving W or Z-bosons (e.g. $Z \to \tau\tau$ or $W \to \tau\nu$) but also interesting for low mass Higgs searches [79]. The background to the fully hadronic $Z \to \tau\tau$ decay is dominated by QCD multi-jets within a p_T range of [12–100] GeV, while for the leptonic $Z \to \tau\tau$ the background mainly comes from $Z \to \mu\mu$ and $Z \to ee$ events (due to prompt leptons) [1)]. For τ-lepton reconstruction and identification efficiency determination the semi-leptonic $Z \to \tau\tau$ channel can provide good background suppression. Although the $W \to \tau\nu$ channel has a ten times larger rate (production cross section) than the $Z \to \tau\tau$ channel, the latter has more robust prospects for data analysis. Since all lepton efficiencies will be measured in the $Z \to \ell\ell$ channels, the $Z \to \tau\tau$ process will give an excellent handle on calibrating τ-lepton identification efficiencies.

In addition, a measurement of the visible mass of the semi-leptonic (τ, τ) system has sensitivity to the energy scale of the reconstructed τ-leptons. This channel can be used as a control sample for $X \to \tau\tau$ final states and to prepare the analysis procedure for the $H \to \tau\tau$ discovery. Also due to the produced neutrinos the (τ, τ) final state is a good probe for the E_T^{miss} scale determination.

6.1 Event cleaning and lepton selection

The first stage in selecting τ-lepton candidates from data is the rejection of so called 'bad' events. The following criteria must be met in order to pass the event cleaning selection [80]:

- Event must be recorded during stable beam conditions.
- The event must pass quality requirements for the inner detector and the calorimeter.
- No 'bad' jets in the event allowed [81].

[1)] One option to study the leptonic decay modes is the combined $Z \to \tau\tau \to \mu e + 4\ \nu$ decay.

- At least one vertex reconstructed with more than four tracks is required.

Since the τ-lepton reconstruction and identification efficiency measurement is based on $Z \rightarrow \tau\tau$ events, the reconstruction and identification of muons and electrons should also be discussed as leptonically decaying τ-leptons will be reconstructed as electrons or muons.

6.1.1 Reconstruction and identification of electron candidates

The electron reconstruction uses both track-seeded and calorimeter-seeded methods. The expected ratio of electrons to QCD-jets in the p_T region of [20–50] GeV is 10^{-5}. This illustrates how important good electron reconstruction and identification is. Two algorithms are be used in ATLAS [82, 83, 84]. The `calorimeter-seeded` algorithm (seeded from electromagnetic calorimeter) starts from clusters reconstructed in the calorimeters. It builds the identification variables by using inner detector and calorimeter information. The `track-seeded` algorithm uses only information from the inner detector. This algorithm is optimised for low energy electrons ($E < 2.4$ GeV) and selects tracks matching a relatively isolated deposition of energy in the electromagnetic calorimeter.

6.1.2 Reconstruction and identification of muon candidates

The reconstruction of muons is done by the inner detector and the muon detector system. The muon drift tubes (MDT) are arranged in chambers around the beam axis. The muon trigger chambers are the resistive plate chambers (RPC) and the thin gap chambers (TGC). As described in Chapt. 3 the muon system covers the largest contribution to the ATLAS detector. The muon detector system has to analyse possible muon candidates within the bunch spacing time to provide trigger information. The main strategy for the muon reconstruction and identification is to define `standalone` muons and `combined` muons. The standalone selection finds tracks in the muon spectrometer and extrapolates these tracks to the beam line. All three muon detector components (MDT, `cathode strip chambers` (CSC), RPC see 3.2.3) provide position information to reconstruct a muon track. This track is then extrapolated to the beam line using different algorithms [85, 86, 87]. The advantage of the standalone algorithm is the greater pseudo-rapidity coverage compared with the inner detector ($|\eta| < 2.7$ versus $|\eta| < 2.5$). A disadvantage is the existence of coverage gaps near $|\eta| = 0$ and $|\eta| = 1.2$. In addition, pion or kaon decays in the calorimeter can fake a reconstructed muon, giving a possible background contribution. The "combined" muon selection uses muon spectrometer tracks in combination with inner detector tracks, combined based on a χ^2-match.

6.2 Tau lepton selection

Before discussing the τ-lepton reconstruction and identification procedure, general properties of the hadronic τ-lepton decay will be discussed in order to show the basic conditions for an efficient background suppression. In the hadronic τ-lepton decay the W-boson decays into a quark-antiquark pair. The colour connection allows to produce for example an additional neutral pion or if enough energy is available, two additional charged pions.

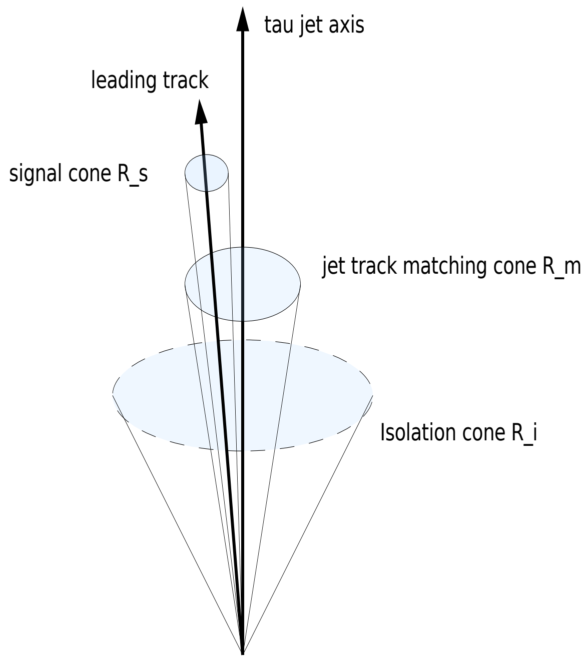

Figure 6.1: *The track isolation for the hadronically decaying τ-lepton.*

If the momentum of the τ-lepton is large compared to the mass a very collimated jet is produced. For example for a transverse momentum $p_T > 50\,\mathrm{GeV}$, 90 % of the energy is contained in a cone of radius $\Delta R = 0.2$. Hadronically decaying τ-leptons leave a significant electromagnetic energy deposition in the calorimeters due to photons coming from the decay of neutral pions. The energy deposits in the electromagnetic and hadronic calorimeter are localised. τ-leptons are accompanied by well collimated tracks with a small multiplicity.

The tau-jet/gluon-jet and tau-jet/quark-jet separation Tau-jets[2)] and gluon (or quark) initiated jets have different properties which provides a good separation of both.

The track isolation is shown in Fig. 6.1. The direction of the τ-lepton jet is defined by the axis of the calorimeter jet. The tracks with a p_T above the required threshold located in a matching cone of radius R_m around the calorimeter jet direction are considered in the search for signal tracks. The leading track is defined as the track with the highest p_T. Any other track in the narrow signal cone R_s around the leading track and with z-impact parameter z_{tr} close to the z-impact parameter of the leading track is assumed to come from the τ-lepton decay. Tracks with Δz_{tr} (impact parameter distance from the leading track) smaller than a given cut-off and transverse momentum above a threshold of p_T are then reconstructed inside a larger cone of the size R_i. If no tracks are found in the R_i cone, except

[2)]Tau-jet means the same as τ-lepton. In this discussion tau-jet is chosen in order to enhance the jet character of τ-leptons and multi-jets.

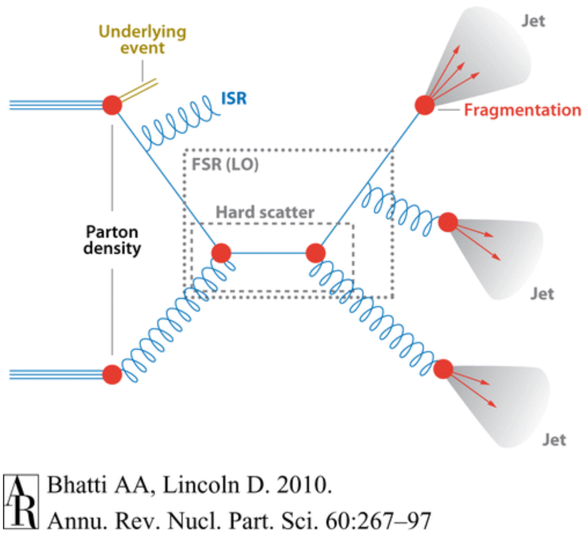

Figure 6.2: *The jet production at LHC.*

for the ones which are already in the R_s cone, the isolation criteria is fulfilled [88].

The jet production is shown in Fig. 6.2. In parton interactions hard quarks and gluons are produced. If the colour field has enough energy new quark-antiquark fields are produced in a cascade process which forms colour neutral hadrons (fragmentation). The colour flow disperses the quarks and gluons which increases the jet shape. The final state are hadron jets.

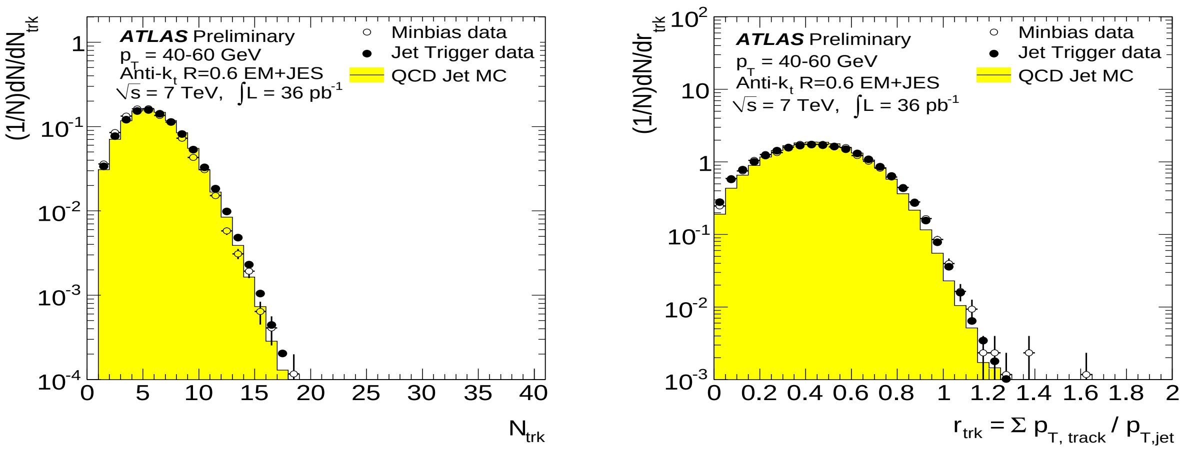

Figure 6.3: *The charged particle multiplicity distributions (a) and the R_{trk} multiplicity distributions (b) for $40\,GeV < 60\,GeV$ for the pseudo rapidity range $0 < |\eta_{jet}| < 1.2$ for anti-k_t jets [89].*

The number of tracks as well as the ratio of the sum of the tracks p_T over the jet p_T is shown in Fig. 6.3.

6.2.1 Reconstruction of tau candidates

As described above, τ-lepton reconstruction starts from either calorimeter or track seeds.

`Track-seeded` candidates have a track with $p_T > 6\,\mathrm{GeV}$ and have to fulfil several criteria like number of hits in the silicon tracker and impact parameter with respect to the interaction vertex. An important aspect is the `track association`. Tracks associated to a τ-lepton candidate must fulfil the following quality criteria [90]:

- Within the `core cone`: $\Delta R = \sqrt{(\Delta\eta)^2 + (\Delta\phi)^2} < 0.2$, defined from the axis of the seed jet
- $p_T > 1\,\mathrm{GeV}$
- $N_{hit}^{b-layer} \geq 1$
- $N_{hit}^{pixel} \geq 2$
- $N_{hit}^{pixel} + N_{hit}^{SCT} \geq 7$
- $|d_0| < 1.0\,\mathrm{mm}$
- $|z_0 \sin\Theta| < 1.5\,\mathrm{mm}$

`Calorimeter-seeded` candidates consists of a jet reconstructed in the calorimeter using a antik_t algorithm [91] starting from topological clusters [92].

The reconstruction of tracks from charged pion decays is an important input for the τ-lepton reconstruction. Both, the track-seeded and the calorimeter-seeded algorithm sum up the charge of the tracks reconstructed around the τ-lepton candidate to determine the charge of the τ-lepton candidate. Track reconstruction has to be highly efficient to ensure a good separation of τ-lepton candidates from QCD-jets.

The track efficiency depends upon the behaviour of the charged pions in the detector. Hadronic interactions of the pion in the inner detector can decrease the track selection efficiency [84]. In addition, a standard quality selection has been defined [93].

Another important aspect of the τ-lepton reconstruction is the charge mis-identification. As mentioned above the charge of the τ-lepton candidate is calculated as the sum of the reconstructed tracks. For the leading track the charge mis-identification is about 0.2 % [84] using the quality criteria mentioned above. For the total sum of the charge, the mis-identification rate is larger and depends upon combinatorial effects: single prong decays can migrate to three prong decays due to photon conversion[3)] or additional tracks from underlying events. Furthermore, three prong decays can be reconstructed as one prong decay due to inefficient track reconstruction.

The lifetime of the τ-lepton ($c\tau = 87.11\,\mu\mathrm{m}$) allows for three prong decay vertices to be reconstructed(`secondary vertex reconstruction`) [94, 95, 96].

For prompt[4)] lepton suppression, so called `vetoes` are defined. To suppress tracks from isolated electrons, algorithms check if these tracks could also be good electron candidates. If this is the case, the object (or corresponding event) will not be accepted.

[3)] photon conversions due to the neutral pion decay. Photons from π^0 might convert in the material of the inner detector and then contribute additional tracks

[4)] prompt means leptons (e or μ) from non-τ decay, e.g. $W \to \ell\nu$ or $Z \to \ell\ell$

6.2.2 Identification of tau candidates

Although there is no sharp boundary line between reconstruction and identification criteria, the reconstruction and identification will be discussed separately. The reconstruction is related to the general kinematic aspects of the τ-leptons, while the identification is a tighter list of criteria designed to separate τ-leptons from QCD-jets. Two strategies for the τ-lepton identification were chosen, the `calorimeter-based algorithm` and the `track-based algorithm` [97], [98].

Calorimeter-based algorithm

For τ-lepton candidates reconstructed with the calorimeter based algorithms, several quantities have been combined to discriminate τ-leptons from QCD-jets: [84]. The τ-lepton identification is based on a one-dimensional likelihood ratio constructed of three discrete variables ($\mathrm{N_{tr}}$, $\mathrm{N_{strip}}$ and the τ-lepton charge) and five continuous variables ($\mathrm{R_{em}}$,$\Delta\mathrm{E_T}$,$\Delta\eta$, $\mathrm{sig_{d_0}}$, $\mathrm{E_T/p_T}$).

- The `electromagnetic radius` $\mathrm{R_{em}}$:

$$\mathrm{R_{em}} = \frac{\sum_{\mathrm{i=1}}^{\mathrm{n}} \mathrm{E_{T,i}} \sqrt{(\eta_\mathrm{i} - \eta_\mathrm{cluster})^2 + (\phi_\mathrm{i} - \phi_\mathrm{cluster})^2}}{\sum_{\mathrm{i=1}}^{\mathrm{n}} \mathrm{E_{T,i}}} \tag{6.1}$$

  where i defines all cells in the electromagnetic calorimeter (within $\Delta\mathrm{R} < 0.4$). The quantities $\mathrm{E_{T,i}}$, η_i, and ϕ_i denote the transverse energy and the position in the corresponding cell i. This quantity $\mathrm{R_{em}}$ depends from η and has a good discrimination power at low transverse energies $\mathrm{E_T}$. For higher $\mathrm{E_T}$ the electromagnetic radius becomes less effective.

- The `isolation in the calorimeter:`

$$\Delta\mathrm{E_T} = \frac{\sum_\mathrm{i} \mathrm{E_{T,i}}}{\sum_\mathrm{j} \mathrm{E_{T,j}}} \tag{6.2}$$

  uses the fact that clusters from hadronic τ-lepton decays are well collimated. For that reason, tight isolation criteria can be applied. The chosen isolation region is a ring of $0.1 < \Delta\mathrm{R} < 0.2$ and $\Delta\mathrm{E_T}$ is calculated using all cells in a cone around the cluster axis with $0.1 < \Delta\mathrm{R} < 0.2$ and $\Delta\mathrm{R} < 0.4$ respectively. The isolation is also $\mathrm{E_T}$ dependent and the jet becomes narrower with increasing transverse energies.

- `The transverse energy width in the` η `strip layer:`

$$\Delta\eta = \sqrt{\frac{\sum_{\mathrm{i=1}}^{\mathrm{n}} \mathrm{E_{T,i}} \mathrm{E_{T,i}^{strip}} (\eta_\mathrm{i} - \eta_\mathrm{cluster})^2}{\sum_{\mathrm{i=1}}^{\mathrm{n}} \mathrm{E_{T,i}} \mathrm{E_{T,i}^{strip}}}} \tag{6.3}$$

  where all strip cells are summed in a cone $\Delta\mathrm{R} < 0.4$ with $\mathrm{E_{T,i}^{strip}}$ being the strip transverse energy. Again, $\Delta\eta$ is powerful for low $\mathrm{E_T}$ but inefficient for higher $\mathrm{E_T}$ objects.

- The `number of hits in the` η `strip layer` is also used for likelihood discrimination. If the energy deposit exceeds 200 MeV, the cells in the η strip layer within $\Delta R < 0.4$ will be counted as hits.

- The `number of associated tracks` defines tracks associated with a given cluster ($\Delta R < 0.3$). As the only requirement, those tracks must have a transverse momentum p_T larger than 2 GeV.
- The `charge of the` τ`-lepton candidate` is used as a quantity. As described in Sec. 6.2.1 the charge is the sum over all associated tracks.
- The `lifetime signed pseudo impact parameter significance` and is defined as the distance between the beam axis and the point of the closest approach to the track in the plane perpendicular to the beam axis.

Track-based algorithms The hadronic τ-lepton decay can be classified as a well collimated object consisting of charged pions and neutral pions. The inner detector provides good track information and therefore a set of quantities can be defined [99] to identify τ-lepton candidates.

The quantities for the calorimeter based discrimination are:

- E_T `over` p_T `of the leading track` (E_T/p_T): this is expected to be large for objects with strongly leading jets. QCD jets are expected to have a more uniform p_T distribution among tracks.
- `Ratio of electromagnetic energy and the sum of` p_T `of tracks:`

$$\frac{E_T^{EM}}{p_T^{total}} = \frac{\sum_i E_{T,i}^{EM}}{\sum_{j=1}^{N} p_{T,j}^{track}} \tag{6.4}$$

  with $E_{T,i}^{EM}$ denoting the cell energy after global cell weighting calibration and $p_{T,j}^{track}$ the transverse momenta of the tracks associated to the n-prong candidate.

- `Ratio of hadronic energy and sum of` p_T `of tracks` is defined as:

$$\frac{E_T^{Had}}{p_T^{total}} = \frac{\sum_i E_{T,i}^{Had}}{\sum_{j=1}^{N} p_{T,j}^{track}} \tag{6.5}$$

  with the same definitions as before.

- `Ratio of sum of` p_T `of tracks and total energy:`

$$\frac{p_T^{total}}{E_T^{total}} = \frac{\sum_{k=i}^{N} p_{T,k}^{track}}{\sum_i E_{T,i}^{EM} \sum_i E_{T,j}^{Had}}. \tag{6.6}$$

- `The track spread:`

$$W_{track}^{\tau} = \frac{\sum (\Delta R^{track})^2 p_T^{track}}{\sum p_T^{track}} - \frac{(\sum \Delta R^{track} p_T^{track})^2}{(\sum p_T^{track})^2} \tag{6.7}$$

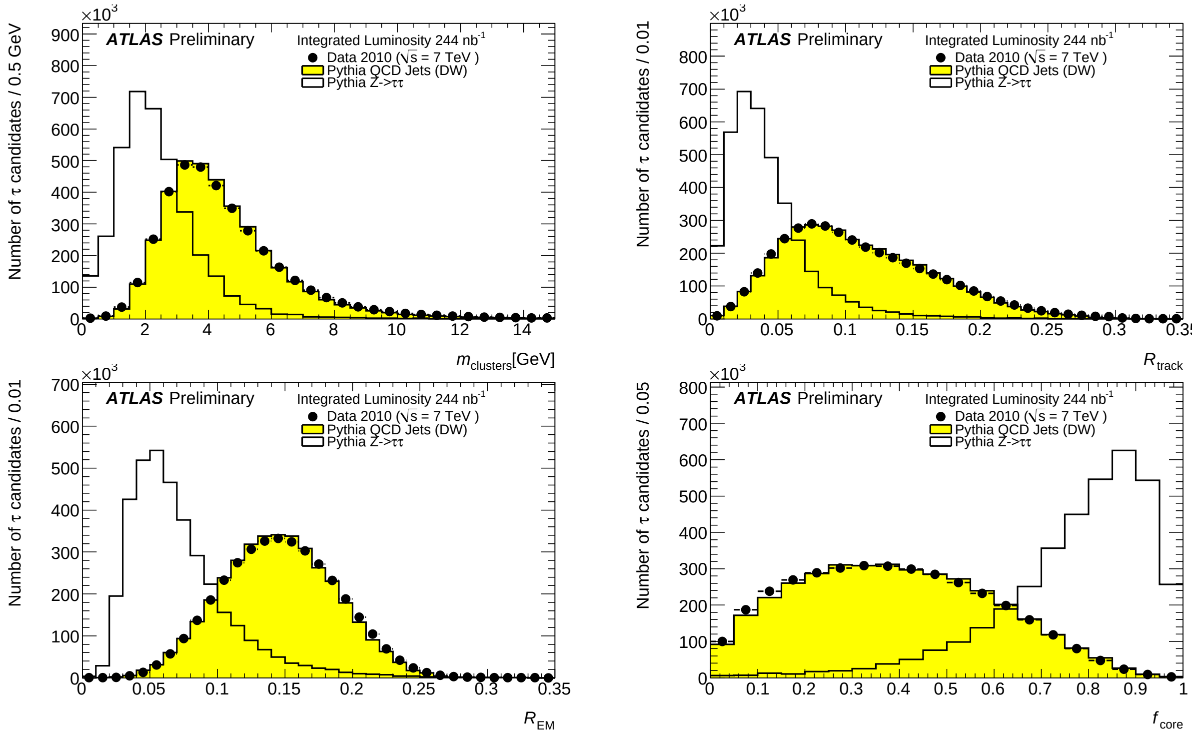

Figure 6.4: *The distributions for selected variables. The cluster mass of τ-lepton candidates (top left), the track radius of τ-lepton candidates (top right), the EM radius of τ-lepton candidates (bottom left) and the core energy fraction of τ-lepton candidates (bottom right). All The number of τ-lepton candidates in MC samples are normalised to the number of tau candidates selected in data [101].*

where $\Delta R^{\mathrm{track}}$ is the distance between the track and the τ-lepton track seed in the η-ϕ space.

- p_T `weighted track width` [100]:

$$R_{\mathrm{track}} = \frac{\sum_{i}^{\Delta R_i<0.2} p_{T,i} \Delta R_i}{\sum_{i}^{\Delta R_i<0.2} p_{T,i}}. \tag{6.8}$$

- `Leading track momentum fraction`:

$$f_{\mathrm{track,l}} = \frac{p_{T,l}^{\mathrm{track}}}{p_T^{\tau}}. \tag{6.9}$$

Figure 6.4 shows few variables discussed above. The performance of all parameters can be found in Figs. 10.5, 10.6, and 10.7 (see App. 10). For (ATLAS) data analysis, different combinations of the described quantities are used. For the first data, `cut based ID`[5] using robust variables is required while for more complex analysis the `projective likelihood` and the `boosted decision tree` variables will be used.

[5] also known as `safe variables` or `robust variables`

`Cut based ID:` The `cut based ID` is defined to have a simple, easily comprehensible identification performance. This is related to the fact, that for the first data, optimal detector performance is not guaranteed. The robust variables pass through a rapid evolution process because they have to fit to the current status of data analysis. The `cut based ID` (as well as `projective likelihood` and `boosted decision tree`) is optimised for three different signal efficiencies: 30 % (tight), 50 % (medium) and 70 % (loose). This allows a large spectrum of studies using the τ-lepton. As described before, the `cut based ID` is foreseen to be a temporary (robust) τ-lepton identification method.

The cut-based selections can be subdivided into the `calorimeter` and the `calorimeter+track` method. An important check of the performance of such variables is the comparison of the signal efficiency $\varepsilon_{\mathrm{signal}}$ and the background efficiency $\varepsilon_{\mathrm{bkg}}$ [99]:

$$\varepsilon_{\mathrm{signal}} = \frac{\text{Number of matched tau candidates passing the cuts}}{\text{Number of true hadronically decaying tau candidate}} \tag{6.10}$$

and

$$\varepsilon_{\mathrm{bkg}} = \frac{\text{Number of reconstructed tau candidates passing the cuts}}{\text{Number of all reconstructed tau candidates}} \tag{6.11}$$

this defines the `background rejection:`

$$\mathrm{B} = \frac{1}{\varepsilon_{\mathrm{bkg}}} - 1 \tag{6.12}$$

The current `cut based ID` strategy uses three variables $\mathrm{R_{em}}$, $\mathrm{R_{track}}$ and $\mathrm{f_{track}}$ for one and multiple tracks candidates [90]. The variables $\mathrm{R_{em}}$ and $\mathrm{R_{track}}$ are parametrised by the $\mathrm{p_T}$ of the τ-lepton candidate. The reason is that optimal cuts are very $\mathrm{p_T}$ dependent because of the Lorentz collimation of the hadronic τ-lepton decay products. As described before, the variables $\mathrm{R_{em}}$ and $\mathrm{R_{track}}$ rely on the narrowness of the hadronic shower in the τ-lepton decay in comparison with QCD-jets. In the ATLAS detector, τ-leptons are not produced at rest, but in the τ-lepton rest frame the decay products vector can point in any direction. The consequence is that in the laboratory frame the τ-lepton decay products will be colliminated along the momentum of the τ-lepton [90]. From the Lorentz boost, it follows that width-like variables (R) should collimate as

$$\mathrm{R(p_T)} \propto \frac{1}{\mathrm{p_T}}. \tag{6.13}$$

which makes $\mathrm{R_{em}}$ and $\mathrm{R_{track}}$ strongly $\mathrm{p_T}$ dependent. Multiplying R by $\mathrm{p_T}$ reduces this $\mathrm{p_T}$ dependence. The remaining $\mathrm{p_T}$ dependence will be parametrised with a second order polynomial to the mean of $\times\mathrm{p_T}$. The parametrisation can be expressed as

$$\mathrm{g(p_T) = a_0 + a_1 p_T + a_2 p_T^2}. \tag{6.14}$$

Conservently the signal against background separation can be constructed as

$$\mathrm{R^{cut}(p_T, x) p_T = (1 - x) g_{sig} p_T + x g_{bkg}(p_T)} \tag{6.15}$$

for different values of the parameter x. The case x=0 is completely along the mean of the signal distribution and x=1 is completely along the mean of the background [90]. This parametrisation can be seen in Fig. 6.5.

After longer periods of data taking and investigations of all components the `cut based ID` will be replaced by the multivariate techniques `projective likelihood` and `boosted decision tree`.

`Projective likelihood:` The projective likelihood is given by

$$\mathrm{L}_{\mathrm{S(B)}} = \prod_{\mathrm{i}=1}^{\mathrm{N}} \mathrm{p}_{\mathrm{i}}^{\mathrm{S(B)}}(\mathrm{x}_{\mathrm{i}}) \tag{6.16}$$

where $\mathrm{p}_{\mathrm{i}}^{\mathrm{S(B)}}(\mathrm{x}_{\mathrm{i}})$ is the signal (background) probability density function (PDF) of the identification variables x_{i} [90]. The likelihood uses a discriminant which is defined as

$$\mathrm{d} = \ln \frac{\mathrm{L}_{\mathrm{S}}}{\mathrm{L}_{\mathrm{B}}} = \sum_{\mathrm{i}=1}^{\mathrm{N}} \ln\left(\frac{\mathrm{p}_{\mathrm{i}}^{\mathrm{S}}(\mathrm{x}_{\mathrm{i}})}{\mathrm{p}_{\mathrm{i}}^{\mathrm{B}}(\mathrm{x}_{\mathrm{i}})}\right) \tag{6.17}$$

i.e. the log-likelihood ratio between signal and background. The PDFs are produced from signal and background samples. To optimise the discriminatory power the samples are subdivided into different p_{T} regions $(0-45, 45-100, >100)$ GeV. The events are sorted with respect to the number of vertices. The projective likelihood method only considers calo seeded candidates. More detailed information can be found in [90].

`Boosted decision tree:` Similar to a simple `cut-based` technique the `boosted decision tree` method makes use of orthogonal cuts on a set of identification variables. BDTs apply cuts on multiple variables in a recursive manner to classify objects as signal or background [90]. Boosted decision trees (BDT) are fast to train, they take correlations between variables into account, they can use discrete variables directly, adding well-modelled variables will not degrade performance and the number of tunable parameters is quite small [103, 90].

6.3 Fake rates from QCD di-jet samples and from the W+jets events

Precise knowledge of the τ fake rate (the probability that a jet will be reconstructed or identified as a τ-lepton) is crucial for many analysis. The strategy to determine this is to use a tag and probe method where selection criteria are applied to the tag jet, leaving the kinematically connected probe jet unbiased by the selection [104]. The fake rate determination can be separated into three sub-methods related to the jet performance [104]:

- **Di-Jets:** a back to back pair of QCD jets defines a probe and a tag jet.
- **ThreeJets:** the tag jet is jet balancing a pair of QCD jets and the probe jet is one of the balanced jets.

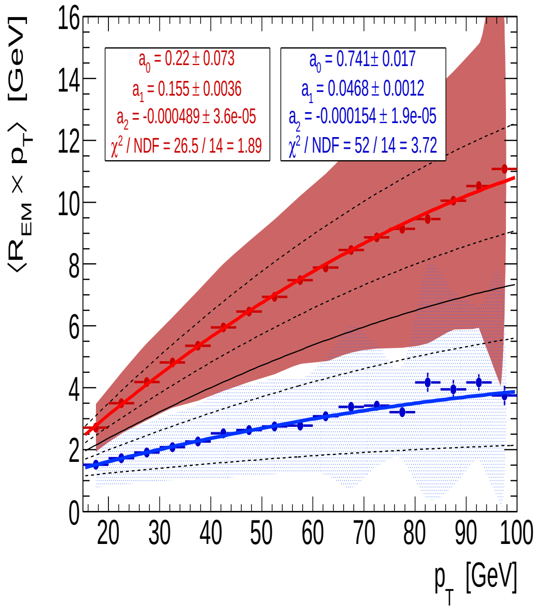

(a) R_{EM} parametrisation for 1-prong

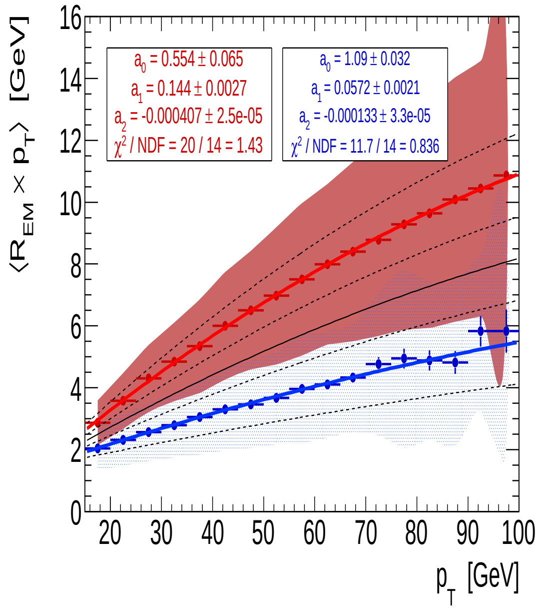

(b) R_{EM} parametrisation for 3-prong

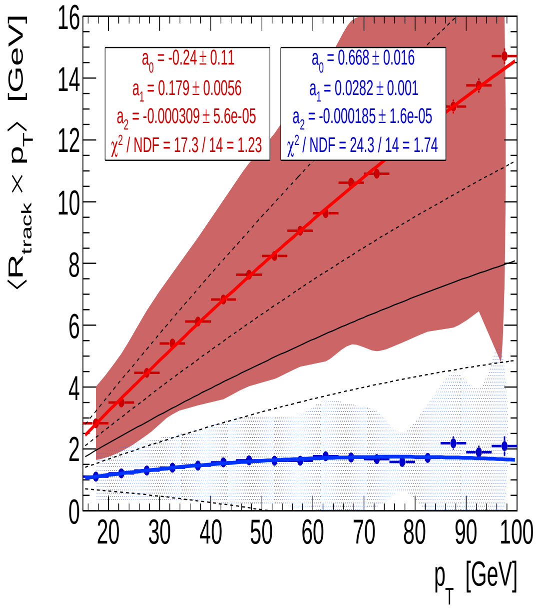

(c) R_{track} parametrisation for 1-prong

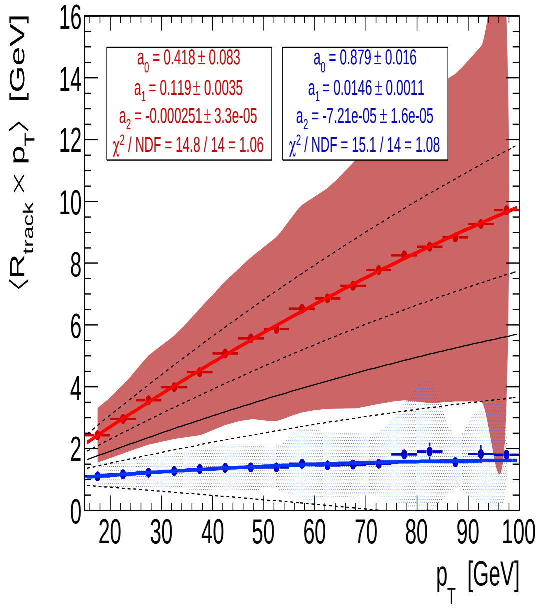

(d) R_{track} parametrisation for 3-prong

Figure 6.5: *The marker points are the means of the $R \times p_{\mathrm{T}}$ distributions in each p_{T} bin, with the error bars indicating the error on the mean. The coloured bands represent the region within one standard deviation of the mean. Signal Monte Carlo is in blue, while the di-jet data sample is in red. The blue line is the best fit curve from Eq. (6.14) to the signal, corresponding to the cut curve in Eq. (6.15) with x=0. The red line is the best fit curve to di-jet sample, corresponding to x=1. The black dashed lines show the parametrised cut curves for x = -0.25, 0.25, 0.75, and 1.25. The solid black line is the parametrised cut curve for x= 0.5 [102].*

- **Photon + Jets:** a photon defines the tag jet and a QCD jet defines the probe jet
- **Z → ee + Jets:** this selection uses Z → ee events from data and estimates the fake rate for an associated jet.

Fake rates using tag and probe in QCD di-jets selection [104] The idea is to identify a (tag) jet with a standard jet selection such as:

- trigger conditions, jet trigger is required
- each jet has to be within $\mid \eta \mid < 2.5$
- the p_T of each jet must be larger than 15 GeV
- the difference of the azimuth angles between the jets has to fulfil $\mid \Delta\Phi \mid = \pi \pm 0.30$ radians
- the p_T of the jets must be balanced → $\frac{p_T^{\text{leading jet}}}{2} > \mid p_T \mid$
- the number of associated tracks N_{tracks} must be ≥ 4 for the tag jet.

The probe jet is then subjected to the τ-lepton reconstruction and identification. If the probe jet is reconstructed or identified as a τ-lepton candidate, this probe jet will be denoted as a fake τ-lepton. The fake rate is then (with N_{fake} as the number of probe jets identified as a τ-lepton and N_{tag} as the number of tag jets):

$$R_{\text{fake}} = \frac{N_{\text{fake}}}{N_{\text{tag}}}. \tag{6.18}$$

This can be separated into the reconstruction and identification fake rates (shown in Fig. 6.6). For completeness, is is also possible to estimate the τ-lepton reconstruction fake rates. The reconstruction fake rates are expected to be almost in the order of 1, while the identification fake rate is expected to be in the order of 10^{-3} to 10^{-2}.

Fake rates using tag and probe in Z → ℓℓ + Jets events [105]:
The second method uses the Z → ℓℓ + Jets channel. The fake rates obtained via this method have to be parametrised for using it as τ-lepton fake rates from QCD di-jets. These differences can affect the τ-lepton identification performance. This is due to the different jet compositions in the two channels, Z → ℓℓ events have higher ratio of quark-initiated jets to gluon-initiated jets.

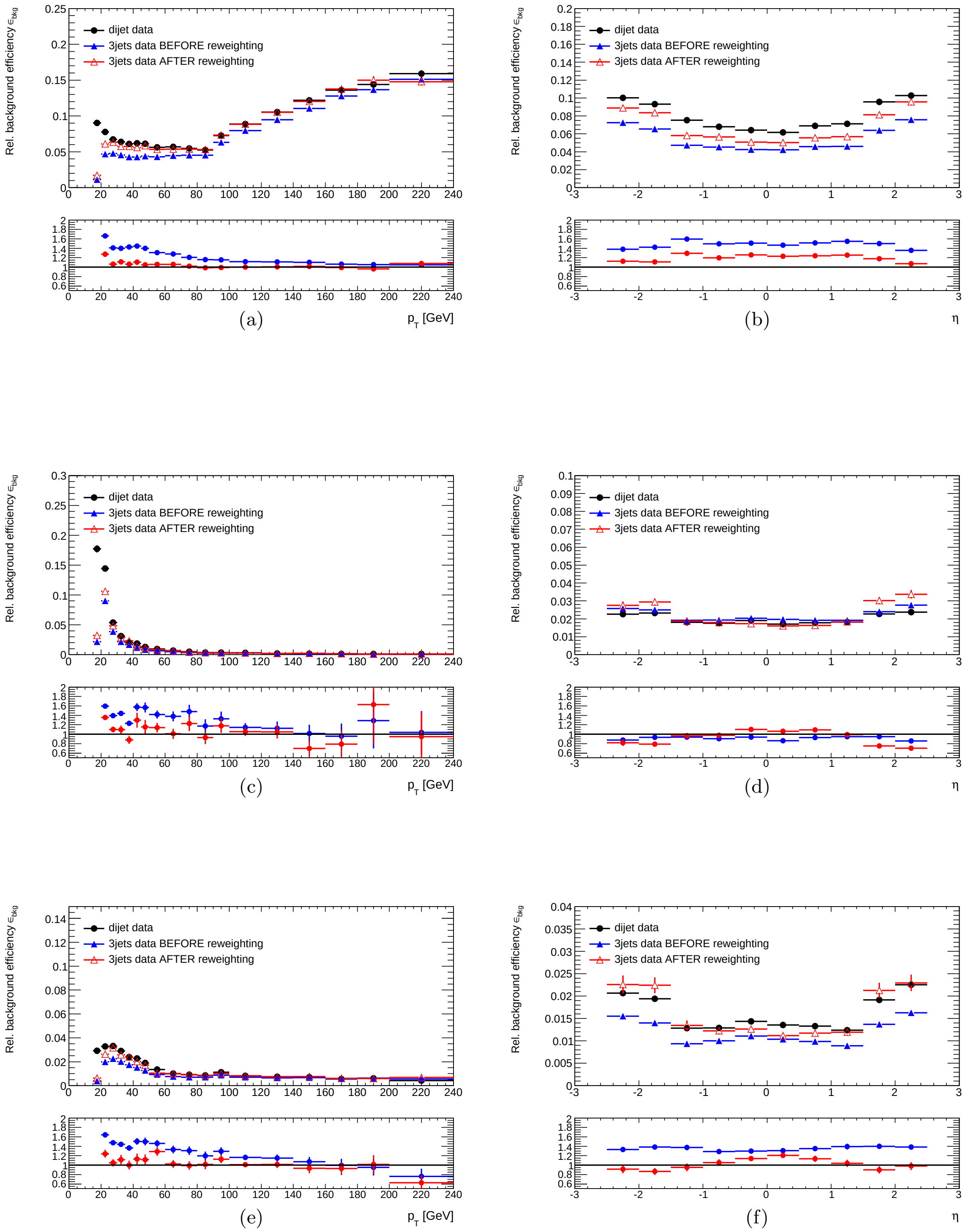

Figure 6.6: *Identification fake rates [104] from all tau candidates for the medium safe cut method (a)(b), the medium boosted decision tree method (c)(d) and the medium likelihood method (e)(f) in dependence of the probe jet transverse momentum p_T and the probe jet pseudo-rapidity η. The result obtained from the di-jet method (black) is compared with the result from the three-jet method before any correction (blue) and p_T and $\Delta R_{\mathrm{closestjet}}$ correction (red).*

Chapter 7

$\mathrm{Z} \to \tau\tau$ object selection

In the previous chapter the role of the Z and the τ-lepton in context of new physics at LHC was discussed. Different methods to trigger, reconstruct and identify hadronically decaying τ-leptons as well as leptonically decaying τ-leptons were introduced. This chapter discusses the semi-leptonic $\mathrm{Z} \to \tau\tau$ selection.

The ATLAS detector has collected data corresponding to an integrated luminosity of about $\mathcal{L} = 35\ \mathrm{pb}^{-1}$. The centre-of-mass energy is $\sqrt{\mathrm{s}} = 7\,\mathrm{TeV}$. For the semi-leptonic $\mathrm{Z} \to \tau\tau$ channel two studies are available:

The `invariant mass` analysis and the `visible mass` analysis. For simplification the hadronically decaying τ-lepton is denoted as τ-lepton (in the text) or τ_{h} (in formulas, decay chains, figures etc.) while the leptonically decaying τ-lepton is denoted as lepton or τ_{ℓ}. The visible mass analysis for the $\mathrm{Z} \to \tau_{\mathrm{h}}\tau_{\ell}$ final state is defined for a mass below the original Z-boson mass $37\,\mathrm{GeV} < \mathrm{m}_{\mathrm{vis}}(\tau_{\mathrm{h}}\tau_{\ell}) < 75\,\mathrm{GeV}$ due to the neutrinos which are not covered by the detector. The expected invariant mass for the Z-boson is $\mathrm{m}_{\mathrm{inv}}(\tau_{\mathrm{h}}\tau_{\ell}){=}91.2\,\mathrm{GeV}$.

This chapter covers methods for background suppression with respect to data-driven techniques. In Sec. 7.1 the pre-selection of events using quality criteria is described. Sections 7.2 and 7.3 cover the selection of events while Sec. 7.4 covers the lepton isolation including a discussion on effects from pile-up events. The background estimation using different data-driven methods is summarised in Sec. 7.7. The final results are summarised in Sec. 7.10. This Section closes with an discussion of an alternative method for the background extraction (Sec. 7.11).

Background sources are QCD multi-jets (because of the very large cross section),W+jets, Z+jets and (with a small contribution) $\mathrm{t\bar{t}}$ events and so called `Drell-Yan`[1)] processes which both found to be negligible. All background processes (except the $\mathrm{t\bar{t}}$ channel) almost involve a true lepton while the τ lepton is generally a misidentified quark or gluon jet[2)]. To avoid confusion it has to be mentioned that real τ coming from $W \to \tau\nu$ or $\mathrm{t\bar{t}}$ events will treat as background. This becomes important for the τ-lepton reconstruction and identification efficiency discussed in Chapt. 8. The data samples used for the analysis are taken during 2010 (March-November). `Data quality requirements` are defined to provide a clean data

[1)]Note: It is the $\mathrm{Z}/\gamma^{\star}$ mediated $\tau\tau$ production for invariant mass $\mathrm{m}_{\mathrm{inv}} < 60\,\mathrm{GeV}$. ATLAS has divided these regions for the MC production

[2)]In case of QCD multi-jets, e.g. the muons from heavy flavour decays, may be real.

Run period	Run number	$\mathcal{L}$ $[pb^{-1}]$ electron channel	$\mathcal{L}$ $[pb^{-1}]$ muon channel
A	152166-153200	-	0.00037
B	153565-155160	-	0.0081
C	155228-156682	-	0.0084
D	158045-159224	-	0.293
E	160387-161948	0.771	1.002
F	162347-162882	1.808	1.808
G	165591-166383	5.738	5.411
H	166466-166964	6.984	6.984
I	167575-167844	20.735	20.735
$\sum$ E3-I		35.73	35.73

Table 7.1: *The run periods and the corresponding run numbers as well as the integrated luminosities for the e and the μ channel corresponding to the following triggers:* `e15_medium, mu10_MG, mu13_MG, mu13_MG_tight`. *The values were corrected with respect to new luminosity measurements in ATLAS. For this study the run periods E3-I were used.*

sample without events influenced by effects from beam pipe or cosmic events. Events passing those criteria required for Z $\rightarrow \tau\tau$ physics [106, 107] are collected into a `good runs list` (GRL). The luminosity was calculated with the official ATLAS web-based lumicalc tool [108]. The overall used integrated luminosity for this data analysis for the electron and the muon channel [3)] as well as the different run periods including the integrated luminosity and the run number are summarised in Tab. 7.1.

Used Monte Carlo samples and correction of the QCD multi-jet background
The used Monte Carlo (MC) samples are collected in Tab. 7.2. First studies showed that the QCD multi-jet Monte Carlos does not describe the data very well. This is due to the low statistic in Monte Carlo samples as well as difficult cross section determination for QCD multi-jets (the cross sections are almost given for the leading order).

In order to have a good QCD multi-jet description those background was estimated using data-driven techniques (see Sec. 7.7.3). The estimated values were used to rescale the Monte Carlos. The Monte Carlo to data correction factor estimated for a QCD rich region was applied on all plots including QCD multi-jet distributions. The systematic effects for the ABCD method are taken into account. Particular for the plots showing distributions after the τ-lepton identification and the lepton isolation, the estimated QCD background provides a better description as the distributions from Monte Carlo.

Since the integrated luminosity has decreased by more than three orders of magnitudes, MC samples have to taken into account the changed pile-up conditions. The number of primary vertices has to be fit with respect to the data conditions.

Table 7.3 and Fig 7.1 show the number of reconstructed vertices considering pile-up effects.

[3)] Electron or muon channel means the semi-leptonic Z $\rightarrow \tau\tau$ decay with $\tau \rightarrow e$ or $\tau \rightarrow \mu$ for the leptonically decaying τ-lepton

Sample	# events	Cross section [pb]	Comment
$Z \rightarrow \tau\tau$	2 M	990	$m_{\tau\tau} > 60$ GeV
$Z \rightarrow ee$	5 M	990	$m_{ee} > 60$ GeV
$Z \rightarrow \mu\mu$	5 M	990	$m_{\mu\mu} > 60$ GeV
$W \rightarrow \tau\nu$	7 M	1046	
$W \rightarrow e\nu$	7 M	1046	
$W \rightarrow \mu\nu$	2 M	1046	
$t\bar{t}$	1 M	91.50	
J1e	998000	8.81×10^5	ele. filter $p_T > 8$ GeV, $\|\eta\| < 3$
J2e	497000	2.54×10^5	ele. filter $p_T > 8$ GeV, $\|\eta\| < 3$
J3e	499000	3.72×10^4	ele. filter $p_T > 8$ GeV, $\|\eta\| < 3$
J0mu	967000	8.48×10^5	mu. filter $p_T > 8$ GeV, $\|\eta\| < 3$
J1mu	997000	8.14×10^5	mu. filter $p_T > 8$ GeV, $\|\eta\| < 3$
J2mu	495000	2.21×10^5	mu. filter $p_T > 8$ GeV, $\|\eta\| < 3$
J3mu	499000	2.85×10^4	mu. filter $p_T > 8$ GeV, $\|\eta\| < 3$
$\gamma^\star/Z \rightarrow \tau^+\tau^-$	190000	396.7	10 GeV $< m_{\tau\tau} <$ 60 GeV
$\gamma^\star/Z \rightarrow ee$	996000	146.2	15 GeV $< m_{ee} <$ 60 GeV
$\gamma^\star/Z \rightarrow \mu\mu$	999000	146.2	15 GeV $< m_{\mu\mu} <$ 60 GeV
WW	250000	11	
ZZ	250000	1.0	
WZ	250000	3.4	

Table 7.2: *List of Monte Carlo samples used for this study. All samples were generated with Pythia, except for $\bar{t}t$ which was generated with MC@NLO.*

Number of vertices	Event weight
1	1.970(8)
2	1.242(4)
3	0.853(3)
4	0.633(2)
5	0.509(3)
6	0.427(4)
7	0.392(6)
8	0.38(1)
9	0.39(2)
10	0.41(5)
>= 11	0.89(14)

Table 7.3: *The pile-up weights for the number of reconstructed vertices.*

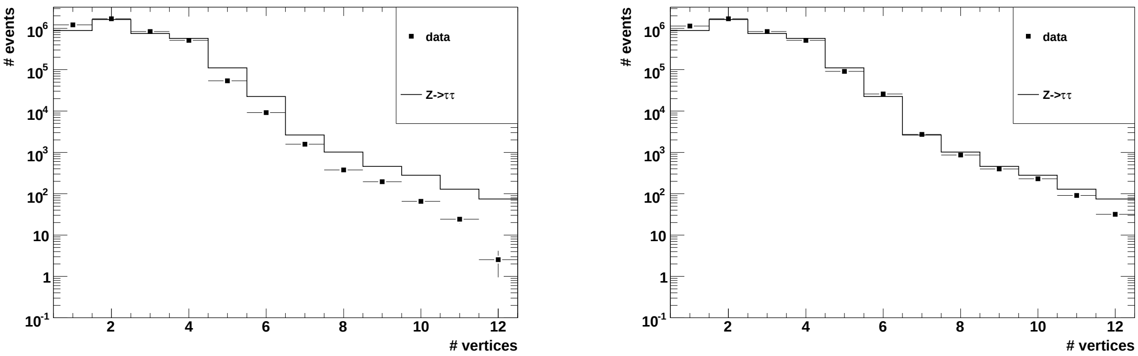

(a) (b)

Figure 7.1: *The vertex distributions for data and signal Monte Carlo before (a) and after (b) reweighting.*

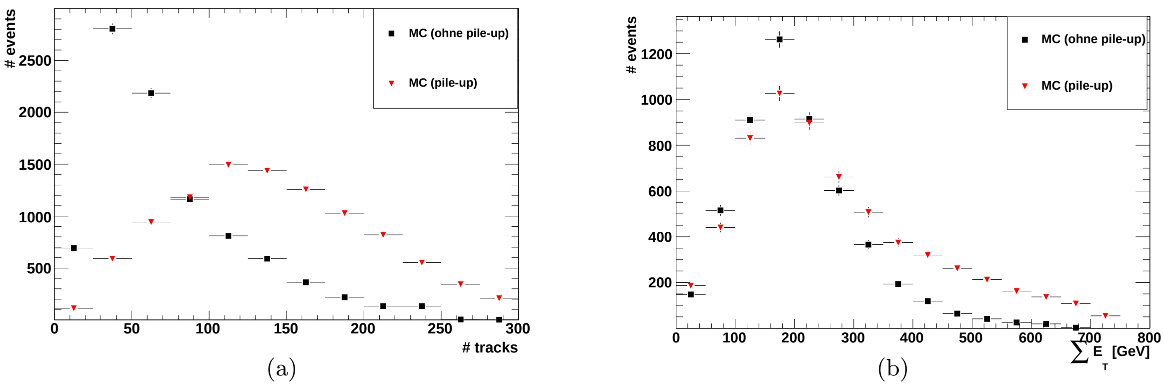

(a) (b)

Figure 7.2: *The effect of pile-up for the number of tracks (a) and the sum of E_T (b).*

It is important to handle effects from pile-up events (due to increasing luminosities). At the design luminosity of $\mathcal{L} = 10^{34}\mathrm{cm}^{-2}\mathrm{s}^{-1}$, in average 23 minimum bias events per bunch crossing are expected (according to a Poisson distribution). For that reason, any collision in ATLAS contains a superposition of particles coming from several events, that means beside the triggered event, also proton-proton interactions both in the same bunch crossing as well as coming from previous bunch crossings have to considered. The mean number per bunch is Poisson distributed and can be expressed as

$$\bar{\mathrm{N}} = \frac{\mathrm{L} \times \sigma}{\mathrm{f} \times \mathrm{N_b}}, \tag{7.1}$$

with the instantaneous luminosity L ([mb/s]), the non-diffractive cross section σ ([mb]), the frequency f at LHC and the number of bunches $\mathrm{N_b}$. The average number of pile-up events is about 1.7–2.2 interactions per bunch crossing, so the effect is not so crucial for the data taking used for this analysis (2010 data). Figure 7.2 shows the increasing number of tracks in the event corresponding to an increasing number of jets and $\sum \mathrm{E_T}$. With respect

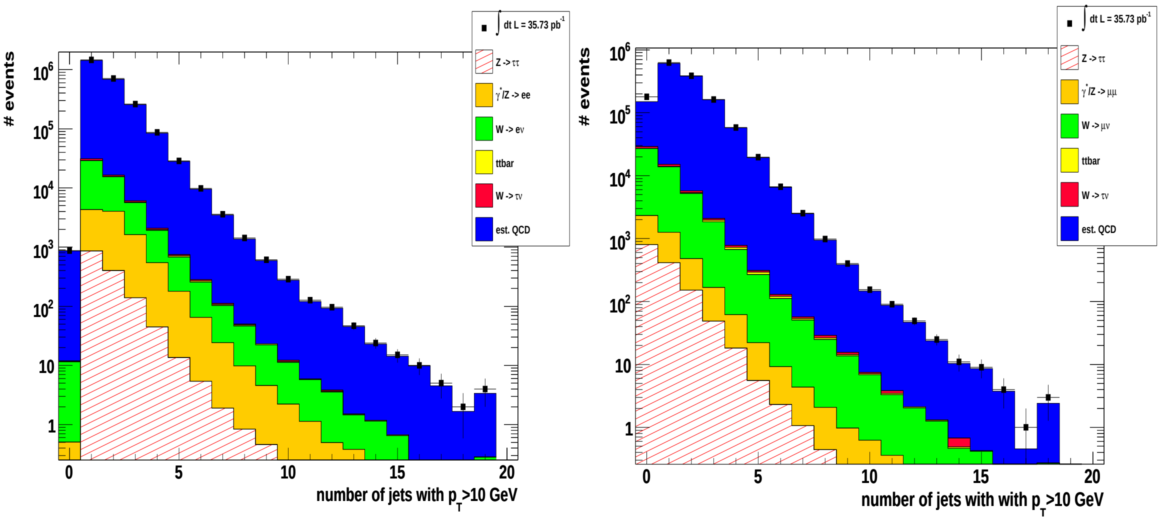

(a) (b)

Figure 7.3: *Jets fulfilling quality criteria for the electron channel (a) and the muon channel (b). All Monte Carlos are normalised to data. The QCD background is estimated as described in Sec. 7.7.*

to the pile-up effects the the Monte Carlo samples were tuned with a bunch train pile-up setup [109].

7.1 Event pre-selection

For this analysis two kinds of variables have to be considered, the `event variable` and the `object variable`. The event variable is unique for each event (e.g. E_T^{miss} or jet multiplicities), while the event can have several objects of the same type (an event can have several τ-lepton candidates and therefore several p_T or charge distributions for the different objects). For the visible mass analysis only the direction of E_T^{miss} not the magnitude is used. It is required to have a precise `jet cleaning` in order to reduce the noise coming from the detector components. Furthermore, an event can be affected by an underlying event, i.e. jets not coming from the interaction point. These underlying events influence variables like E_T^{miss} or $\sum E_T$.

The semi-leptonic $Z \rightarrow \tau\tau$ analysis relies on `single lepton triggers`. Lepton candidates have to pass the last trigger level, the event filter (see Chapt. 4). The muon candidates must have a transverse momentum of at least 13 GeV while the electron trigger requires at least 15 GeV transverse momentum.

To have a sample of collision candidate events, at least one primary vertex with more than three reconstructed tracks is required. Furthermore, events with so called 'bad' jets have to be rejected. The reason is that high energy deposits not originating from the proton-proton collision can be situated in the calorimeter system (e.g. from unexpected discharges in the end-cap or coherent noise in the electromagnetic calorimeter [110]. For that reason several quality criteria were implemented [109]:

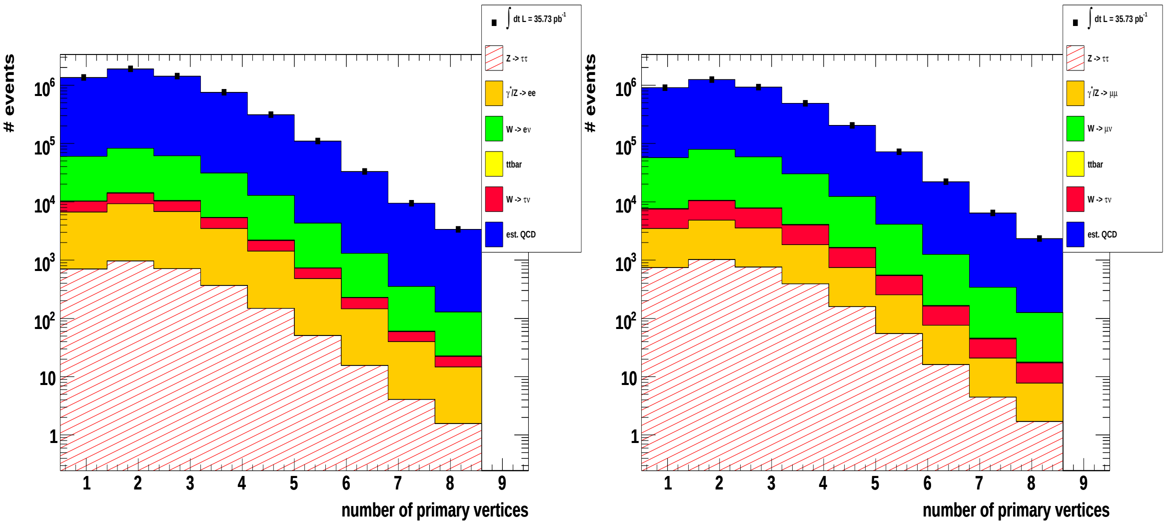

(a) (b)

Figure 7.4: *The number of primary vertices after jet cleaning for the electron channel (a) and the muon channel (b). All MC are normalised to data.*

- If more than 80 % of E^{jet} is deposited in hadronic end-cap (HEC) calorimeter → 90 % of E^{jet} must be distributed over at least 6 calorimeter cells.
- If more than 50 % of E^{jet} is deposited in HEC calorimeter → less than 50 % of E^{jet}_{total} must come from cells with abnormal signal shape.
- If more than 95 % of E^{jet} is deposited in hadronic end-cap (HEC) calorimeter → less than 80 % of E^{jet} must come from cells with abnormal signal shape.
- Jets must primarily contain cells with energy deposit less than 25 ns before and after the proton-proton bunch crossing.
- If the jet has no associated track, at least 5 % of E^{jet} must be deposited in the electromagnetic (EM) calorimeter.
- If a jet is outside a region considered for τ-lepton candidates and contributes only to E_T^{miss} → at least 5 % of E^{jet} must be deposited in the (EM) calorimeter.
- If the jet is central, the maximum fraction of the total energy in a single calorimeter layer must not exceed 99 %.

All jets with E_T greater than 10 GeV have to fulfil these requirements. Otherwise the event will be rejected. The number of jets fulfilling all criteria are shown in Fig. 7.3. The number of primary vertices in events fulfilling the criteria are shown in Fig. 7.4.

7.2 The object pre-selection

The object pre-selection considers looser cuts applied on each individual object. The cuts used for the pre-selection are:

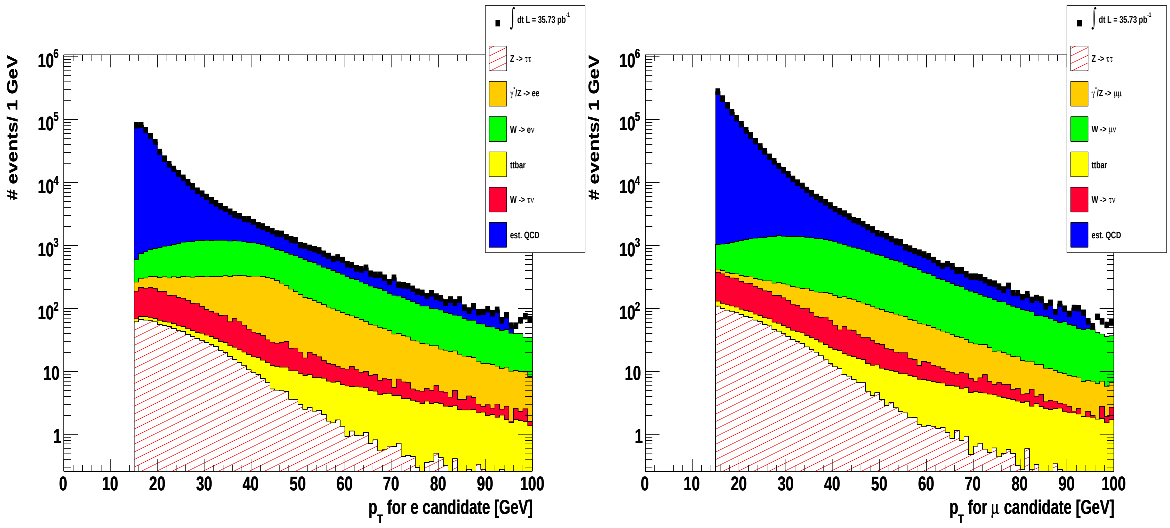

(a) (b)

Figure 7.5: *The p_T distributions for the selected electrons (a) and selected muons (b). The gap between data and Monte Carlo in the region above p_T >90 GeV is due to missing QCD Monte Carlo events in this region, so no rescaling was possible. This does not affect the τ-lepton selection, since τ-leptons coming from the Z $\rightarrow \tau\tau$ decay does not reach this transverse momentum region.*

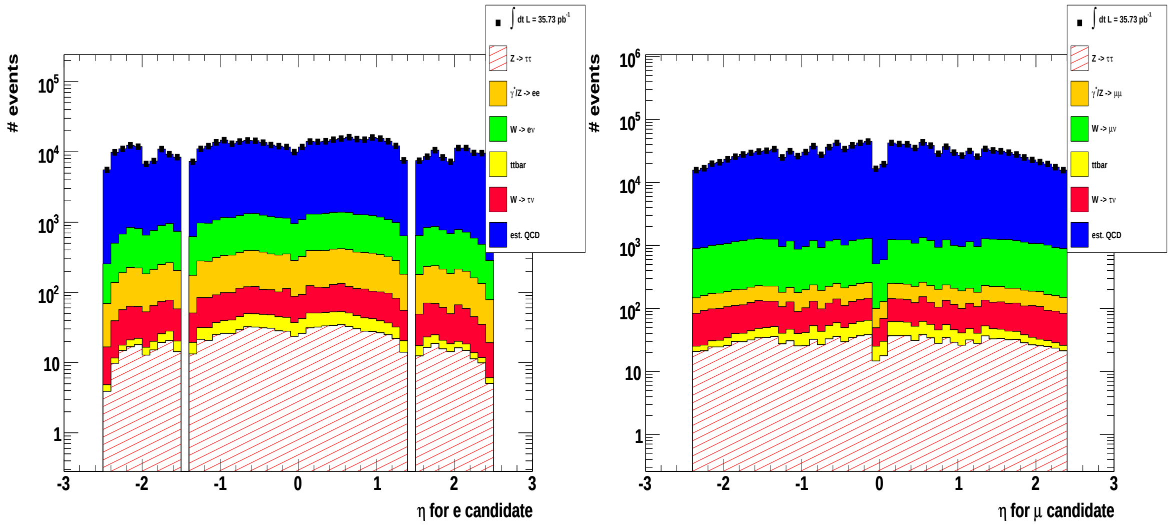

(a) (b)

Figure 7.6: *The η distributions for the selected electrons (a) and selected muons (b). For the electron channel the gap in the region $|\eta| \simeq$1.4 is due to the construction of the calorimeter as described in the text.*

- Pre-selection of an electron candidate:
  - As described in Sec. 6.1.1 the electron reconstruction uses inner detector and calorimeter information. The combination of calorimeter and inner detector information provides a good signal against background separation. In order to suppress background the reconstruction algorithms have to distinguish real electrons from fake electrons due to misidentified jets or photons. To handle different requirements to analysis aims three levels of signal versus purity are defined. As for the τ-lepton identification, the levels related to the signal efficiency are `loose`, `medium` and `tight`. For the visible mass analysis the pre-selected electrons have to fulfil $E_T > 10\,\mathrm{GeV}$ within a pseudo-rapidity of $|\eta| < 2.47$[4]. In addition, they have to pass special electron requirements [111].
- Pre-selection of a muon candidate:
  - The muons in this analysis are reconstructed using the `staco` algorithm. These `standalone muons` are formed from inner detector and muon spectrometer track information. The combined transverse momentum p_T has to be larger than $10\,\mathrm{GeV}$ within a pseudo-rapidity of $|\eta| < 2.4$.
- Pre-selection of a τ-lepton candidate:
  - The τ-lepton candidates are preselected if they fulfil $p_T > 15\,\mathrm{GeV}$ within $|\eta| < 2.5$. In addition they have to pass the looser `cut based ID`.

The fact, that the same object can be identified as more than one candidate it is required to have an `overlap removal`. Electron, muons are not permitted to be in a radius of $\Delta R < 0.2$. The τ-lepton has to be removed if it overlaps with any other lepton within a radius of $\Delta R < 0.4$.

7.3 The object selection

In principle the object selection uses only tighter requirements as defined for the pre-selection.

- Selection of an electron candidate:
  - Electrons have to fulfil a tighter transverse momentum criteria: $p_T > 15\,\mathrm{GeV}$.
  - They also have to pass the `robust tight` selection.
- Selection of a muon candidate:
  - The muon selection uses more detailed information from the sub detector components.
  - Muons have to fulfil a tighter transverse momentum criteria: $p_T > 15\,\mathrm{GeV}$.

[4] excluding the region between barrel and end-cap: $1.37 < |\eta| < 1.52$

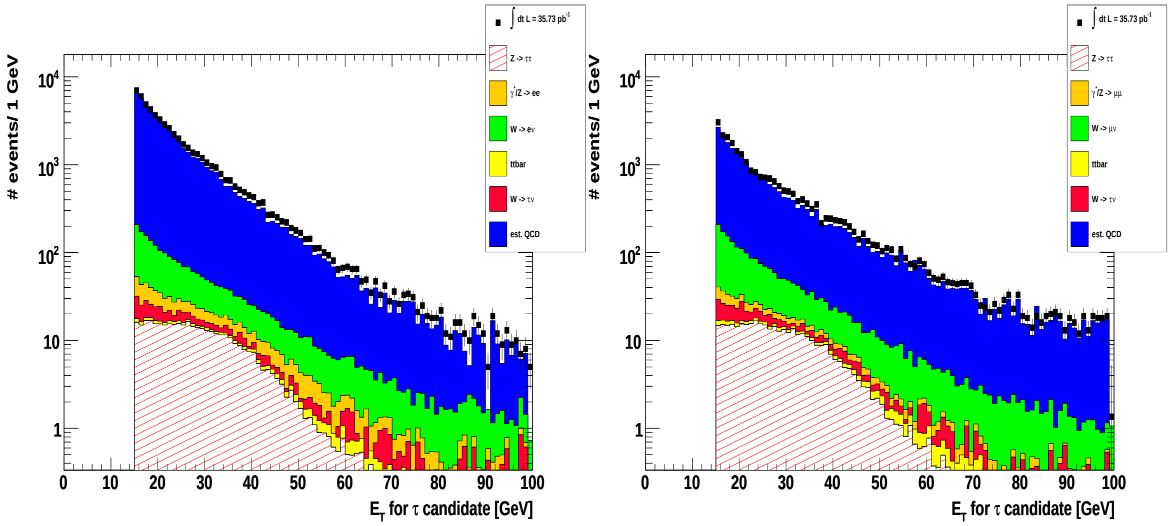

(a) (b)

Figure 7.7: *The selected τ-lepton distribution binned in p_T for the electron channel (a) and the muon channel (b). The τ-lepton selection includes the τ-lepton identification criteria which have a large rejection power against QCD multi-jets. As expected the region above 60 GeV becomes signal free. The remaining background can be further suppressed by applying a combination of τ-lepton candidates with a lepton candidate to perform the charge product as well as the visible mass window.*

  - They must have a (well) reconstructed inner detector track as well as 6 or more hits in the silicon microstrip (SCT) detector. In order to suppress track misreconstructions, the standalone muon track is required to be greater than 60 % of the the track momenta in the inner detector.

- Selection of a τ-lepton candidate:
  - τ-lepton candidates have to fulfil for this analysis the identification criteria `cut based medium`(see Chapt. 6). Furthermore they have to pass electron and muon vetoes (see Chapt. 6).

7.4 Lepton isolation

In order to suppress QCD multi-jet background, lepton isolation is required. Leptons from the τ-lepton decay are preferably isolated while the leptons from QCD multi-jets (particular from b-quark decays) are accompanied by additional tracks (jets) which contributes to the overall energy around the lepton track. The isolation criteria are divided into different quantities:

- The transverse energy (of charged and neutral particles in the electromagnetic calorimeter) in a cone around the lepton: $\mathrm{E_T}$ConeX, with X describing a cone of ΔR of 0.2, 0.3 or 0.4.

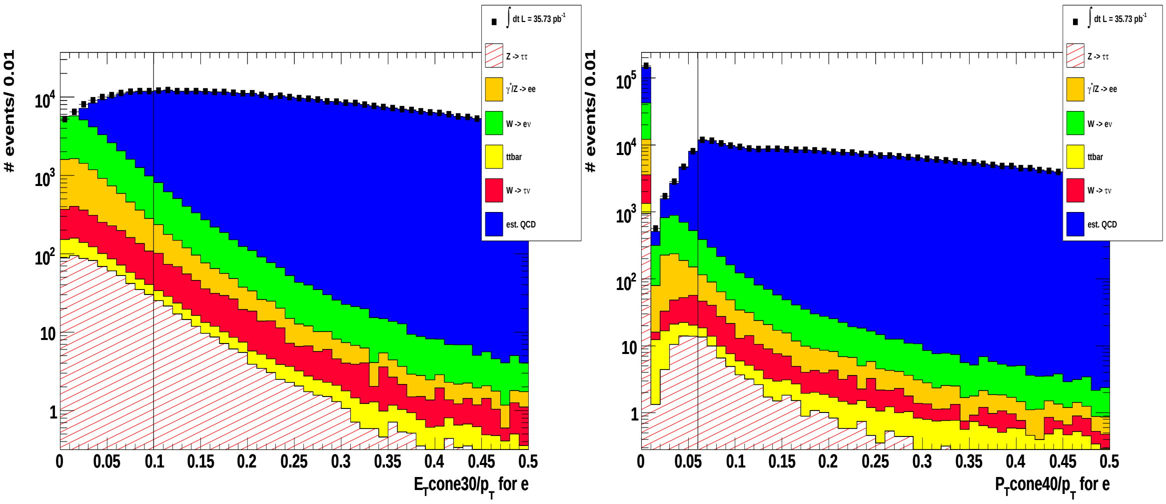

(a) (b)

Figure 7.8: *The isolation criteria for electrons. It can be seen that both variables, E_T (a) and p_T (b) have an efficient rejection power against QCD multi-jets.*

Isolation variable	ε **for signal**	ε **for QCD multi-jets**
Muon ($\mathrm{p_T}$cone40/$\mathrm{p_T}$ < 0.06)	0.926(2)	0.076(1)
Muon ($\mathrm{E_T}$Cone40/$\mathrm{p_T}$ < 0.06)	0.872(3)	0.0309(6)
Electron ($\mathrm{p_T}$Cone40/$\mathrm{p_T}$ < 0.06	0.941(3)	0.232(3)
Electron: ($\mathrm{E_T}$cone30/$\mathrm{p_T}$ < 0.1	0.814(4)	0.0.082(2)

Table 7.4: *The isolation efficiencies for electrons and muons after object selection. For the muons the efficiency is calculated after pre-selection which already includes a (looser)* $\mathrm{p_T}$Cone40/$\mathrm{p_T}$ *< 0.2. The brackets give the statistical error on the last digit.*

- The number of tracks besides the lepton track itself: NuConeX.
- The transverse momentum of associated tracks of charged particles: $\mathrm{p_T}$ConeX.
- $\mathrm{E_T}$ConeX and $\mathrm{p_T}$ConeX can be normalised to the $\mathrm{p_T}$ of the leptons.

The corresponding cut efficiencies are given in Tab. 7.4 [109].

With increasing luminosities these isolation criteria becomes sensitive to pile-up events with the consequence that the isolation efficiency decreases significantly. For $\mathrm{E_T}$ConeX it is not possible to obtain the origin of the energy deposit in the calorimeter. For the increasing number of pile-up events the probability increases that an additional primary vertex points to the same cell and increases the activity in this region (see Fig. 7.10). Although a real lepton from Z → ττ is within this cone those additional tracks can induces a suppression of such an event.

In order to solve such problems for further analysis the $\mathrm{E_T}$ConeX criteria is defined flexible with respect to the number of primary vertices, i.e. for more reconstructed primary vertices in an event the allowed activity around the lepton in the required cone increases.

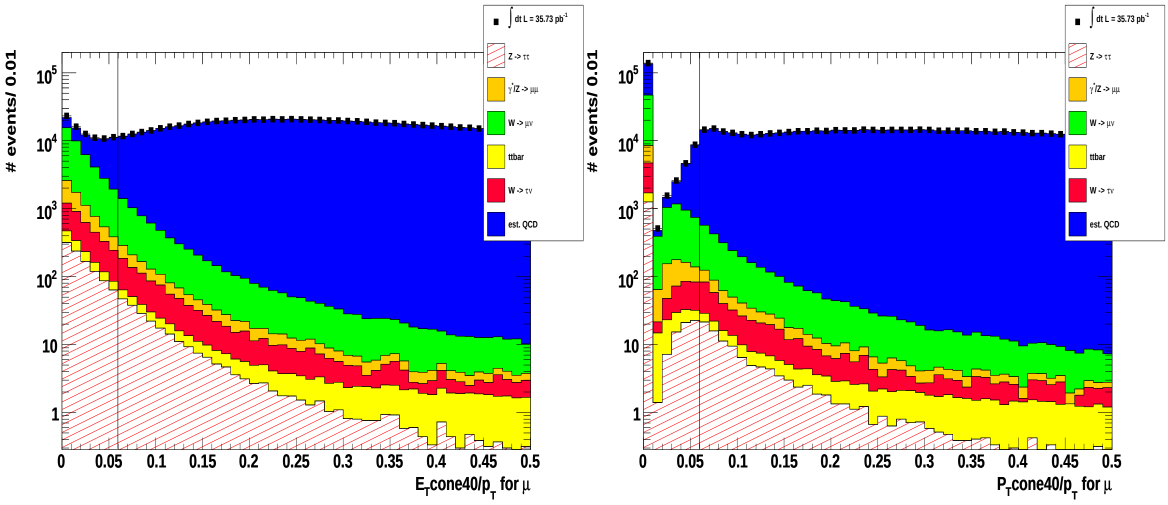

(a) (b)

Figure 7.9: *The isolation criteria for muons. It can be seen that both variables, E_T (a) and p_T (b) have an efficient rejection power against QCD multi-jets.*

Electron pre-selection used for overlap removal and di-lepton veto
$p_T > 10\,\text{GeV}$
$\lvert\eta\rvert < 2.47$, but excluding $1.37 < \lvert\eta\rvert < 1.52$
Not in bad OQmaps region
electron author 1 or 3
`robust medium` electron
Electron selection
$p_T > 15\,\text{GeV}$
`robuster tight` electron

Table 7.5: *Pre-Selection and selection cuts of electrons [109].*

Figure 7.11 shows the variable $E_T$coneX/p_T depending from the number of vertices studied with a Monte Carlo sample.

Tabs. 7.5, 7.6, and 7.7 summarise all cuts for the electron, muon, and τ-lepton selection.

7.5 Transverse missing energy E_T^{miss}

The visible mass selection[5)] does not use the magnitude of the missing energy E_T^{miss}. Only the direction of E_T^{miss} is used (see $W \to \ell\nu$ suppression). The missing energy is based on energy deposits in the calorimeter and reconstructed muon tracks and can be expressed as [109]:

$$E_T^{miss} = E_T^{miss}(\text{cell}) + E_T^{miss}(\text{combined muon}) - E_T^{miss}(\text{correction}) \tag{7.2}$$

[5)] For the invariant mass analysis also the magnitude of the missing energy is used.

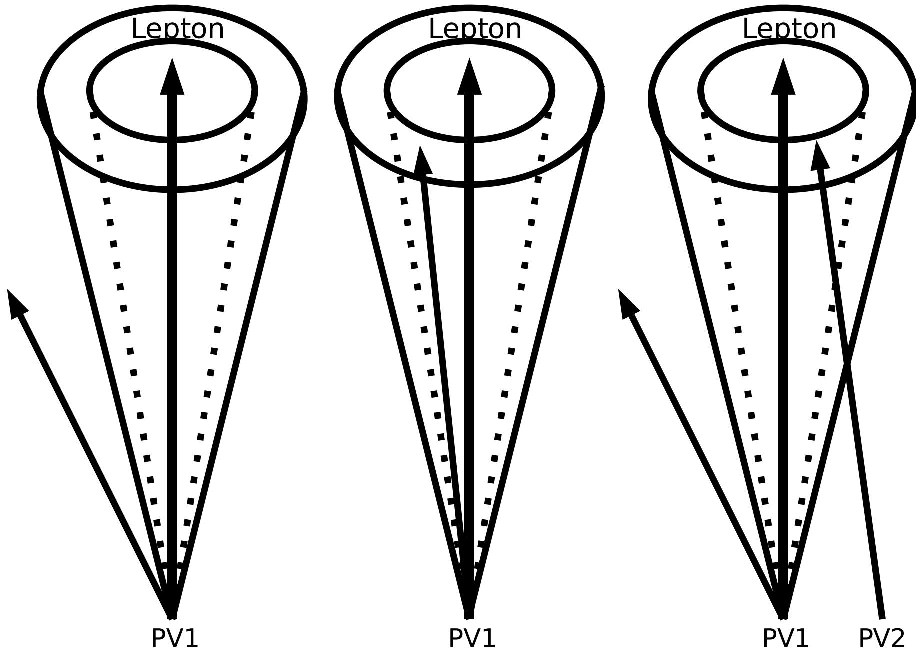

Figure 7.10: *Illustration of the effect of pile-up on isolation criteria. Left: for the normal non pile-up signal event the additional track is outside the isolation cone around the lepton and therefore this event has less activity in the isolation cone. Middle: for a typical QCD event an additional track situated within the isolation cone and contributes to the sum of transverse energy. Right: a signal event is affected by pile-up. Although the additional track from the original primary vertex is outside the cone, the track from the additional primary vertex is situated within the isolation cone of the original lepton. This event would be removed since* $\mathrm{E_T}$Cone$X$ *is larger than the required threshold.*

Muon pre-selection used for overlap removal and di-lepton veto
$\mathrm{p_T} > 10\,GeV$
$\lvert\eta\rvert < 2.4$
`isCombinedMuon`
$\lvert\mathrm{z_0}\rvert < 10\,\mathrm{mm}$
Muon selection
$\mathrm{p_T} > 15\,GeV$
$\mathrm{p_T}(\mathrm{mu^{MS}_{Track}}) < 50$ GeV : $(\mathrm{p_T}(\mathrm{mu^{MS}_{Track}}) - \mathrm{p_T}(\mathrm{mu^{ID}_{Track}}))/\mathrm{p_T}(\mathrm{mu^{ID}_{Track}}) > -0.4$
nPixHits> 0
nSCTHits> 5
$\lvert\eta\rvert < 1.9$: nTRT Outliers / (nTRT Hits + nTRT Outliers) < 0.9
$\lvert\eta\rvert >= 1.9$ & nTRT Hits > 5: nTRT Outliers / (nTRT Hits + nTRT Outliers) < 0.9
`match` $\chi^2 < 150$

Table 7.6: *Pre-Selection and selection cuts of muons [109].*

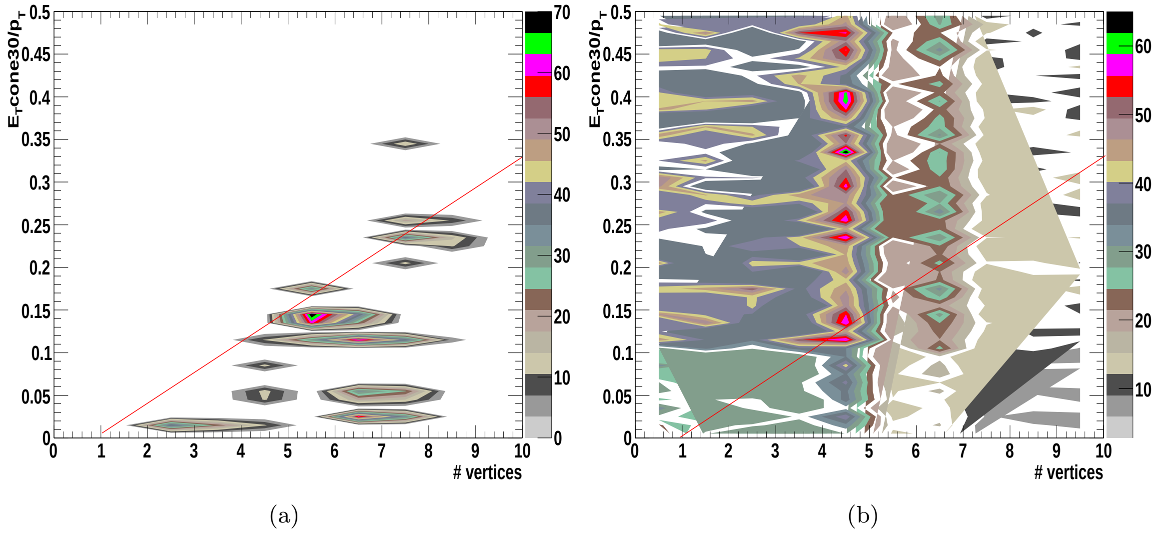

Figure 7.11: *$E_T cone30/p_T$ versus the number of primary vertices. The average number of primary vertices is 5. The signal distribution is shown in (a) while the QCD multi-jet background is shown in (b). This MC based study is not considered in the current analysis but becomes important for increasing luminosities.*

τ-lepton candidate pre-Selection			
$p_T > 15$ GeV			
$\lvert\eta\rvert < 2.5$			
`loose` simple cuts τ-lepton-ID			
τ-lepton candidate selection			
author 1 or 3			
passes e and μ vetoes			
`medium` simple cuts τ-ID			
`medium` τ-ID cut values			
	R_{EM}	R_{trk}	$f_{trk,1}$
1 track	< 0.05	< 0.08	> 0.12
$\geq$ 2 tracks	< 0.09	< 0.05	> 0.32

Table 7.7: *The τ-lepton candidate selection cuts summary and the exact cut values for the* `medium` *cut-based τ-lepton candidate identification [109].*

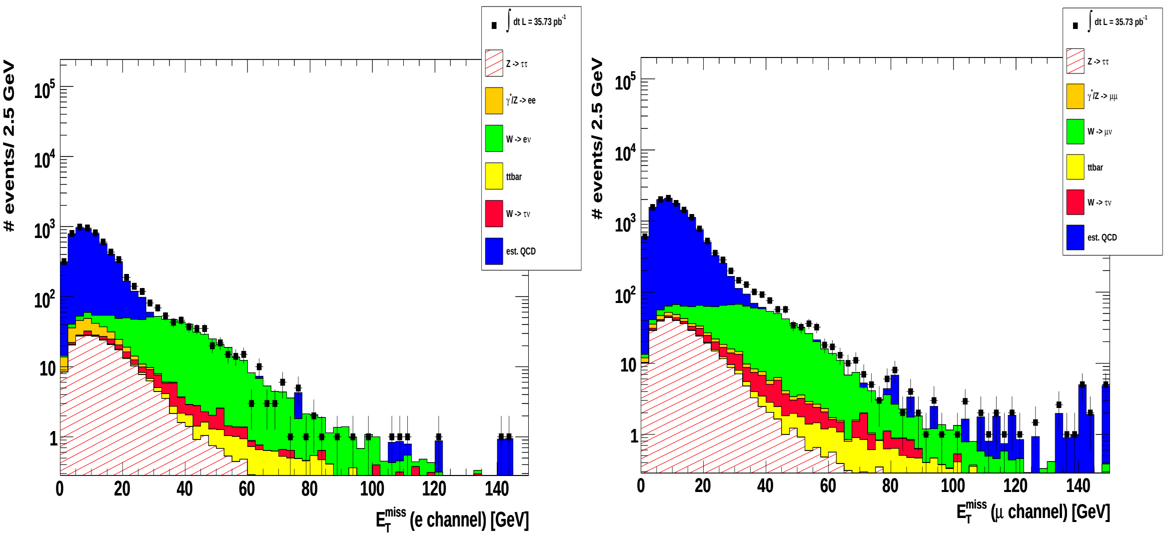

(a) (b)

Figure 7.12: *The E_T^{miss} distributions for the electron channel (a) and the muon channel (b). The distributions show that a $E_T^{miss} > 20\,\mathrm{GeV}$ requirement would reject most of the QCD background but also a significant number of τ-lepton candidates.*

with $\mathrm{E_T^{miss}}$(cell) calculated from the cells in the calorimeter and $\mathrm{E_T^{miss}}$(combined muon) for the momenta of all isolated combined muons[6] but also all non-isolated muons reconstructed as tracks in the calorimeter. To avoid double counting, the last term is subtracted. $\mathrm{E_T^{miss}}$(correction) is the sum of the energy in the calorimeter cells crossed by an isolated lepton.

7.6 Event selection

Up to now all pre-selection cuts as well as object selection criteria for electrons, muons and τ-leptons have been discussed.

In order to suppress remaining background all selected objects for an event are combined to (τ_h, τ_ℓ) objects. Those combinations allow to define new criteria like the charge product or the visible (invariant) mass. Requiring isolation criteria on leptons and identification cuts on the τ-lepton suppresses the QCD multi-jet background very efficient with the result that electro-weak background becomes the dominant background. In order to suppress electro-weak background (i.e. $Z \to \ell\ell$ and $W \to \ell\nu$ events) further cuts are defined. The first cut is the `di-lepton veto` to reject $Z \to \ell\ell$ events. If two (or more) pre-selected electron or muon candidates are found then the event will not be accepted. The pre-selected leptons were chosen since looser lepton selection cuts increase the probability to reconstruct the second lepton. The charge product for (τ, ℓ) is require to be -1 in order to have two objects coming from a Z-boson decay. Furthermore, the visible mass window

[6]Reminder: combined muons denotes muons selected with track (inner detector) and muon spectrometer information (see 6).

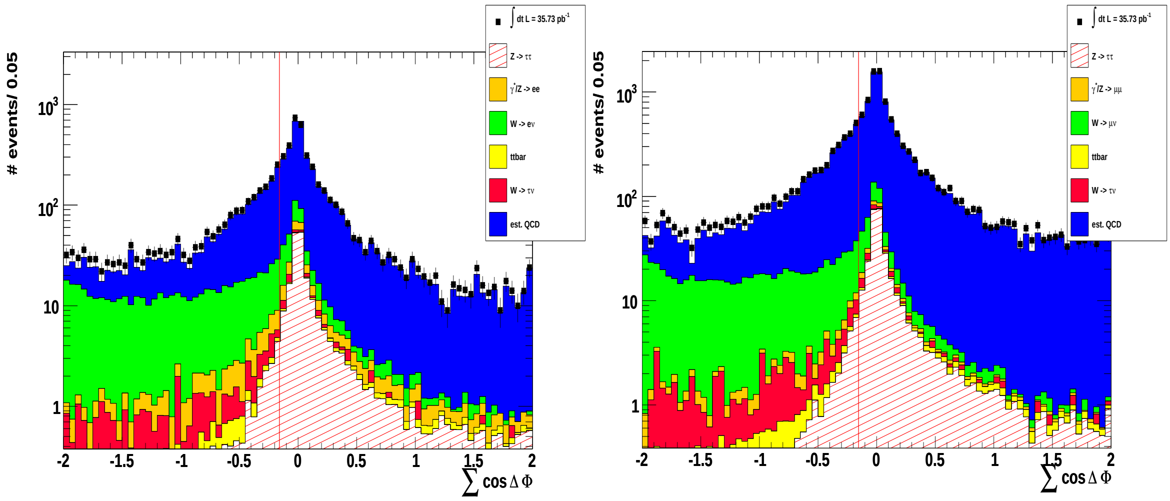

(a) (b)

Figure 7.13: *The $\sum cos\Delta\phi$ distributions for the electron channel (a) and the muon channel (b). Events with $\sum cos\Delta\phi > -0.15$ which provides a good $W \to \ell\nu$ suppression.*

$37\,\mathrm{GeV} < \mathrm{m_{vis}}(\tau_\mathrm{h}, \tau_\ell) < 75\,\mathrm{GeV}$ also provides a good suppression since $Z \to \ell\ell$ have a smaller $\mathrm{E_T^{miss}}$ contribution than $\mathrm{Z} \to \tau\tau$ events and therefore a higher visible mass.

The next electro-weak background source is the $W \to \ell\nu$+jets channel. While the lepton from the W decay is almost correctly identified the associated quark-jet can fake the τ-lepton. In order to suppress the W channel two variables, the $\sum \cos\Delta\phi$ and $\mathrm{m_T}(\ell, \mathrm{E_T^{miss}})$ variables are applied.

Figure 7.15 illustrates the position of $\mathrm{E_T^{miss}}$ relative to the Z decay products [109]. Since the mass of the Z-boson is much larger than the mass of the τ-lepton the latter will be boosted such that their decay products are collimated along the original trajectory. The $\mathrm{E_T^{miss}}$ is the vector sum of the neutrino $\mathrm{p_T}$. As shown in Fig. 7.15(a) the $\mathrm{E_T^{miss}}$ falls for boosted Z-bosons within the neutrinos. In W events the lepton, the neutrino and the jet should fly in different directions and balancing $\mathrm{p_T}$ in the transverse plane (see Fig. 7.15(b)). For the $\mathrm{W} \to \mathrm{tau}\nu$ one more neutrino is taken into account. In Fig. 7.15(c)) it is visible that the $\mathrm{E_T^{miss}}$ vector still points in the direction between the lepton and the fake τ-lepton. The first variable is

$$\sum \cos\Delta\phi = \cos\left(\phi(\ell) - \phi(\mathrm{E_T^{miss}})\right) + \cos\left(\phi(\tau_\mathrm{h}) - \phi(\mathrm{E_T^{miss}})\right) \tag{7.3}$$

and the second variable is

$$\mathrm{m_T}(\ell, \mathrm{E_T^{miss}}) = \sqrt{2\,\mathrm{p_T}(\ell) \cdot \mathrm{E_T^{miss}} \cdot (1 - \cos\Delta\phi(\ell, \mathrm{E_T^{miss}}))}. \tag{7.4}$$

The $\mathrm{m_T}(\ell, \mathrm{E_T^{miss}})$ is the transverse mass between the lepton and $\mathrm{E_T^{miss}}$. The performance of these variables is shown in Fig. 7.13 and Fig. 7.14. Since the $\sum \cos\Delta\phi$ criteria has a large rejection power against W events, the $\mathrm{m_T}(\ell, \mathrm{E_T^{miss}})$ criteria can be defined looser

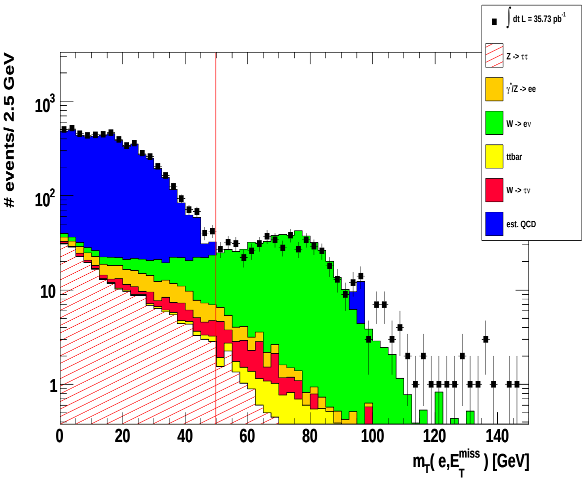

(a)

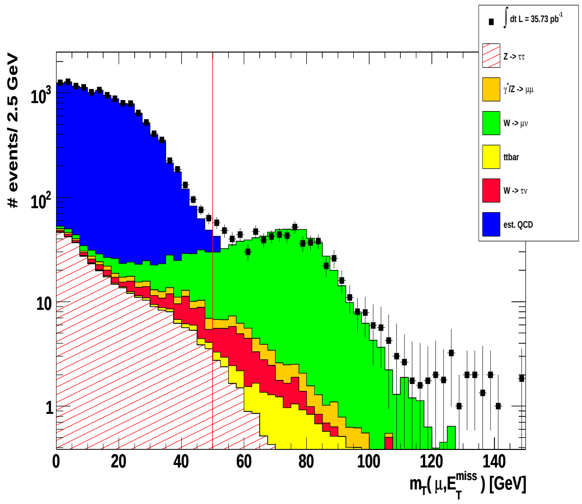

(b)

Figure 7.14: *The $m_T(\ell, E_T^{miss})$ distributions for the electron channel (a) and the muon channel (b). Events fulfilling $m_T(\ell, E_T^{miss}) < 50\,\mathrm{GeV}$ are accepted.*

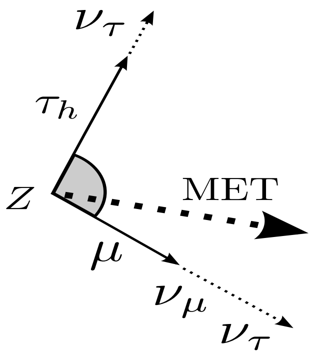

(a) $Z \rightarrow \tau\tau \rightarrow \mu\tau_{\mathrm{h}}$

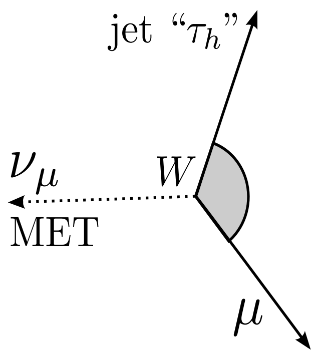

(b) $W \rightarrow \mu\nu$

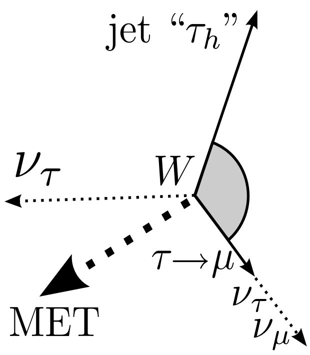

(c) $W \rightarrow \tau\nu \rightarrow \mu\nu\nu\nu$

Figure 7.15: *Drawings of representative transverse plane orientations of W and Z decay products and the E_T^{miss}. The shaded angles indicate the angle less than π between the lepton and the (fake) τ-lepton. In (a), the Z is depicted to have nonzero p_T, which must be balanced on the left by some other activity omitted for clarity.*

as for previous studies ($m_T(\ell, E_T^{miss}) < 50\,\mathrm{GeV}$ instead of $m_T(\ell, E_T^{miss}) < 40\,\mathrm{GeV}$ as defined without $\sum \cos\Delta\phi$).

As mentioned before, the charge product is required to be -1 (opposite sign charge). The option that the charge product is +1 defines the same sign charge distribution and is background dominated. As discussed in Sec 6.2.1 due to charge mis-identification also true $Z \to \tau\tau$ events can assigned to the same sign region but the number of events is small compared with the real background in these region. Finally, a cut on the visible mass is applied. The visible (τ, ℓ) mass divided into opposite sign charge (OS) and same sign charge (SS) is shown in Fig 7.16.

With the requirement that all τ-lepton candidates must have one or three associated tracks all criteria to reconstruct and identify (τ_h, τ_ℓ) pairs are applied.

7.7 Background estimation

In order to reduce the QCD multi-jet and electro-weak background further the opposite sign charge minus same sign charge method (OS-SS) will be applied. The OS-SS bases on the fact that for statistical reasons the charge combinations are well balanced. The probability to combine (lepton,(fake)τ-lepton) pairs with opposite charges should be in the same order as for the same sign charge combination. The remaining background would be completely rejected.

Contrary, the assumption for the signal region is that more or less all selected events having a τ-lepton and a lepton combination are supposed to be opposite charged[7)]. The basic idea is that no charge is preferred for the fake τ-leptons. Since jets mostly fake the τ-leptons and events have more than one jet it should result in a balanced charge combination for the two visible mass candidates.

Unfortunately, for the electro-weak background (W+jets, Z+jets) the relation is OS/SS $\neq 1$. In order to rescale OS/SS data-driven methods were developed which will be discussed in section 7.7.1. For the QCD multi-jet background Monte Carlo studies favour charge symmetry. Due to the large statistic for the QCD multi-jet background small deviations from OS/SS = 1 could have crucial consequences for the background performance. The symmetry study for the QCD will be summarised in 7.7. The Z+jets channel has also a significant charge asymmetry and will be discussed in section 7.7.2. It has to be mentioned that $t\bar{t}$ has also an OS/SS asymmetry but the main difference from the other background sources is that both, the lepton and the τ-lepton candidate, may be real. This cannot be solved with the methods introduced in the following sections. Fortunately, $t\bar{t}$ founds to be negligible.

The di-boson channels WW, WZ, and ZZ have small cross sections (see Tab. 7.2) compared with the signal and therefore the expected contribution is about ten times smaller as the number of events for $t\bar{t}$.

[7)]Due to charge mis-identification or wrong object selection a true event can also identified as a same sign charged event. The statistic should be very small (compared with the remaining SS-background) after τ-lepton identification cuts.

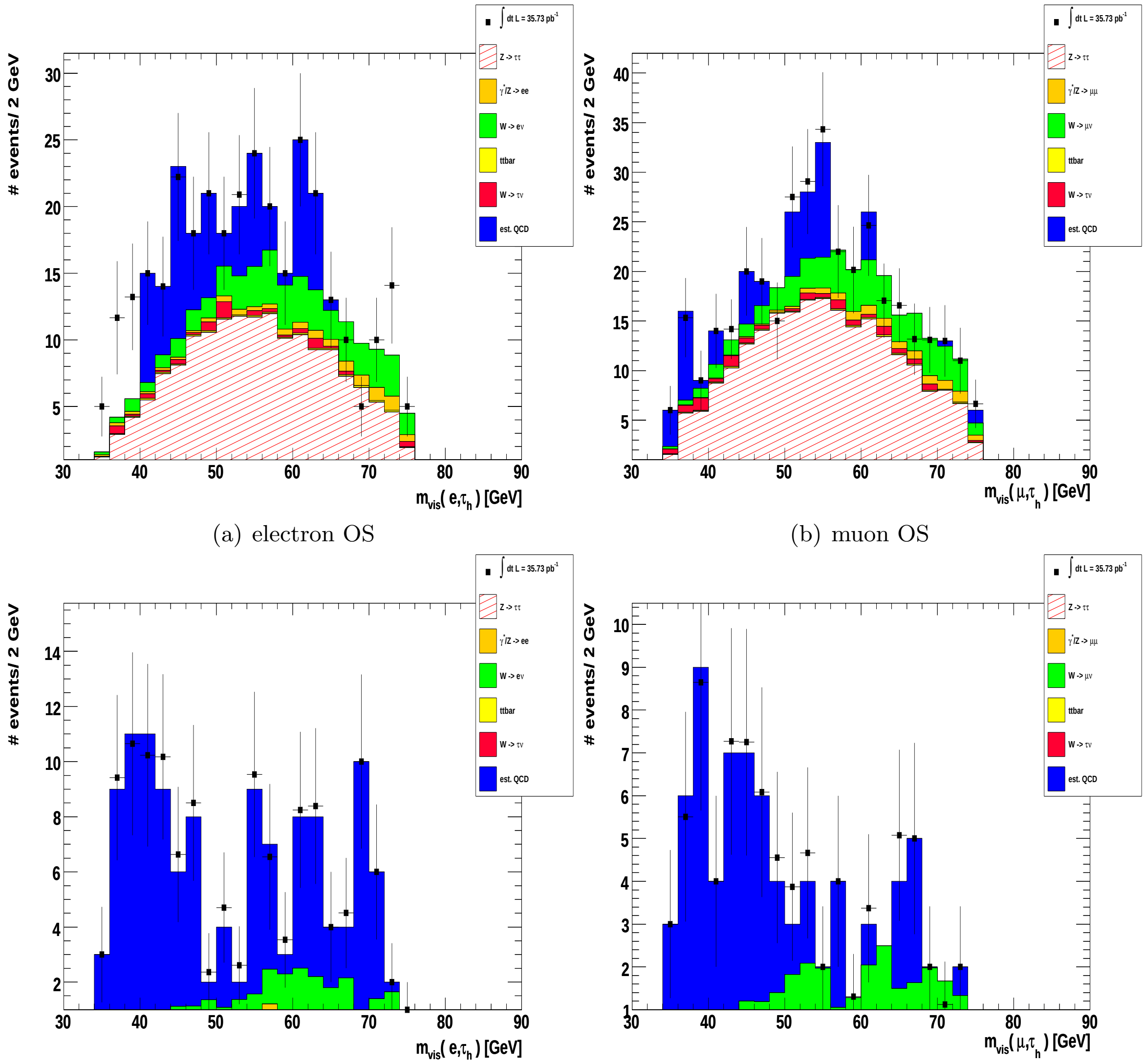

(a) electron OS

(b) muon OS

(c) electron SS

(d) muon SS

Figure 7.16: *The visible mass distributions for the electron channel for OS (a) and SS (b) and the muon channel for OS (c) and SS (d). It can be seen, that QCD background is dominant for the lower visible mass region. The same sign regions (c,d) are dominated by QCD and $W \rightarrow \ell\nu$ background. As expected the QCD background tends to be symmetric while the electro-weak background shows an asymmetry due to less events in the same sign region.*

7.7.1 OS-SS asymmetry in $W \to \ell\nu$+jets events

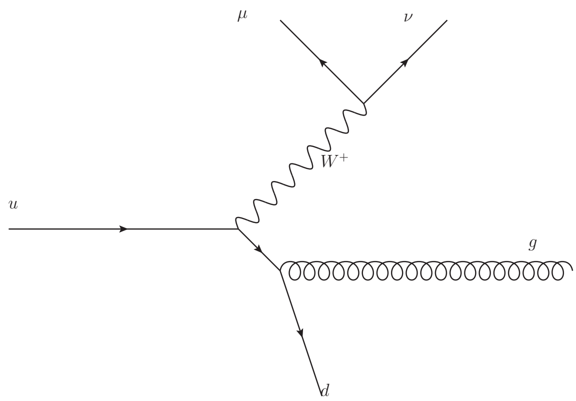

Figure 7.17: *The W+jet production for the one parton final state.*

As mentioned already, the W+jets channel has a significant asymmetry in its charge combination. This section discusses the reasons and used (data-driven) methods. Two

W $\to$ eν				
Parton final state	σ **[pb]**	$(\frac{\mathrm{OS}}{\mathrm{SS}})^{\mathrm{MC}}_{\mathrm{tight}}$	$(\frac{\mathrm{OS}}{\mathrm{SS}})^{\mathrm{MC}}_{\mathrm{medium}}$	$(\frac{\mathrm{OS}}{\mathrm{SS}})^{\mathrm{MC}}_{\mathrm{loose}}$
0	6.87×10^3	0.5$\pm$0.43	1.16$\pm$0.51	1.95$\pm$0.49
1	1.29×10^3	2.58 $\pm$0.73	3$\pm$0.49	2.56$\pm$0.28
2	0.376×10^3	2.63$\pm$0.66	1.89$\pm$0.23	1.72$\pm$0.12
3	0.101×10^3	2$\pm$0.7	2.71$\pm$0.6	1.93$\pm$0.31
4	0.025×10^3	3$\pm$2	1.8$\pm$0.7	1.5$\pm$0.45
W $\to$ $\mu\nu$				
Parton final state	σ **[pb]**	$(\frac{\mathrm{OS}}{\mathrm{SS}})^{\mathrm{MC}}_{\mathrm{tight}}$	$(\frac{\mathrm{OS}}{\mathrm{SS}})^{\mathrm{MC}}_{\mathrm{medium}}$	$(\frac{\mathrm{OS}}{\mathrm{SS}})^{\mathrm{MC}}_{\mathrm{loose}}$
0	687×10^3	OS only	2.5$\pm$1.2	1.83$\pm$0.47
1	1.29×10^3	3.41$\pm$0.94	2.67$\pm$0.41	2.01$\pm$0.19
2	0.376×10^3	3.2 $\pm$0.67	2.99$\pm$0.34	2.35$\pm$0.19
3	0.101×10^3	3.36 $\pm$1.15	2.72$\pm$0.53	2.27$\pm$0.33
4	0.025×10^3	2.2 $\pm$1.18	1.65$\pm$0.46	1.80$\pm$0.44

Table 7.8: *For $W \to \ell\nu$: different parton final states with the corresponding cross sections and separated into three* `cut based ids` *for the τ-lepton.*

effects causes the charge asymmetry in the W-boson decay channels:

- An intrinsic charge asymmetry due to proton-proton interactions which slightly prefer W^+ bosons [112], [113].
- The outgoing quark, which almost fakes the τ-lepton, has the opposite charge to the outgoing lepton. For higher jet multiplicities it is expected that the OS/SS asymmetry

Cut	Signal region	Control region
$\sum \cos\Delta\phi$	$>$ -0.15	$<$ -0.15
$m_T(\ell, E_T^{miss})$	$<$ 50 GeV	$>$ 50 GeV

Table 7.9: *Modified control cuts for the $W \rightarrow \ell\nu$ region.*

becomes smaller because of the higher probability that an additional jet fakes the τ-lepton. This is in fact true, but events with higher jet multiplicity have a smaller cross section compared with the one parton final state.

Table 7.8 shows the OS/SS asymmetry for $W \rightarrow e\nu$ and $W \rightarrow \mu\nu$ events with respect to the `cut based` identification for τ-leptons. The channels are separated into (0–4) parton final states. The samples are generated with `AlpgenJimmy` including pile-up with an average of two primary vertices per event. As can be seen, the OS/SS ratio has the tendency to decrease for increasing number of parton final states. But this effect cannot compensate the larger asymmetry for events with lower jet multiplicity.

The conclusion is that the same sign charge combinations have to be rescaled from data. Due to the small number of $W \rightarrow \ell\nu$ background events in the current analysis the rescaling factor is taken from Monte Carlo predictions. The estimated OS/SS charge asymmetry is checked with the OS/SS asymmetry obtained from a data-driven method as described below. To fulfil the requirement OS/SS $\simeq 1$, the SS distribution is rescaled with a factor g_W where W denotes the W-boson decay channels. In order to estimate such rescaling factors a so called `control region` is defined. Control regions are regions where only (with highest purity) the channel of interest fakes the τ-lepton (e.g. the control region for the $W \rightarrow e\nu$ channel only contains $W \rightarrow e\nu$ events faking a τ-lepton). The factor g_W, estimated in those control region, will be extrapolated to the signal region. The challenge is the suppression of additional background and, more complicated, real $Z \rightarrow \tau\tau$ events. The basic assumption is that the ratio OS/SS is similar (within an acceptable uncertainty), for the original selection (`signal region`) and the new selection defining the control region.

The requirement is to change the cuts as less as possible. For the $W \rightarrow \ell\nu$ control region the changed cuts are summarised in Tab. 7.9. In Figs. 7.13 and 7.14 it can be seen that an inversion of the cuts results in a region dominated by $W \rightarrow \ell\nu$ events.

Figure 7.18 shows the p_T distribution of the (fake) τ-lepton for the muon channel. For the tight τ-lepton identification the Monte Carlo was found to overestimate the data. Fake rate studies result in the conclusion that also the τ-lepton fake rate from jets is overestimated by the Monte Carlo prediction [80]. In order to get the correct numbers, the W Monte Carlo was normalised to the data found in the W control region. The normalisation also considers contributions from further electro-weak channels like $Z \rightarrow \ell\ell$, $t\bar{t}$ or the di-boson channels. The high transverse mass requirement suppresses the QCD multi-jet contribution significantly. The correction factor for the overestimated Monte Carlo is

$$N_W^{WCR} = k_W N_W^{WCR} = N_W^{data} - N_{Z\rightarrow\ell\ell}^{WCR} - N_{t\bar{t}}^{WCR}. \tag{7.5}$$

The measured k_W factors are:

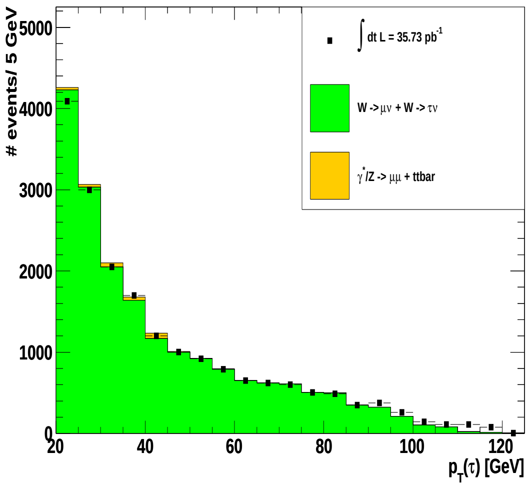

(a) (b)

Figure 7.18: *The p_T distribution of the (fake) τ-lepton without τ-lepton identification (a) and with tight τ-lepton identification (b). The deviation between data and Monte Carlo in (b) is due to the W overestimation by the Monte Carlo.*

Sample	OS mu channel	SS mu channel	OS e channel	SS e channel
$W \to \ell\nu$	21±4	8±3	16±4	7±3
$W \to \tau\nu$	8±2	3±2	4±2	2±2

Table 7.10: *Number of events in the OS and SS signal region after all cuts using the MC scaling factor k_W.*

- Muon channel:
  - (opposite sign, loose + not tight tau): $\mathrm{k_W} = 0.93 \pm 0.04$
  - (opposite sign, tight tau): $\mathrm{k_W} = 0.73 \pm 0.06$
  - (same sign, tight tau): $\mathrm{k_W} = 0.94 \pm 0.13$.
- Electron channel:
  - (opposite sign, loose + not tight tau): $\mathrm{k_W} = 0.97 \pm 0.04$
  - (opposite sign, tight tau): $\mathrm{k_W} = 0.63 \pm 0.07$
  - (same sign, tight tau): $\mathrm{k_W} = 0.83 \pm 0.15$.

The number of estimated $W \to \ell\nu$ events in the signal region is summarised in Tab. 7.10. The values for OS and SS are compared with the number of events obtained from the data control region. The OS/SS asymmetry obtained from the data control region is $\mathrm{R_{OSSS}} = 2.34 \pm 0.67$ while the value obtained from MC is 2.22 ± 0.34.

The OS/SS asymmetry can be different depending from the $\mathrm{p_T}$ region. This can affect the estimated overall efficiency using the extrapolation from the control region to the signal region. The $\mathrm{p_T}$ distributions for real τ-leptons and fake τ-leptons from $W \to \ell\nu$ are different.

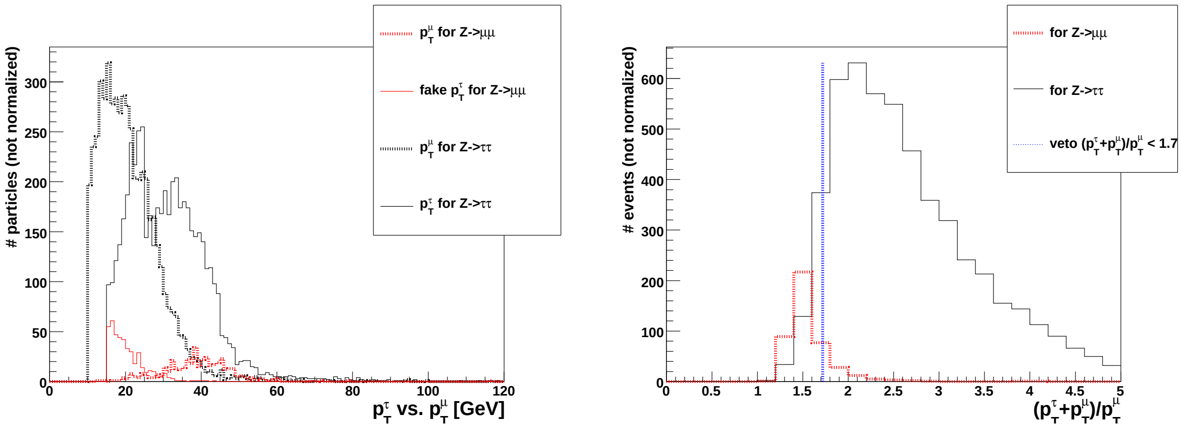

(a) (b)

Figure 7.19: *The p_T spectrum for τ-lepton and muon candidates for* Z $\to \mu\mu$ *and* Z $\to \tau\tau$ *(a) and* $\frac{p_T^\tau + p_T^\mu}{p_T^\mu}$ *for* Z $\to \mu\mu$ *and* Z $\to \tau\tau$ *(b). A requirement that* $\frac{p_T^\tau + p_T^\mu}{p_T^\mu} > 1.72$ *can be imposed.*

The fake τ-leptons from $W \to \ell\nu$ have a larger $\mathrm{p_T}$ while the real τ-leptons (from Z $\to \tau\tau$) have in general a lower $\mathrm{p_T}$.

7.7.2 OS-SS asymmetry in $Z \to \ell\ell$+jet events

Also the $Z \to \ell\ell$ +jets channel causes a significant charge asymmetry. The $Z \to \ell\ell$ +jets channel can contribute to the overall background by two effects:

- One lepton is identified as it is while the outgoing jet is mis-identified as a τ-lepton. The di-lepton veto (see Sec. 7.6) can suppress such events.

- One lepton will be identified as it is while the second lepton will be mis-identified as a τ-lepton. Since the charge distributions are similar to the ones in the Z $\to \tau\tau$ channel, the $Z \to \ell\ell$ +jets channel has an OS/SS asymmetry in order of the expected OS/SS asymmetry for the Z $\to \tau\tau$ region (see Sec. 7.7).

The $\mathrm{E_T^{miss}}$ cut is not used in the visible mass analysis. Therefore the expected number of $Z \to \ell\ell$ +jets background is in the order of the $W \to \ell\nu$ background.

Figure 7.19 shows the $\mathrm{p_T}$ distribution for the true muon and the true τ-lepton and for the fake τ-lepton coming from a Z $\to \mu\mu$ decay.

The reconstructed $\mathrm{p_T}$ of the muon which fakes a τ-lepton is almost smaller compared with the true value of the muon $\mathrm{p_T}$. This can be exploited by requiring $\frac{\mathrm{p_T^\tau} + \mathrm{p_T^\mu}}{\mathrm{p_T^\mu}} > 1.7$, as shown in Fig. 7.19. About 3.4 % of signal is lost, while 87 % of Z $\to \mu\mu$ events are rejected. Nevertheless, it is also required to define Z control regions. For the Z control region the di-lepton veto has to be inverted.

Furthermore the visible mass window can be extended from 37 GeV $< \mathrm{m_{vis}}(\tau_\mathrm{h}\, \tau_\ell) <$ 75 GeV up to 30 GeV $< \mathrm{m_{vis}}(\tau_\mathrm{h}, \tau_\ell) <$ 120 GeV. Due to the small statistic for the $Z \to \ell\ell$ channel the number of background events is also taken from the Monte Carlo.

7.7.3 OS-SS (a)symmetry in QCD multi-jet events

As previously discussed, the background remaining after the full selection in the visible mass analysis is subtracted using same sign data. This technique makes use of the fact that the background in the opposite sign (OS) visible mass distribution should be very similar to the observed same sign (SS) visible mass distribution. In order to subtract the background in the OS distribution using the SS distribution, the agreement between the two must be measured in data. This is done in separate control regions for the two dominant contributions of the expected background, the $W \to \ell\nu$ component and QCD background. Significantly more than 50 % of the remaining background is composed of QCD events. This section describes a measurement of the agreement between OS and SS and a study of the expected difference between signal region and control region for the QCD background. The result is given in terms of the ratio $\mathrm{R_{OS/SS}} = \mathrm{N_{OS}}/\mathrm{N_{SS}}$, and is used to reweight the SS distribution after subtracting the expected $W \to \ell\nu$ component. The uncertainty of the measurement of $\mathrm{R_{OS/SS}}$ is used as systematic uncertainty.

In order to measure $\mathrm{R_{OS/SS}}$ of the QCD background events, particular regions in the selection are defined, that are expected to be dominated by contributions from QCD processes. The stability of $\mathrm{R_{OS/SS}}$ is checked in these regions using all MC samples used for these studies. For all regions, no lepton isolation criteria are applied, so that QCD background events are the dominant contribution. The regions are defined as follows:

- **pre-selection**
  - pre-selection cuts as described in Section 7.2
- **pre-selection with** `cut based loose`
  - pre-selection cuts and `cut based loose` τ-lepton ID instead of `cut based tight`
- **pre-selection with** `cut based medium`
  - pre-selection and `cut based medium` τ-lepton ID instead of `cut based tight`
- **control region**
  - pre-selection cuts
  - use `cut based medium` τ-lepton ID instead of `cut based tight`
  - $25\,\mathrm{GeV} < \mathrm{m_{vis}}(\tau_\mathrm{h}, \tau_\ell) < 57\,\mathrm{GeV}$
  - reject events with a τ-lepton candidate with 1 or 3 tracks (to reduce the contribution from $Z \to \tau\tau \to \ell\tau_h$ events).

In each of the regions defined above, the histogram of $\mathrm{m_{vis}}(\tau_\mathrm{h}, \tau_\ell)$ for SS is subtracted from the same histogram for OS. The resulting distributions for pre-selection only and for the control region, containing all contributions from QCD and other samples, can be seen in Fig. 7.20. Table 7.11 summarises the results in the different regions. It can be seen that within the available MC statistics the results for $\mathrm{R_{OS/SS}}$ are slightly larger than 1 for almost all cut regions. The uncertainty in Table 7.11 is derived from the available MC statistic.

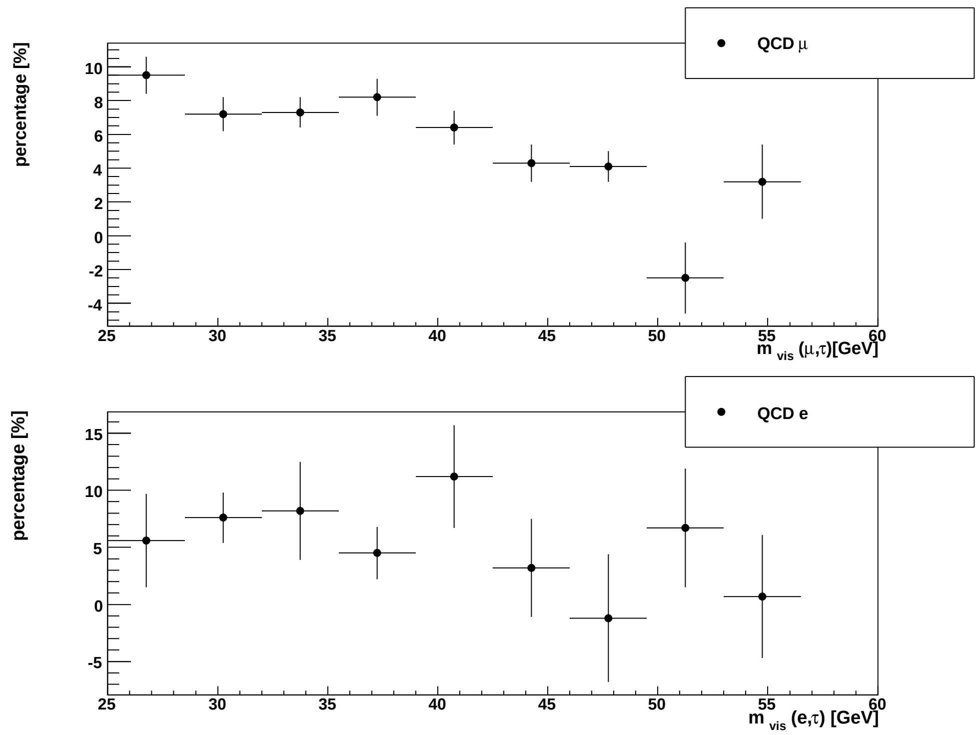

(a) pre-selection region

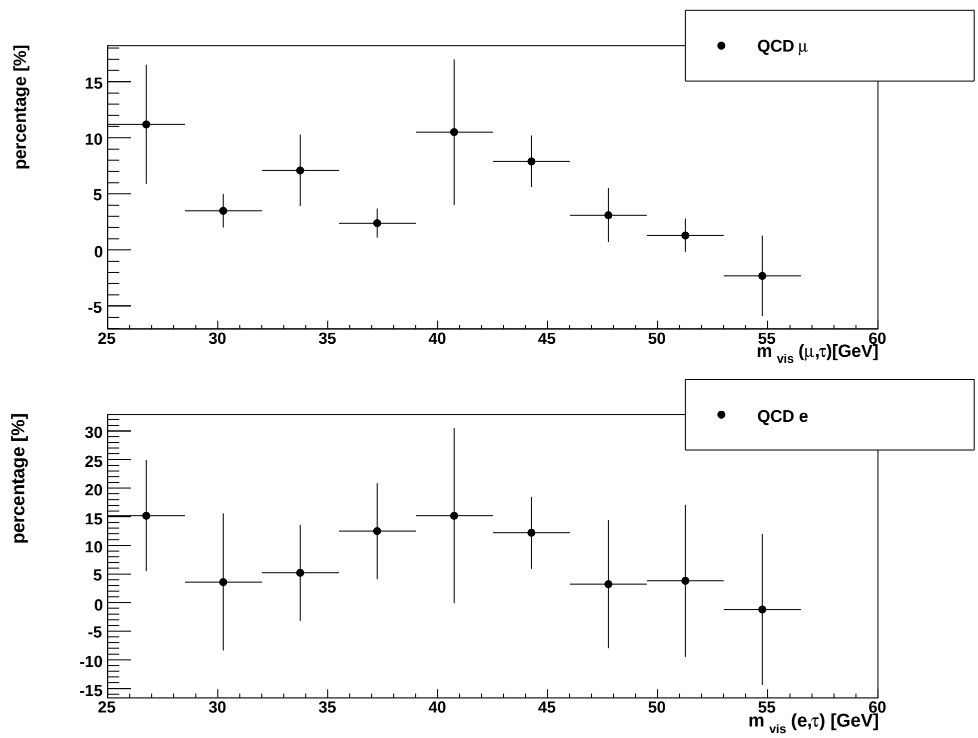

(b) control region

Figure 7.20: *The ratio $R_{\mathrm{OS/SS}}$ as a function of the visible mass $m_{\mathrm{vis}}(\tau_h, \tau_\ell)$ the pre-selection and control regions.*

Cuts		**QCD μ**
	$\mathrm{R_{OS/SS}}$	ΔR (MC)
Pre-selection	1.06	0.01
Pre-selection+`TauCutSafeLoose`	1.05	0.01
Pre-selection+`TauCutSafeMedium`	1.03	0.03
Control region	1.06	0.04
Cuts		**QCD e**
	$\mathrm{R_{OS/SS}}$	ΔR (MC)
Pre-selection	1.06	0.03
Pre-selection+`TauCutSafeLoose`	1.04	0.04
Pre-selection+`TauCutSafeMedium`	0.99	0.07
Control region	1.13	0.10

Table 7.11: *The values of $R_{OS/SS}$ for the different regions for QCD lepton filtered samples.*

It can be observed that the result is stable in the different regions, such that it can be expected that the measured result in the control region will agree with the asymmetry in the signal region. The expected uncertainty from data of around 1 % on $\mathrm{R_{OS/SS}}$ is expected to be insignificant for the measurement of the rate and the τ-lepton reconstruction efficiency.

In order to get the number of expected QCD multi-jet events in data two data-driven methods were developed:

- The first method relies on the charge of the τ-lepton candidate and the lepton candidate.
- The second method uses non-isolated leptons.

The first method will be discussed in more detail. The basic idea is to define different regions (as described above) to estimate the QCD multi-jet background in the signal region by using QCD rich regions. The assumption is that the QCD background distributions are similar for both combinations: (τ^-, ℓ^+) and (τ^+, ℓ^-). The relation

$$\frac{\mathrm{N^A_{QCD}}}{\mathrm{N^B_{QCD}}} = \frac{\mathrm{N^C_{QCD}}}{\mathrm{N^D_{QCD}}} \tag{7.6}$$

is used with the following definitions:

- A: signal region (opposite sign charge and lepton selection)
- B: control region (same sign charge and lepton isolation)
- C: control region (opposite sign charge and inverted lepton isolation)
- D: control region (same sign charge and inverted lepton isolation).

Due to fact that for signal all leptons have an opposite charge to the τ-lepton and are isolated, the control regions B,C, and D are expected to be almost signal free. Except the discussed charge and isolation criteria, for all regions the same cuts are applied in order to reduce the systematics.

For each of the control regions the expected number of events from data corrected with the electro-weak predictions using MC samples can be expressed as:

$$\mathrm{N^{i}_{QCD}} = \mathrm{N^{i}_{data}} - \mathrm{N^{i}_{Z\to\tau\tau}} - \mathrm{N^{i}_{Z\to\ell\ell}} - \mathrm{N^{i}_{tt}} - \mathrm{k_W}(\mathrm{N^{i}_{W\to\ell\nu}} + \mathrm{N^{i}_{W\to\tau\nu}}) \tag{7.7}$$

with i=(B,C,D).

The ratio $\mathrm{R_{OS/SS}}$ can be estimated using region C and D (expected to be pure QCD regions). The values are:

- $\mathrm{R_{OS/SS}}$ = 0.969±0.034(stat.)±0.031(syst.) (electron channel)
- $\mathrm{R_{OS/SS}}$ = 1.033±0.024(stat.)±0.021(syst.) (muon channel).

To estimate the contribution of QCD in the signal region $\mathrm{N^{A}_{QCD}}$ the ratio is used to scale the QCD from B to A

$$\mathrm{N^{A}_{QCD}} = \frac{\mathrm{N^{C}_{QCD}}}{\mathrm{N^{D}_{QCD}}}\mathrm{N^{B}_{QCD}} = \mathrm{R_{OS/SS}}\mathrm{N^{B}_{QCD}}. \tag{7.8}$$

The expected number of events in the region A is:

- $\mathrm{N^{A}_{QCD}}$ = 94±10(stat.)±6(syst.) (electron channel)
- $\mathrm{N^{A}_{QCD}}$ = 59±8(stat.)±2(syst.) (muon channel).

The values for data-driven QCD events and further background obtained from MC predictions are summarised in Tab. 7.12.

In order to have a good description of expected QCD events in the signal region, the QCD background contributions (drawn in all plots in this chapter) were estimated by rescaling the multi-jet Monte Carlos with respect to the values summarised in Tab. 7.12. The expected number of QCD background for each selection step is therefore affected by an additional systematic uncertainty due to the data-driven QCD multi-jet background estimation.

7.8 Systematic uncertainties

Several systematic uncertainties affects the visible mass analysis as well as the data-driven background estimation:

- Pile-up effects for Monte Carlo predictions:
  - As mentioned previously one important source for uncertainties is the presence of pile-up. Pile-up events affect variables obtained from cell information used for the lepton isolation (e.g. Etcone) or the τ-lepton identification (e.g. $\mathrm{R_{EM}}$). A method was applied for pile-up reweighting of Monte Carlo to data [109] which bases on the recomputing of vertex dependent weights for each individual channel (e,μ).

Opposite sign events and final selection				
Sample	isol. mu. (**A**)	non-isol. mu. (**C**)	isol. ele (**A**)	non-isol. ele. (**C**)
Data	328±19	3726±61	308±18	1616±40
Z $\rightarrow \tau\tau$	223±14	10±3	155±12	5±2
QCD	59±11	3714±61	94±16	1610±40
$W \rightarrow \ell\nu$	21±4	<1	16±4	<1
$W \rightarrow \tau\nu$	8±2	<0.2	4±2	<0.1
$Z \rightarrow \ell\ell$	6±2	<0.2	8±2	<0.2
$\bar{t}t$	1±1	<1	0	0
Same sign events and final selection				
Sample	isol. mu. (**B**)	non-isol. mu. (**D**)	isol. ele. (**B**)	non-isol. ele. (**D**)
Data	71±8	3599±60	110±10	1661±41
Z $\rightarrow \tau\tau$	2±1	<1	2±1	<1
QCD	56±7	3597±60	95±10	1660±41
$W \rightarrow \ell\nu$	8±3	<1	7±3	<1
$W \rightarrow \tau\nu$	3±2	<1	2± 1	<1
$Z \rightarrow \ell\ell$	1±1	<1	5±2	<1
$\bar{t}t$	0	0	1±1	<1

Table 7.12: *The number of events for different control regions and the signal region.*

- Effects from trigger efficiency estimation:
  - Another systematic effect is caused by the lepton trigger efficiency. Comparing trigger efficiencies from Monte Carlo with trigger efficiencies from data results in a systematic uncertainty of 2 % for the muon trigger and 1 % for the electron trigger. For different data periods (runs) different triggers were used. In order to estimate the trigger efficiencies a tag and probe method considering reconstructed and identified leptons was used [114]. Correction factors were defined as the ratio between measured trigger efficiencies and efficiencies obtained from Monte Carlo predictions. The scaling shows a good agreement of data and Monte Carlo predictions. Figures 7.21 show the muon trigger efficiencies for p_T and η.
- Effects from lepton reconstruction and identification:
  - The muon reconstruction and identification efficiency was measured using a Z $\rightarrow \mu\mu$ tag and probe method and the result showed an efficiency of about 93 % over the full p_T spectrum.
  - The measured uncertainty for the muon reconstruction efficiency was larger than the MC expectation [115]. For that reason the measured uncertainty was taken to be 2.7 %.
  - For the electron channel the reconstruction efficiency is well described by the Monte Carlo predictions.
  - The systematic uncertainty is evaluated bin-by-bin in p_T and η [109] and is in the order of 1.5 % [116].

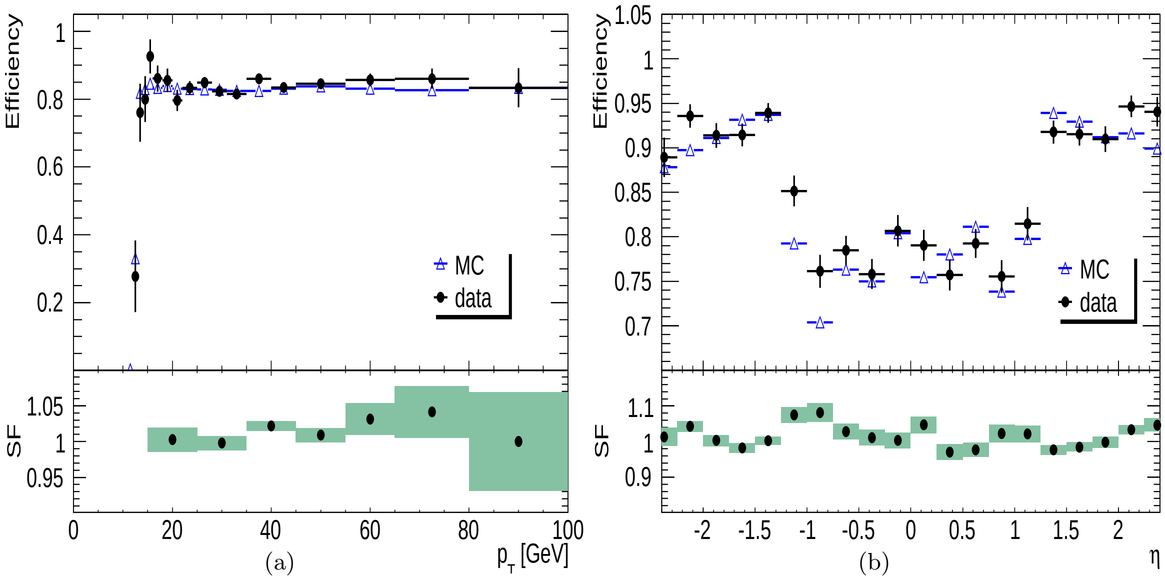

Figure 7.21: *The muon trigger efficiencies and the scale factors for p_T (a) and η (b) for the trigger mu13MG_tight. Plots from [114].*

- Effects from fake rates measurements:
  - As discussed in the previous section, there is a non-negligible probability of background faking a τ-lepton. These fake rates have to be take into account during background estimation procedure. As also described (see Chapt. 6), these fake rates are estimated using data-driven techniques.
- Effects from cross section and luminosity measurements:
  - For MC to data normalisation the measured integrated luminosity and the theoretical cross section has to be known. The measured integrated luminosity has an uncertainty of about 11 % [117] while for the Z → $\tau\tau$ cross section it is about 5 % [118].
- Lepton isolation
  - As discussed in this chapter, lepton isolation is a useful criteria to reduce QCD multi-jet background.
  - Also for the lepton isolation efficiency tag and probe methods using $Z \to \ell\ell$ were used:
    * In principle leptons were measured using all criteria except the isolation (tag-leptons).
    * A probe-lepton was required in order to fulfil the charge product to be -1 and a Z-boson mass window of [80–100] GeV.
    * For the electron channel the isolation efficiency in data was found to be larger than in data while for the muon channel a good agreement of data to Monte Carlo was confirmed.

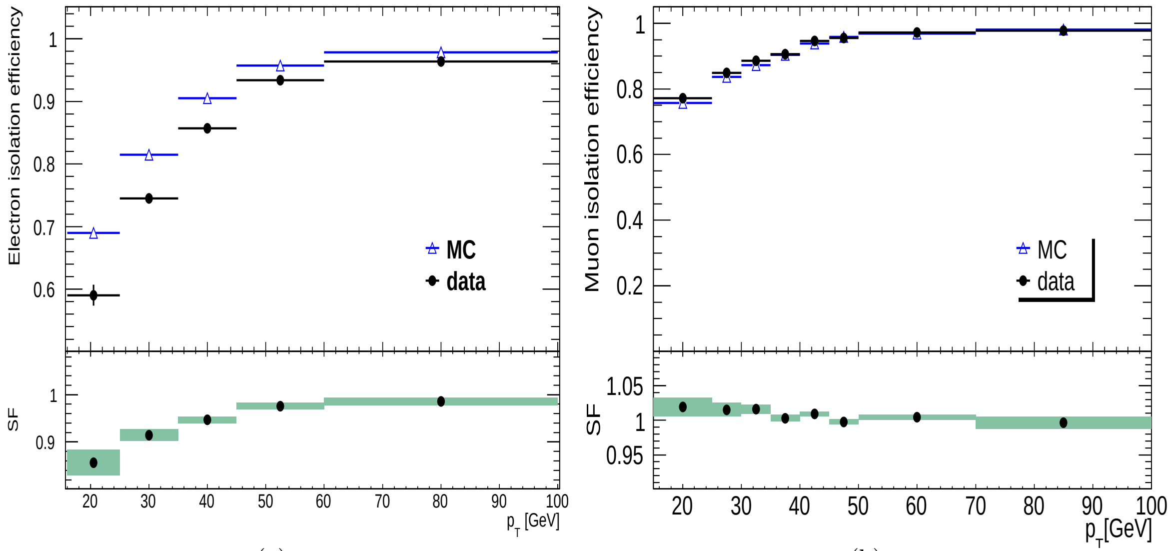

(a) (b)

Figure 7.22: *Lepton isolation efficiencies and scale factors for electrons (a) and muons (b). The isolation cut for electrons is $p_T cone40/p_T < 0.06$ and $E_T cone30/p_T < 0.1$. The isolation for muons is $p_T cone40/p_T < 0.06$ and $E_T cone40/p_T < 0.06$. Plots from [114].*

  * As for the trigger efficiency, also for the lepton isolation scaling factors were applied.

- In general the lepton isolation efficiency shows a $\mathrm{p_T}$ dependence as shown in Fig. 7.22.

• QCD background estimation

- The background estimation using the ABCD method was built on the assumption that the OS/SS is independent of the isolation variables.
- It is expected that QCD control regions with inverted lepton isolation cuts tends to be richer in $c\bar{c}$ and $b\bar{b}$.
- For QCD control regions with lepton isolation cuts it is expected that light flavour jets faking the lepton.
- The effect for the ratio OS/SS was studied by inverting the τ-lepton identification
- This control region is plotted against the calorimeter lepton isolation variables $\mathrm{E_T cone40/p_T}$ for the electron channel and $\mathrm{E_T cone30/p_T}$ for the muon channel.
- Figs. 7.23 and 7.23 show the stability of OS/SS as a function of the calorimeter isolation and the τ-lepton identification (`cut based loose`, `cut based medium`, `cut based tight`, see Chapt. 6).

• A summary of all systematic uncertainties for $Z \to \tau\tau$ studies regarding background estimation can be found in Tab. 10.1 and Tab. 10.2.

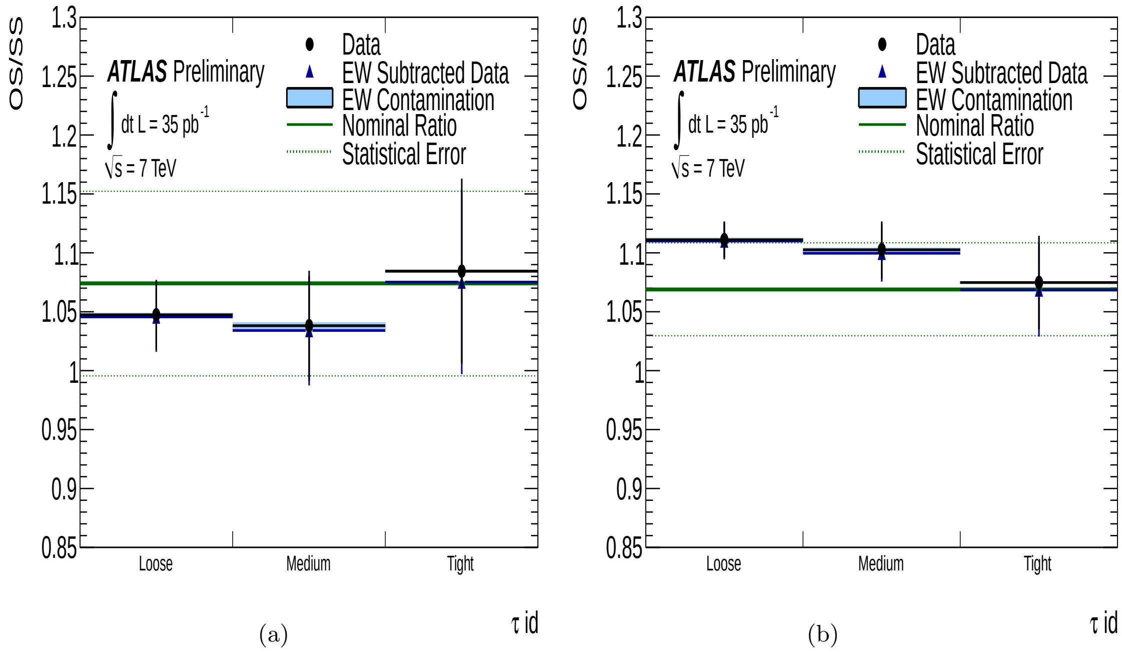

Figure 7.23: *The stability of OS/SS as a function of the τ-lepton identification. The solid lines shows the nominal ratio, while the dashed lines represents the statistical error on the nominal ratio. The expected electro-weak impurity from MC is shown with the shaded box (at each bin). Plots from [114].*

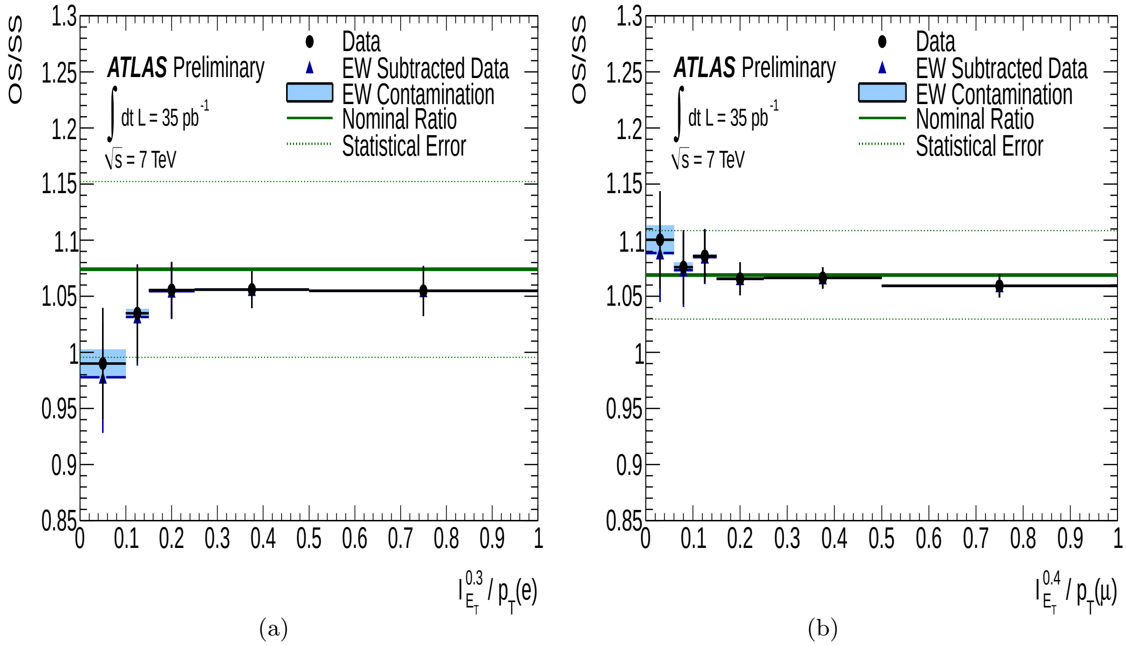

Figure 7.24: *The stability of OS/SS as a function of the calorimeter isolation. The solid lines shows the nominal ratio, while the dashed lines represents the statistical error on the nominal ratio. The expected electro-weak impurity from MC is shown with the shaded box (at each bin). Plots from [114].*

7.9 The $\gamma^{\star}/\mathrm{Z}$ exchange in the region $\mathrm{m_{inv}} < 60\,\mathrm{GeV}$

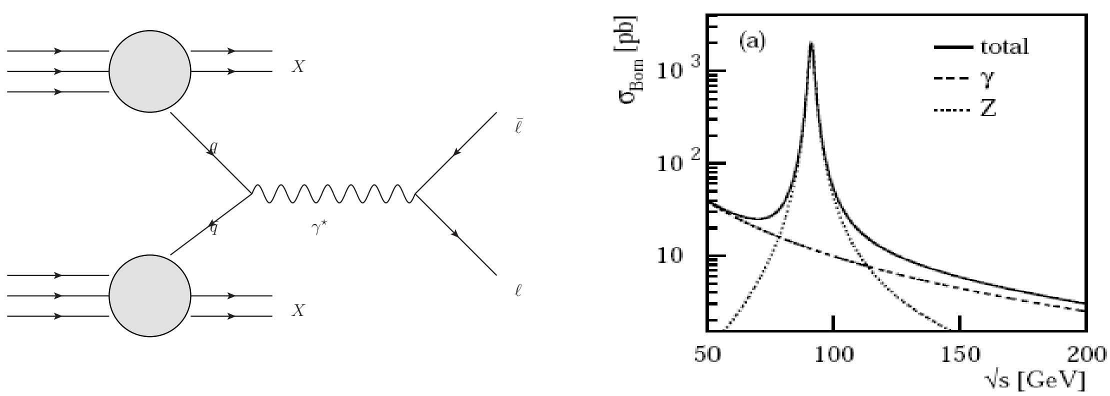

Figure 7.25: *Virtual $\gamma^{\star}$ (and Z) exchange (left) and cross section for γ and Z (from $e^{+}e^{-} \rightarrow \gamma$ / $Z \rightarrow X$) (right).*

As mentioned in the introduction also possible contributions in the low visible mass spectrum are expected (in ATLAS called Drell Yan process). As shown in Fig. 7.26 the Drell Yan process affects the lowest visible mass regions. For that reason the lower visible mass bound is changed from $\mathrm{m_{vis}}(\ell,\tau) > 20\,\mathrm{GeV}$ to $\mathrm{m_{vis}}(\ell,\tau) > 37\,\mathrm{GeV}$ which suppresses such events. It has to be mentioned that Drell Yan could be more crucial for leptonic $\mathrm{Z} \rightarrow \tau\tau$ events with two leptons in the final state.

(a) (b)

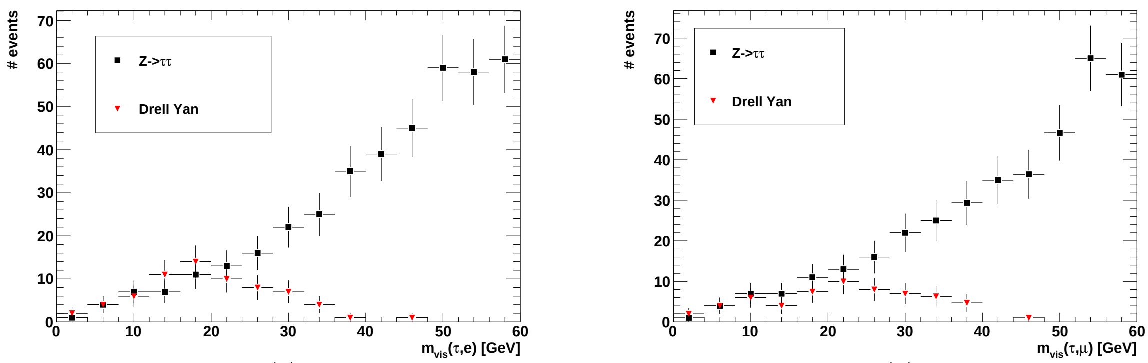

(a) (b)

Figure 7.26: *Drell Yan events affect the lowest $\mathrm{Z} \rightarrow \tau\tau$ signal region.*

7.10 Final results for the full (inclusive OS-SS) selection

With the described methods the signal over background distribution can be estimated.

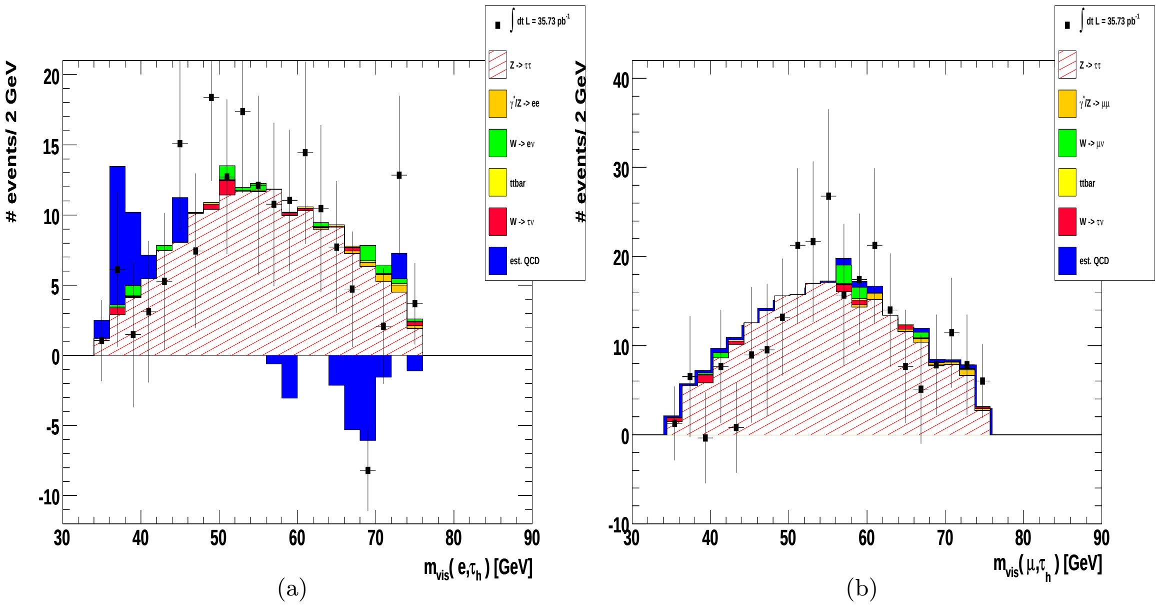

Figure 7.27: *The visible mass after OS-gSS rescaling for the electron channel (a) and the muon channel (b). The uncertainty for the measured values is composed of the statistical and the systematic uncertainty. The latter considers the effects from the OS/SS estimation as described in Sec. 7.7.3.*

Figure 7.27 shows the visible mass $m_{vis}(\tau_h, \tau_\ell)$ after full selection including the SS rescaling. Tables 7.13 and 7.14 summarise the full visible mass selection without the OS-gSS rejection. The overall rescaling factor g which is applied on the data sample is calculated as the weighted average over all OS/SS ratios for the different background channels. The values are:

- g = 1.58±0.21 for the electron channel
- g = 1.32±0.23 for the muon channel.

The numbers of signal events estimated with the OS-gSS rescaling are:

- g = 171±13(stat.)±8(syst.) for the electron channel
- g = 222±15(stat.)±12(syst.) for the muon channel.

Cut	**Data**	$\sum$(MC)	est.QCD*	$Z\tau\tau$	W $\to$ eν	$W \to \tau_\ell\nu$	Z $\to$ ee	$t\bar{t}$
All	11800123±3435	11728060±3493	10927363±3702	35579±188	358359±598	373191±610	31493±177	2075±45
GRL	10113587±3180	10041524±3232	9240827±3404	35579±188	358359±598	373191±610	31493±177	2075±45
Trigger	5940260±2437	5917389±2481	5663267±2665	2973±54	210508±458	14731±121	25235±158	675±25
Vertex	5940149±2437	5917278±2481	5663156±2665	2973±54	210508±458	14731±121	25235±158	675±25
Jet cleaning	5902063±2429	5879192±2473	5625070±2656	2973±54	210508±458	14731±121	25235±158	675±25
Pre-selected ℓ	5137222±2266	5117418±2307	4897381±2478	2495±49	181186±425	12531±111	23243±152	582±24
Overlap removed ℓ	5136629±2266	5116826±2307	4896794±2478	2494±49	181186±425	12528±111	23243±152	581±24
Trigger matched ℓ	5136629±2266	5116826±2307	4896794±2478	2494±49	181186±425	12528±111	23243±152	581±24
Overlap removed τ_h	2555195±1598	2550221±1628	2494962±1769	2455±38	40747±201	3311±57	9169±95	577±24
Selected ℓ	551177±742	547178±754	502750±794	1036±32	32728±180	2423±49	7767±88	474±21
Isolated ℓ	76156±275	72604±274	33145±203	817±28	29131±170	1908±43	7213±84	390±19
Selected τ_h	2485±49	2338±49	706±29	222±14	1105±33	68±8	210±14	27±5
Di-lepton veto	2384±48	2245±48	702±29	220±14	1104±33	68±8	128±11	23±4
$\sum\cos\Delta\phi > -0.15$	1229±35	1173±34	556±26	202±14	294±17	28±5	82±9	11±3
$\mathrm{m_T} < 50\,\mathrm{GeV}$	1012±31	976±31	582±27	194±13	99±9	24±4	72±8	5±2
$\mathrm{m_{vis}} = [0-200]\,\mathrm{GeV}$	987±31	952±31	574±26	193±13	88±9	23±4	70±8	4±2
$\mathrm{m_{vis}} = [35-75]\,\mathrm{GeV}$	640±25	617±25	369±21	171±13	42±6	11±3	23±4	1±1
$\mathrm{N_{tracks}}(\tau_\mathrm{h}) = 1\,\mathrm{or}\,3$	409±20	390±20	189±15	157±12	23±4	6±2	14±3	1±1
$\lvert\mathrm{charge}(\tau_\mathrm{h})\rvert = 1$	418±20	389±20	189±15	157±12	23±4	6±2	13±3	1±1
Opposite sign	308±17	279±16	94±16	155±12	16±4	4±2	8±2	0
$\mathrm{E_T^{miss}} > 20\,\mathrm{GeV}$	45±6	41±6	1±1	35±5	4±2	1±1	0	0
$\Delta\phi(\ell,\tau_\mathrm{h}) = 1-2.9$	25±5	23±4	3±1	18±4	2±1	0	0	0
$\mathrm{m_{inv}} = [0-200]\,\mathrm{GeV}$	16±4	15±3	2±1	11±3	1±1	0	0	0
$\mathrm{m_{inv}} = [60-150]\,\mathrm{GeV}$	16±4	14±3	4±2	10±3	1±1	0	0	0

Table 7.13: *The $Z \to \tau\tau \to \tau_h e$ cut flow. The $\sum(MC)$ includes all MC as well as the estimated QCD. QCD events ($\star$) include also a systematic uncertainty due to the QCD background estimation as described in Sec. 7.7.3.*

Cut	**Data**	$\sum$(MC)	est.QCD*	$Z\tau\tau$	W $\rightarrow \mu\nu$	$W \rightarrow \tau_\ell\nu$	Z $\rightarrow \mu\mu$	$t\bar{t}$
All	7262907±2694	7211499±2765	6420618±2812	35579±188	365485±604	373191±610	14551±120	2075±45
GRL	6131311±2476	6079903±2539	5289022±2552	35579±188	365485±604	373191±610	14551±120	2075±45
Trigger	3903796±1975	3887987±2030	3644774±2119	3153±56	210526±458	17166±131	11661±107	707±26
Vertex	3903782±1975	3887973±2030	3644760±2119	3153±56	210526±458	17166±131	11661±107	707±26
Jet cleaning	3869752±1967	3853943±2022	3610730±2109	3153±56	210526±458	17166±131	11661±107	707±26
Pre-selected ℓ	1891911±1375	1877467±1411	1655253±1428	2509±50	194448±440	13422±115	11187±105	648±25
Overlap removed ℓ	1891911±1375	1877467±1411	1655253±1428	2509±50	194448±440	13422±115	11187±105	648±25
Trigger matched ℓ	1891911±1375	1877467±1411	1655253±1428	2509±50	194448±440	13422±115	11187±105	648±25
Overlap removed τ_h	1444723±1201	1441375±1236	1389868±1308	1425±37	43244±207	3404±58	2791±52	643±25
Selected ℓ	1421796±1192	63192±258	19179±153	1408±37	42774±206	3366±58	2778±52	635±25
Isolated ℓ	66053±257	63192±258	19179±153	1154±33	37116±192	2710±52	2602±51	431±20
Selected τ_h	2282±47	2153±47	179±14	315±17	1406±37	109±10	115±10	29±5
Di-lepton veto	2151±46	2026±46	115±11	314±17	1403±37	109±10	60±7	25±5
$\sum \cos\Delta\phi > -0.15$	987±31	939±31	214±16	286±16	352±18	41±6	34±5	12±3
$m_T < 50$ GeV	757±27	727±27	266±18	275±16	122±11	35±5	24±4	5±2
$m_{vis} = [0-200]$ GeV	745±27	715±27	268±18	275±16	110±10	33±5	24±4	5±2
$m_{vis} = [35-75]$ GeV	541±23	519±23	186±15	247±15	56±7	20±4	9±3	1±1
$N_{tracks}(\tau_h) = 1$ or 3	400±20	390±19	116±16	225±15	29±5	12±3	7±2	1±1
$\lvert charge(\tau_h)\rvert = 1$	399±19	388±19	115±16	225±15	29±5	11±3	7±2	1±1
Opposite sign	328±19	318±17	59±11	223±14	21±4	8±2	6±2	1±1
$E_T^{miss} > 20$ GeV	65±8	61±8	1±1	51±7	5±2	4±2	0	0
$\Delta\phi(\ell,\tau_h) = 1-2.9$	34±5	32±5	2±1	26±5	2±1	2±1	0	0
$m_{inv} = [0-200]$ GeV	26±5	24±5	7±2	17±4	0	0	0	0
$m_{inv} = [60-150]$ GeV	25±5	24±5	7±2	15±3	0	0	0	0

Table 7.14: *The Z $\rightarrow \tau\tau \rightarrow \tau_h\mu$ cut flow. The $\sum(MC)$ includes all MC as well as the estimated QCD. QCD events ($\star$) include also a systematic uncertainty due to the QCD background estimation as described in Sec. 7.7.3.*

7.11 Alternative background suppression using fake rates

The discussion before showed possible sources for uncertainties:

- The modification of defined cuts for control regions.
- The conclusion from control region to signal region.
- The correct determination of electro-weak background is MC dependent.
- No background estimation on reconstruction level (important for τ-lepton efficiency studies).

An alternative ansatz will be discussed to show the potential of τ-lepton fake rates in context of signal background separation. The fake rates were introduced in Chapt. 6 and are estimated completely data-driven. The signal is almost located in opposite charge (OS) regions (the contribution to the same sign (SS) region due to charge mis-identification or selection of wrong objects is expected to be negligible for tighter τ-lepton identification criteria. For lower τ-lepton identification criteria the mis-identification probability can be estimated). The fake rates can be determined for different τ-lepton identification criteria: `cut based ID`, `projective likelihood`, and `boosted decision tree` (see Chapt. 6) as well as on reconstruction level.

For a certain τ-lepton identification variable the OS and SS regions can be expressed as

$$\begin{aligned} \text{I)}\, \mathrm{OS1} &= \mathrm{S1} + \mathrm{QCD_{OS}} + \mathrm{W_{OS}} + \mathrm{Z_{OS}} \\ \text{II)}\, \mathrm{SS1} &= \mathrm{QCD_{SS}} + \mathrm{W_{SS}} \end{aligned} \tag{7.9}$$

with OS and SS describing the measured values. The different values (for the signal S1[8)], the OS QCD background $\mathrm{QCD_{OS}}$, the OS electro-weak backgrounds $\mathrm{W_{OS}}$ and $\mathrm{Z_{OS}}$ as well as for the SS backgrounds $\mathrm{QCD_{SS}}$ and $\mathrm{W_{SS}}$) are not known.

A second τ-lepton identification variable[9)] results in two additional equations which results in a equation system of four equations:

$$\begin{aligned} \text{I)}\, \mathrm{OS1} &= \mathrm{S1} + \mathrm{QCD_{OS}} + \mathrm{W_{OS}} + \mathrm{Z_{OS}} \\ \text{II)}\, \mathrm{SS1} &= \mathrm{QCD_{SS}} + \mathrm{W_{SS}} \\ \text{III)}\, \mathrm{OS2} &= \mathrm{S2} + \mathrm{A} \times \mathrm{QCD_{OS}} + \mathrm{B} \times \mathrm{W_{OS}} + \mathrm{C} \times \mathrm{Z_{OS}} \\ \text{IV)}\, \mathrm{SS2} &= \mathrm{A} \times \mathrm{QCD_{SS}} + \mathrm{B} \times \mathrm{W_{SS}} \end{aligned} \tag{7.10}$$

with

$$\mathrm{A} = \frac{\text{QCD fake rate for the second tau ID}}{\text{QCD fake rate for the first tau ID}} \tag{7.11}$$

and

$$\mathrm{B(C)} = \frac{\text{electro-weak fake rate for the second tau ID}}{\text{electro-weak fake rate for the first tau ID}} \tag{7.12}$$

[8)] S1 denotes the number of expected signal events for a certain τ-lepton identification variable. $\mathrm{QCD_{OS}}$ the number of QCD background events selected in the opposite sign region etc.

[9)] Note: always one τ-lepton identification is used! The first identification variable is switched off when the second variable is applied.

as the relative fake rates R_{rel} obtained from data. Since fake rates are charge independent OS and SS regions are modified with the same relative fake rate for each background channel. For four equations seven unknown variables have to be considered: S1, S2, QCD_{OS}, W_{OS}, Z_{OS}, QCD_{SS}, W_{SS}. Each new τ-lepton identification variable contributes with two additional equations and one additional unknown variable (signal SX). To get the same number of equations and unknown variables, at least 10 equations are needed which requires five different τ-lepton identification variables.

$$
\begin{aligned}
\text{I)}\ \mathrm{OS1} &= \mathrm{S1} + \mathrm{QCD_{OS}} + \mathrm{W_{OS}} + \mathrm{Z_{OS}} \\
\text{II)}\ \mathrm{SS1} &= \mathrm{QCD_{SS}} + \mathrm{W_{SS}} \\
\text{III)}\ \mathrm{OS2} &= \mathrm{S2} + \mathrm{A} \times \mathrm{QCD_{OS}} + \mathrm{B} \times \mathrm{W_{OS}} + \mathrm{C} \times \mathrm{Z_{OS}} \\
\text{IV)}\ \mathrm{SS2} &= \mathrm{A} \times \mathrm{QCD_{SS}} + \mathrm{B} \times \mathrm{W_{SS}} \\
\text{V)}\ \mathrm{OS3} &= \mathrm{S3} + \mathrm{D} \times \mathrm{QCD_{OS}} + \mathrm{E} \times \mathrm{W_{OS}} + \mathrm{F} \times \mathrm{Z_{OS}} \\
\text{VI)}\ \mathrm{SS3} &= \mathrm{D} \times \mathrm{QCD_{SS}} + \mathrm{E} \times \mathrm{W_{SS}} \\
\text{VII)}\ \mathrm{OS4} &= \mathrm{S4} + \mathrm{G} \times \mathrm{QCD_{OS}} + \mathrm{H} \times \mathrm{W_{OS}} + \mathrm{I} \times \mathrm{Z_{OS}} \\
\text{VIII)}\ \mathrm{SS4} &= \mathrm{G} \times \mathrm{QCD_{SS}} + \mathrm{H} \times \mathrm{W_{SS}} \\
\text{IX)}\ \mathrm{OS5} &= \mathrm{S5} + \mathrm{J} \times \mathrm{QCD_{OS}} + \mathrm{K} \times \mathrm{W_{OS}} + \mathrm{L} \times \mathrm{Z_{OS}} \\
\text{X)}\ \mathrm{SS5} &= \mathrm{J} \times \mathrm{QCD_{SS}} + \mathrm{K} \times \mathrm{W_{SS}}.
\end{aligned}
\tag{7.13}
$$

7.11.1 The mathematical solution of the equation system

The equation system can be rewritten in matrices notation $\mathbf{A} \times \vec{X} = \vec{L}$ with $\mathbf{A}$ as the coefficient matrix, $\vec{L}$ for the measured values and the required solution vector $\vec{X}$:

$$
\begin{pmatrix}
1 & 0 & 0 & 0 & 0 & 1 & 1 & 1 & 0 & 0 \\
0 & 1 & 0 & 0 & 0 & \mathrm{A} \pm \mathrm{u.} & \mathrm{B} \pm \mathrm{u.} & \mathrm{C} \pm \mathrm{u.} & 0 & 0 \\
0 & 0 & 1 & 0 & 0 & \mathrm{D} \pm \mathrm{u.} & \mathrm{E} \pm \mathrm{u.} & \mathrm{F} \pm \mathrm{u.} & 0 & 0 \\
0 & 0 & 0 & 1 & 0 & \mathrm{G} \pm \mathrm{u.} & \mathrm{H} \pm \mathrm{u.} & \mathrm{I} \pm \mathrm{u.} & 0 & 0 \\
0 & 0 & 0 & 0 & 1 & \mathrm{J} \pm \mathrm{u.} & \mathrm{K} \pm \mathrm{u.} & \mathrm{L} \pm \mathrm{u.} & 0 & 0 \\
0 & 0 & 0 & 0 & 0 & 0 & 0 & 0 & 1 & 1 \\
0 & 0 & 0 & 0 & 0 & 0 & 0 & 0 & \mathrm{A} \pm \mathrm{u.} & \mathrm{B} \pm \mathrm{u.} \\
0 & 0 & 0 & 0 & 0 & 0 & 0 & 0 & \mathrm{D} \pm \mathrm{u.} & \mathrm{E} \pm \mathrm{u.} \\
0 & 0 & 0 & 0 & 0 & 0 & 0 & 0 & \mathrm{G} \pm \mathrm{u.} & \mathrm{H} \pm \mathrm{u.} \\
0 & 0 & 0 & 0 & 0 & 0 & 0 & 0 & \mathrm{J} \pm \mathrm{u.} & \mathrm{K} \pm \mathrm{u.}
\end{pmatrix}
\times
\begin{pmatrix}
\mathrm{S1} \\ \mathrm{S2} \\ \mathrm{S3} \\ \mathrm{S4} \\ \mathrm{S5} \\ \mathrm{QCD_{OS}} \\ \mathrm{W_{OS}} \\ \mathrm{Z_{OS}} \\ \mathrm{QCD_{SS}} \\ \mathrm{W_{SS}}
\end{pmatrix}
=
\begin{pmatrix}
\mathrm{OS1} \pm \mathrm{u.} \\ \mathrm{OS2} \pm \mathrm{u.} \\ \mathrm{OS3} \pm \mathrm{u.} \\ \mathrm{OS4} \pm \mathrm{u.} \\ \mathrm{OS5} \pm \mathrm{u.} \\ \mathrm{SS1} \pm \mathrm{u.} \\ \mathrm{SS2} \pm \mathrm{u.} \\ \mathrm{SS3} \pm \mathrm{u.} \\ \mathrm{SS4} \pm \mathrm{u.} \\ \mathrm{SS5} \pm \mathrm{u.}
\end{pmatrix}
\tag{7.14}
$$

The first five equations (in the matrix) describing the OS regions while the last five equations are the SS related equations. The coefficients (in the matrix) have a systematic and statistical uncertainty due to fake rate measurements. The measured values (vector on the right side) have a statistical uncertainty which is denoted as `u.`.

An equation system is strongly sensitive to uncertainties of its coefficients. The matrix $\mathbf{A}$ must be invertible to guarantee a unique (single) solution for the equation system. Different methods can be used to solve this equation system. The most preferred method is the so called `Gauss-Seidel iteration` which is optimal for under-determined matrices and uncertain coefficients:

$$x_i^k = \frac{b_i - \sum_{j<i} a_{ij} x_j^{(k)} - \sum_{j>i} a_{ij} x_j^{(k-1)}}{a_{ii}}. \tag{7.15}$$

Firstly, the computations appear to be serial. Since each component of the new iterate depends upon all previously computed components, the updates cannot be done simultaneously.

Secondly, the new iterate $x^{(k)}$ depends upon the order in which the equations are examined. If this ordering is changed, the components of the new iterates (and not just their order) will also change [119]. It has to be mentioned that the Gauss-Seidel always converges if the matrix is main diagonal dominant otherwise it can be possible that the iteration diverges. To obtain the different relative fake rate one has to measure all individual (depending from the τ-lepton identification variable) fake rates from data.

7.11.2 Working example on Monte Carlo level

A working example using Monte Carlo samples illustrates the principle:

$$\begin{pmatrix} 1 & 0 & 0 & 0 & 0 & 1 & 1 & 1 & 0 & 0 \\ 0 & 1 & 0 & 0 & 0 & 0.56 & 0.58 & 0.9 & 0 & 0 \\ 0 & 0 & 1 & 0 & 0 & 0.46 & 0.62 & 1.1 & 0 & 0 \\ 0 & 0 & 0 & 1 & 0 & 4 & 4.7 & 1.5 & 0 & 0 \\ 0 & 0 & 0 & 0 & 1 & 3.1 & 4.0 & 2.0 & 0 & 0 \\ 0 & 0 & 0 & 0 & 0 & 0 & 0 & 0 & 1 & 1 \\ 0 & 0 & 0 & 0 & 0 & 0 & 0 & 0 & 0.56 & 0.58 \\ 0 & 0 & 0 & 0 & 0 & 0 & 0 & 0 & 0.46 & 0.62 \\ 0 & 0 & 0 & 0 & 0 & 0 & 0 & 0 & 4 & 4.7 \\ 0 & 0 & 0 & 0 & 0 & 0 & 0 & 0 & 3.1 & 4.0 \end{pmatrix} \times \begin{pmatrix} \mathrm{S1} \\ \mathrm{S2} \\ \mathrm{S3} \\ \mathrm{S4} \\ \mathrm{S5} \\ \mathrm{QCD_{OS}} \\ \mathrm{W_{OS}} \\ \mathrm{Z_{OS}} \\ \mathrm{QCD_{SS}} \\ \mathrm{W_{SS}} \end{pmatrix} = \begin{pmatrix} 638 \\ 547 \\ 544 \\ 1602 \\ 1478 \\ 148 \\ 80 \\ 59 \\ 662 \\ 542 \end{pmatrix} \tag{7.16}$$

The values in the coefficient matrix and in the vector on the right hand side are obtained from a Monte Carlo study. For the Gauss-Seidel iteration one has to chose starting points for the left hand vector. In principle all chosen values should converge to the final solution depending on the number of iteration steps. With a `Gaussian normal distribution` the uncertainty is simulated within three different intervals (10 %, 20 % and 30 %).

S1 represents in this case the number of signal for the `cut based tight` τ-lepton identification. The value estimated with the Gauss Seidel iteration is 404. The uncertainties depends from the level of initial uncertainties on the fake rates (as described before). It can be seen in Fig. 7.28 that the uncertainty is relative stable with respect to the initial uncertainty assumed for the fake rate measurements. The MC value is 412±20. It shows a good agreement between both values. Further, the different background contributions can be estimated as can seen in Fig. 10.8.

7.11.3 Further studies using fake rates

The background studies with fake rates open a wide field of additional investigations:

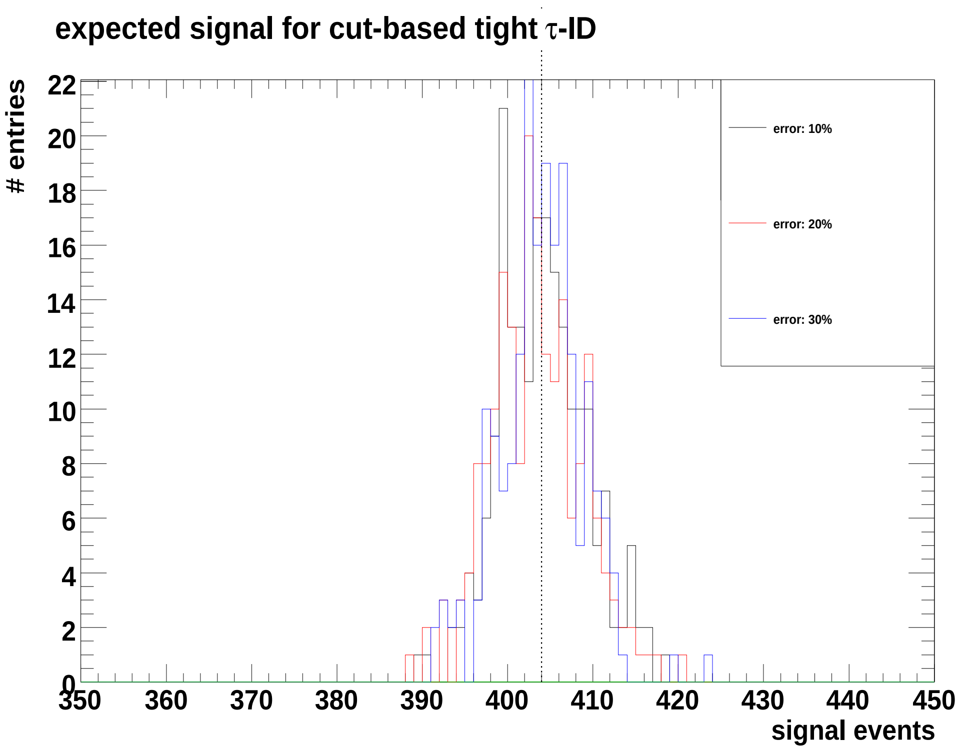

Figure 7.28: *The gaussian distribution for the first variable (S1) with respect to the three uncertainty levels 10%, 20% and 30%.*

I: Signal over background estimation on reconstruction level: It is possible to apply the OS/SS rescaling factors obtained from 7.7.

$$
\begin{aligned}
\text{I)}\ \mathrm{OS1} &= \mathrm{S1} + \mathrm{QCD_{OS}} + \mathrm{W_{OS}} + \mathrm{Z_{OS}} \\
\text{II)}\ \mathrm{SS1} &= \mathrm{a_1} \times \mathrm{QCD_{OS}} + \mathrm{b_1} \times \mathrm{W_{OS}} \\
\text{III)}\ \mathrm{OS2} &= \mathrm{S2} + \mathrm{A} \times \mathrm{QCD_{OS}} + \mathrm{B} \times \mathrm{W_{OS}} + \mathrm{C} \times \mathrm{Z_{OS}} \\
\text{IV)}\ \mathrm{SS2} &= \mathrm{a_2} \times \mathrm{A} \times \mathrm{QCD_{OS}} + \mathrm{b_2} \times \mathrm{B} \times \mathrm{W_{OS}} \\
\text{V)}\ \mathrm{OS3} &= \mathrm{S3} + \mathrm{D} \times \mathrm{QCD_{OS}} + \mathrm{E} \times \mathrm{W_{OS}} + \mathrm{F} \times \mathrm{Z_{OS}} \\
\text{VI)}\ \mathrm{SS3} &= \mathrm{a_3} \times \mathrm{D} \times \mathrm{QCD_{SS}} + \mathrm{b_3} \times \mathrm{E} \times \mathrm{W_{SS}} \\
\text{VII)}\ \mathrm{OS4} &= \mathrm{S4} + \mathrm{G} \times \mathrm{QCD_{OS}} + \mathrm{H} \times \mathrm{W_{OS}} + \mathrm{I} \times \mathrm{Z_{OS}} \\
\text{VIII)}\ \mathrm{SS4} &= \mathrm{X} + \mathrm{a_4} \times \mathrm{G} \times \mathrm{QCD_{SS}} + \mathrm{b_4} \times \mathrm{H} \times \mathrm{W_{SS}}
\end{aligned}
\tag{7.17}
$$

with equation VII and VIII for the reconstruction with X as the number of signal events in the SS region due to charge mis-identification or wrong object selection. The factors $\mathrm{a_n}$ and $\mathrm{b_n}$ (n=1..4) are the rescaling factors with respect to the corresponding τ-lepton IDs. Furthermore, a good cross check of the fake rate method with the various OS-SS methods can be applied. From a well known S/B ratio on reconstruction level the τ-lepton identification efficiency determination can benefit.

II: Determination of visible mass shapes for $\mathrm{Z} \rightarrow \tau\tau$: The fake rates are jet-$\mathrm{p_T}$ dependent so the OS distribution can be composed of

$$\begin{aligned} a)\mathrm{OS}(\mathrm{p_T^1}) &= \mathrm{S} + \mathrm{QCD_{OS}} + \mathrm{W_{OS}} + \mathrm{Z_{OS}} \\ b)\mathrm{OS}(\mathrm{p_T^2}) &= \mathrm{S} + \mathrm{f} \times \mathrm{QCD_{OS}} + \mathrm{g} \times \mathrm{W_{OS}} + \mathrm{h} \times \mathrm{Z_{OS}} \end{aligned} \tag{7.18}$$

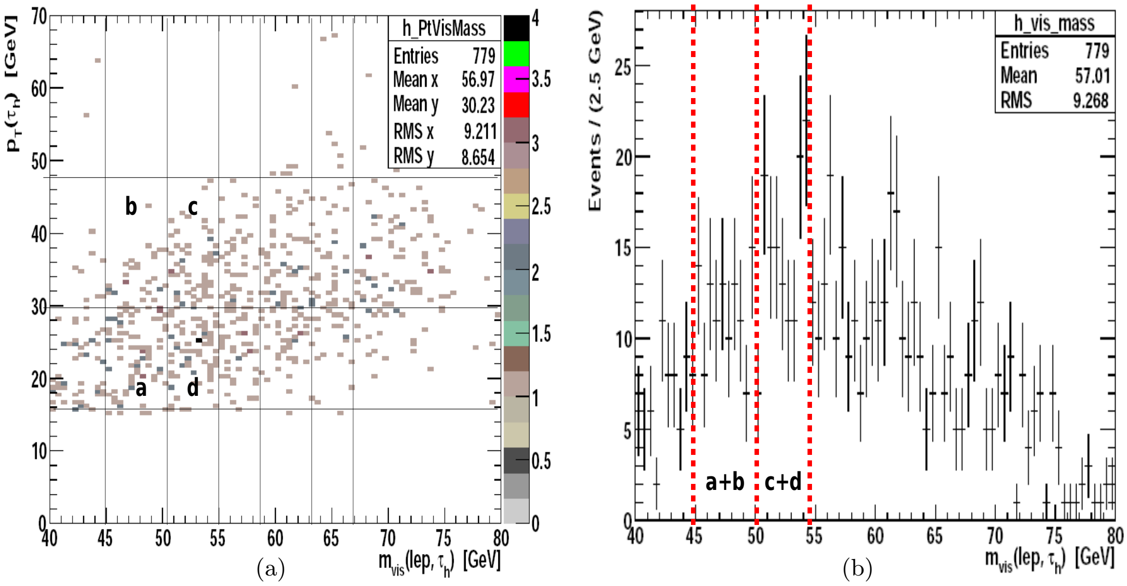

Figure 7.29: *The transverse τ-lepton momentum versus the visible mass (a) and the interpolation to the visible ($\tau\tau$) mass (b).*

The factors f,g and h are refered to the different contribution of the background with respect to the τ-lepton $\mathrm{p_T}$.

III: Estimation of relative τ-lepton identification efficiencies: Furthermore, e.g. the ratio

$$\frac{\mathrm{S1}}{\mathrm{S2}} = \frac{\varepsilon^{\mathrm{ID}}_{\mathrm{tight}}}{\varepsilon^{\mathrm{ID}}_{\mathrm{medium}}} \tag{7.19}$$

with $\varepsilon^{\mathrm{ID}}$ as the τ-lepton identification efficiency can be determined. It allows to estimate the relative efficiencies for the τ-lepton identification which can be used as a cross section for the usual efficiency determination described in the next chapter.

IV: Background studies in order to estimate the contribution of $\mathrm{Z} \rightarrow \tau\tau$ to the low mass $H^0 \rightarrow \tau\tau$ channel: A result from the fake rate studies is the possible estimation of the Z $\rightarrow \tau\tau$ background to the low mass H $\rightarrow \tau\tau$[10] the spectrum.

$$\begin{aligned}
\text{I)}\ \mathrm{OS1} &= \mathrm{H1} + \mathrm{QCD_{OS}} + \mathrm{W_{OS}} + \mathrm{Z^{\tau\tau}_{OS}} \\
\text{II)}\ \mathrm{SS1} &= \mathrm{QCD_{SS}} + \mathrm{W_{SS}} \\
\text{III)}\ \mathrm{OS2} &= \mathrm{H2} + \mathrm{A} \times \mathrm{QCD_{OS}} + \mathrm{B} \times \mathrm{W_{OS}} + \mathrm{C} \times \mathrm{Z^{\tau\tau}_{OS}} \\
\text{IV)}\ \mathrm{SS2} &= \mathrm{A} \times \mathrm{QCD_{SS}} + \mathrm{B} \times \mathrm{W_{SS}} \\
\text{V)}\ \mathrm{OS3} &= \mathrm{H3} + \mathrm{D} \times \mathrm{QCD_{OS}} + \mathrm{E} \times \mathrm{W_{OS}} + \mathrm{F} \times \mathrm{Z^{\tau\tau}_{OS}} \\
\text{VI)}\ \mathrm{SS3} &= \mathrm{D} \times \mathrm{QCD_{SS}} + \mathrm{E} \times \mathrm{W_{SS}} \\
\text{VII)}\ \mathrm{OS4} &= \mathrm{H4} + \mathrm{G} \times \mathrm{QCD_{OS}} + \mathrm{H} \times \mathrm{W_{OS}} + \mathrm{I} \times \mathrm{Z^{\tau\tau}_{OS}} \\
\text{VIII)}\ \mathrm{SS4} &= \mathrm{G} \times \mathrm{QCD_{SS}} + \mathrm{H} \times \mathrm{W_{SS}} \\
\text{IX)}\ \mathrm{OS5} &= \mathrm{H5} + \mathrm{J} \times \mathrm{QCD_{OS}} + \mathrm{K} \times \mathrm{W_{OS}} + \mathrm{L} \times \mathrm{Z^{\tau\tau}_{OS}} \\
\text{X)}\ \mathrm{SS5} &= \mathrm{J} \times \mathrm{QCD_{SS}} + \mathrm{K} \times \mathrm{W_{SS}}
\end{aligned} \tag{7.20}$$

With the requirement that $\mathrm{E_T^{miss}} > 30\,\mathrm{GeV}$ the $Z \rightarrow \ell\ell$ becomes negligible. Similar to III) it is possible to determine the relative τ-lepton efficiencies using the Higgs channel.

7.12 Summary of the visible mass selection

In this chapter the full semi-leptonic Z $\rightarrow \tau\tau$ selection was discussed. As a pre-study, event quality criteria as well as effects of pile-up on the lepton isolation were discussed. An important result of the visible analysis is the fact that the QCD multi-jet as well as the electroweak background can be efficiently suppressed using data-driven methods (ABCD, control regions). The ratio of opposite sign and same sign charge events was found to be $\mathrm{R_{OS/SS}} \neq 1$ for the electroweak background. The QCD multi-jet background tends to be symmetric. In order to estimate a rescaling factor g for the same sign (SS) region, so called control regions were defined where the studied background are expected to be dominant. Since the individual contributions of the different background channels are not known, the aim was to define the number of expected background events with the ABCD method. The low statistic for the considered data set has forced the usage of Monte Carlo samples in order to calculate the expected electroweak background. The OS-gSS rescaling with g estimated with the introduced methods, results in a visible mass shape for the $\mathrm{m_{vis}}(\tau_\mathrm{h}, \tau_\ell)$ in the range of [37–75] GeV. The uncertainties were obtained and considered. These uncertainties have motivated an alternative method for the signal over background estimation using τ-lepton fake rates. In this thesis the idea was discussed theoretically and on Monte Carlo level.

[10] H1..H2 denotes the signal H $\rightarrow \tau\tau$ for the different τ-lepton identification cuts.

Chapter 8

Determination of the overall hadronic tau efficiency and $\mathrm{Z} \rightarrow \tau\tau$ cross section measurements

This section covers two data-driven methods for the τ-lepton reconstruction and identification efficiency determination:

Linear approximation technique: refers to the linear correlation between final selected events and selected events without τ-lepton identification and will be described in Sec. 8.2.

Embedding technique: uses a technique which replaces selected muons by τ-leptons and will be discussed in Sec. 8.6.

A general introduction of the overall efficiency will be given in Sec. 8.1. The performance of both methods on first data is described in Sec. 8.2.5 and Sec. 8.6.4. The measurement of the production cross section for $\mathrm{Z} \rightarrow \tau\tau \rightarrow \tau_{\mathrm{h}}\tau_{\ell}$[1)] is summarised in Sec. 8.5. Further studies can be found in Sec. 8.7.

8.1 General description of the overall tau reconstruction and identification efficiency

Equation 8.1 expresses all variables important for the efficiency determination. The overall efficiency $\varepsilon_{\mathrm{full}}$ for the $\mathrm{Z} \rightarrow \tau_{\mathrm{h}}\tau_{\ell}$ final state can be defined as

$$\varepsilon_{\mathrm{full}} = \varepsilon_{\mathrm{ID}}^{\tau_{\mathrm{h}}} \times \varepsilon_{\mathrm{reco}}^{\tau_{\mathrm{h}}} \times \varepsilon_{\mathrm{Z}\rightarrow\tau_{\mathrm{h}}\tau_{\ell}}^{\mathrm{kin}} \times \varepsilon_{\mathrm{ID}}^{\ell} \times \varepsilon_{\mathrm{reco}}^{\ell} \times \varepsilon_{\mathrm{trigger}}^{\ell} = \frac{\mathrm{N}_{\mathrm{Z}\rightarrow\tau_{\mathrm{h}}\tau_{\ell}}^{\mathrm{final}}}{\mathrm{N}_{\mathrm{Z}\rightarrow\tau_{\mathrm{h}}\tau_{\ell}}^{\mathrm{produced}}}, \tag{8.1}$$

with:

1) For simplification the hadronically decaying τ-lepton will be denoted as τ_h while the leptonically decaying τ-lepton will be denoted as τ_ℓ.

	tau selection	**correlation**	**lepton selection**	**efficiency**
Step 1		no	lepton trigger	$\varepsilon^{\ell}_{\mathrm{trigger}}$
Step 2	reconstruction	no	reconstruction	$\varepsilon^{\ell}_{\mathrm{reco}}$,$\varepsilon^{\tau_\mathrm{h}}_{\mathrm{reco}}$
Step 3	kinematic cuts	yes	kinematic cuts and lepton ID	$\varepsilon^{\mathrm{Z}\to\tau_\mathrm{h}\tau_\ell}_{\mathrm{kin}}$
Step 4	tau ID	no		$\varepsilon^{\tau_\mathrm{h}}_{\mathrm{ID}}$

Table 8.1: *The four steps for the $\mathrm{Z}\to\tau_\mathrm{h}\tau_\ell$ selection.* ***Step 1:*** *the event is triggered using the lepton trigger.* ***Step 2:*** *the τ-lepton candidate as well as the lepton candidate is reconstructed* ***Step 3:*** *all kinematic cuts for the τ-lepton and lepton candidates as well as the identification cuts for the leptons are applied to estimate the combined (τ_h, τ_ℓ) mass.* ***Step 4:*** *apply the identification cuts for the τ-lepton. The correlation considers dependencies of the tau efficiency from the lepton efficiency.*

- $\mathrm{N}^{\mathrm{final}}_{\mathrm{Z}\to\tau_\mathrm{h}\tau_\ell}$: number of selected $\mathrm{Z}\to\tau_\mathrm{h}\tau_\ell$ events
- $\mathrm{N}^{\mathrm{produced}}_{\mathrm{Z}\to\tau_\mathrm{h}\tau_\ell}$: number of $\mathrm{Z}\to\tau_\mathrm{h}\tau_\ell$ events in data
- $\varepsilon^{\mathrm{kin}}_{\mathrm{Z}\to\tau_\mathrm{h}\tau_\ell}$: probability to find $\mathrm{Z}\to\tau_\mathrm{h}\tau_\ell$ events with all cuts, except identification
- $\varepsilon^{\tau_\mathrm{h}}_{\mathrm{reco}}$: probability to reconstruct the τ-lepton with track seed and calorimeter seeded information
- $\varepsilon^{\tau_\mathrm{h}}_{\mathrm{ID}}$: probability to identify a reconstructed τ-lepton.
- $\varepsilon^{\ell}_{\mathrm{ID}}$: lepton identification efficiency
- $\varepsilon^{\ell}_{\mathrm{reco}}$: probability to identify a reconstructed lepton
- $\varepsilon^{\ell}_{\mathrm{trigger}}$: efficiency to trigger the lepton (for a better background suppression instead of the tau trigger the single lepton trigger will be used in this study).

The last three variables have to be obtained from lepton performance groups. Table 8.1 shows the different steps for event selection and efficiency determination.

8.2 A general description of the linear approximation for the τ-lepton identification efficiency determination

To get the background contribution (in particular on reconstruction level) under control, the linear approximation technique is developed.

The events selected without τ-lepton identification criteria (`pre-ID`) and all events with τ-lepton identification criteria (`post-ID`) are linear correlated. The overall efficiency (see Eq. 8.1) can be expressed as[2)]

$$\varepsilon^{\mathrm{Z}}_{\mathrm{kin}} \times \varepsilon^{\tau_\mathrm{h}}_{\mathrm{ID}} \times \varepsilon^{\tau_\mathrm{h}}_{\mathrm{reco}} = \frac{\mathrm{N}^{\mathrm{final}}_{\mathrm{Z}}}{\mathrm{N}^{\mathrm{produced}}_{\mathrm{Z}}} \times \mathrm{C}_1 \Rightarrow \mathrm{N}^{\mathrm{final}}_{\mathrm{Z}} = \left\{\varepsilon^{\mathrm{Z}}_{\mathrm{kin}} \times \varepsilon^{\tau_\mathrm{h}}_{\mathrm{ID}} \times \varepsilon^{\tau_\mathrm{h}}_{\mathrm{reco}}\right\} \times \mathrm{N}^{\mathrm{produced}}_{\mathrm{Z}}. \tag{8.2}$$

[2)] with Z denoting $\mathrm{Z}\to\tau_\mathrm{h}\tau_\ell$.

The product of identification and kinematic efficiency can be expressed as

$$\varepsilon^{\mathrm{Z}}_{\mathrm{kin}} \times \varepsilon^{\tau_h}_{\mathrm{ID}} = \frac{\mathrm{N}^{\mathrm{final}}_{\mathrm{Z}}}{\mathrm{N}^{\mathrm{reconstructed}}_{\mathrm{Z}}} \times \mathrm{C}_2 \Rightarrow \mathrm{N}^{\mathrm{final}}_{\mathrm{Z}} = \left\{\varepsilon^{\mathrm{Z}}_{\mathrm{kin}} \times \varepsilon^{\tau_h}_{\mathrm{ID}}\right\} \times \mathrm{N}^{\mathrm{reconstructed}}_{\mathrm{Z}}. \tag{8.3}$$

Finally, the identification efficiency can be expressed as

$$\varepsilon^{\tau_h}_{\mathrm{ID}} = \frac{\mathrm{N}^{\mathrm{final}}_{\mathrm{Z}}}{\mathrm{N}^{\mathrm{kin}}_{\mathrm{Z}}} \times \mathrm{C}_3 \Rightarrow \mathrm{N}^{\mathrm{final}}_{\mathrm{Z}} = \left\{\varepsilon^{\tau_h}_{\mathrm{ID}}\right\} \times \mathrm{N}^{\mathrm{kin}}_{\mathrm{Z}} \tag{8.4}$$

with $\mathrm{C}_{\mathrm{n}}(\mathrm{n} = 1, 2, 3)$ containing all further variables not directly correlated to the linear approximation technique (see Eq. 8.1). The linear correlation is expressed in Eq. 8.4 with the efficiency ($\left\{\varepsilon^{\tau_h}_{\mathrm{ID}}\right\}$) as slope (see solid lines in Fig. 8.2).

Interpretation of the linearity The linear correlation could be mis-interpreted as the claim that the τ-lepton identification efficiency is linear over an arbitrary range which is not the case. For example, all studies agree that the τ-lepton identification efficiency increases for an increasing τ-lepton transverse momentum $\mathrm{p_T}$. The basis for the linearity is the fact, that it is always possible to subdivide the used $\mathrm{p_T}$ (or η) range into several regions where the estimated efficiency is the same (e.g. events from a lower $\mathrm{p_T}$ region combined with events from an upper $\mathrm{p_T}$ range can result in the same efficiency as events for a medial $\mathrm{p_T}$ range). Furthermore, it is not required that the background has to be linear.

For further discussions, Eq. 8.4 is rewritten as

$$\varepsilon^{\tau_h}_{\mathrm{ID}} = \frac{\mathrm{N}^{\mathrm{post-ID}}_{\mathrm{Z}}}{\mathrm{N}^{\mathrm{pre-ID}}_{\mathrm{Z}}} \times \mathrm{C}_3 \Rightarrow \mathrm{N}^{\mathrm{post-ID}}_{\mathrm{Z}} = \left\{\varepsilon^{\tau_h}_{\mathrm{ID}}\right\} \times \mathrm{N}^{\mathrm{pre-ID}}_{\mathrm{Z}}. \tag{8.5}$$

Without background contribution the simplest way to estimate the efficiency is to build the ratio of post-ID over pre-ID events with the restriction that exactly one τ-lepton candidate and one lepton candidate per event is allowed. This simplifies the τ-lepton identification efficiency to

$$\varepsilon^{\tau_h}_{\mathrm{ID}} = \frac{\mathrm{N}^{\mathrm{post-ID}}_{\mathrm{Z}}}{\mathrm{N}^{\mathrm{pre-ID}}_{\mathrm{Z}}}. \tag{8.6}$$

A significant background affects this relation with the result that the τ-lepton identification efficiency becomes under-estimated. A method to handle this background contribution is the separation of all pre-ID and post-ID events into several sub-regions. This procedure allows additional conditions for background extraction and suppression.

8.2.1 Separation of events into three sub regions

All events on pre-ID and post-ID level will be sub-divided into three (or more[3)]) sub-regions (R1, R2, R3). The requirement is that for all sub-regions the expected signal efficiency is equal within a defined uncertainty.

[3)] Three regions are the lower limit. For more statistic the number of sub-regions can be larger.

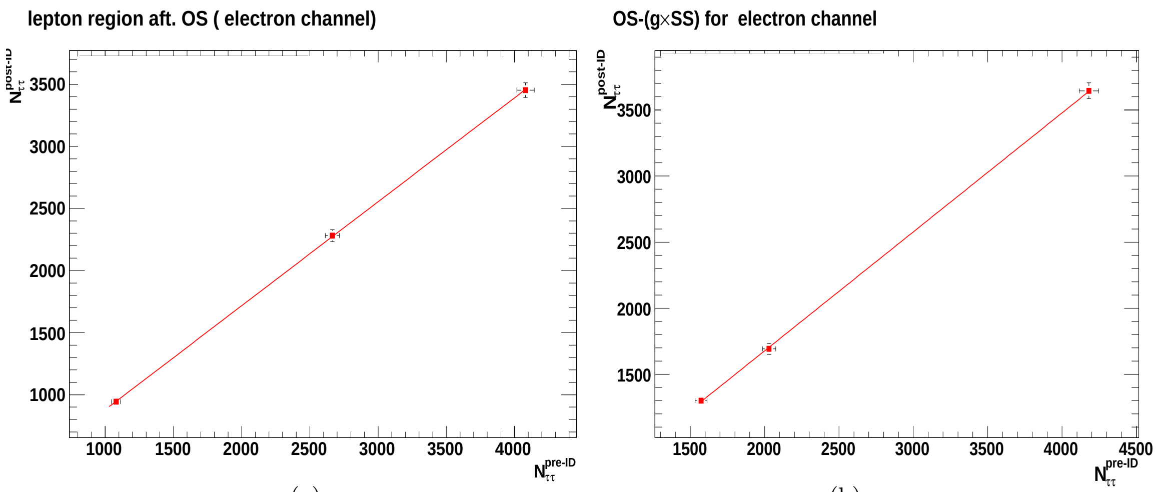

Figure 8.1: *Linear fit through three points binned for τ-leptons in η (a) and p_T (b) obtained from a signal Monte Carlo for the electron channel.*

The binning for a certain region on pre-ID and post-ID level has to be the same. The variables chosen for the separation in this analysis are the pseudo-rapidity η of the τ-lepton and the transverse momentum p_T for the τ-lepton as well as for the reconstructed lepton.

Binning using transverse momentum p_T: The binning of R1, R2, and R3 in p_T allows a good signal background suppression. The dis-advantage is that the τ-lepton identification efficiency differs significantly over a wider p_T range. This affects the linearity requirement and increases the uncertainty for the data to MC calibration. For smaller p_T binning the efficiency tends to be constant.

Binning using the pseudo-rapidity η: The binning in η is profitable because the efficiency does not differ significantly (particular in comparison with the p_T binning). The dis-advantage is that no good background suppression can be applied. For that reason a combination of both (η and p_T) is striven.

Defining the three regions R1, R2, R3 (binned in η and p_T): The first step is to define the optimal η and p_T ranges for R1, R2, and R3 using a signal Monte Carlo.

Figure 8.1 shows the linear fit through three points binned in η and p_T of the τ-lepton (the ranges are summarised in Tab. 8.2).

All three regions refer to the same efficiency and with an optimal binning in η and p_T the offset on the x-axis and the y-axis becomes negligible. This well balanced conditions are affected by additional background. This background contribution can be estimated with the following procedure.

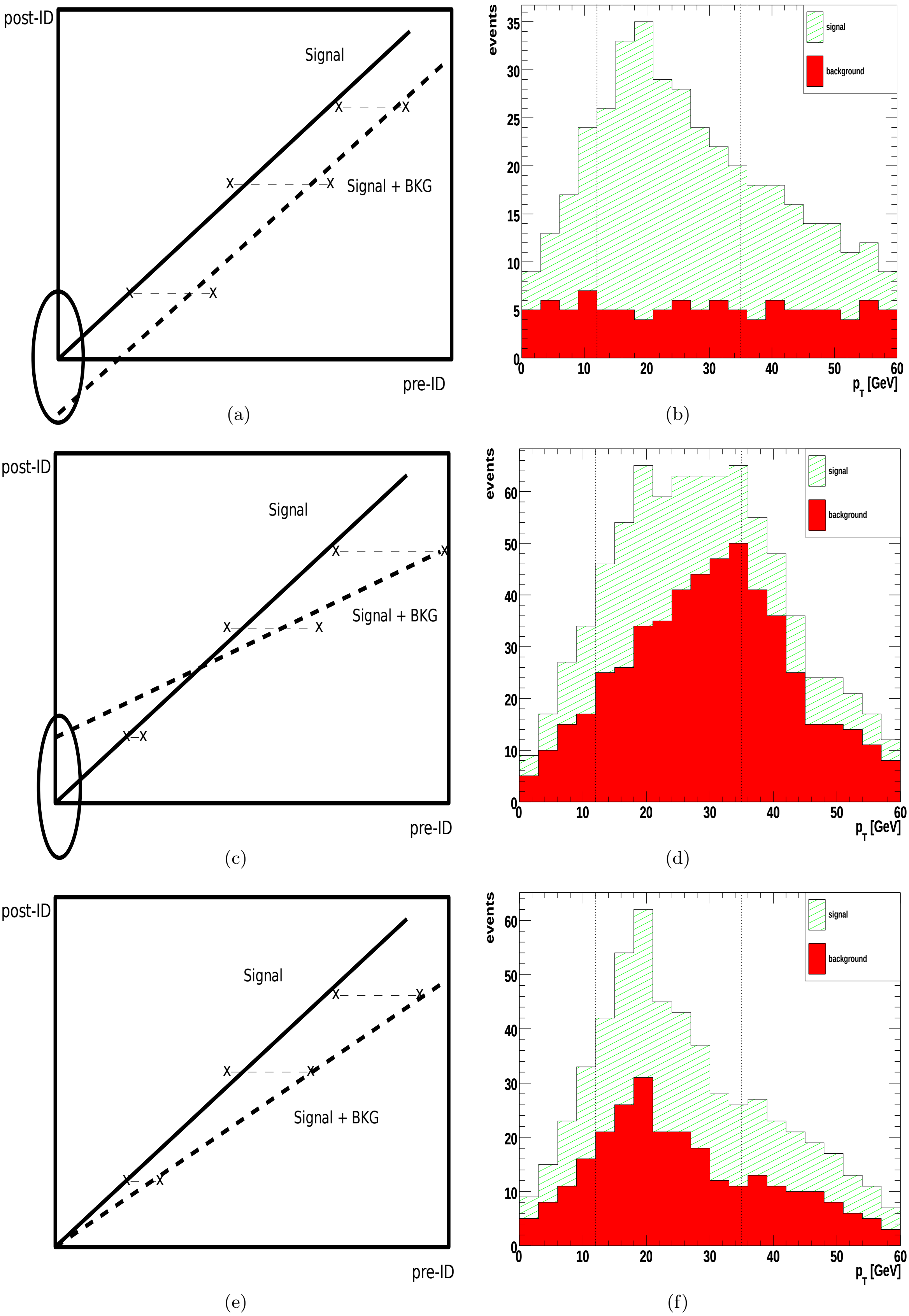

Figure 8.2: *The three possible scenarios for the linear approximation including background.*

region	η	$\mathrm{p_T}$ **(Tau CR) [GeV]**	$\mathrm{p_T}$ **(Lepton CR) [GeV]**
R1	-3–0	18–22 and 44–60	19–22
R2	0–1	22–37	22–39
R3	1–3	15–18 and 37–44	15–19 and 39–60

Table 8.2: *The different η and p_T binning for the τ-lepton and the reconstructed lepton. CR denotes the control regions.*

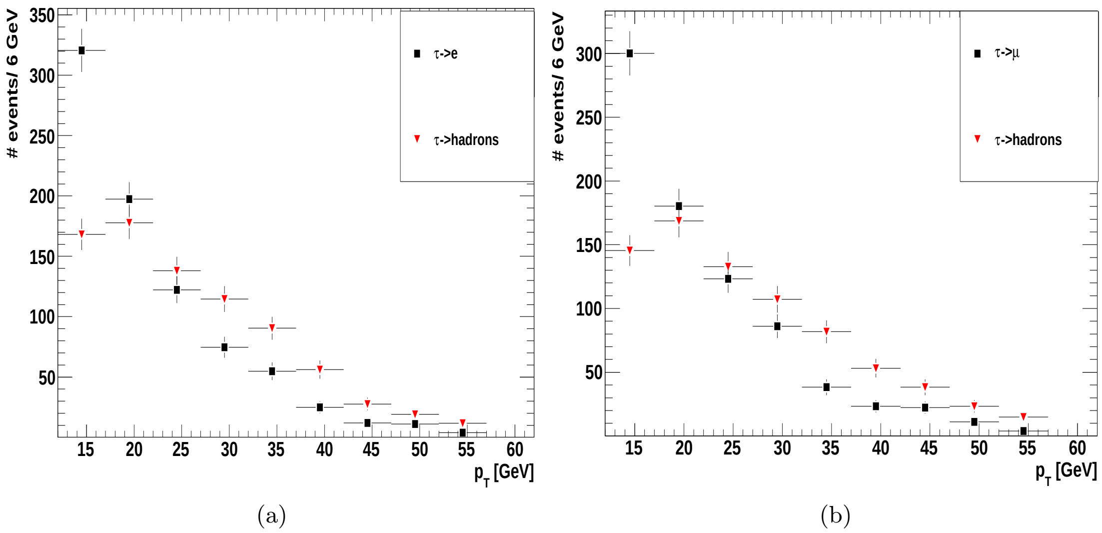

Figure 8.3: *The transverse momentum for the hadronically decaying and for the leptonically decaying τ-lepton for electron channel (a) and the muon channel (b) on truth level. The p_T distributions are slightly different because of the different neutrino contributions.*

8.2.2 Conditions for background suppression

The solid lines in Figs. 8.2(a,c,e) show the correlation for the number of pre-ID events (x-axis) and post-ID events (y-axis). The dotted lines represent signal plus background events. Figures 8.2(b,d,f) show the illustration of the τ-lepton $\mathrm{p_T}$ distribution with different background scenarios. For background free data the offset is expected to be (x,y) = (0,0). The first case (a,b) is related to a signal overlaid by a flat background. The values on the x-axis moves to the right while the slope does not change significantly. The offset becomes (x,y) = (>0 , <0).

The second case (c,d) illustrates a signal overlaid by a non-flat background. For one (or two) regions the background contribution becomes disproportionate larger. The slop decreases and the offset becomes (x,y) = (<0,>0).

The last case (e,f) is the most difficult one. Although the background effects the slope, the offset is in the order of the signal offset (x,y) = (0,0). A solution for this scenario will be discussed in the corresponding text.

In order to exclude the significant background described in Fig. 8.2 (a–d) the the y-offset (y+Δy) has to be in the order of $\mathcal{O}$ = 0 particular for the η binned regions. The last case

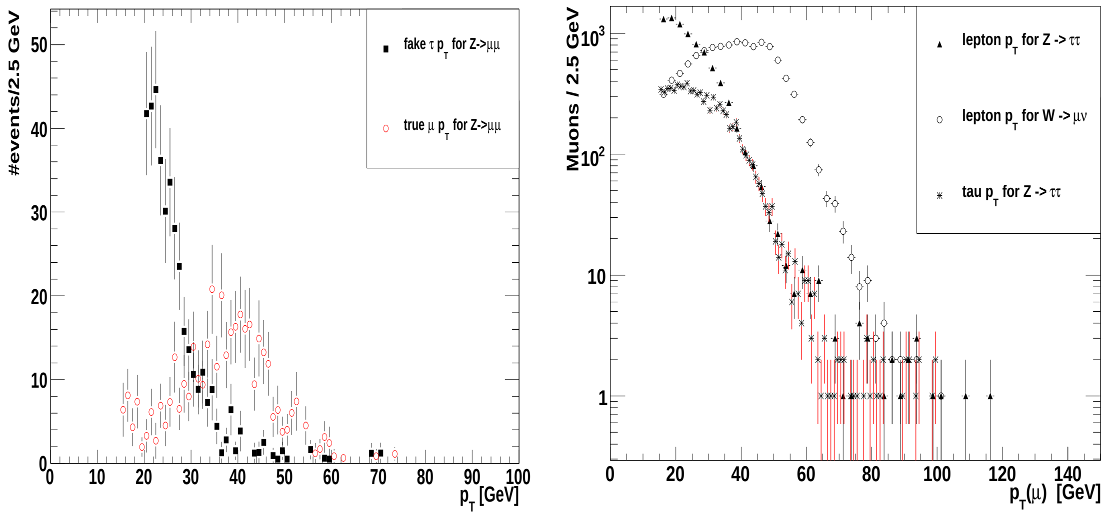

(a) (b)

Figure 8.4: *The τ-lepton transverse momentum for the corresponding lepton p_T distribution for background region.5 The Z → μμ background distribution (a). The correct reconstructed muon has the expected peak at about 45 GeV while the second muon which fakes the τ-lepton has a lower p_T. The W → μν background distribution (b). Since almost the jet in W+jets events fakes the τ-lepton while the lepton is true, the p_T of the lepton depends from the kinematic of the W boson and has therefore a peak nearby 45 GeV.*

(8.2(e,f)) will be discussed in the following. The binning in $\mathrm{p_T}$ can be extended to the reconstructed lepton candidate. Two regions are defined:

Tau control region: The original binning with respect to the reconstructed hadronically decaying τ-lepton defines the tau control region.

Lepton control region: The binning with respect to the reconstructed leptonically decaying τ-lepton defines the lepton control region

As shown in Fig. 8.3 the $\mathrm{p_T}$ distributions for the τ-lepton and the lepton are quite similar considering the different neutrino contributions. The conclusion is that for background free data the number of events for each region (R1, R2, R3) has to be the same:

$$\mathrm{N_{Rx}^{tau-control}} = \mathrm{c}_\nu \mathrm{N_{Rx}^{lepton-control}} \tag{8.7}$$

with (x=1,2,3) and c_ν as the correction factor considering the different visible $\mathrm{p_T}$.

Additional background affects these condition. For example, the $W \to \ell\nu$ background is characterised as an outgoing jet faking the τ-lepton while the lepton is almost true. The $\mathrm{p_T}$ kinematic of a lepton coming from a W-boson is different compared with the lepton coming from a Z-boson. For that reason the content of R1, R2, and R3 is expected to be different. Figure 8.4(b) shows the behaviour on MC level. The $\mathrm{p_T}$ of the lepton coming from the W-boson has a peak at about 45 GeV. The number of events in this region becomes larger.

The following conditions are defined (it is not necessary that all conditions have to be used):

- I) Demand at least three uncorrelated fit points fulfilling the following conditions:
  - Each event has to be unique, no overlap of events is allowed.
  - If significant statistic is available, all points have to contain a significant number of events (points are not allowed to be nearby x,y=(0,0) per default)
- II) The offset (inclusive uncertainty) on x and y axis (x $\pm$ Δx and y $\pm$ Δy) has to be in the order of $\mathcal{O} = 0$.
  - For a background free data sample the fit goes through (x,y) = (0,0). The scenarios Fig. 8.2(a) and Fig. 8.2(c) can be excluded. The last scenario (Fig. 8.2(e)) has to be studied in more detail.
- III) The calculated number $\mathrm{N_{calculated}} = \frac{\mathrm{N_{post-ID}}}{\mathrm{N_{pre-ID}}}$ has to be in the same order as the efficiency obtained from the linear fit.
  - This requirement makes sure that the slope from the linear fit represents the actual event content in the studied $\mathrm{p_T}$ region. A significant deviation points out that the fit does not work or the sample is still overlaid by background.
- IV) The estimated SS-rescaling factors g have to be in the same order on reconstruction level.
  - The main challenge is the background estimation on pre-ID level. For that reason the OS-gSS rescaling is applied. Independent from the used τ-lepton identification variable, the number of signal and background events on pre-ID level is not affected and therefore the same. For that reason all OS-gSS procedures on post-ID level must result in the same g factors on pre-ID level.
- V) Muon and electron channel should produce reasonable and comparable results for the identification efficiency.
  - The τ-lepton efficiency does not depend from the lepton selection.

The described conditions (I-V) can be applied on the tau control region or the lepton control region individually. Conditions (VI-VIII) are defined for the combination of both regions.

- VI) The numbers of events for each region (R1, R2, R3) must be in the same order for the tau region and the lepton control region.
  - This condition is related to the fact that the signal $\mathrm{p_T}$ distributions for the τ-lepton and the lepton are congruent with respect to the different neutrino multiplicity (see Fig. 8.3). For background the $\mathrm{p_T}$ distributions are almost different (e.g. Fig. 8.4).

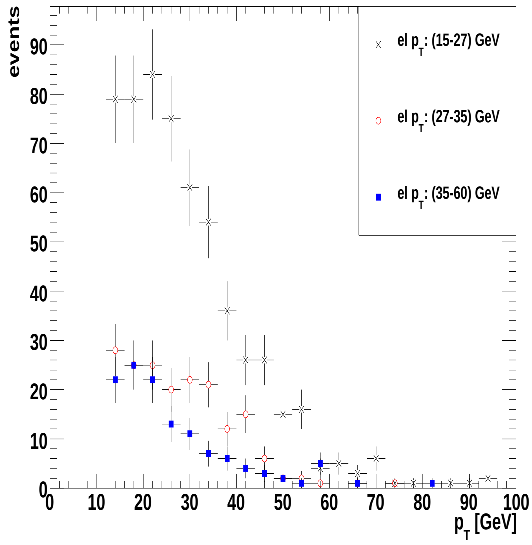

(a)

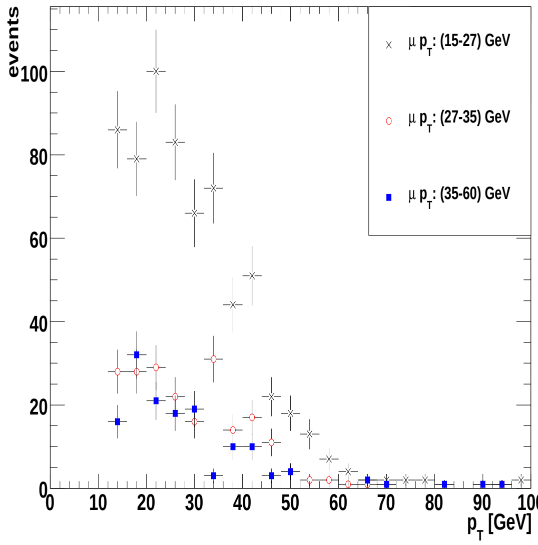

(b)

Figure 8.5: *The p_T distributions for the hadronically decaying τ-leptons for different electron p_T bins (a) and for different muon p_T bins (b) on truth level.*

- It has to be mentioned that the visible p_T for hadronically decaying τ-leptons is larger compared with the leptonically decaying τ-lepton. The reason is that for the latter two neutrinos are produced while for the first only the tau-neutrino appears.

• VII) The tau-region and the lepton-control region must have the same efficiency and the same offset Δx and Δy.

- This can be expressed by the following relations

$$\begin{aligned} \frac{\varepsilon_\tau}{\varepsilon_\ell} &\simeq 1 \\ \frac{y(\tau) \pm \Delta y(\tau)}{y(\ell) \pm \Delta y(\ell)} &\simeq 1 \\ \frac{x(\tau) + \Delta x(\tau)}{x(\ell) \pm \Delta x(\ell)} &\simeq 1 \end{aligned} \tag{8.8}$$

- The kinematic of the $Z \to \tau\tau$ event is well understood. In Fig. 8.5 the truth τ-lepton p_T depending from the truth lepton p_T is drawn. It shows that for background free data the distributions would be congruent if the number of events would be the same.

• VIII) The conditions

$$\begin{aligned} &\frac{\mid y(\tau) + \Delta y(\tau) \mid + \mid y(\ell) \pm \Delta y(\ell) \mid}{\varepsilon_\tau + \varepsilon_\ell}, \frac{\mid x(\tau) + \Delta x(\tau) \mid + \mid x(\ell) \pm \Delta x(\ell) \mid}{\varepsilon_\tau + \varepsilon_\ell}, \\ &\frac{\mid y(\tau) + \Delta y(\tau) \mid + \mid x(\tau) + \Delta x(\tau) \mid}{\varepsilon_\tau}, \frac{\mid y(\ell) \pm \Delta y(\ell) \mid + \mid x(\ell) \pm \Delta x(\ell) \mid}{\varepsilon_\ell} \end{aligned} \tag{8.9}$$

must be in the order of $\mathcal{O}$=0.

- These conditions consider the fact that small efficiencies (e.g. a flat slope due to background) can also result in a small y (and/or x) offset. For this case the conditions become larger due to the small value in the denominator of the conditions. An overestimated background would results in a larger efficiency but mostly also in a larger y (and/or x) offset. Also for this case the conditions are not minimal. So the strategy is to smear out the OS-SS (see Sec. 8.2.3) to estimate the minimum for all these conditions. For a pure MC signal sample it can be shown that all these conditions are minimal.

- IX) For each region the efficiency has to be in the same order.
  - This important relation $\varepsilon_{\mathrm{R1}} = \varepsilon_{\mathrm{R2}} = \varepsilon_{\mathrm{R3}}$ is the basis for the whole method.

8.2.3 OS-SS rescaling

The OS/SS ratio for pre-ID events is not precisely available, since the uncertainties due to the large input of background cannot be accurately calculated. The OS-SS subtraction can be rescaled with respect to the discussed properties from the last section.

For background suppression on pre-ID level the subtraction will be modified with an SS rescaling factor g:

$$\mathrm{OS} - \mathrm{SS} \rightarrow \mathrm{OS} - \mathrm{gSS}. \tag{8.10}$$

Since OS/SS can be different for each $\mathrm{p_T}$ region, also g can be different. Each region (R1, R2, R3) is represented its own g-factor. For three regions it results into three g-factors for the pre-ID level and three g-factors for the post-ID level.

$$\mathrm{g}_1^{\mathrm{pre-ID}}, \mathrm{g}_2^{\mathrm{pre-ID}}, \mathrm{g}_3^{\mathrm{pre-ID}}, \mathrm{g}_1^{\mathrm{post-ID}}, \mathrm{g}_2^{\mathrm{post-ID}}, \mathrm{g}_3^{\mathrm{post-ID}} \tag{8.11}$$

The following conditions have to be considered:

- The g-factors on pre-ID level have to be independent from identification variable.
- The g-factors on post-ID level can be different depending on theτ-lepton identification cut (e.g. `cut based medium, cut based tight` etc.).
- The g-factors represents the overall SS-rescaling for the overall background (the different background contributions from QCD, W, or Z have different values which does not have to be estimated.)

With a normal random distribution the factor g is modified around the expected value in order to estimate OS-gSS. For each estimated value of $\mathrm{g_i}$ the conditions described above will be checked. If all defined conditions are fulfiled the efficiency can be estimated. Because of the fact that different values of $\mathrm{g_i}$ can fulfil all conditions, the modification of the factors is reproduced. Finally, for each region (R1, R2, R3) on pre-ID and post-ID level a g-factor $\mathrm{g} \pm \Delta\mathrm{g}$ can be obtained. The uncertainty on g also affects the number of OS-gSS events and therefore also the estimated efficiency. Further uncertainties on the linear approximation will be discussed in the following section.

8.2.4 Systematic uncertainties affecting the linear approximation

The linear approximation technique is affected by several systematic uncertainties:

- The correct definition of the p_T and η regions calibrated with MC information.
  - As discussed before, the linearity is defined for a certain p_T or η region. It can be calibrated by MC information to define the correct binning. Since the τ-lepton efficiency can be different for different p_T regions, the assumption of a pure linearity has to be confirmed within an uncertainty which has to be estimated. To minimise this uncertainty the chosen p_T interval should be defined as small as possible.
- The uncertainty due to deviations from the discussed requirements.
  - All requirements discussed in Sec. 8.2.2 are background exclusion conditions. The probability $\mathcal{P}$ of remaining background decreases implementing all requirements but it can still be possible that $\mathcal{P} > 0$. In addition, to have a significant statistic, the allowed range for conditions (I-VIII) can be increased. The remaining background probability $\mathcal{P}$ becomes larger.
- The upper limit due to remaining background can be estimated.
  - In general, the remaining background on pre-ID level is correlated with the measured efficiency. For example, if the remaining background on pre-ID level is 10 % then the maximal deviation (if all background events are rejected on post-ID level) from the truth efficiency is about 10 % (e.g. 300 pre-ID events with 30 background events $\rightarrow \varepsilon_{\mathrm{truth}} = 150/270 = 0.55$ while the measured efficiency $\varepsilon_{\mathrm{measured}} = 150/300 = 0.5$).
  - Since the requirement of a negligible offset and same efficiencies for R1, R2, and R3 has to be fulfilled the possibility for the background to be unseen decreases.
  - This requirement is strongly sensitive to modifications in the cut selection. A further cut like E_T^{miss} can distort the relative background contribution and therefore also the fit performance.

8.2.5 Tau-ID efficiency with linear approximation technique for first ATLAS data (integrated luminosity of $\mathcal{L} = 35\ pb^{-1}$)

The $Z \rightarrow \tau_h \tau_\ell$ selection is described in Chapt. 7. The identification of τ-leptons depends from the different identification cuts (`cut based`, `LLH`, or `BDT`) and the electron vetoes (medium or tight) and can be expressed as

$$\varepsilon_{\mathrm{ID}}^{\tau_h} = \frac{N_Z^{\mathrm{post-ID}}}{N_Z^{\mathrm{pre-ID}}} \times C_3 \Rightarrow N_Z^{\mathrm{post-ID}} = \left\{\varepsilon_{\mathrm{ID}}^{\tau_h}\right\} \times N_Z^{\mathrm{pre-ID}}. \tag{8.12}$$

The full procedure from the MC calibration to the final τ-lepton efficiency will be discussed for `cut based medium`, `electron veto medium` in order to have comparable results

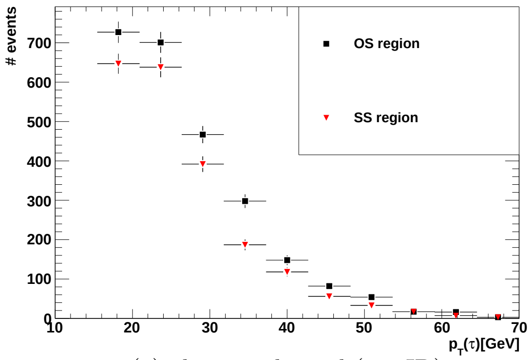

(a) electron channel (pre-ID)

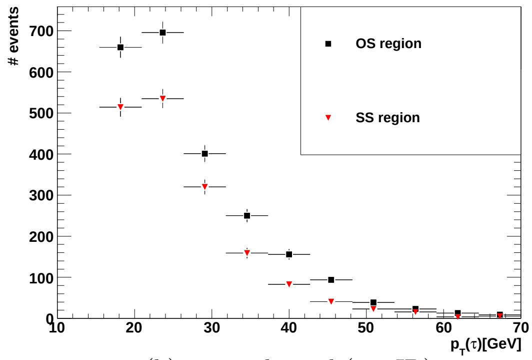

(b) muon channel (pre-ID)

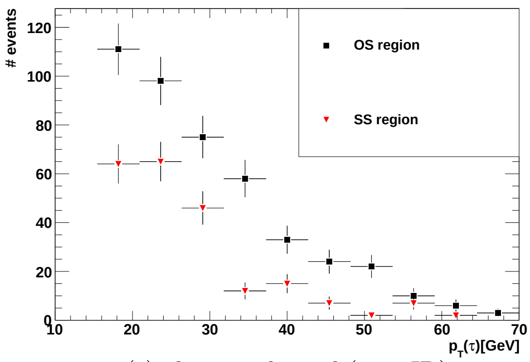

(c) electron channel (post-ID)

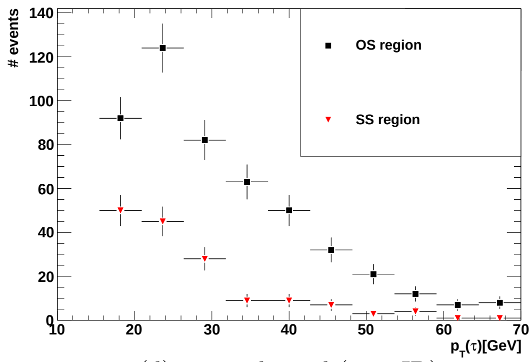

(d) muon channel (post-ID)

Figure 8.6: *The p_T distribution of hadronically decaying τ-lepton candidates for opposite sign (OS) and same sign (SS) charge combinations. For the electron channel for pre-ID (a) and post-ID (c) and for the muon channel for pre-ID (b) and post-ID (d). It can be seen, that for the pre-ID selection OS/SS is closer to one compared with OS/SS for the post-ID selection.*

with the visible mass analysis. Both channels[4)] (electron, muon) will be discussed. Figure 8.6 shows the $\mathrm{p_T}$ distributions for the τ-lepton candidates and the lepton candidates for the pre-ID and the post-ID selection. Figure 8.7 shows the η distributions for the τ-lepton candidates and the lepton candidates for the pre-ID and the post-ID selection.

Figures 8.8 and 8.9 show the $\mathrm{p_T}$ and η distributions for the τ-lepton and the reconstructed lepton before and after `cut based medium`. For Fig. 8.8 it can be seen that on pre-ID level the leptons dominating higher ($\mathrm{p_T} > 40\,\mathrm{GeV}$) transverse momentum regions. This indicates remaining background (e.g. $W \to \ell\nu$ events) on pre-ID level. The η region is not optimal for background suppression by using tau control and lepton control regions.

The full selection procedure will now discussed for `cut based medium`, for the electron and the muon channel, $15\,\mathrm{GeV} < \mathrm{p_T} < 60\,\mathrm{GeV}$ and `electron veto medium`

- MC calibration (see Tab. 8.2) in order to get the correct binning.

[4)]Reminder: electron or muon channel denote the $\mathrm{Z} \to \tau\tau \to \tau_h\tau_e$ or $\mathrm{Z} \to \tau\tau \to \tau_h\tau_\mu$ channel

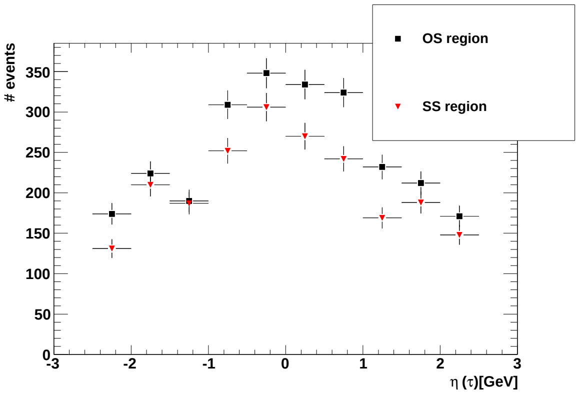

(a) electron channel (pre-ID)

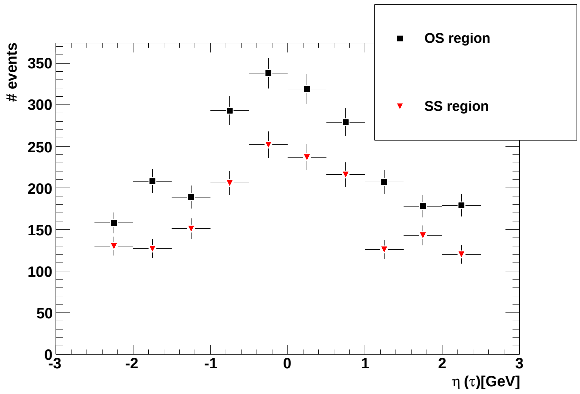

(b) muon channel (pre-ID)

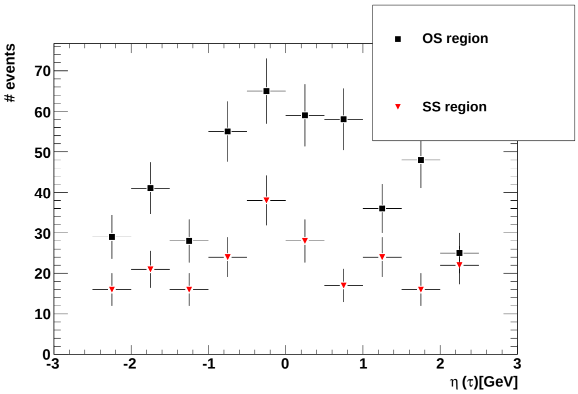

(c) electron channel (post-ID)

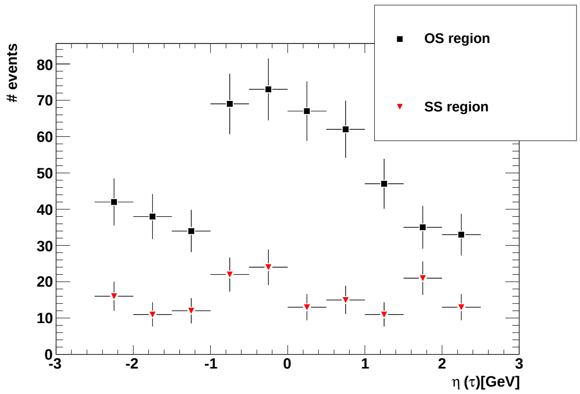

(d) muon channel (post-ID)

Figure 8.7: *The η distributions for hadronically decaying τ-lepton candidates for opposite sign (OS) and same sign (SS) charge combinations. For the electron channel for pre-ID (a) and post-ID (c) and for the muon channel for pre-ID (b) and post-ID (d). It can be seen, that for the pre-ID selection OS/SS is closer to 1 compared with OS/SS for the post-ID selection.*

  – The MC calibration results in the following sub-regions R1,R2, and R3:

- Apply the OS-$\mathrm{g_i}$SS subtraction (i=1,2...6) for each region on pre-ID level and post-ID level (R1,R2,R3). Apply normal random distribution $\mathcal{R}_i$ within interval [0,0.6] and define $\mathrm{g_i} \pm \mathcal{R}_i$. Replicate this procedure n-times (e.g. n=500). Determine the linear fit and check all requirements discussed previously. The first step is the independent processing of the tau and lepton control regions

  – The different behaviour with respect of modified g is shown in Fig. 8.10. As expected the background changes the content of the different regions. This affects all parameter (χ^2/ndf, the χ^2 probability, the offset and the slope representing the efficiency). Since the pre-ID level is QCD dominated it is expected to have OS/SS $\simeq$ 1. For that reason an increasing g factor optimises the fit performance.

For first data and given statistic it is not possible to apply all conditions as described above. For the overall efficiency the efficiency determination is sub divided into two steps.

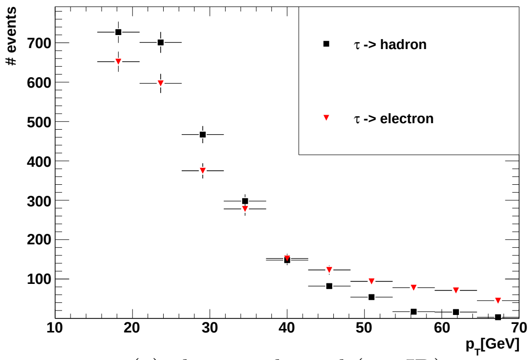

(a) electron channel (pre-ID)

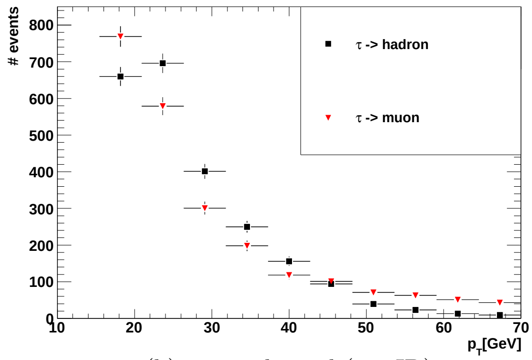

(b) muon channel (pre-ID)

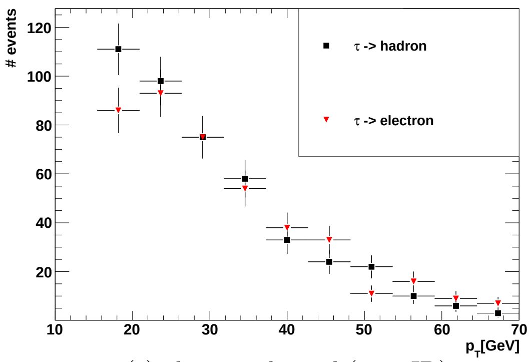

(c) electron channel (post-ID)

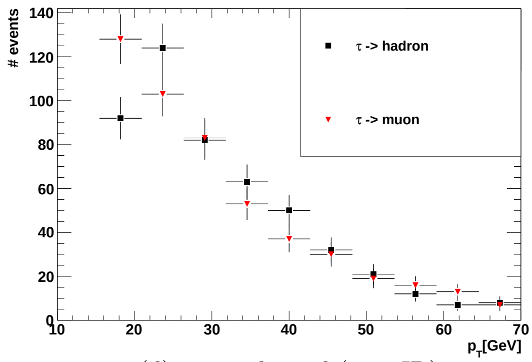

(d) muon channel (post-ID)

Figure 8.8: *The p_T distributions for the τ-lepton and the reconstructed lepton for opposite sign events. For the electron channel for pre-ID (a) and post-ID (c) events. For the muon channel for the pre-ID (b) and post-ID (d) selection.*

- Step 1: η-binning
  - require condition I and VIII.
  - require offset $|\mathrm{y} \pm \Delta\mathrm{y}| \simeq 0$ (condition II)
  - require that all efficiencies for all regions are in the same order (condition IX)
  - the value from the fit has to be in the same order as the calculated value (condition III).
- Step 2: $\mathrm{p_T}$ binning for the τ-lepton and the lepton candidate:
  - require condition I and VIII.
  - require that all efficiencies for all regions are in the same order (condition IX)
  - the value from the fit has to be in the same order as the calculated value (condition III)
  - require offset $|\mathrm{y} \pm \Delta\mathrm{y}| \simeq 0$ (condition II)

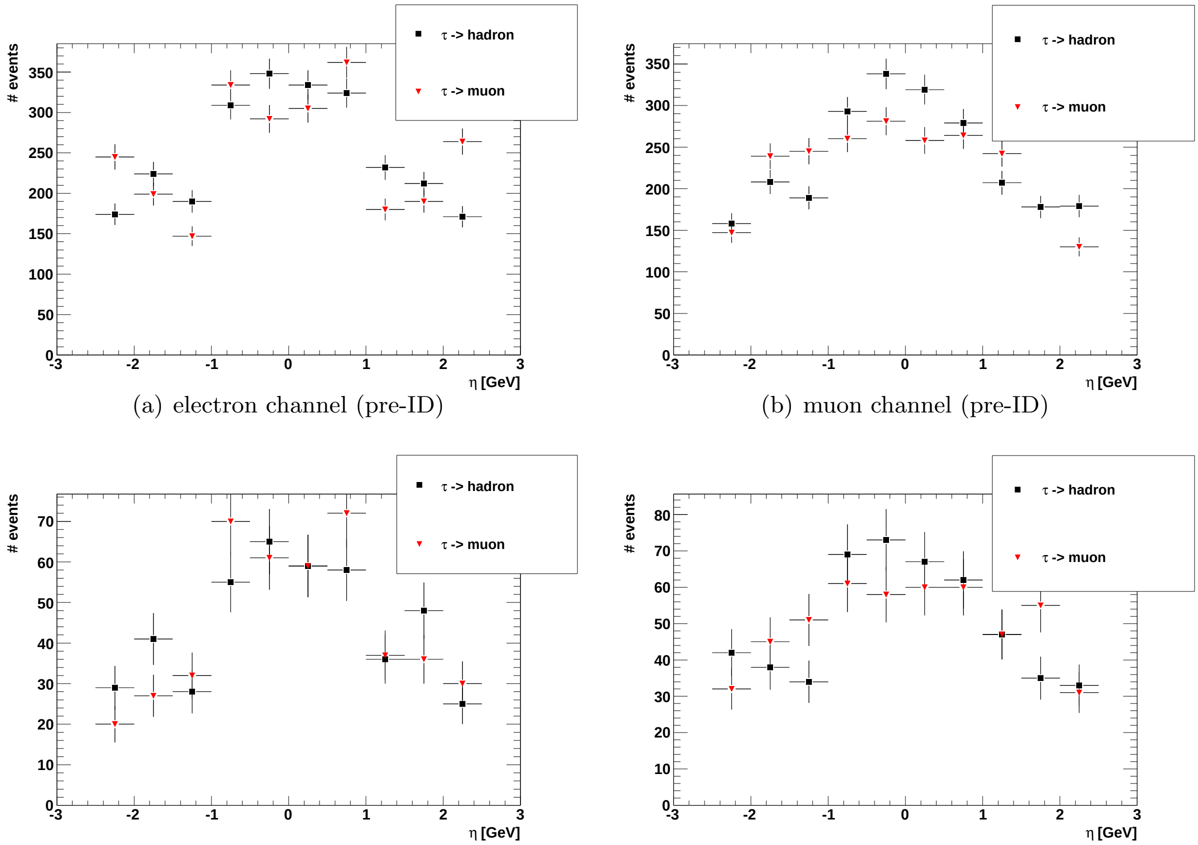

(a) electron channel (pre-ID) (b) muon channel (pre-ID)

(c) electron channel (post-ID) (d) muon channel (post-ID)

Figure 8.9: *The η distributions for the τ-lepton and the reconstructed lepton for opposite sign events. For the electron channel for pre-ID (a) and post-ID (c) events. For the muon channel for the pre-ID (b) and post-ID (d) selection.*

– the number of events for each region has to be the same for $p_T(\ell)$ and $p_T(\tau_h)$ rescaled considering the neutrino contribution (condition VI).

8.3 Tau identification efficiency for the electron channel

Step 1: η binning for the reconstructed τ-lepton in the electron channel

The first step is the definition of the three regions using η binning.

Table 8.4 shows the pre-ID number of events without OS-gSS subtraction. The SS rescaling factor g is smeared out with a random distribution. Considering all required conditions the following number of events and values for the SS-rescaling factors are obtained and summarised in Tab. 8.5.

The summarised values are

$$\varepsilon_{\text{fit}} = 0.42 \pm 0.05 \,\text{and}\, \varepsilon_{\text{calculated}} = 0.44 \pm 0.03. \tag{8.13}$$

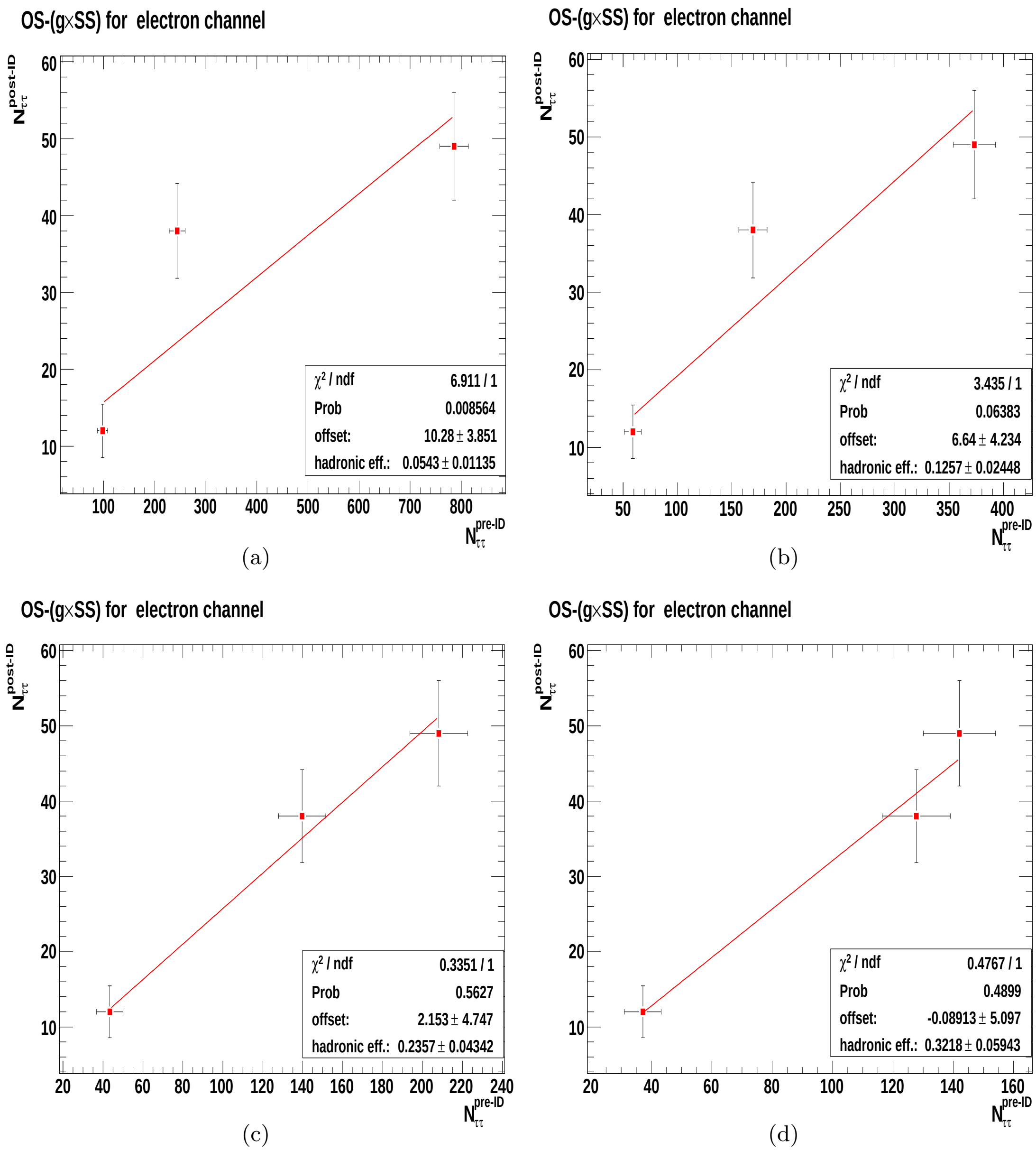

Figure 8.10: *The linear fit for the described p_T regions R1,R2, and R3 for different SS rescaling factors g=0 (a), g=0.5 (b), g=0.7 (c), and g=0.78 (d). The expected rescaling factor is in the order of $\mathcal{O}$ = 1. The factor g=0 refers to the largest background contribution. As larger g as smaller becomes the remaining background.*

region	η	$\mathrm{p_T}$ **(Tau CR) [GeV]**	$\mathrm{p_T}$ **(Lepton CR) [GeV]**
R1	-3–0	18–22 and 44–60	19–22
R2	0–1	22–37	22–39
R3	1–3	15–18 and 37–44	15–19 and 39–60

Table 8.3: *The different η and p_T binning for the τ-lepton and the reconstructed lepton.*

η **region**	N^{OS}_{pre-ID}	N^{SS}_{pre-ID}	$N^{OS}_{post-ID}$	$N^{SS}_{post-ID}$
-3–0	1325±36	1144±33	180±13	70±8
0–1	524±23	413±20	65±8	9±3
1–3	669±26	546±23	90±9	46±7

Table 8.4: *The number of OS and SS events for pre-ID events and post-ID events in the electron channel for η binning.*

η **region**	N^{OS-gSS}_{pre-ID}	$N^{OS-gSS}_{post-ID}$	g_{pre-ID}	$g_{post-ID}$	ε
-3–0	163±13	71±8	1.015±0.012	1.55±0.012	0.44±0.04
0–1	111±11	49±7	1.00±0.010	1.40±0.014	0.45±0.05
1–3	73±9	33±6	1.09±0.013	1.23±0.012	0.45±0.06

Table 8.5: *The number of OS-gSS events for pre-ID events and post-ID events in the electron channel for η binning.*

Step 2: p_T **binning for the reconstructed τ-lepton (tau control region) and the reconstructed electron (lepton control region)**

The second step is the definition of the three regions using p_T binning of the reconstructed τ-lepton candidate and the electron candidate in order to check the signal over background relation. Table 8.6 shows the initial number of events without OS-gSS subtraction. Considering all conditions described above the following number of events and values for the SS-rescaling factors are obtained and summarised in Tab. 8.7.

Tau control region				
p_T**[GeV]**	N^{OS}_{pre-ID}	N^{SS}_{pre-ID}	$N^{OS}_{post-ID}$	$N^{SS}_{post-ID}$
18–22 and 44–60	727±27	661±26	94±10	38±6
22–37	995±32	753±27	136±12	38±6
15–18 and 37–44	793±28	688±26	103±10	51±7
Lepton control region				
p_T**[GeV]**	N^{OS}_{pre-ID}	N^{SS}_{pre-ID}	$N^{OS}_{post-ID}$	$N^{SS}_{post-ID}$
19–22	504±22	430±21	64±8	26±5
22–39	870±29	717±27	131±11	50±7
15–19 and 39–60	1126±34	942±31	135±12	50±7

Table 8.6: *The number of OS and SS events for pre-ID events and post-ID events in the electron channel for $p_T(\tau)$ binning (top) and the $p_T(\ell)$ binning (bottom).*

The summarised values for the efficiency are:

$$\varepsilon_{\text{fit}} = 0.44 \pm 0.04 \,\text{and}\, \varepsilon_{\text{calculated}} = 0.44 \pm 0.03 \tag{8.14}$$

for the tau control region and

$$\varepsilon_{\text{fit}} = 0.44 \pm 0.05 \,\text{and}\, \varepsilon_{\text{calculated}} = 0.42 \pm 0.03 \tag{8.15}$$

Tau control region					
p_T **[GeV]**	N^{OS-gSS}_{pre-ID}	$N^{OS-gSS}_{post-ID}$	g_{pre-ID}	$g_{post-ID}$	ε
18–22 and 44–60	105±10	46±7	0.94±0.01	1.25±0.02	0.440±0.052
22–37	189±14	82±9	1.07±0.01	1.43±0.02	0.431±0.043
15–18 and 37–44	91±9	41±6	1.02±0.01	1.21±0.01	0.456±0.049
Lepton control region					
p_T **[GeV]**	N^{OS-gSS}_{pre-ID}	$N^{OS-gSS}_{post-ID}$	g_{pre-ID}	$g_{post-ID}$	ε
19–22	65±8	29±5	1.02±0.01	1.33±0.02	0.449±0.06
22–39	145±12	65±8	1.01±0.02	1.31±0.02	0.449±0.04
15–19 and 39–60	165±13	71±8	1.02±0.01	1.28±0.02	0.429±0.04

Table 8.7: *The number of OS-gSS events for pre-ID events and post-ID events in the electron channel for $p_T(\tau_h)$ binning (top) and $p_T(\ell)$ binning (bottom). In addition the corresponding rescaling factors g a listed.*

Region	$(\frac{N^{taucontrol}}{N^{leptoncontrol}})^{lin.App.}_{pre-ID}$	$(\frac{N^{taucontrol}}{N^{leptoncontrol}})^{lin.App.}_{post-ID}$	$(\frac{N^{taucontrol}}{N^{leptoncontrol}})^{MC}$
R1	105/65 = 1.61±0.25	46/29 = 1.59±0.38	1.52±0.13
R2	188/145 = 1.30±0.14	82/65 = 1.26±0.21	1.16±0.09
R3	91/165 = 0.55±0.07	41/71 = 0.57±0.11	0.65±0.11

Table 8.8: *The number of events for each region on pre-ID level as well as the relative numbers in comparison with MC truth prediction.*

for the lepton control region.

By construction multiple solutions (different combinations of the SS rescaling factors) could be possible. In order to reduce this effect the number of overall pre-ID events and overall post-ID events for the η and the $p_T(\tau)$ binning has to be in the same order. The sum of all events for R1,R2, and R3 on pre-ID level is

$$N_\eta : N_{p_T}(\tau) = (347 \pm 19) : (375 \pm 19). \tag{8.16}$$

On post-ID level the relation is

$$N_\eta : N_{p_T}(\tau) = (153 \pm 12) : (165 \pm 13). \tag{8.17}$$

The numbers are consistent among each other. Table 8.8 shows the number of events for the tau control and for the lepton control region. The MC values are obtained from a truth signal sample. The identification efficiency estimated for all three steps is:

$$\begin{aligned} \bar{\varepsilon} &= \frac{1}{6}(0.42 + 0.44 + 0.44)^{\text{fit}} + (0.44 + 0.44 + 0.42)^{\text{calc.}} \\ &= 0.43 \pm 0.04^{\text{fit}} \pm 0.02^{\text{syst.}} \end{aligned} \tag{8.18}$$

The uncertainty from the fit includes the statistical uncertainty as well as the effects from the fit performance. The systematic uncertainty includes the effects from the Δy offset, the difference for the individual efficiencies for the sub regions and the MC to data calibration for the correct binning in η and p_T.

8.4 Tau identification efficiency for the muon channel

The MC calibration forces the same η and p_T binning as for the electron channel.

Step 1: η binning for the reconstructed τ-lepton in the muon channel

The first step is the definition of the three regions using η binning. Table 8.9 shows the

η **region**	N^{OS}_{pre-ID}	N^{SS}_{pre-ID}	$N^{OS}_{post-ID}$	$N^{SS}_{post-ID}$
-3–0	1257±35	909±30	183±14	38±6
0–1	472±22	379±19	72±8	15±4
1–3	619±25	420±20	89±9	24±5

Table 8.9: *The number of OS and SS events for pre-ID and post-ID for η binning in the muon channel.*

pre-ID number of events without OS-gSS subtraction. Considering all required conditions the following number of events and values for the SS-rescaling factors are obtained and summarised in Tab. 8.10.

The summarised values for the efficiency are:

$$\varepsilon_{\mathrm{fit}} = 0.44 \pm 0.05 \,\mathrm{and}\, \varepsilon_{\mathrm{calculated}} = 0.44 \pm 0.02. \tag{8.19}$$

Step 2: p_T binning for the reconstructed τ-lepton (tau control region) and the reconstructed muon (lepton control region) in the muon channel

The second step is the definition of the three regions using p_T binning of the reconstructed muon candidate. Table 8.11 shows the initial number of events without OS-gSS subtraction. Considering all conditions the following number of events and values for the SS-rescaling factors are obtained and summarised in Tab. 8.12. The summarised values for the efficiency

η **region**	N^{OS-gSS}_{pre-ID}	$N^{OS-gSS}_{post-ID}$	g_{pre-ID}	$g_{post-ID}$	ε
-3–0	302±17	132±11	1.05±0.02	1.34±0.02	0.44±0.03
0–1	110±10	46±7	0.96±0.01	1.68±0.03	0.43±0.05
1–3	136±12	59±8	1.15±0.02	1.21±0.02	0.44±0.04

Table 8.10: *The number of OS-gSS events for pre-ID and post-ID for η binning in the muon channel. The uncertainties for the rescaling factors g_i consider the allowed interval for all requirements. The offset is not exactly but in the order of 0. Slightly different combinations of rescaling factors on pre-ID and post-ID level can be possible.*

Tau control region				
p_T **region [GeV]**	N^{OS}_{pre-ID}	N^{SS}_{pre-ID}	$N^{OS}_{post-ID}$	$N^{SS}_{post-ID}$
18–22 and 44–60	733±27	555±24	96±10	25±5
22–37	910±30	603±25	154±12	22±5
15–18 and 37–44	710±27	546±23	93±10	30±5
Lepton control region				
p_T **region [GeV]**	N^{OS}_{pre-ID}	N^{SS}_{pre-ID}	$N^{OS}_{post-ID}$	$N^{SS}_{post-ID}$
19–22	508±23	357±19	77±9	16±4
22–39	656±26	428±21	131±11	21±5
15–19 and 39–60	1163±34	907±30	133±12	40±6

Table 8.11: *The number of OS and SS events for pre-ID and post-ID for the $p_T(\tau)$ binning (top) and the $p_T(\ell)$ binning (bottom) in the muon channel.*

Tau control region					
p_T **[GeV]**	N^{OS-gSS}_{pre-ID}	$N^{OS-gSS}_{post-ID}$	g_{pre-ID}	$g_{post-ID}$	ε
18–22 and 44–60	161±13	68±8	1.03±0.01	1.10±0.03	0.42±0.04
22–37	267±16	118±11	1.05±0.02	1.61±0.02	0.44±0.05
15–18 and 37–44	109±10	48±7	1.11±0.02	1.49±0.02	0.44±0.05
Lepton control region					
p_T **[GeV]**	N^{OS-gSS}_{pre-ID}	$N^{OS-gSS}_{post-ID}$	g_{pre-ID}	$g_{post-ID}$	ε
19–22	115±11	51±7	1.11±0.01	1.58±0.02	0.45±0.05
22–39	249±16	107±10	0.95±0.02	1.12±0.02	0.43±0.03
15–19 and 39–60	165±13	77±8	1.11±0.01	1.43±.02	0.47±0.04

Table 8.12: *The number of OS-gSS events for pre-ID and post-ID for $p_T(\tau)$ binning and the $p_T(\ell)$ binning in the muon channel. The uncertainties for the rescaling factors g_i consider the allowed interval for all requirements. The offset is not exactly but in the order of 0. Slightly different combinations of rescaling factors on pre-ID and post-ID level can be possible.*

are:

$$\varepsilon_{\text{fit}} = 0.45 \pm 0.06 \,\text{and}\, \varepsilon_{\text{calculated}} = 0.44 \pm 0.02 \tag{8.20}$$

for the tau control region and

$$\varepsilon_{\text{fit}} = 0.42 \pm 0.07 \,\text{and}\, \varepsilon_{\text{calculated}} = 0.45 \pm 0.02 \tag{8.21}$$

for the lepton control region. The cross check to avoid multiple solutions is

$$\mathrm{N}_\eta : \mathrm{N}_{\mathrm{p_T}}(\tau) = (548 \pm 23) : (537 \pm 23). \tag{8.22}$$

On post-ID level the relation is

$$\mathrm{N}_\eta : \mathrm{N}_{\mathrm{p_T}}(\tau) = (237 \pm 15) : (234 \pm 15). \tag{8.23}$$

Region	$(\frac{\mathrm{N^{taucontrol}}}{\mathrm{N^{leptoncontrol}}})^{\mathrm{lin.App.}}$ **pre-ID**	$(\frac{\mathrm{N^{taucontrol}}}{\mathrm{N^{leptoncontrol}}})^{\mathrm{lin.App.}}$ **post-ID**	$(\frac{\mathrm{N^{taucontrol}}}{\mathrm{N^{leptoncontrol}}})^{\mathrm{MC}}$
R1	161/115= 1.39±0.17	68/51= 1.33±0.25	1.52±0.13
R2	267/249= 1.07±0.09	118/107= 1.10±0.15	1.16±0.09
R3	109/165= 0.66±0.08	48/77= 0.62±0.11	0.65±0.11

Table 8.13: *The number of events for each region on pre-ID level as well as the relative numbers in comparison with MC truth prediction.*

The numbers are consistent among each other.

Table 8.8 shows the comparison of tau control and lepton control region for pre-ID and post-ID level. The MC values are obtained from a truth signal sample. The identification efficiency estimated for all three steps is

$$\bar{\varepsilon} = \frac{1}{6}(0.44 + 0.45 + 0.42)^{\mathrm{fit}} + (0.44 + 0.44 + 0.45)^{\mathrm{calc.}} = \\ 0.44 \pm 0.05^{\mathrm{fit}} \pm 0.02^{\mathrm{syst.}}. \tag{8.24}$$

The uncertainty from the fit includes the statistical uncertainty as well as the effects from the fit performance. The systematic uncertainty includes the effects from the Δy offset, the difference for the individual efficiencies for the sub regions and the MC to data calibration for the correct binning in η and $\mathrm{p_T}$.

The full procedure for the linear approximation for `cut based medium` identification cuts for one prong and multi prong τ-lepton candidates, medium veto against electrons, for a $\mathrm{p_T}(\tau_h)$ range of [15–60] GeV. The number of signal events expected with the linear approximation are

$$\mathrm{N^{electron}} = 160 \pm 10 \,\mathrm{and}\, \mathrm{N^{muon}} = 237 \pm 15. \tag{8.25}$$

The expected number of signal events estimated for the electron channel and the muon channel (see Chapt. 7 is

$$\mathrm{N^{electron}} = 171 \pm 21 \,\mathrm{and}\, \mathrm{N^{muon}} = 222 \pm 27. \tag{8.26}$$

The values agree within the uncertainty.

Finally, the common efficiency for the electron and the muon channel can be expressed as

$$\varepsilon_{\mathrm{all}} = \frac{1}{2}(0.43 + 0.44) = 0.44 \pm 0.04^{\mathrm{fit}} \pm 0.02^{\mathrm{syst.}}. \tag{8.27}$$

The value obtained from a regular MC truth estimation is

$$\varepsilon_{\mathrm{MC}} = 0.42 \pm 0.02. \tag{8.28}$$

The values agree within the statistical and systematic uncertainty.

8.4.1 Visible mass shape correction for the electron channel

In Sec. 7.10 the visible mass distributions are shown. For the electron channel (see Fig. 7.27(a)) the measured data as well as the QCD background is over-estimated or under-estimated for different bins. This is due to the global rescaling factor for the QCD background (see Sec. 7.7.3). which does not take into account the different $R_{OS/SS}$ for different p_T bins.

For the linear approximation procedure described in previous sections, the η and the p_T binning was used. For the correction of the visible mass shape, the regions R1, R2, and R3 are binned in $m_{vis}(\tau_h, \tau_\ell)$. The current statistic limits the width of these regions. The current bin regions are:

- R1=[37-40] GeV, R2=[40-44] GeV, R3=[44-50] GeV

and

- R1=[50-54] GeV, R2=[54-58] GeV, R3=[58-75] GeV.

Assuming that the efficiency estimated with the linear approximation is correct, and the ratio $R_{OS/SS}$ for the QCD on pre-ID level is in the order of $\mathcal{O} = 1 \pm 0.01$ results in separate rescaling factors g for each binning defined above.

The rescaled visible mass for the electron channel is shown in Fig. 8.11.

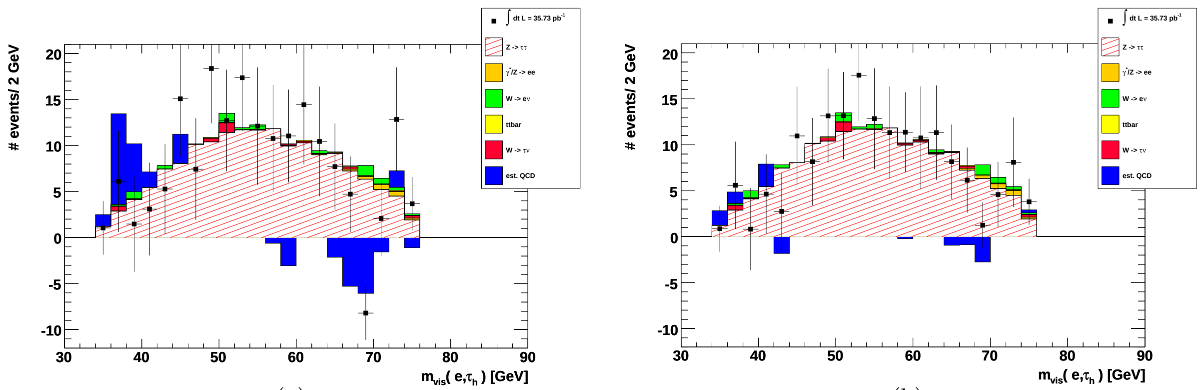

(a) (b)

Figure 8.11: *The visible mass for the electron channel with the global rescaling factor g estimated with the ABCD method (see Sec. 7.7.3) in (a) and for the bin-corrected rescaling factors g estimated with the linear approximation technique (b).*

8.5 Cross section measurements for Z $\rightarrow \tau_h\tau_\ell$

Since the linear approximation provides a good background suppression on pre-ID level, the method can also be used for cross section estimation for the semi-leptonic Z $\rightarrow \tau_h\tau_\ell$ decay.

The general definition of the cross section is [114]

$$\sigma(Z\tau\tau) \times BR(\tau \rightarrow \ell\nu\nu, \tau \rightarrow \tau_h\nu) = \frac{N_{obs} - N_{bkg}}{C_Z A_Z \mathcal{L}} \tag{8.29}$$

with the number of observed events N_{obs}, the number of background events N_{bkg} and the integrated luminosity $\mathcal{L}$. The kinematic and geometric acceptance is denoted as A_Z (obtained from [114]). This is required in order to compare the estimated cross section with theoretical cross sections on Born level for an invariant mass region of [66,116] GeV. By construction the factor A_Z includes a correction for events that migrate from outside the invariant mass window in the fiducial cuts. The used MC samples [120] have a lower mass bound of 10 GeV for the invariant mass. For that reason the sample includes a tail of low-mass $\gamma^\star/Z$ events from outside the Z-mass peak. The difference for electron and muon channel selection is due to the crack region in the calorimeter for the electron selection.

The fiducial cross section is defined as

$$\sigma(Z\tau\tau) \times BR(\tau \to \ell\nu\nu, \tau \to \tau_h\nu) = \frac{N_{obs} - N_{bkg}}{C_Z \mathcal{L}} \tag{8.30}$$

without the acceptance correction A_Z. The value C_Z denotes the full efficiency for a selection of a $Z \to \tau_h \tau_\ell$ event. This includes all different variables discussed in Eq. 8.2. The strategy is to define C_Z as the number of full selected $Z \to \tau_h \tau_\ell$ events divided by $Z \to \tau_h \tau_\ell$ event candidates only lepton triggered. The estimated cross section has to be rescaled considering the lepton (e or μ) selection using the efficiencies for the lepton trigger, reconstruction, and identification.

With the assumption that the event cleaning and quality criteria does not affect the selection significantly, the lowest level for the $Z \to \tau_h \tau_\ell$ event selection is the lepton trigger. The trigger efficiency (and the corresponding uncertainty) has to be obtained from lepton trigger performance groups [114].

To avoid double counting of events it is required to have exact one τ-lepton and one lepton candidate. The strategy is to define the ratio of full selected $Z \to \tau_h \tau_\ell$ events over triggered $Z \to \tau_h \tau_\ell$ events[5)].

$$C_Z = \frac{N^{post-ID}_{Z\to\tau\tau}}{N^{trigger}_{Z\to\tau\tau}}. \tag{8.31}$$

8.5.1 Cross section determination using the linear approximation

The estimation of the cross section using linear approximation is defined along the lines of the general description.

Step 1: η binning for the reconstructed τ-lepton

The first step is the definition of the three regions using η binning. The same conditions as for the τ-lepton efficiency estimation will be used.

Table 8.14 shows the initial number of events without OS-gSS subtraction. Again, the conditions which have to be fulfilled are:

5) Note that also the τ-lepton identification cut can be applied on the triggered events in order to reduce the background. The τ_h ID lepton efficiency can be estimated as described in the previous section. This study does not considers this additional cut in order to avoid effects from the τ_h identification efficieny estimation.

	Electron channel		**Muon channel**	
η **region**	$N^{OS}_{trigger}$	$N^{SS}_{trigger}$	$N^{OS}_{trigger}$	$N^{SS}_{trigger}$
-3–0	95106±308	86725±294	211219 ±460	192924±439
0–1	36250±190	32726±181	82057±286	74036±272
1–3	48634±221	45195±213	105994±326	98228±313

Table 8.14: *The raw number of events after trigger selection for the electron and the muon channel.*

	Electron channel			**Muon channel**		
η **region**	$N^{OS-gSS}_{trigger}$	$g_{trigger}$	ε	$N^{OS-gSS}_{trigger}$	$g_{trigger}$	ε
-3–0	584±24	1.09±0.02	0.14±0.01	724±27	1.05±0.02	0.21±0.02
0–1	316±18	1.10±0.02	0.16±0.02	302±17	1.06±0.02	0.21±0.02
1–3	225±15	1.07±0.01	0.15±0.02	320±18	1.04±0.02	0.22±0.02

Table 8.15: *The selected number of events after OS-gSS subtraction on trigger level for both lepton channels.*

- The offset $y \pm \Delta y$ has to be in the order of $\mathcal{O}$=0.
- The efficiency for each sub-region has to be the same.
- The value from the fit has to be in the same order as the calculated value.

Considering all these conditions the following number of events and values for the SS-rescaling factors are obtained and shown in Tab. 8.15.

Step 2: p_T binning for the reconstructed τ-lepton (tau control region) and the reconstructed lepton (lepton control region)

The second step is the definition of the three regions using p_T binning of the reconstructed τ-lepton candidate. Table 8.16 shows the initial number of events without OS-gSS subtraction. Considering all conditions the following number of events and values for the SS-rescaling factors are obtained and summarised in Tab. 8.17 while Tab. 8.18 shows the number of events for the tau control region and the lepton control region. It can be seen that a good background suppression can be reached with the OS-gSS rescaling. The values for the η binning, tau control region and lepton control region are summarised in Tab. 8.19

Measured total cross section

As described above the total cross section is defined as

$$\sigma(Z\tau\tau) \times BR(\tau \rightarrow \ell\nu\nu, \tau \rightarrow \tau_h\nu) = \frac{N_{obs} - N_{bkg}}{C_Z A_Z \mathcal{L}}. \tag{8.32}$$

The trigger efficiency is estimated using a tag and probe method [114] and is summarised in Tab. 8.21.

Tau control region	**Electron channel**		**Muon channel**	
p_T **region [GeV]**	$N^{OS}_{trigger}$	$N^{SS}_{trigger}$	$N^{OS}_{trigger}$	$N^{SS}_{trigger}$
	49980±224	44846±211	126257±355	121363±348
	76857±277	71710±267	177294±421	167359±409
	40825±202	37325±193	90030±300	88194±297
Lepton control region	**Electron channel**		**Muon channel**	
p_T **region [GeV]**	$N^{OS}_{trigger}$	$N^{SS}_{trigger}$	$N^{OS}_{trigger}$	$N^{SS}_{trigger}$
	38411±196	35941±190	102399±320	98733±314
	37861±195	32996±182	90130±300	85676±293
	100380±317	93348±306	269519±519	256511±506

Table 8.16: *The raw number of events after trigger selection for the electron and the muon channel.*

Tau CR	**Electron channel**			**Muon channel**		
p_T **[GeV]**	$N^{OS-gSS}_{trigger}$	$g_{trigger}$	ε	$N^{OS-gSS}_{trigger}$	$g_{trigger}$	ε
R1	308±18	1.11±0.01	0.15±0.02	318±18	1.04±0.01	0.22±0.02
R2	536±23	1.06±0.02	0.15±0.02	541±23	1.06±0.02	0.22±0.02
R3	281±17	1.09±0.01	0.15±0.02	222±15	1.02±0.01	0.22±0.03
Lepton CR	**Electron channel**			**Muon channel**		
p_T **[GeV]**	$N^{OS-gSS}_{trigger}$	$g_{trigger}$	ε	$N^{OS-gSS}_{trigger}$	$g_{trigger}$	ε
R1	194±14	1.06±0.02	0.15±0.03	232±15	1.03±0.02	0.22±0.03
R2	438±21	1.13±0.02	0.15±0.02	487±22	1.05±0.02	0.22±0.02
R3	470±22	1.07±0.02	0.15±0.02	362±19	1.05±0.02	0.21±0.02

Table 8.17: *The selected number of events after OS-gSS subtraction for trigger selection.*

Region	$(\frac{N^{taucontrol}}{N^{leptoncontrol}})^{lin.App.}_{electron}$	$(\frac{N^{taucontrol}}{N^{leptoncontrol}})^{lin.App.}_{muon}$	$(\frac{N^{taucontrol}}{N^{leptoncontrol}})^{MC}$
R1	308/194 = 1.58±0.15	318/232 = 1.37±0.12	1.52±0.13
R2	543/433 = 1.25±0.08	541/487 = 1.11±0.07	1.16±0.09
R3	275/473 = 0.58±0.04	222/362 = 0.61±0.05	0.65±0.11

Table 8.18: *The number of events for tau control as well lepton control region in comparison with MC truth prediction.*

Region	**Electron channel**	**Muon channel**
η	0.148±0.019	0.214±0.021
Tau control region	0.15±0.02	0.22±0.02
Lepton control region	0.15±0.02	0.22±0.02
$\sum$	0.15±0.02	0.22±0.02

Table 8.19: *The overall efficiency C_Z for both channels.*

	Electron channel	Muon channel
N_{events}	171±13(stat.)±8(syst.)	222±15(stat.)±12(syst.)
C_Z	0.15±0.19	0.22±0.02
A_Z	0.1017±0.0049±0.0031	0.1169±0.0055±0.035
$\mathcal{L}$	35.75±1.22	35.51±1.21

Table 8.20: *The number of events estimated with the different binning, the acceptance A_Z obtained from [114] and the luminosity [121].*

Trigger	$\mathrm{p_T}$ **[GeV]**	**Efficiency**
`EF_e15_medium`	[16,18]	95.8±2.2(stat.)±0.6(syst.)
`EF_e15_medium`	[18,20]	96.5±2.1(stat.)±0.4(syst.)
`EF_e15_medium`	[>20]	99.05±0.22(stat.)±0.08(syst.)
`EF_mu10_MG`	[>15]	82.9±0.09(stat.)±0.3(syst.)
`EF_mu13_MG`	[>15]	84.5±0.04(stat.)±0.1(syst.)
`EF_mu13_MG_tight`	[>15]	83.1±0.4(stat.)±0.2(syst.)

Table 8.21: *Lepton trigger efficiencies estimated with a tag and probe method in the $Z \rightarrow \ell\ell$ channel.*

The production cross section is

$$\begin{aligned}\sigma(\mathrm{Z} \rightarrow \tau\tau) \times \mathrm{BR}(\mathrm{Z} \rightarrow \tau_{\mathrm{h}}\tau_{\mathrm{e}}) = \frac{\mathrm{N_{obs}} - \mathrm{N_{bkg}}}{\mathrm{C_Z A_Z}\mathcal{L}}\mathrm{F_c} = \frac{171}{35.75 \times 0.1017 \times 0.15} \times 0.77 = \\ (241 \pm 26(\mathrm{stat.}) \pm 31(\mathrm{syst.}) \pm 7(\mathrm{lumi.}))\,\mathrm{pb}\end{aligned} \tag{8.33}$$

for the electron channel and

$$\begin{aligned}\sigma(\mathrm{Z} \rightarrow \tau\tau) \times \mathrm{BR}(\mathrm{Z} \rightarrow \tau_{\mathrm{h}}\tau_{\mu}) = \frac{\mathrm{N_{obs}} - \mathrm{N_{bkg}}}{\mathrm{C_Z A_Z}\mathcal{L}}\mathrm{F_c}\frac{223}{35.75 \times 0.1169 \times 0.22} \times 0.75 = \\ (191 \pm 21(\mathrm{stat.}) \pm 38(\mathrm{syst.}) \pm 10(\mathrm{lumi.}))\,\mathrm{pb}\end{aligned} \tag{8.34}$$

for the muon channel. The correction factor $\mathrm{F_c}$ is explained in Sec. 8.5.2.

Measured fiducial cross section

Without considering the acceptance A_Z the fiducial cross section can be estimated as

$$\begin{aligned}\sigma(\mathrm{Z} \rightarrow \tau\tau) \times \mathrm{BR}(\mathrm{Z} \rightarrow \tau_{\mathrm{h}}\tau_{\mathrm{e}}) = \frac{\mathrm{N_{obs}} - \mathrm{N_{bkg}}}{\mathrm{C_Z}\mathcal{L}} \times \mathrm{F_c} = \frac{171}{35.75 \times 0.15} \times 0.77 = \\ (24.26 \pm 3.1(\mathrm{stat.}) \pm 5.3(\mathrm{syst.}) \pm 0.8(\mathrm{lumi.}))\,\mathrm{pb}\end{aligned} \tag{8.35}$$

for the electron channel and

$$\begin{aligned}\sigma(\mathrm{Z} \rightarrow \tau\tau) \times \mathrm{BR}(\mathrm{Z} \rightarrow \tau_{\mathrm{h}}\tau_{\mu}) = \frac{\mathrm{N_{obs}} - \mathrm{N_{bkg}}}{\mathrm{C_Z}\mathcal{L}} \times \mathrm{F_c} = \frac{223}{35.75 \times 0.22} \times 0.71 = \\ (22.22 \pm 4.02(\mathrm{stat.}) \pm 4.2(\mathrm{syst.}) \pm 1.1(\mathrm{lumi.}))\,\mathrm{pb}\end{aligned} \tag{8.36}$$

for the muon channel.

Without the acceptance A_Z the cross section is independent from the phase extrapolation and therefore less affected by theoretical uncertainties. The fiducial regions are defined by the following cuts [114]:

- Electron: $p_T > 16\,\text{GeV}$ and $|\eta| < 2.47$ (excluding $1.37 < |\eta| < 1.52$)
- Tau: $E_T > 20\,\text{GeV}$ and $|\eta| < 2.47$ (excluding $1.37 < |\eta| < 1.52$)
- Event: $\sum \cos\Delta\phi >$ -0.15, $m_T(\ell, E_T^{miss}) < 50\,\text{GeV}$, $35\,\text{GeV} < m_{vis} < 75\,\text{GeV}$

for the electron channel and

- Muon: $p_T > 15\,\text{GeV}$ and $|\eta| < 2.4$
- Tau: $E_T > 20\,\text{GeV}$ and $|\eta| < 2.47$ (excluding $1.37 < |\eta| < 1.52$)
- Event: $\sum \cos\Delta\phi >$ -0.15, $m_T(\ell, E_T^{miss}) < 50\,\text{GeV}$, $35\,\text{GeV} < m_{vis} < 75\,\text{GeV}$

for the muon channel.

Inclusive cross section

Using the corrected branching ratios [122]

- BR $(\tau \to e\nu\nu, \tau \to \text{had}\nu) = 0.22495 \pm 0.00074$

for the electron channel and

- BR $(\tau \to \mu\nu\nu, \tau \to \text{had}\nu) = 0.23130 \pm 0.00074$

for the muon channel, the inclusive cross section can be estimated

$$\sigma(Z\tau\tau, m_{inv}[66, 116]\,\text{GeV}) = (1041 \pm 123(\text{stat.}) \pm 212(\text{syst.}) \pm 40(\text{lumi.}) \pm 4(\text{theo.}))\,\text{pb} \tag{8.37}$$

for the electron channel and

$$\sigma(Z\tau\tau, m_{inv}[66, 116]\,\text{GeV}) = (845 \pm 102(\text{stat.}) \pm 167(\text{syst.}) \pm 30(\text{lumi.}) \pm 3(\text{theo.}))\,\text{pb} \tag{8.38}$$

for the muon channel.

8.5.2 Systematic uncertainties for the cross section measurements with the linear approximation technique

The theoretical uncertainties on the cross section are taken from [123] and considers both the Z and the $\gamma^\star$ processes in combination.

The experimental uncertainties consider the uncertainty of the luminosity which is in the order of 3.4% [121].

Lepton trigger efficiencies were taken with a tag and probe method [124]. The corresponding uncertainties are summarised in Tab. 8.21.

The uncertainty for the OS-gSS rescaling is related to the factor $g \pm \Delta g$ which affects the measured number of events $N_{obs} \pm \Delta N_{obs}$.

Furthermore, the charge mis-identification for the τ-lepton candidates affects the OS-gSS rescaling. Charge mis-identification is dominated by two effects:

- One-prong decays migrate to three-prong decays due to photon conversions or tracks from underlying events.
- An inefficient track reconstruction can identify three-prong decays as one-prong decays.

With additional quality criteria the overall charge mis-identification can be further reduced. On trigger or reconstruction level the rate is below 3.6% [125].

The used data samples were skimmed by requiring one electron with $p_T > 10\,\mathrm{GeV}$, $|\eta| < 3$, author 1 or 3, medium_withTrackMatch or one muon from either muid or mustaco with $p_T > 10\,\mathrm{GeV}$, $|\eta| < 3$, and `isCombined` and a τ-lepton with $E_T > 15\,\mathrm{GeV}$ and $|\eta| < 3$. For that reason the lepton reconstruction and identification efficiency as well as the τ-lepton reconstruction efficiency have to be considered.

The correction factor for the cross section is

$$F_c = n_{(\text{trigger})} \cdot n_{(\text{tau reconstruction efficiency})} \cdot n_{(\text{mis-ident.})} \cdot n_{(\text{lepton efficiency})} \tag{8.39}$$

is $F_c = 0.77 \pm 0.06$ for the electron channel and $F_c = 0.71 \pm 0.08$ for the muon channel with (see [116] and [126]):

- $n_{(\text{trigger})} = 0.95 \pm 0.02$ for the electron channel and 0.85 ± 0.01 for the muon channel [126].
- $n_{(\text{lepton efficiency})} = 0.86 \pm 0.09$ for the electron channel [127] and 0.94 ± 0.09 for the muon channel.
- $n_{(\text{charge mis-ident.})} = 0.99 \pm 0.01$ for both channels
- $n_{(\text{tau reconstruction efficiency})} = 0.95 \pm 0.04$ (see Sec. 8.6.4).

Systematic effects for the acceptance A_Z:

- The theoretical uncertainty on the acceptance is dominated by the limited knowledge of the proton PDFs [128].
- Furthermore, the modelling of the Z-boson production is not well known at LHC, the QED radiation as well as the τ-lepton decay modelling can affect the systematic uncertainty on the acceptance A_Z. The QED radiation is modelled by PHOTOS [129] and the τ-lepton decay is modelled by TAUOLA [130].

8.6 Substitution of $Z \rightarrow \mu\mu$ events into $Z \rightarrow \tau_h\tau_\ell$ events

As discussed in Chapt. 7 the $Z \rightarrow \tau_h\tau_\ell$ signal is expected to be overlain by non precisely predictable QCD background. For that reason and because of the fact that the number

$\mathrm{N}^{\mathrm{produced}}_{\mathrm{Z}\to\tau_{\mathrm{h}}\tau_{\ell}}$ of produced $\mathrm{Z} \to \tau_{\mathrm{h}}\tau_{\ell}$ events is not known in data, these number will be replaced by (from data selected) $\mathrm{Z} \to \mathrm{ee}$ or $\mathrm{Z} \to \mu\mu$ events[6)] . From previous experiments (e.g. LEP) we know that the decay of the Z-boson into these three lepton channels has equal widths, corrected with the corresponding branching ratios.

As expressed in Eq. 8.40 there a three types of variables. The branching ratios (BR) are precisely known from literature. The lepton related trigger, reconstruction, and identification efficiencies have to be obtained from lepton performance groups. All numbers of events as well as the kinematic efficiencies have to be measured from data. It is not necessary to know any initial number of produced $\mathrm{Z} \to \tau\tau$ or $\mathrm{Z} \to \ell\ell$ events.

Furthermore, the ratio $\mathrm{R}_{\mathrm{kin}} = \frac{\varepsilon^{\mathrm{kin}}_{\mathrm{Z}\to\ell\ell}}{\varepsilon^{\mathrm{kin}}_{\mathrm{Z}\to\tau_{\mathrm{h}}\tau_{\ell}}}$ in Eq. 8.41 allows to get the background uncertainty under control. The kinematic[7)] selection of the lepton from $\mathrm{Z} \to \ell\ell$ and the kinematic selection of the hadronically decaying τ-lepton as well as the lepton from the leptonic decay, are the same. The $\mathrm{Z} \to \ell\ell$ channel allows to investigate the kinematic behaviour of leptons in the detector. Therefore, only the value of $\mathrm{R}_{\mathrm{kin}}$ is necessary and not the kinematic efficiencies individually. For the following discussion the notation `pre-ID` is changed into `trigger`, `kin` or `reco`.

A substitution of $\mathrm{N}^{\mathrm{produced}}_{\mathrm{Z}\to\tau_{\mathrm{h}}\tau_{\ell}}$ with

$$\mathrm{N}^{\mathrm{post-ID}}_{\mathrm{Z}\to\ell\ell} \times \frac{\mathrm{BR}_{\mathrm{Z}\to\ell\ell}}{\varepsilon^{\mathrm{kin}}_{\mathrm{Z}\to\ell\ell} \times (\varepsilon^{\ell}_{\mathrm{ID}} \times \varepsilon^{\ell}_{\mathrm{reco}})^2 \times (1-(1-\varepsilon^{\ell}_{\mathrm{trigger}})^2) \times \mathrm{BR}_{\mathrm{Z}\to\tau_{\mathrm{h}}\tau_{\ell}}} \tag{8.40}$$

expresses the hadronic reconstruction and identification efficiency as:

$$\varepsilon^{\tau_{\mathrm{h}}}_{\mathrm{ID}} \times \varepsilon^{\tau_{\mathrm{h}}}_{\mathrm{reco}} = \frac{\varepsilon^{\mathrm{kin}}_{\mathrm{Z}\to\ell\ell}}{\varepsilon^{\mathrm{kin}}_{\mathrm{Z}\to\tau_{\mathrm{h}}\tau_{\ell}}} \times \frac{\mathrm{N}^{\mathrm{post-ID}}_{\mathrm{Z}\to\tau_{\mathrm{h}}\tau_{\ell}} \times \mathrm{BR}_{\mathrm{Z}\to\ell\ell}}{\mathrm{N}^{\mathrm{post-ID}}_{\mathrm{Z}\to\ell\ell} \times 2 \times \mathrm{BR}_{\tau\to\mathrm{lep}} \times \mathrm{BR}_{\tau\to\mathrm{had}} \times \mathrm{BR}_{\mathrm{Z}\to\tau\tau}} \times \mathrm{F}(\varepsilon^{\ell}_{\mathrm{n}}) \tag{8.41}$$

with

- $\varepsilon^{\mathrm{kin}}_{\mathrm{Z}\to\ell\ell}$: probability to find $\mathrm{Z} \to \ell\ell$ decays with kinematic cuts only.
- $\mathrm{F}(\varepsilon^{\ell}_{\mathrm{n}}) = \varepsilon^{\ell}_{\mathrm{ID}} \times \varepsilon^{\ell}_{\mathrm{reco}} \times \frac{1-(1-\varepsilon^{\ell}_{\mathrm{trigger}})^2}{\varepsilon^{\ell}_{\mathrm{trigger}}}$ denotes the lepton related efficiencies.
- $\frac{1-(1-\varepsilon^{\ell}_{\mathrm{trigger}})^2}{\varepsilon^{\ell}_{\mathrm{trigger}}}$ is related to the fact that for the $\mathrm{Z} \to \ell\ell$ selection only one lepton has to be triggered which increases the probability to trigger those events compared with the one lepton in semi-leptonic $\mathrm{Z} \to \tau_{\mathrm{h}}\tau_{\ell}$ channel.

To determine $\varepsilon^{\mathrm{kin}}_{\mathrm{Z}\to\ell\ell}/\varepsilon^{\mathrm{kin}}_{\mathrm{Z}\to\tau\tau}$ the selection of $\mathrm{Z} \to \ell\ell$ events is implemented, which is closely along the lines of the $\mathrm{Z} \to \tau\tau$ selection of Chapt. 7.

The following cuts are used:

- $\mathrm{N}_{\mu} = 2$ or $\mathrm{N}_{\mathrm{e}} = 2$
- Isolation criteria:

[6)] $\mathrm{Z} \to \mathrm{ee}$ or $\mathrm{Z} \to \mu\mu$ events will be often denoted as $\mathrm{Z} \to \ell\ell$.

[7)] As mentioned previously, the kinematic selection contains all cuts applied on triggered and reconstructed leptons as well as reconstructed τ-leptons.

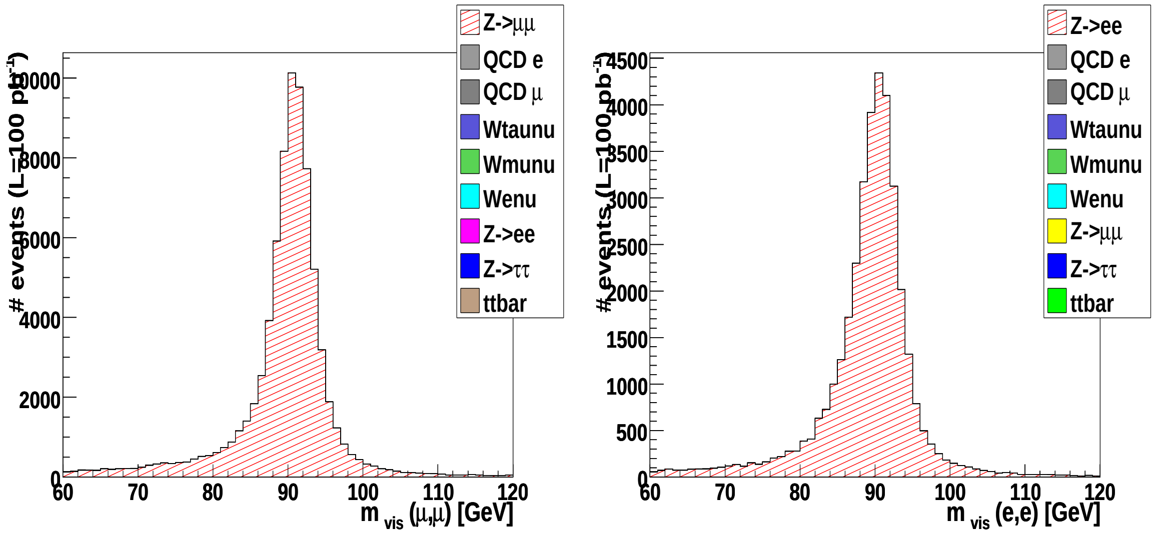

(a) $\mathrm{Z} \to \mu\mu$ (b) $\mathrm{Z} \to \mathrm{ee}$

Figure 8.12: *Visible mass after OS-SS subtraction for* $\mathrm{Z} \to \ell\ell$ *normalised to* $\mathcal{L} = 100\ pb^{-1}$.

  - for muons: `nucone40` < 1 and `etcone40`$/p_{\mathrm{T}}(\mu) < 0.1$
  - for electrons: `nucone40` < 1 and `etcone30`$/p_{\mathrm{T}}(e) < 0.12$

- `isEM = medium` instead of `isEM = tight`
- $\mathrm{p_T} > 20\,\mathrm{GeV}$ for muons and $\mathrm{p_T} > 15\,\mathrm{GeV}$ for electrons
- $\mathrm{m_T}(\ell, \mathrm{E_T^{miss}}) < 40\,\mathrm{GeV}$
- $|\ \mathrm{Charge}(\ell)\ | = 1$
- $85\,\mathrm{GeV} < \mathrm{m_{vis}}(\ell\ell) < 95\,\mathrm{GeV}$
- $0.9 < \Delta\Phi(\ell, \ell) < 3.1$

The tighter $\mathrm{p_T}$ cut for muons compared with the original $\mathrm{p_T} > 15\,\mathrm{GeV}$ cut is motivated by the muon trigger efficiency which becomes flat for $\mathrm{p_T}$ above 20 GeV. This cut is also implemented in the $\mathrm{Z} \to \tau\tau$ channel. Since the semi-leptonic $\mathrm{Z} \to \tau\tau$ analysis is sensitive to the lepton selection the number of events decreases compared with Chapt. 7. The results of the $\mathrm{Z} \to \mathrm{ee}$ and $\mathrm{Z} \to \mu\mu$ selections (including the data-driven corrections for OS-SS asymmetries, see Chapt. 7) and including the full SM background can be observed in Fig. 8.12. A very clean sample is obtained for $\mathrm{Z} \to \ell\ell$. Since the number of events is not similar for $\mathrm{Z} \to \tau_{\mathrm{h}}\tau_\ell$ and $\mathrm{Z} \to \ell\ell$, it is obvious that $\varepsilon^{\mathrm{kin}}_{\mathrm{Z}\to\ell\ell}/\varepsilon^{\mathrm{kin}}_{\mathrm{Z}\to\tau_{\mathrm{h}}\tau_\ell}$ is not close to 1. This is due to the required combination of a lepton candidate and a τ-lepton candidate which decreases the number of events compared with $\mathrm{Z} \to \ell\ell$.

8.6.1 Introduction of the embedding technique

To determine the systematic uncertainty of the kinematic ratio $\varepsilon^{\mathrm{kin}}_{\mathrm{Z}\to\ell\ell}/\varepsilon^{\mathrm{kin}}_{\mathrm{Z}\to\tau_{\mathrm{h}}\tau_\ell}$ a method which replaces reconstructed muons from $\mathrm{Z} \to \mu\mu$ with τ-leptons will be discussed. Note

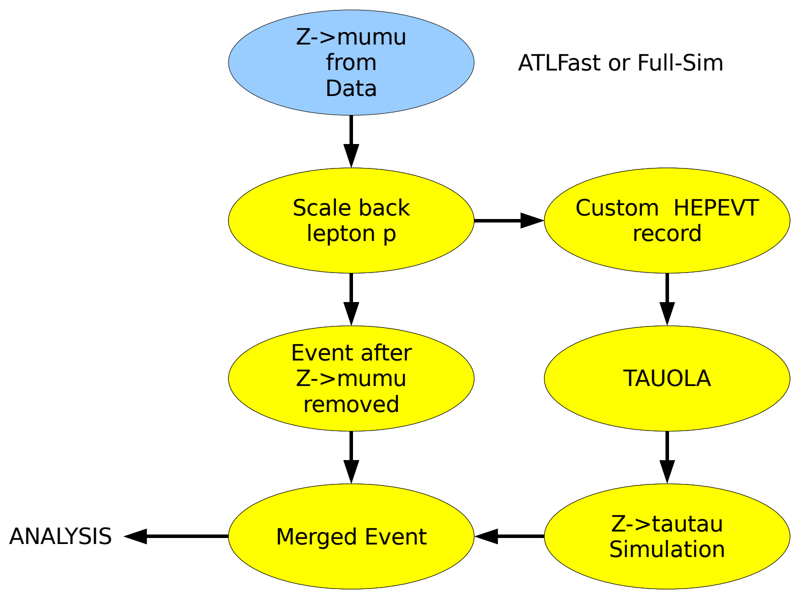

Figure 8.13: *The general scheme of the Embedding technique.*

that the embedding technique is only available for the Z → $\mu\mu$ channel but not for Z → ee.

Although the embedding is still Monte Carlo based, it has significant advantages compared with a pure MC based analysis. The first aspect is the kinematic of the Z-boson. Since the embedding uses real Z-bosons obtained from the Z → $\mu\mu$ channel, uncertainties coming from the simulation of the Z-boson properties, can be reduced. The kinematic of leptons from Z → $\ell\ell$ decay can be assumed as equal as for the τ-leptons from Z → $\tau\tau$. The differences appears when the τ-lepton decays. Due to the fast decay (still in the beam pipe line) τ-lepton decays are accompanied by a large $\mathrm{E}_{\mathrm{T}}^{\mathrm{miss}}$ contribution.

The general procedure (illustrated in 8.6.1) of converting Z → $\mu\mu$ into Z → $\tau\tau$ events can be divided into four basic steps [131]:

- Z-boson decay identification: the two muons of the Z-boson decay are selected.
- Replacement of the Z → $\mu\mu$ decay with Z → $\tau\tau$ Monte Carlo decay:
  - Replacement of muons with τ-leptons, with the $\mathrm{p_T}$ of the Z-boson decay daughters changed to take into account the larger mass of the τ-lepton. A correction factor $\frac{\mathrm{E}_{\ell}-\mathrm{m}_{\tau}}{\mathrm{p}_{\ell}^{2}}$ is applied to correct the transverse momentum.
  - The decay of the τ-leptons to $Z \to \tau\tau \to \ell\tau_h$ is performed by TAUOLA [132].
  - The re-simulation and reconstruction of the $Z \to \tau\tau \to \ell\tau_h$ process is executed.
- Embedding: the Z → $\mu\mu$ decay in the original event is replaced by the Z → $\tau\tau$ event using calorimeter cell and track information:

- The calorimeter cells in a cone around the muons from the $Z \rightarrow \mu\mu$ decay are replaced by the corresponding calorimeter cells from simulated $Z \rightarrow \tau\tau$ decay (replace the energy and timing information). All track segments in the muon spectrometer inside a certain cone around the original muons are deleted and the track segments in the muon spectrometer of the $Z \rightarrow \tau\tau$ decay, within the same cone are inserted into the original event.

- Re-reconstruction with the new embedded cells and track information.

The missing energy E_T^{miss} must be recalculated because of the additional neutrinos present in the τ-lepton decays. Because the same number of input events is used for this technique, the ratio $\frac{\varepsilon^{kin}_{Z\rightarrow\mu\mu}}{\varepsilon^{kin}_{Z\rightarrow\tau-h\tau_\ell}}$ is given by $\frac{N^{kin}_{Z\rightarrow\mu\mu}}{N^{kin}_{Z\rightarrow\tau_h\tau_\ell}}$. With the embedding method the systematic uncertainties for the kinematic efficiency cancel, but the trigger efficiency can introduce an additional systematic uncertainty that must be taken into account.

There is a larger probability to trigger a $Z \rightarrow \ell\ell$ event due to the presence of an extra lepton than a $Z \rightarrow \tau\tau$ event. Because the two leptons in the $Z \rightarrow \ell\ell$ event are required to be identified by the trigger, but no trigger requirement on the hadronically decaying τ-lepton is applied, the ratio $\frac{\varepsilon^{kin}_{Z\rightarrow\ell\ell}}{\varepsilon^{kin}_{Z\rightarrow\tau\tau}}$ must be corrected by a factor considering the trigger efficiency.

The embedding method has a statistical uncertainty for the kinematic selected events but in addition an uncertainty for the correct $Z \rightarrow \mu\mu$ selection from data has to be considered.

The main idea is the substitution of the initial number $N^{ini}_{Z\rightarrow\tau\tau}$ with the number of measured $Z \rightarrow \ell\ell$ events. This is expressed in the second formula which contains the ratio $\varepsilon^{kin}_{Z\rightarrow\ell\ell}/\varepsilon^{kin}_{Z\rightarrow\tau\tau}$ for the kinematic $Z \rightarrow \tau\tau$ and $Z \rightarrow \ell\ell$ selection. Since the kinematic efficiency does not depend strongly from the energy spectrum of the τ-lepton in the calorimeter the procedure of the embedding tries to separate the effects relevant for the τ-lepton identification from those which are relevant for the kinematic τ-lepton selection. The problem of the different p_T dependency of the leptons and the τ-lepton will be considered with the embedding method.

8.6.2 Systematic uncertainties for the embedding technique

Although the $Z \rightarrow \mu\mu$ selection (used for the embedding technique) has a better signal over background performance compared with the $Z \rightarrow \tau\tau$ selection, several systematic uncertainties have to be considered.

- Efficiency and purity of the $Z \rightarrow \mu\mu$ signal sample:
  - It cannot be guaranteed that the $Z \rightarrow \mu\mu$ sample has 100 % purity. The consequence is that also fake muons can be taken for the substitution. This affects all common proberties of the event also used for the $Z \rightarrow \tau\tau$ procedure (e.g. the E_T^{miss} distribution or the jet multiplicity).

- Detector mis-alignment:
  - The effect from the detector mis-alignment for this study is negligible.

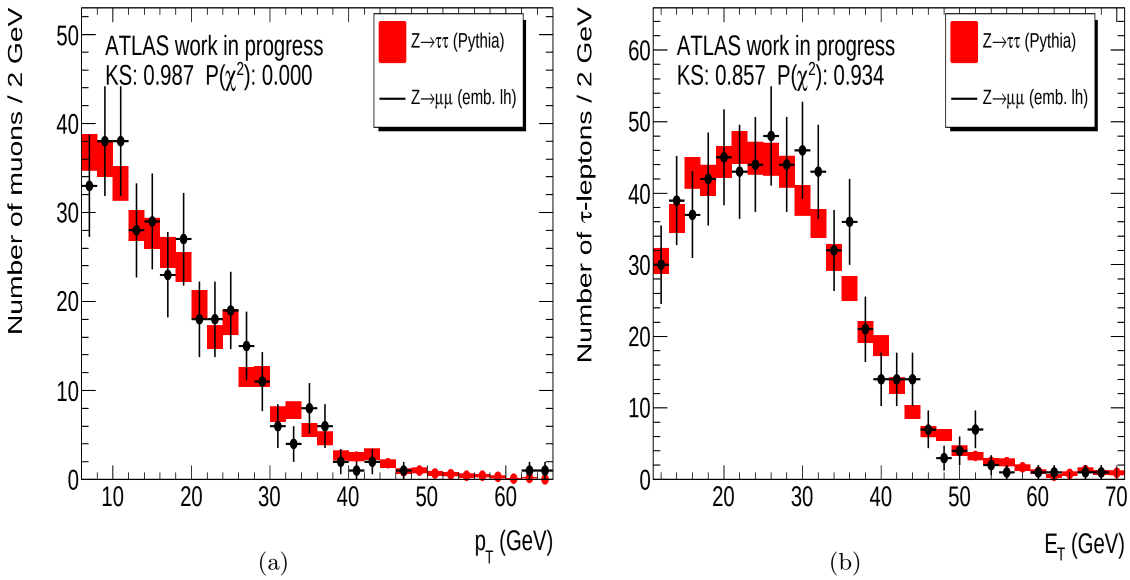

Figure 8.14: *Monte Carlo cross check for Z $\rightarrow \tau\tau$ events with Z $\rightarrow \mu\mu \xrightarrow{embedding} \tau\tau$ events [133]. The p_T of the muon from the leptonically τ-lepton decay is compared with the prompt muon(a). The p_T of the τ-lepton is compared with the prompt muon (b).*

- Effects from pile-up:
  - As discussed previously, pile-up events affects the general data performance due to additional primary vertices.
- TAUOLA simulation and ATLAS re-reconstruction:
  - The properties of the Z $\rightarrow \tau\tau$ decay simulation are well understood. The advantage of the embedding technique is that it uses real Z-bosons obtained from data. This reduces the uncertainty of the Z-boson kinematic in MC simulations. Furthermore, the general event information (e.g. tracks or jet multiplicities) will be kept. The re-calculation of E_T^{miss} induces a systematic uncertainty. In addition, the full ATLAS simulation and reconstruction chain (inclusive detector simulation) causes further systematic uncertainties.

8.6.3 Tau identification and reconstruction efficiency with the embedding technique on Monte Carlo level

To validate the embedding technique a cross check with a standard efficiency determination using Monte Carlo information on truth level is performed. The determined efficiencies from this method are shown in Table 8.24.

Figure 8.14 shows the Monte Carlo cross check for semi-leptonic Z $\rightarrow \tau\tau$ events produced with the embedding and a regular Z $\rightarrow \tau\tau$ Monte Carlo (Pythia).

The uncertainties are determined with error propagation. The systematic uncertainty is related to the different branching ratios and depends from lepton related variables like the

muon channel	ε_τ (`cb tight`)	ε_τ (`cb medium`)	ε_τ (`cb loose`)
signal	0.228±0.031	0.453±0.07	0.6314±0.10
signal+background	0.221±0.030	0.461±0.081	0.621±0.13
electron channel	ε_τ (`cb tight`)	ε_τ (`cb medium`)	ε_τ (`cb loose`)
signal	0.224±0.22	0.462±0.054	0.633±0.085
signal+background	0.229±0.04	0.468±0.073	0.64±0.13

Table 8.22: *The τ-lepton reconstruction and identification efficiency for muon and electron channels for different τ-lepton identification criteria. The uncertainties are estimated from MC samples scaled to $\mathcal{L}$ = 35 pb^{-1}. For the overall lepton identification efficiency a value of 0.85±0.085 is assumed. The trigger efficiency has to be obtained from lepton trigger efficiency studies and has to be taken into account.*

	Reconstruction	Embedding (MC statistic)	Embedding ($\mathcal{L}$ = 35 pb^{-1})
$\frac{\varepsilon_{\mu\mu}}{\varepsilon_{\tau\tau}}$	4.32±0.12	4.12±0.45	4.12±0.21

Table 8.23: *Compare $\frac{\varepsilon_{\mu\mu}}{\varepsilon_{\tau\tau}}$ for MC based study and for Embedding method.*

identification efficiency, the reconstruction and trigger efficiency. For all these variables an uncertainty of 10 % was assumed.

Table 8.22 shows the τ-identification efficiencies obtained from a regular Monte Carlo based efficiency determination. Table 8.23 shows the kinematic ratio R_{kin} estimated with regular Z $\rightarrow \mu\mu$ and Z $\rightarrow \tau\tau$ samples (reconstruction) and R_{kin} estimated with the embedding technique (MC statistic). The uncertainty from the embedding method is rescaled to the used integrated luminosity.

8.6.4 Tau identification and reconstruction efficiency with the embedding technique for first ATLAS data ($\mathcal{L}$=35 pb^{-1})

Figure 8.15(a) shows the p_T distributions for muons from the selected Z $\rightarrow \mu\mu$ event and for the substituted τ-lepton which decays into a muon. Figure 8.15(b) shows the p_T distributions for muons from the selected Z $\rightarrow \mu\mu$ event and for the substituted τ-lepton which decays hadronically. As expected, the visible p_T for the τ-lepton is in both cases smaller due to the E_T^{miss} contribution shown in Fig. 8.16(a).

In Fig. 8.17 the number of primary vertices and the number of tracks per primary vertex

τ-lepton ID criterion	**Determined Efficiency**
`Cut based loose`	$0.631 \pm 0.024^{stat.} \pm 0.041^{syst.} \pm 0.021^{embed.}$
`Cut based medium`	$0.462 \pm 0.021^{stat.} \pm 0.042^{syst.} \pm 0.019^{embed.}$
`Cut based tight`	$0.226 \pm 0.012^{stat.} \pm 0.030^{syst.} \pm 0.012^{embed.}$

Table 8.24: *The projected τ-lepton identification efficiencies for different τ-lepton identification criteria for the Z $\rightarrow \mu\mu$ substitution channel, using the embedding method.*

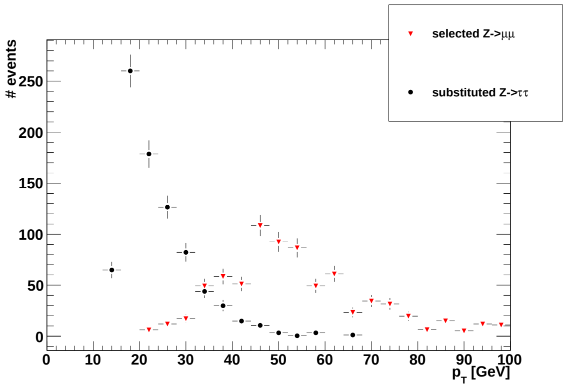

(a)

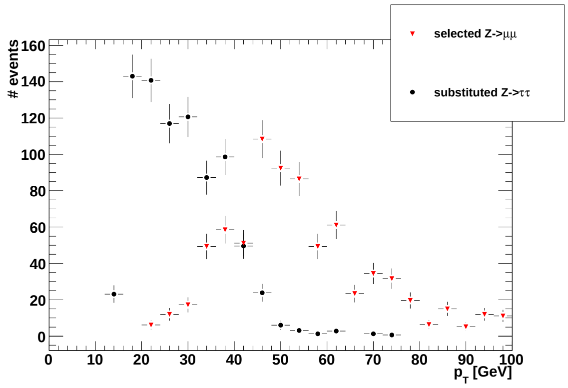

(b)

Figure 8.15: *The p_T distributions for muons from original Z $\rightarrow \mu\mu$ event and for leptonically decaying τ-leptons produced with the embedding (a). The p_T distributions for muons from original Z $\rightarrow \mu\mu$ event and for hadronically decaying τ-leptons produced with the embedding(b).*

is shown.

Table 8.25 shows the cut flow for the Z $\rightarrow \tau\tau$ selection for embedded events. Table 8.26 shows the number of selected Z $\rightarrow \mu\mu$ events from data.

Cut	$N^{\text{embedding}}_{Z\rightarrow\tau\tau}$	ε	$\varepsilon_{\text{culm.}}$	$N^{\text{MC}}_{Z\rightarrow\tau\tau}$	ε	$\varepsilon_{\text{culm.}}$
Preselect. ℓ	906±30	1	1	906±	1	1
OLR (ℓ)	906±30	1	1	906±30	1	1
OLR (τ_h)	540±23	0.60±0.02	0.60±0.02	373±19	0.41±0.02	0.41±0.012
Selected ℓ	428±21	0.79±0.02	0.47±0.02	370±19	0.99±0.01	0.41±0.02
Isolated ℓ	315±18	0.74±0.03	0.35±0.02	297±17	0.80±0.02	0.33±0.02
Selected τ_h	314±18	1.00±0.01	0.35±0.02	294±17	0.99±0.01	0.32±0.02
Di lepton veto	278±17	0.86±0.02	0.31±0.02	263±16	0.90±0.02	0.29±0.02
$\sum\cos\Delta\phi$	230±15	0.83±0.02	0.25±0.01	219±15	0.83±0.03	0.24±0.01
$m_T(\ell, E_T^{\text{miss}})$	223±15	0.97±0.01	0.25±0.01	196±14	0.90±0.02	0.22±0.01
$m_{\text{vis}}(\tau_h, \tau_\ell)$	219±15	0.98±0.01	0.24±0.01	188±14	0.96±0.02	0.21±0.01
$N_{\text{tracks}} = 1$ or 3	166±13	0.76±0.03	0.18±0.01	134±12	0.72±0.04	0.15±0.01
Unit charge	155±12	0.93±0.02	0.17±0.01	134±12	1	0.15±0.01
OS	147±12	0.95±0.02	0.02±0.01	123±11	0.92±0.03	0.14±0.01

Table 8.25: *The cut flow for embedded Z $\rightarrow \tau\tau \rightarrow \tau_h\ \tau_\mu$ events without τ_h identification in comparison with Z $\rightarrow \tau\tau \rightarrow \tau_h\ \tau_\mu$ events from regular Monte Carlo.*

As discussed for the linear approximation, the method is described for the `cut based medium` and `electron veto medium`, within a p_T interval of [15,60] GeV for the reconstructed τ-lepton and the reconstructed lepton. The η interval is defined as [-3,3].

The number of selected $Z \rightarrow \tau\tau \rightarrow \tau_\mu\tau_h$ events obtained from Chapt. 7 is 222±15(stat.)±12(syst.).

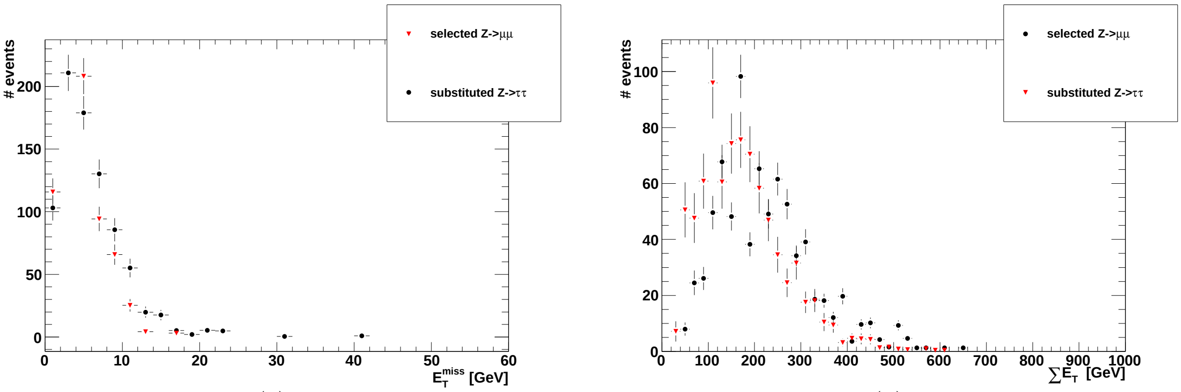

(a) (b)

Figure 8.16: *The E_T^{miss} distribution for original Z $\to \mu\mu$ events and Z $\to \tau\tau$ events produced with the embedding (a). $\sum E_T$ is shown in (b).*

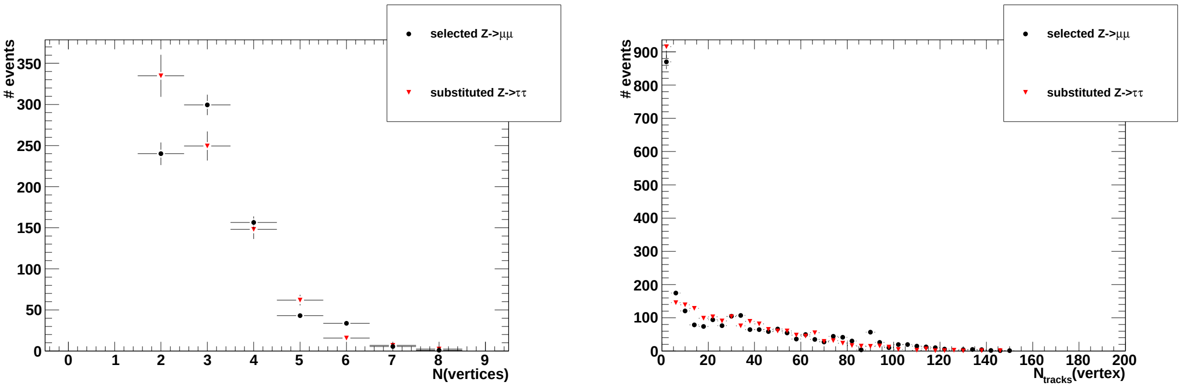

(a) (b)

Figure 8.17: *The number of primary vertices for original Z $\to \mu\mu$ events and Z $\to \tau\tau$ events produced with the embedding (a). The number of tracks per vertex is drawn in (b).*

The estimated ratio is

$$\varepsilon^{\mathrm{kin}}_{Z\to\mu\mu}/\varepsilon^{\mathrm{kin}}_{Z\to\tau\tau} = \frac{683 \pm 26}{147 \pm 12} = 4.63 \pm 0.04. \tag{8.42}$$

The branching ration fraction is

$$\frac{\mathrm{BR}_{Z\to\mu\mu}}{\mathrm{BR}_{Z\to\tau\tau} 2\mathrm{BR}_{\tau\to\mathrm{had}\nu_\tau}\mathrm{BR}_{\tau\to\mu\bar{\nu}_\mu\nu_\tau}} = 4.81 \pm 0.03. \tag{8.43}$$

with the seperate values [122]

- $\frac{\mathrm{BR}_{Z\to\mu\mu}}{\mathrm{BR}_{Z\to\tau\tau}} = 0.998 \pm 0.001$
- $\mathrm{BR}_{\tau\to\mathrm{had}\nu_\tau} = 0.61 \pm 0.0004$

Cut	$N^{\text{embedding}}_{Z\rightarrow\mu\mu}$	ε	$\varepsilon_{\text{culm.}}$	$N^{\text{data}}_{Z\rightarrow\mu\mu}$	ε	$\varepsilon_{\text{culm.}}$
All	908	1	1	1997042±1413	1	1
GRL	908	1	1	1997042±1413	1	1
Trigger	908	1	1	182651±427	0.091	0.091
Vertex	908	1	1	181759±426	0.995	0.091
Jet cleaning	908	1	1	181412±426	0.998	0.090
Pre	906	1	1	82350±287	0.454	0.041
OLR	906	1	1	79138±281	0.961	0.039
Sel.	906	1	1	78024±279	0.986	0.039
OS	906	1	1	27225±165	0.349	0.014
$m_T(\ell, E_T^{\text{miss}})$	779±28	0.86±0.02	0.86±0.02	24202±155	0.88	0.012
m_{inv}	683±26	0.87±0.02	0.75±0.02	11960±109	0.49	0.006

Table 8.26: *The cut flow for the kinematic cuts for the events selected for the embedding procedure and for the normal $Z \rightarrow \mu\mu$ selection as described previously. The cut efficiency for the embedded sample (second column) is large compared with the regular selection. This is reasonable since the $Z \rightarrow \mu\mu$ are already selected. For all efficiencies in the last and second last column the uncertainty is smaller than 1%.*

- $BR_{\tau\rightarrow\mu\bar{\nu}_\mu\nu_\tau} = 0.1737 \pm 0.0007$.

The number of final selected $Z \rightarrow \mu\mu$ events from data[8] is 11960±109. The number of initial $Z \rightarrow \mu\mu$ events used for the embedding and the number of final selected $Z \rightarrow \mu\mu$ events (see Tab. 8.25) are not normalised to each other. The kinematic ratio R_{kin} can be estimated 'decoupled' from the term in Eq. 8.41. The lepton related efficiencies are

$$F(\varepsilon^\mu) = (\varepsilon^\mu_{\text{ID}} \times \varepsilon^\mu_{\text{reco}}) \times \left(\frac{1 - (1 - \varepsilon^\mu_{\text{trigger}})^2}{\varepsilon^\mu_{\text{trigger}}} \right) = (0.94) \times (1.15) = 1.067 \pm 0.023 \qquad (8.44)$$

with the muon trigger efficiency $\varepsilon^\mu_{\text{trigger}} = 0.85 \pm 0.01$.

The estimated combined reconstruction and identification efficiency is (see Eq. 8.41)

$$\varepsilon^{\tau_h}_{\text{ID}} \times \varepsilon^{\tau_h}_{\text{reco}} = 0.42 \pm 0.03(\text{stat}). \pm 0.02(\text{syst.}). \qquad (8.45)$$

The systematic uncertainty considers the embedding procedure. The τ-lepton identification efficiency estimated with the linear approximation technique is 0.44±0.07. The τ-lepton reconstruction efficiency is then in the order of

$$\varepsilon^{\tau_h}_{\text{reco}} = 0.95 \pm 0.04. \qquad (8.46)$$

The τ-lepton identification efficiency estimated with the embedding technique is then

$$\varepsilon^{\tau_h}_{\text{ID}} = 0.45 \pm 0.05(\text{stat.}) \pm 0.02(\text{syst.}). \qquad (8.47)$$

[8] As discussed previously, the $Z \rightarrow \mu\mu$ selection for this study differs with the regular strategy for the general $Z \rightarrow \mu\mu$ selection. The used $Z \rightarrow \mu\mu$ selection is along the lines of the lepton selection in $Z \rightarrow \tau\tau$.

The identification efficiency can be estimated with $\mathrm{Z} \to \tau_\mathrm{h}\tau_\ell$ sample produced from the selected $\mathrm{Z} \to \mu\mu$ events. The τ-lepton identification efficiency for `cut based medium`, for medium electron veto and $\mathrm{p_T} > 15\,\mathrm{GeV}$ is $\varepsilon^{\mathrm{ID}}_{\tau_\mathrm{h}} = 0.43 \pm 0.06$.

The values (0.43 ± 0.06), (0.45 ± 0.05) and (0.44 ± 0.07) agree within the statistical and systematic uncertainties. This indirect cross check confirms that the linear approximation technique and the embedding technique are consistent.

8.7 Additional cross checks

In order to confirm the efficiencies estimated in Sec. 8.2 and Sec. 8.6.4 the basic conditions for the embedding and the linear approximation are permuted. The substitution discussed in Sec. 8.6.4 is applied on the linear approximation (see Sec 8.7.1 and the embedded $\mathrm{Z} \to \tau\tau$ sample will be used to determine the τ-lepton identification efficiency.

8.7.1 Linear approximation technique with $\mathrm{N}^{\mathrm{produced}}_{Z\to\tau_h\tau_\ell}$ to $\mathrm{N}^{\mathrm{final}}_{Z\to\ell\ell}$ substitution

Identification efficiency $\varepsilon^{\tau_\mathrm{h}}_{\mathrm{ID}}$

The procedure is the same as for the linear approximation described before. Following the procedure described in Eq. 8.40 and Eq. 8.41 the identification efficiency $\varepsilon^{\tau_\mathrm{h}}_{\mathrm{ID}}$ becomes

$$\varepsilon^{\tau_\mathrm{h}}_{\mathrm{ID}} \times \frac{\varepsilon_{\mathrm{Z}\to\tau_\mathrm{h}\tau_\ell}}{\varepsilon^{\mathrm{kin}}_{\mathrm{Z}\to\ell\ell}} = \frac{\mathrm{N}^{\mathrm{post-ID}}_{\mathrm{Z}\to\tau_\mathrm{h}\tau_\ell}}{\mathrm{N}^{\mathrm{post-ID}}_{\mathrm{Z}\to\ell\ell}} \times \mathrm{C} \times \frac{1}{\varepsilon^{\tau_\mathrm{h}}_{\mathrm{reco}}} \tag{8.48}$$

with C denoting all lepton related variables as well as the branching ratios. The kinematic efficiency describes the property to select events which are preselected by the trigger and the reconstruction algorithms. The relation can be expressed as

$$\frac{\varepsilon^{\mathrm{kin}}_{\mathrm{Z}\to\ell\ell}}{\varepsilon^{\mathrm{kin}}_{\mathrm{Z}\to\tau_\mathrm{h}\tau_\ell}} = \frac{\mathrm{N}^{\mathrm{kin}}_{\mathrm{Z}\to\ell\ell} \times \mathrm{N}^{\mathrm{reco}}_{\mathrm{Z}\to\tau_\mathrm{h}\tau_\ell}}{\mathrm{N}^{\mathrm{kin}}_{\mathrm{Z}\to\tau_\mathrm{h}\tau_\ell} \times \mathrm{N}^{\mathrm{reco}}_{\mathrm{Z}\to\ell\ell}}. \tag{8.49}$$

The inverse reconstruction efficiency for the τ-lepton can be written as

$$\frac{1}{\varepsilon^{\tau_\mathrm{h}}_{\mathrm{reco}}} = \frac{\mathrm{N}^{\mathrm{trigger}}_{\mathrm{Z}\to\tau_\mathrm{h}\tau_\ell} \times \varepsilon^{\ell}_{\mathrm{reco}}}{\mathrm{N}^{\mathrm{reco}}_{\mathrm{Z}\to\tau_\mathrm{h}\tau_\ell}}. \tag{8.50}$$

Equation 8.48 can be written as

$$\varepsilon^{\tau_\mathrm{h}}_{\mathrm{ID}} \times \frac{\mathrm{N}^{\mathrm{kin}}_{\mathrm{Z}\to\tau_\mathrm{h}\tau_\ell}}{\mathrm{N}^{\mathrm{kin}}_{\mathrm{Z}\to\ell\ell}} = \frac{\mathrm{N}^{\mathrm{post-ID}}_{\mathrm{Z}\to\tau_\mathrm{h}\tau_\ell}}{\mathrm{N}^{\mathrm{post-ID}}_{\mathrm{Z}\to\ell\ell}} \times \varepsilon^{\ell}_{\mathrm{ID}} \times \frac{\mathrm{BR}_{\mathrm{Z}\to\ell\ell}}{\mathrm{BR}_{\mathrm{Z}\to\tau_\mathrm{h}\tau_\ell}}. \tag{8.51}$$

As already discussed, the τ-lepton identification efficiency does not depend from the lepton trigger efficiency or τ-lepton or lepton reconstruction efficiency. If the τ-lepton identification cuts are not applied, the contributing background is quite large. In order to suppress the background and the corresponding systematic effects, the kinematic ratio $\mathrm{R_{kin}} = \frac{\varepsilon^{\mathrm{kin}}_{\mathrm{Z}\to\ell\ell}}{\varepsilon^{\mathrm{kin}}_{\mathrm{Z}\to\tau_\mathrm{h}\tau_\ell}}$

was introduced (see Sec. 8.6.1).

R_{kin} is constructed with an almost background free numerator while the denominator (which contains the $Z \to \tau_h \tau_\ell$ candidates) is affected by additional background events. The higher statistic in the numerator causes a reduction of background since the kinematic for $Z \to \ell\ell$ and $Z \to \tau_h \tau_\ell$ is the same.

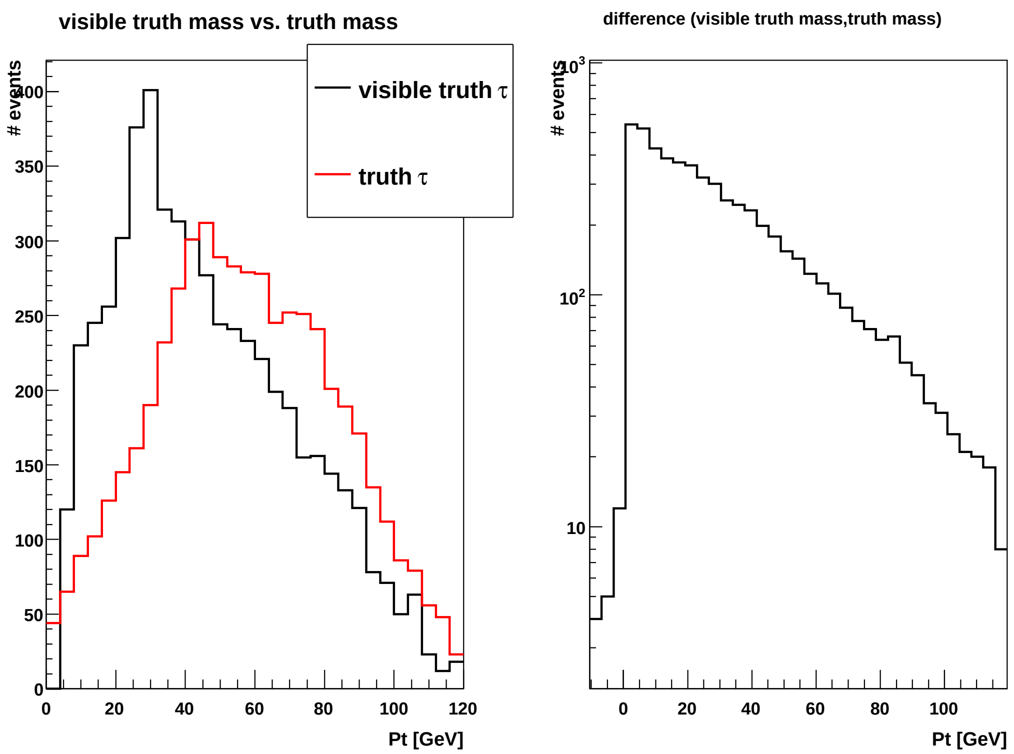

Figure 8.18: *$Z \to \tau\tau$ kinematic for visible truth τ-lepton and the truth τ-lepton. The plot on the left shows the p_T spectra. The plot on the right shows the difference of the transverse momentum to illustrate that the p_T of the daughter is always smaller than the p_T of the mother particle.*

Lepton assignment The linear approximation combined with the substitution technique requires a precise assignment of the different p_T regions for the leading lepton from $Z \to \ell\ell$ and the τ-lepton from $Z \to \tau\tau$. In order to fulfil this condition the p_T regions are defined using Monte Carlo truth information as well as information from the embedding technique. The basic idea was to replace produced $Z \to \tau\tau$ events by final selected $Z \to \ell\ell$ events (see Eqs. 8.40 and 8.41). Based on this idea the embedding was introduced to estimate the kinematic ratio $R_{kin} = \frac{\varepsilon^{kin}_{Z\to\mu\mu}}{\varepsilon^{kin}_{Z\to\tau_h\tau_\ell}}$. For the linear approximation technique the events are binned in p_T or η. For that reason, the assignment of leptons to τ-leptons becomes more difficult due to the higher E_T^{miss} for the τ-lepton decay. The lepton which is assigned to the τ-lepton has a larger p_T. Figure 8.18 shows the p_T distributions for the hadronically decaying τ-lepton and the leptonically decaying τ-lepton.

η	$N^{ele.}$	ε^{cross} (ele.)	ε^{main} (ele.)	$N^{mu.}$	ε^{cross} (mu.)	ε^{main} (mu.)
-3–0	5880±77	0.42±0.04	0.44±0.04	5102±71	0.44±0.03	0.44±0.03
0–1	3771±61	0.43±0.03	0.45±0.05	4101±64	0.45±0.04	0.43±0.05
1–3	2290±48	0.44±0.04	0.45±0.06	2257±53	0.45± 0.04	0.44±0.04

Table 8.27: *The summarised values for the modified linear approximation for the η binning of the leading p_T lepton. The efficiencies ε^{cross} denotes the values estimated with this cross check. The original efficiencies are denoted with ε^{main} and are taken from Tab. 8.5 for the electron channel and from Tab. 8.10 for the muon channel. The number of events is related to the number of leading p_T leptons.*

$p_T(\tau)$	$p_T(e)$	$N^{electrons}$	ε^{cross}	ε^{main}
18–22 and 44–60	20–25 and 46–62	4461±67	0.44±0,05	0.43±0.03
22–37	25–43	3602±60	0.43±0.04	0.43±0.04
15–18 and 37–44	15–20 and 43–46	3518±59	0.45±0.05	0.44±0.04

Table 8.28: *The summarised values for the modified linear approximation for the electron channel. The p_T regions for the τ-lepton and the leading p_T electron consider the correct assignment as discussed in the text (see Fig. 8.18).The efficiencies ε^{cross} denotes the values estimated with this cross check. The original efficiencies are denoted with ε^{main} and are taken from Tab. 8.7 for the electron channel and from Tab. 8.12 for the muon channel. The number of electron events is related to the leading p_T electron. The lepton p_T binning in the second column is related to these electrons.*

The results are summarised in Tabs. 8.27, 8.28, and 8.29. The values for the efficiencies agree within their uncertainties.

Reconstruction efficiency $\varepsilon^{\tau_h}_{reco}$

The substitution procedure allows to estimate the τ-lepton reconstruction efficiency also with the linear approximation technique. For the determination of $\varepsilon^{\tau_h}_{reco}$ the relation becomes

$$\varepsilon^{\tau_h}_{reco} \times \frac{\varepsilon^{kin}_{Z\rightarrow\tau_h\tau_\ell}}{\varepsilon^{kin}_{Z\rightarrow\ell\ell}} = \frac{N^{post-ID}_{Z\rightarrow\tau_h\tau_\ell}}{N^{post-ID}_{Z\rightarrow\ell\ell}} \times C \times \frac{1}{\varepsilon^{\tau_h}_{ID}}. \tag{8.52}$$

For the τ-lepton reconstruction efficiency Eq. 8.49 becomes important. On reconstruction level the background can only be handled by allowing large uncertainties. In order to reduce the systematic uncertainty all cuts which does not affect the τ-lepton reconstruction efficiency, are applied. All lepton related cuts as well as all τ-lepton related cuts (e.g. identification cuts visible mass window) can be used. The τ-lepton identification efficiency can be estimated and the visible mass window does not reduces the number of signal events significantly.

$p_T(\tau)$	$p_T(e)$	N^{muons}	ε^{cross}	ε^{main}
18–22 and 44–60	20–25 and 46–62	4617±68	0.43±0.03	0.42±0.04
22–37	25–43	3990±63	0.43±0.04	0.44±0.05
15–18 and 37–44	15–20 and 43–46	3899±62	0.42±0.03	0.44±0.05

Table 8.29: *The summarised values for the modified linear approximation for the electron channel. The p_T regions for the τ-lepton and the leading p_T muon consider the correct assignment as discussed in the text (see Fig. 8.18).The efficiencies ε^{cross} denotes the values estimated with this cross check. The original efficiencies are denoted with ε^{main} and are taken from Tab. 8.7 for the electron channel and from Tab. 8.12 for the muon channel. The number of muon events is related to the leading p_T muon. The lepton p_T binning in the second column is related to these muons.*

The reconstruction efficiency is estimated for a τ-lepton candidate with a certain p_T and one or three tracks (one-prong or three-prong).

The following τ-lepton related cuts have to be discussed in more detail:

- Due to charge mis-identification the charge and therefore the opposite sign charge cut has an uncertainty which has to be estimated.

- Another important cut is the $\sum \cos\Delta\phi$ cut (which mainly suppresses $W \to \ell\nu$ background) which cannot be used for this study since also a significant number of reconstructed lepton candidates can be rejected (see Fig. 7.13). To reduce the $W \to \ell\nu$ background the $m_T(\ell)$ cut is defined with a tighter threshold (change from $m_T(\ell) < 50\,\mathrm{GeV}$ to $m_T(\ell) < 20\,\mathrm{GeV}$). The kinematic $Z \to \ell\ell$ efficiency has to be recalculated.

The number of events $Z \to \ell\ell$ and $Z \to \tau\tau$ events becomes:

$$N^{reco}_{Z\to\ell\ell} = N^{final(m_T^{modified})}_{Z\to\ell\ell} \times \frac{1}{F(\varepsilon^{\ell}) \times \varepsilon^{kin}_{Z\to\ell\ell}} \tag{8.53}$$

and

$$N^{reco}_{Z\to\tau_h\tau_\ell} = N^{final(\sum\cos\Delta\phi)} \times \frac{1}{\varepsilon^{ID}_{\tau_h} \times \varepsilon^{kin}_{Z\to\tau_h\tau_\ell}}. \tag{8.54}$$

Substituting the ratio $\frac{Z\to\tau_h\tau_\ell}{Z\to\ell\ell}$ with the terms from Eq. 8.53 and Eq. 8.54 results in

$$\varepsilon^{\tau_h}_{reco} \times \varepsilon^{\tau_h}_{ID} = \left(\frac{N^{kin}_{Z\to\ell\ell}}{N^{kin}_{Z\to\tau_h\tau_\ell}}\right)_{modified} \times \left(\frac{N^{final}_{Z\to\tau_h\tau_\ell}}{N^{final}_{Z\to\ell\ell}}\right)_{modified} \times \frac{BR_{Z\to\ell\ell}}{BR_{Z\to\tau_h\tau_\ell}} \times F(\varepsilon^{\ell}). \tag{8.55}$$

The lepton efficiencies are:

$$F(\varepsilon^{e}) = (\varepsilon^{e}_{ID} \times \varepsilon^{e}_{reco}) \times \left(\frac{1-(1-\varepsilon^{e}_{trigger})^2}{\varepsilon^{e}_{trigger}}\right) = (0.86) \times (1.05) = 0.892 \pm 0.019 \tag{8.56}$$

for the electron channel and

$$\mathrm{F}(\varepsilon^{\mu}) = (\varepsilon^{\mu}_{\mathrm{ID}} \times \varepsilon^{\mu}_{\mathrm{reco}}) \times \left(\frac{1-(1-\varepsilon^{\mu}_{\mathrm{trigger}})^2}{\varepsilon^{\mu}_{\mathrm{trigger}}} \right) = (0.94) \times (1.15) = 1.067 \pm 0.023 \quad (8.57)$$

for the muon channel.

η	$\varepsilon^{\mathrm{ID}}_{\mathrm{ele.}}$	$\varepsilon^{\mathrm{ID}\times\mathrm{reco}}_{\mathrm{ele.}}$	$\varepsilon^{\mathrm{reco}}_{\mathrm{ele.}}$	$\varepsilon^{\mathrm{ID}}_{\mathrm{mu.}}$	$\varepsilon^{\mathrm{ID}\times\mathrm{reco}}_{\mathrm{mu.}}$	$\varepsilon^{\mathrm{reco}}_{\mathrm{mu.}}$
-3–0	0.44± 0.04	0.41±0.04	0.95±0.05	0.43±0.03	0.42±0.03	0.95±0.06
0–1	0.45± 0.05	0.43±0.04	0.94±0.045	0.43±0.04	0.41±0.03	0.96±0.06
1–3	0.45± 0.06	0.41±0.04	0.91±0.05	0.44±0.04	0.40±0.03	0.91±0.06

Table 8.30: *The τ-lepton reconstruction efficiencies estimated with the linear approximation technique for the η binning. The lower index 'electron'('muon') refers to the electron or muon channel.*

$\mathrm{p_T}$	$\varepsilon^{\mathrm{ID}}$	$\varepsilon^{\mathrm{ID}\times\mathrm{reco}}_{\mathrm{ele.}}$	$\varepsilon^{\mathrm{reco}}_{\mathrm{ele.}}$	$\varepsilon^{\mathrm{ID}}_{\mathrm{mu.}}$	$\varepsilon^{\mathrm{ID}\times\mathrm{reco}}_{\mathrm{mu.}}$	$\varepsilon^{\mathrm{reco}}_{\mathrm{mu.}}$
R1	0.44±0.05	0.43±0.04	0.99±0.06	0.42±0.04	0.41±0.03	0.974±0.061
R2	0.43±0.04	0.42±0.04	0.98±0.06	0.44±0.05	0.43±0.03	0.96±0.05
R3	0.46±0.05	0.43±0.03	0.93±0.05	0.44±0.05	0.42±0.03	0.97±0.05

Table 8.31: *The τ-lepton reconstruction efficiencies estimated with the linear approximation technique for the p_T binning defined for the tau control region. The lower index 'electron'('muon') refers to the electron or muon channel.*

The estimated values for the τ-lepton reconstruction efficiency are summarised in Tab. 8.31. The values are related to τ-leptons with one or three tracks and at least a transverse momentum of $\mathrm{p_T} > 15\,\mathrm{GeV}$.

The estimated average τ-lepton reconstruction efficiency is

$$\varepsilon^{\tau_{\mathrm{h}}}_{\mathrm{reco}} = 0.951 \pm 0.054, \quad (8.58)$$

which agrees with the value estimated with the embedding (see Sec. 8.6.4). It has to mentioned that the separate reconstruction efficiencies for the η and the $\mathrm{p_T}$ binning differ:

$$\frac{\varepsilon^{\tau_{\mathrm{h}}}_{\mathrm{reco}}(\eta)}{\varepsilon^{\tau_{\mathrm{h}}}_{\mathrm{reco}}(\mathrm{p_T})} = \frac{0.936}{0.966} \simeq 0.97. \quad (8.59)$$

The conclusion is that also the τ-lepton reconstruction efficiency can be estimated with the linear approximation technique.

8.8 Further studies

The linear approximation technique (with or without $\mathrm{N}^{\mathrm{produced}}_{Z\rightarrow\tau_h\tau_\ell}$ to $\mathrm{N}^{\mathrm{final}}_{Z\rightarrow\ell\ell}$ substitution) is also available for further decay channels including τ-leptons in the final state. In Sec. 8.8.1

the $t\bar{t} \to \tau_h \tau_\ell$ channel will be discussed while the $W \to \tau_h \nu$ will be discussed in Sec. 8.8.2. Both studies bases on Monte Carlo level.

8.8.1 The $t\bar{t} \to \tau_h \tau_\ell$ channel

The next studied channel is the semi-leptonic $t\bar{t}$ channel with both top quarks decaying into τ-lepton with one τ-lepton decaying hadronically and one τ-lepton decaying leptonically. It is difficult to distinguish a lepton coming from τ-lepton decay, from a lepton coming from a direct top quark decay. The main background contributions comes from QCD multi-jet events as well as electro-weak channels.

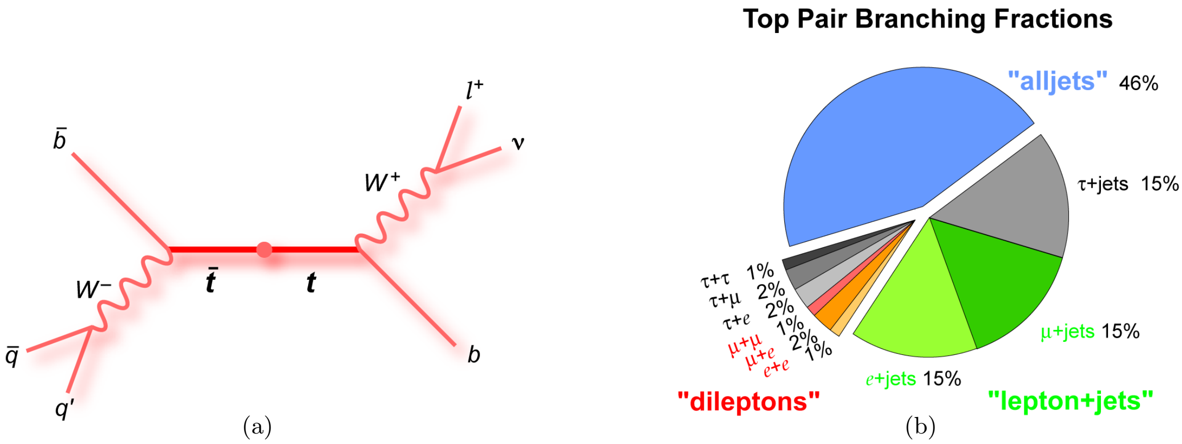

Figure 8.19: *The $t\bar{t}$ decay channel with $W \to \tau\nu$ as tag channel and $W \to X$ as probe channel, in our case $W \to e\nu$, $W \to \mu\nu$ or $W \to \tau\nu$ (a) and the $t\bar{t}$ pair branching ratios (b).*

Equation 8.5 can be expressed as

$$\varepsilon_{\mathrm{ID}}^{\tau_h} = \frac{\mathrm{N}_{t\bar{t}}^{\mathrm{post-ID}}}{\mathrm{N}_{t\bar{t}}^{\mathrm{pre-ID}}} \times \mathrm{C}_3 \Rightarrow \mathrm{N}_{t\bar{t}}^{\mathrm{post-ID}} = \{\varepsilon_{\mathrm{ID}}^{\tau_h}\} \times \mathrm{N}_{t\bar{t}}^{\mathrm{preID}}. \tag{8.60}$$

The basic cuts are:

- $\mathrm{E}_{\mathrm{T}}^{\mathrm{miss}} > 80\,\mathrm{GeV}$
- $\mathrm{p}_{\mathrm{T}}^{\tau} > 40\,\mathrm{GeV}$
- $\mathrm{p}_{\mathrm{T}}^{\mu} > 40\,\mathrm{GeV}$ or $\mathrm{p}_{\mathrm{T}}^{\mathrm{e}} > 40\,\mathrm{GeV}$
- $\mathrm{m}_{\mathrm{T}}(\ell, \mathrm{E}_{\mathrm{T}}^{\mathrm{miss}}) < 100\,\mathrm{GeV}$
- $|\mathrm{Charge}(\ell)| = 1$
- $\mathrm{m}_{\mathrm{vis}}^{t\bar{t}\to\ell\ell} < 85\,\mathrm{GeV}$ or $\mathrm{m}_{\mathrm{vis}}^{t\bar{t}\to\ell\ell} > 95\,\mathrm{GeV}$ to exclude Z decay
- $|\eta(\ell)| < 2.5$
- at least two jets with $\mathrm{p}_{\mathrm{T}}^{\mathrm{jet1}} > 80\,\mathrm{GeV}$ and $\mathrm{p}_{\mathrm{T}}^{\mathrm{jet2}} > 50\,\mathrm{GeV}$.

Region	$p_T^{\tau_h}$ [GeV]	p_T^{ℓ} [GeV]	$\varepsilon(p_T)$	$\eta(\tau)$	$\varepsilon(\eta)$
R1	40–51	44–54	0.51±0.03	-3–0	0.51±0.04
R2	51–60	54–64	0.52±0.02	0–1	0.53±0.02
R3	60–100	64–100	0.50±0.02	1–3	0.53±0.02

Table 8.32: *The binning in p_T and η for the electron and the muon channel. The efficiencies are estimated for the combined lepton channels.*

Table 8.32 summarises the estimated binning for the definition of the three regions. Since the τ-lepton identification efficiency becomes flatter for higher p_T, the binning in p_T has a smaller uncertainty compared with the Z $\rightarrow \tau_h\tau_\ell$ channel. The results for this MC based study (`cut based medium` and `electron veto medium`) are:

- $\varepsilon_{\tau_h}^{ID} = 0.53 \pm 0.03^{\mathrm{fit}} \pm 0.02^{\mathrm{syst.}}$

for the combined lepton channel. The values are different from the values estimated for the Z $\rightarrow \tau\tau$ channel since a higher p_T region is covered.

8.8.2 The W $\rightarrow \tau_h\nu$ channel

The W $\rightarrow \tau_h\nu$ channel has a 10 times larger cross section compared with Z $\rightarrow \tau\tau$. A disadvantage is the background suppression due to the missing lepton. For that reason also the OS-gSS rescaling cannot be used. Instead of the OS-gSS method used for the (τ_h, τ_ℓ) channels, the number of selected events for the W $\rightarrow \tau_h\nu$ channel is modified defining $N_W - gN_W$. That means, the number of W events is rescaled in order to perform the linear approximation[9]. The following cuts are defined for the $W \rightarrow \tau\nu$ selection:

- $E_T^{miss} > 20\,\mathrm{GeV}$
- $20\,\mathrm{GeV} < p_T^{\tau} < 60\,\mathrm{GeV}$
- $|\mathrm{Charge}(\tau)| = 1$
- $|\eta(\tau)| < 2.5$
- $\Delta\phi \mathrm{jet}, E_T^{miss} > 0.5$

This selection is along the lines of the validated standard W $\rightarrow \tau_h\nu$ selection but not using all required cuts. Equation 8.5 can be expressed as

$$\varepsilon_{ID}^{\tau_h} = \frac{N_W^{post-ID}}{N_W^{pre-ID}} \times C_3 \Rightarrow N_W^{post-ID} = \{\varepsilon_{ID}^{\tau_h}\} \times N_W^{preID}. \tag{8.61}$$

The result for this study is:

[9] The idea is that OS-gSS is comparable to N_{signal}-gN_{signal}. The goal is to estimate a rescaling factor in order to fulfil all conditions on the linear approximation technique. The advantage of OS-gSS is that the interval for the g-factor can be restricted.

- $\varepsilon_{\tau_\mathrm{h}}^{\mathrm{ID}} = 0.45 \pm 0.02(\mathrm{stat.}) \pm 0.01(\mathrm{syst.})$

This value is slightly larger compared with the value from the $\mathrm{Z} \rightarrow \tau_\mathrm{h}\tau_\ell$ selection but it agrees within the estimated uncertainties.

8.9 Summary of the efficiency determination

In this chapter the τ-lepton reconstruction and identification efficiency was discussed. Two data-driven techniques were studied in detail in order to provide a almost Monte Carlo free background estimation. Furthermore, the production cross section, the fiducial cross section as well as the inclusive cross section were estimated. Also an outlook for coming studies was given.

Cut based ID	**Linear Approximation**	**Embedding**
`medium` (electron)	0.43±0.04(stat.)±0.02(syst.)	-
`tight` (electron)	0.24±0.05(stat.)±0.03(syst.)	-
`medium` (muon)	0.44±0.05(stat.)±0.02(syst.)	0.45±0.05(stat.)±0.021(syst.)
`tight` (muon)	0.26±0.05(stat.)±0.03(syst.)	0.243±0.044(stat.)±0.022(syst.)

Table 8.33: *The estimated efficiencies for the linear approximation technique and the embedding technique for cut based τ-lepton identification (medium, tight). As mentioned previously, the embedding is not available for the electron channel.*

The results for the efficiencies are summarised in Tab. 8.33. The method was explained for the τ-lepton identification criteria `cut based medium`. The same procedure was done with the `cut based tight` criteria. The corresponding efficiencies are also given. The higher systematic uncertainties for the `cut based tight` selection (linear approximation) is caused by the MC to data calibration. For the studied τ-lepton $\mathrm{p_T}$ range of [15–60] GeV the tighter efficiency increases significantly up to higher $\mathrm{p_T}$ regions. The efficiency for the `cut based medium` case is almost flat over the full $\mathrm{p_T}$ range. For the embedding (which includes the full $\mathrm{p_T}$ range) this effect can be neglected.

Furthermore the τ-lepton reconstruction efficiency was estimated with both methods. The values are:

- $\varepsilon_{\mathrm{reco}}^{\tau_\mathrm{h}} = 0.95 \pm 0.05$ with the linear approximation technique
- $\varepsilon_{\mathrm{reco}}^{\tau_\mathrm{h}} = 0.95 \pm 0.04$ with the embedding technique

Cross section	**Electron channel** [pb]
Production	241±26(stat.)±31(syst.)±7(lumi.)
Fiducial	24.26±3.1(stat.)±5.3(syst.)±0.8(lumi.)
Inclusive	1041±123(stat.)±212(syst.)±40(lumi.)±4(theor.)

Table 8.34: *The summarised cross sections estimated with the linear approximation for the electron channel.*

Cross section	**Muon channel** [pb]
Production	191±21(stat.)±38(syst.)±10(lumi.)
Fiducial	22.22±4.02(stat.)±4.2(syst.)±1.1(lumi.)
Inclusive	845±102(stat.)±107(syst.)±30(lumi.)±3(theor.)

Table 8.35: *The summarised cross sections estimated with the linear approximation for the muon channel.*

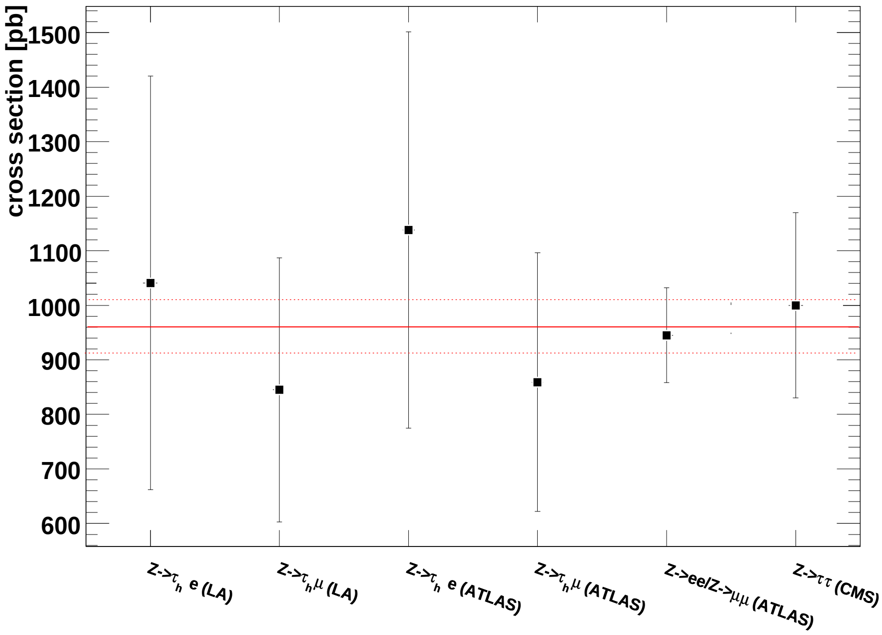

Figure 8.20: *Comparison of the estimated cross sections to theory, to the combined* $Z \to \ell\ell$ *cross section measured by ATLAS and the measurement from CMS.*

The estimated cross sections are listed in Tabs. 8.34 and 8.35. In Fig. 8.20 the results for the linear approximation (LA) are compared with other studies at ATLAS, and the combined cross section (4 channels $Z \to \tau_\mu\tau_h, Z \to \tau_e\tau_h, Z \to \tau_e\tau_\mu$, and $Z \to \tau_\mu\tau_\mu$) measured by the CMS collaboration [134]. In the CMS measurement an additional fit is applied in order to reduce the systematic uncertainties. Furthermore, the theoretical prediction (960±49.5) pb is shown.

Chapter 9

Summary and Outlook

9.1 Summary

The last two years were quite successful for the field of particle physics. LHC has reached new energy regions in proton-proton collisions. Many known processes of the Standard Model were reproduced in order to optimise the detector performance. All experiments at LHC worked as expected and first results concerning new physics processes were published in order to set new limits on discovery potential.

The detection and confirmation of the last building block in the current Standard Model, the Higgs boson, could be possible in the next years. The Higgs boson coupling is proportional to the mass of the particle. The branching ratio for the decay into τ-leptons is large for low mass Higgs bosons compared to electrons or muons as well as light quarks. The decay $\mathrm{Z} \rightarrow \tau\tau$ and the $\mathrm{H} \rightarrow \tau\tau$ have similar properties. For that reason it is quite important to study the $\mathrm{Z} \rightarrow \tau\tau$ in order to understand the Higgs decay. In addition the τ-lepton is often part of the final state for supersymmetric cascade decays.

The most important τ-lepton decay channel is the hadronic decay into pions or kaons. In order to select these decays, the QCD multi-jet background has to be suppressed. This also reduces the signal efficiency. For the estimation of Z-boson cross sections the efficiency to reconstruct and identify a hadronically decaying τ-lepton has to be known very precisely. The τ-lepton reconstruction and identification is connected to a large number of variables describing the kinematic of the decay products as well as the detector response. The corresponding signal efficiencies are estimated with data driven methods.

In this thesis methods for the τ-lepton reconstruction and identification efficiency determination were developed and studied. Both methods were consistent with Monte Carlo based studies. Both methods are data-driven with only a small contribution from Monte Carlo predictions. The embedding technique bases on selected $\mathrm{Z} \rightarrow \mu\mu$ events which have a high purity. For that reason the kinematic properties of the Z-boson can be obtained from data instead from a Monte Carlo prediction. This reduces the systematic uncertainties. The linear approximation only depends from Monte Carlo predictions on the $\mathrm{Z} \rightarrow \tau\tau$ signal. No assumptions about the background are required. This makes this method quite interesting for new physics processes.

The object selection was discussed in order to estimate the number of semi-leptonic

$Z \rightarrow \tau\tau$ signal events. The background with and without τ-lepton identification was significantly suppressed keeping the signal efficiency constant. The estimated τ-lepton identification efficiency is in the order of [44–45] % for both developed methods and is in agreement with the expected values from Monte Carlo predictions. The measured inclusive Z-boson cross section is (1041±379) pb for the electron channel and (845±242) pb for the muon channel which both agree with the theoretical prediction (960±49.5) pb within the measurement uncertainties. For the combined electron and muon channel 393 $Z \rightarrow \tau\tau$ events which decay semileptonically were selected. The first τ-leptons coming from the semi-leptonic $Z \rightarrow \tau\tau$ decay were observed. The systematic uncertainties were discussed and reduced. Finally, the production cross section for Z-bosons which decay into a τ-lepton pair was determined. Also the potential of the developed methods related to new physical process was discussed.

9.2 Outlook

The analysis discussed in this thesis refers to an integrated luminosity of about $35\,\mathrm{pb}^{-1}$. During the first months in 2011 more than $300\,\mathrm{pb}^{-1}$ were recorded. The next coming step is the update including the full data available at ATLAS. This allows for example a more precise measurement of all current values particular the efficiencies for smaller η or p_T binning. Furthermore, the alternative ansatz using τ-lepton fake rates which is explained in Chapt. 7 can be validated with data.

Since the neutral (low mass) Higgs boson also prefers the coupling to τ-leptons, the $H \rightarrow \tau\tau$ could also be studied with the discussed methods. The embedding technique is also used for the $H \rightarrow \tau\tau$ selection but as a method to estimate the $Z \rightarrow \tau\tau$ background. A combination of the embedding technique with the linear approximation technique allows to study a possible separation of the $Z \rightarrow \tau\tau$ from the $H \rightarrow \tau\tau$ channel.

The next coming years will be very exciting and many theoretical predictions will be checked in order to confirm or discard them.

Chapter 10

Appendix

Further performance plots

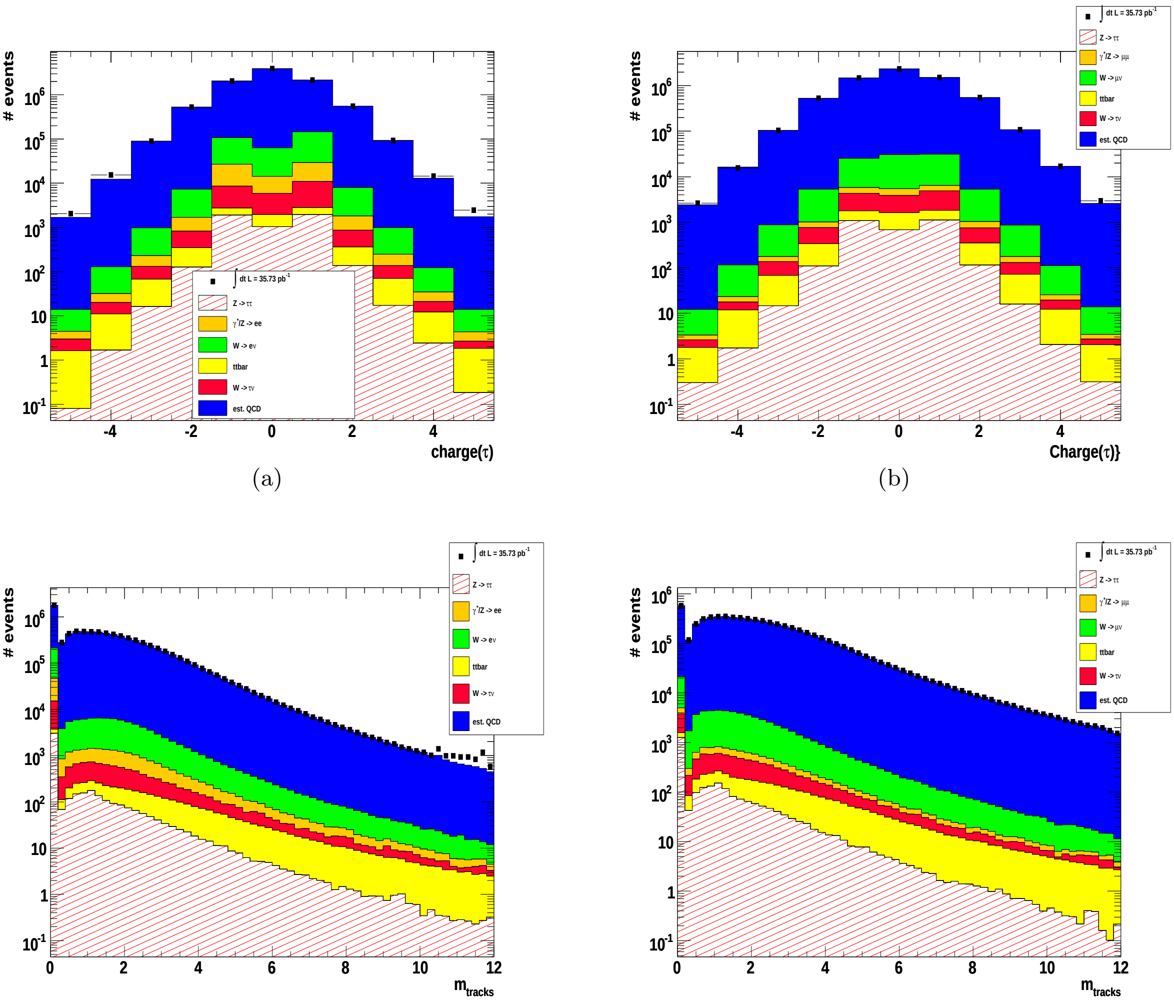

Figure 10.1: *The τ-lepton charge for the electron (a) and the muon (b) channel. The mass of the track system for the electron (c) and the muon (b) channel. All variables are shown on pre-selection level.*

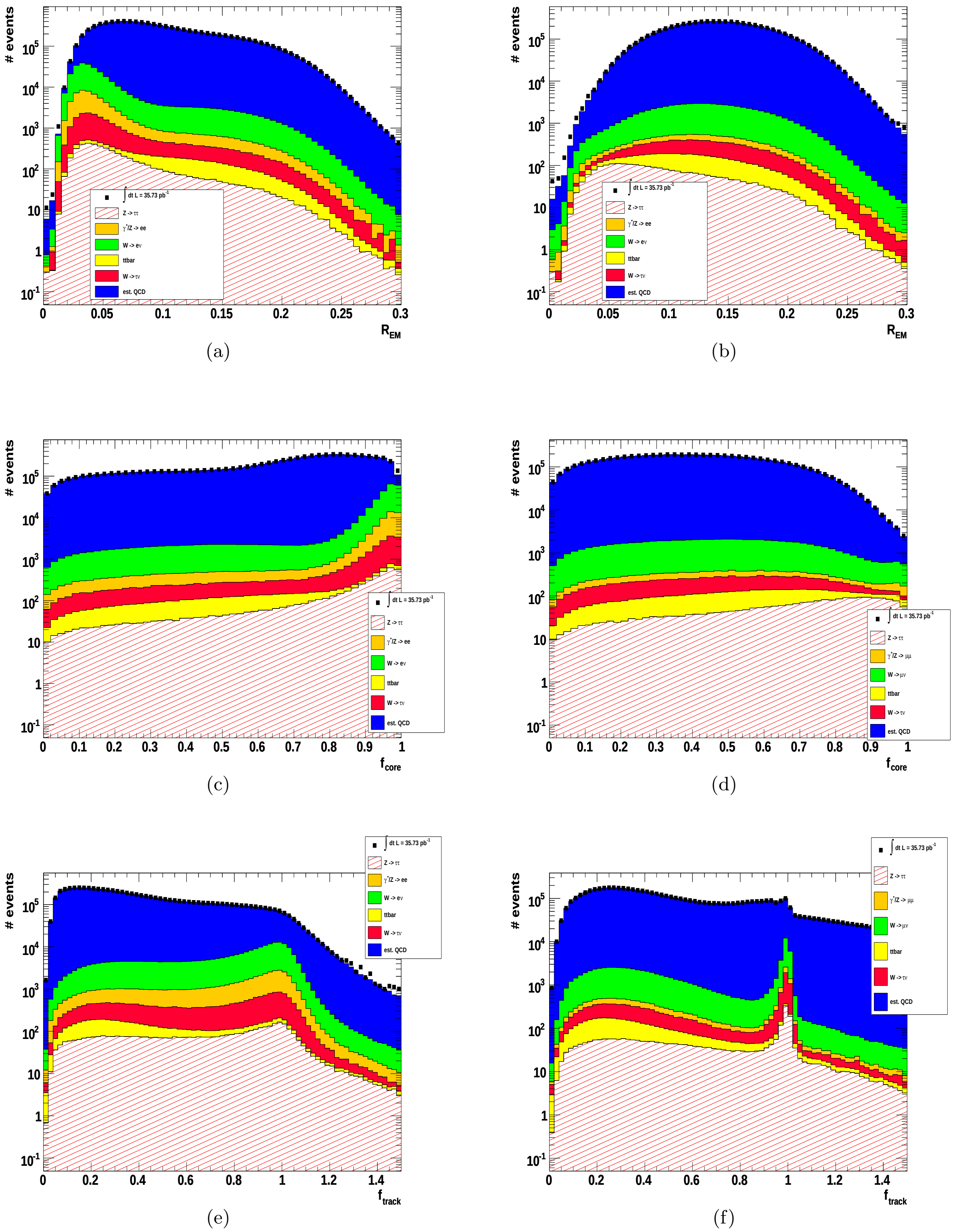

Figure 10.2: *The R_{EM} for the electron (a) and the muon channel (b). The central fraction for electrons (c) and muons (d). The leading track p_T over E_T for electrons (e) and muons (f). All variables are shown on pre-selection level.*

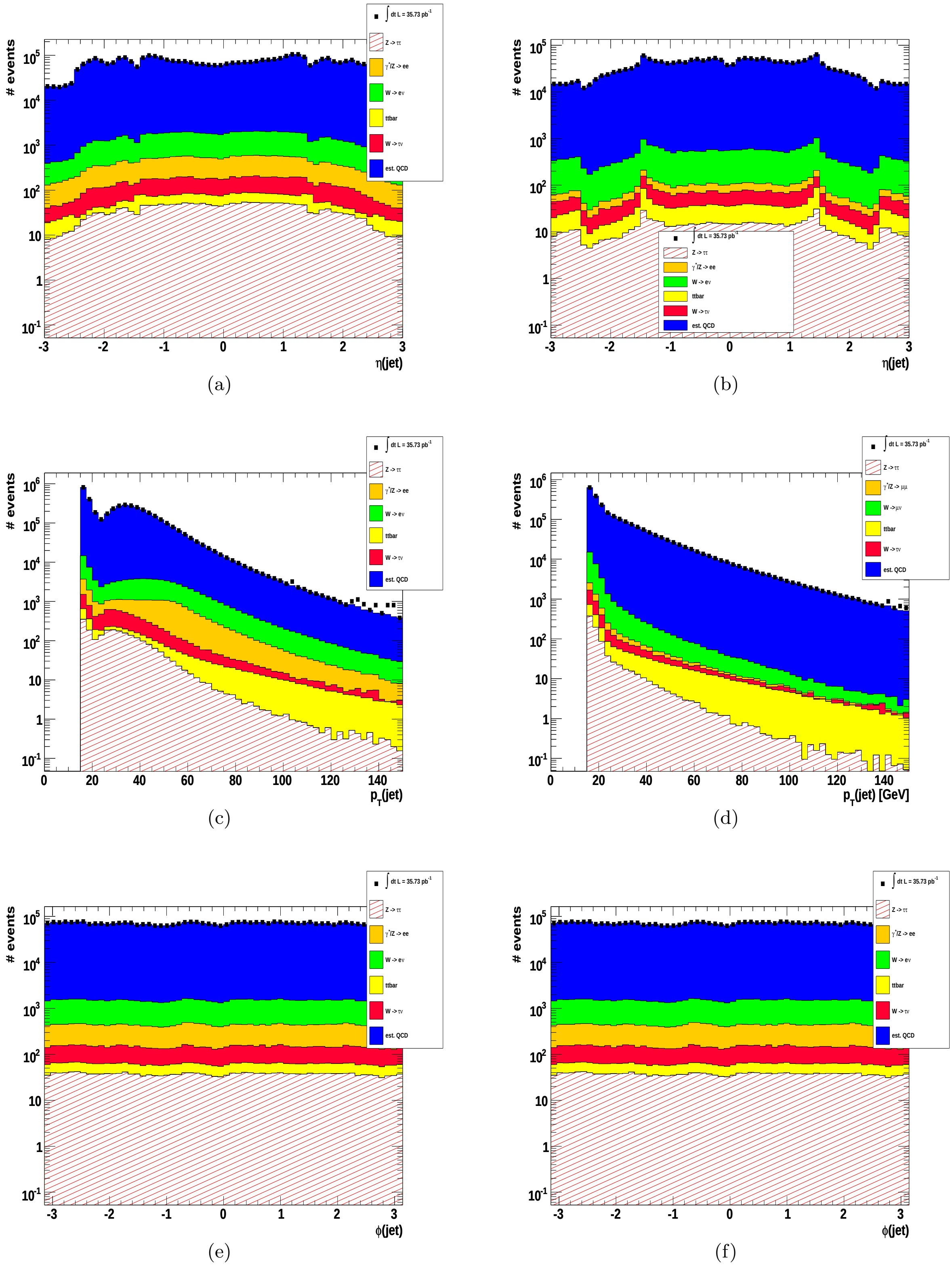

Figure 10.3: *η(jet) for electron (a) and muon (b) channel. p_T(jet) for electron (c) and muon (d) channel. ϕ(jet) for electron (e) and muon (f) channel. All variables are shown on pre-selection level.*

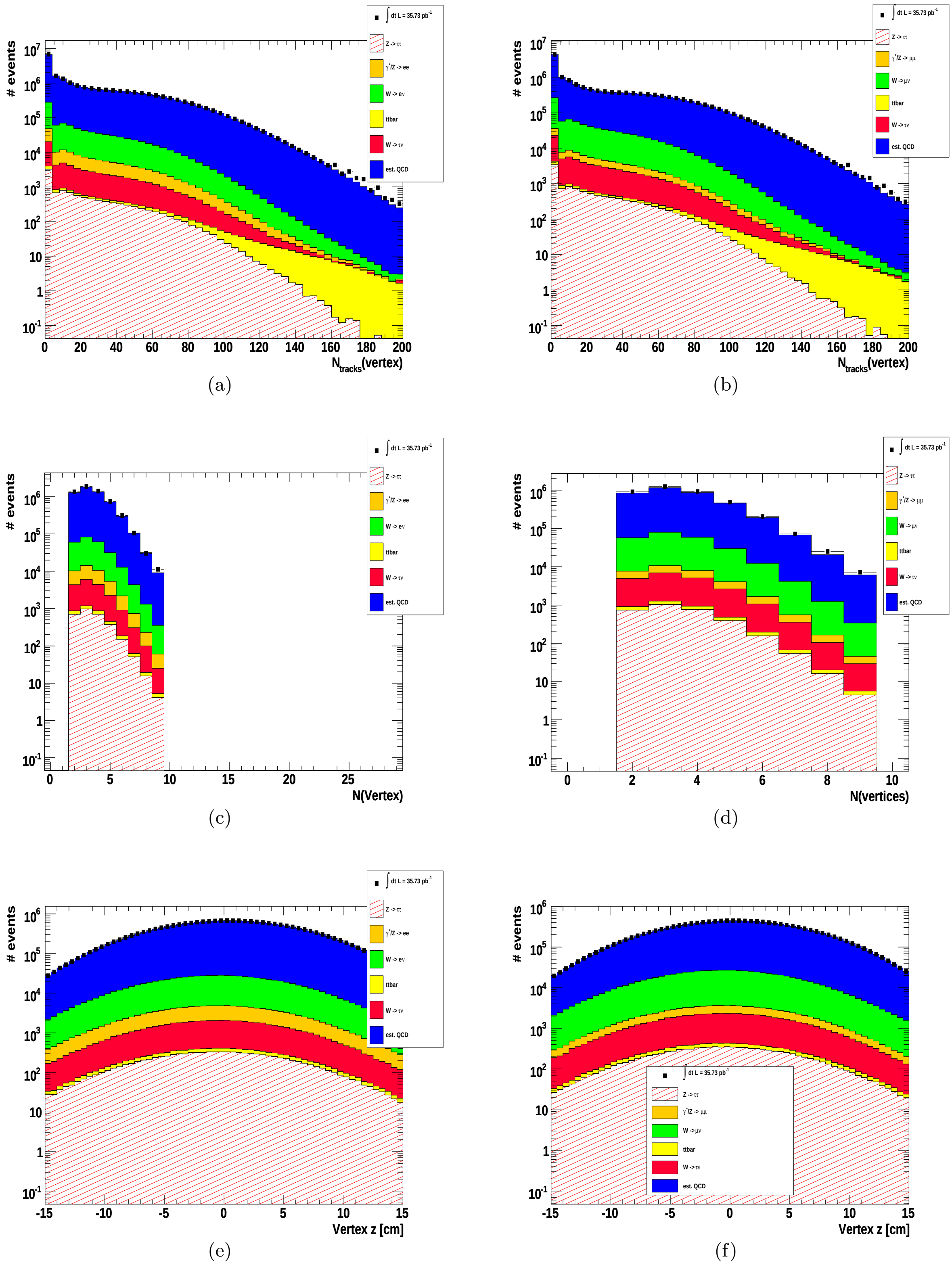

Figure 10.4: *The number of tracks per vertex for electron (a) and muon (b) channel. The number of vertices for electron (c) and muon (b) channel. The distance in z for electron (e) and muon (f) channel. All variables are shown on pre-selection level.*

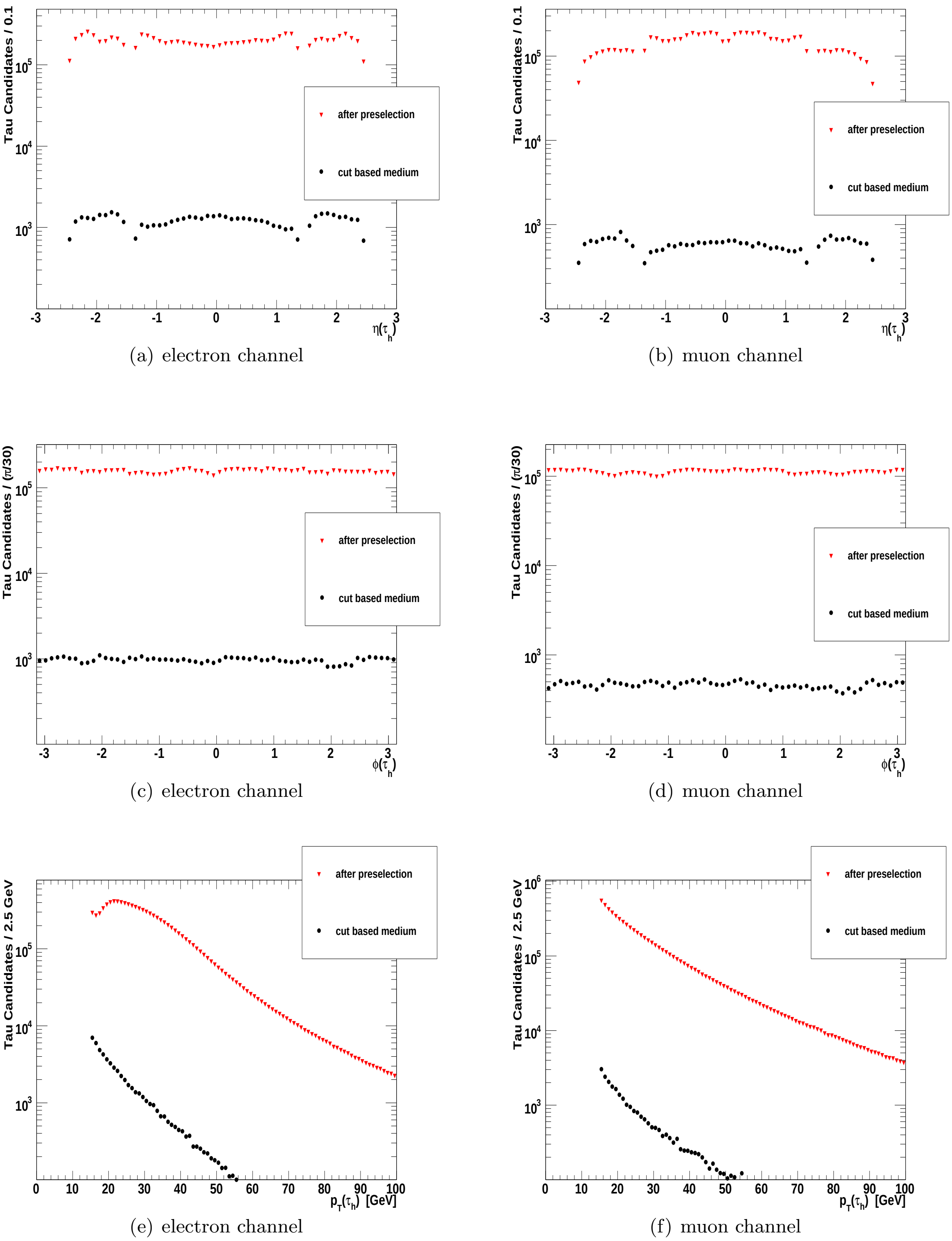

(a) electron channel (b) muon channel

(c) electron channel (d) muon channel

(e) electron channel (f) muon channel

Figure 10.5: *The kinematic distributions for the τ-lepton on pre-selection level and after selection including cut based medium identification.*

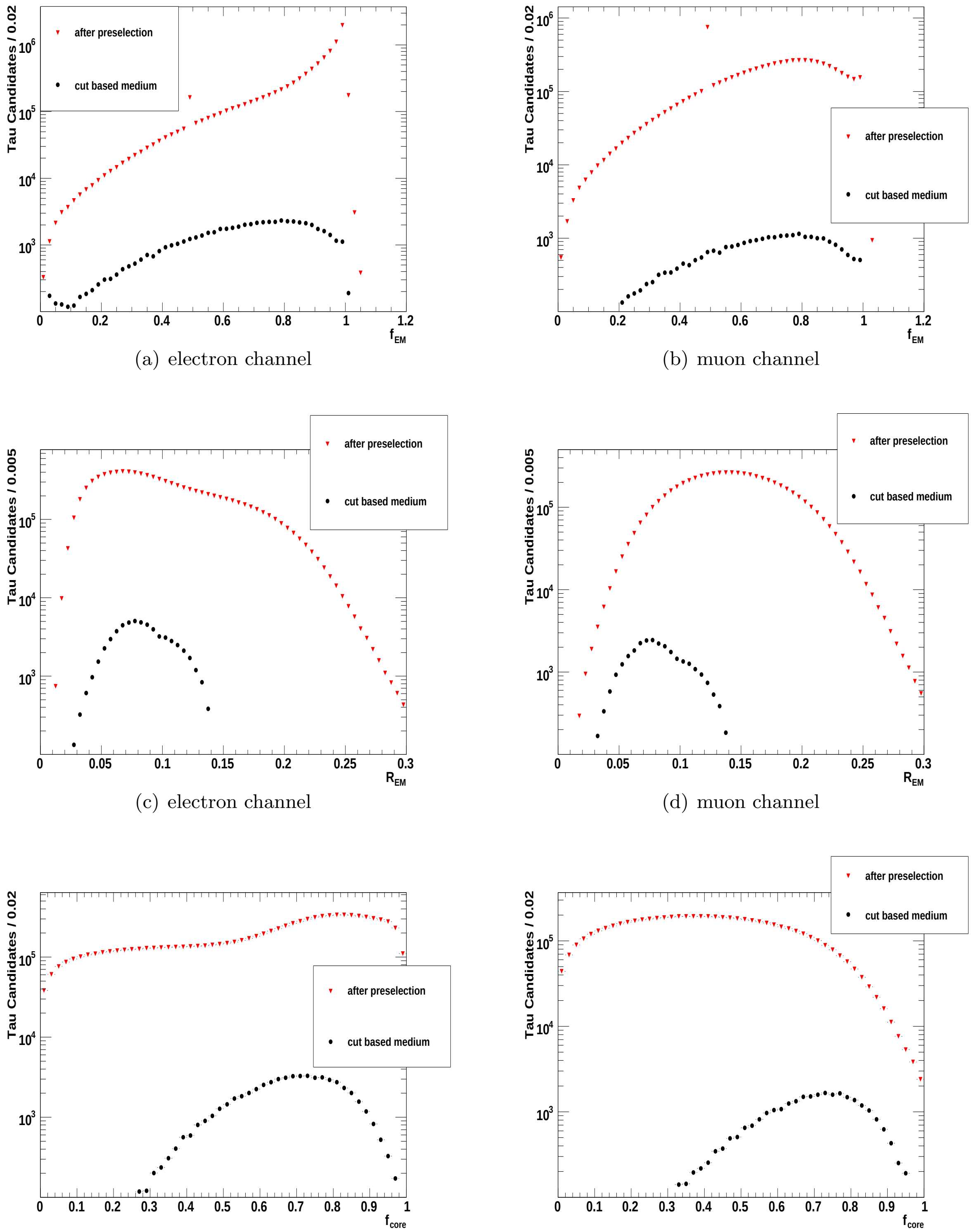

(a) electron channel (b) muon channel

(c) electron channel (d) muon channel

(e) electron channel (f) muon channel

Figure 10.6: *Calorimeter seeded variables for the τ-lepton reconstruction and identification on pre-selection level and after selection including cut based medium identification.*

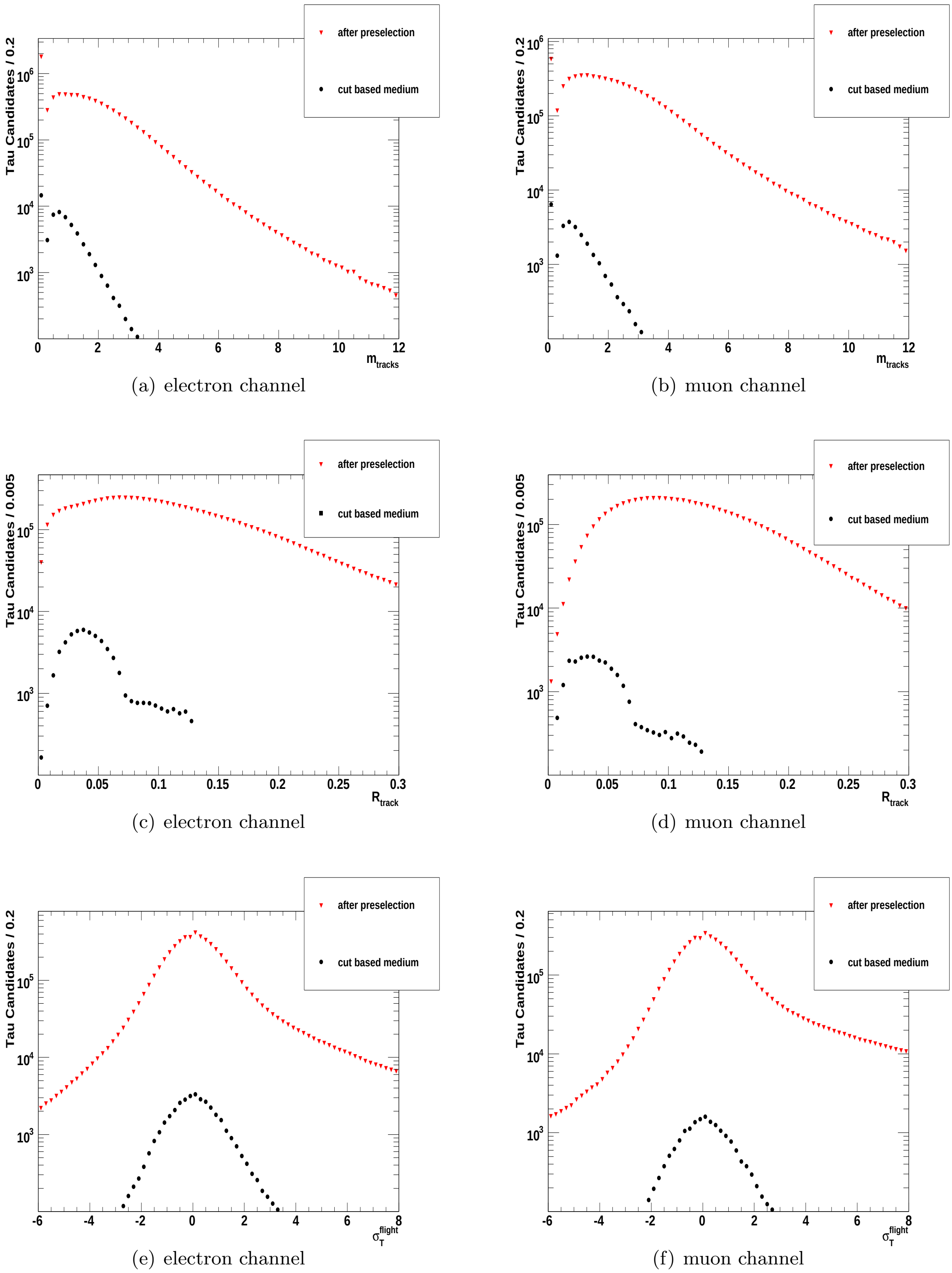

(a) electron channel
(b) muon channel
(c) electron channel
(d) muon channel
(e) electron channel
(f) muon channel

Figure 10.7: *Calorimeter based variables for the τ-lepton reconstruction and identification on pre-selection level and after selection including cut based medium identification.*

Object selection and visible mass analysis

Systematic	Uncertainty	QCD (non-isolated)	QCD (OS/SS)	W+jets	Z & $t\bar{t}$	$Z \to \tau\tau$
μ efficiency	2.7%	$\pm0.03^*$	$\pm0.03^*$	-	±0.07	±1.1
μ trigger efficiency	2.0%	$\pm0.01^*$	$\pm0.02^*$	-	±0.05	±0.8
μ isolation	1.6%	$\pm0.01^*$	$\pm0.02^*$	-	±0.04	±0.7
Jet τ fake rate	50%	$\pm0.17^*$	$\pm0.23^*$	-	±1.34	-
Energy scale	13% ($W \to \mu\nu$) / 16% ($W \to \tau\nu$)	$\pm0.26^*$	$\pm0.27^*$	±0.28	±0.40	±2.4
	6% (signal) / 13% (Z) / 21% (tt)					
Pile-up re-weighting	0.5% (signal) / 0.58% (tt)	$\pm0.01^*$	$\pm0.018^*$	-	±0.10	±0.20
	3.9% (Z)					
MC underlying event model	7%	$\pm0.04^*$	$\pm0.04^*$	-	-	±2.8
MC showering model	6%	$\pm0.04^*$	$\pm0.04^*$	-	-	±2.4
Luminosity	11%	$\pm0.07^*$	$\pm0.12^*$	-	±0.30	±4.4
Theoretical cross-section	5% (Z)	$\pm0.03^*$	$\pm0.05^*$	-	±0.12	±2.0
	6% ($t\bar{t}$)	$\pm0.01^*$	$\pm0.01^*$	-	±0.02	-
W rescaling factor	8.8% in A, B	$\pm0.04^*$	$\pm0.1^*$	±0.17	-	-
	2.1% in C, D	-	-	-	-	
Multijet est. (bkg subtraction)	-	±0.34	±0.40	-	-	-
Multijet est. (method systematics)	-	±0.56	±0.13	-	-	-
Total system.	-	±0.66	±0.42	±0.33	±1.44	±6.7

Table 10.1: *The summary of all systematic uncertainities for the muon channel [109]. All systematic uncertainties affects the background estimation as well as the signal performance.*

Systematic	Uncertainty	QCD (non-isolated)	QCD (OS/SS)	W+jets	Z & $t\bar{t}$	$Z \rightarrow \tau\tau$
e efficiency	η, p_T dependent	$\pm 0.1^*$	$\pm 0.1^*$	-	± 0.25	± 4.7
e trigger efficiency	1%	$\pm 0.01^*$	$\pm 0.02^*$	-	± 0.02	± 0.2
e isolation	p_T dependent	$\pm 0.15^*$	$\pm 0.1^*$	-	± 0.17	± 3.7
e τ fake rate	33.5%	$\pm 0.19^*$	$\pm 0.26^*$	-	± 0.65	-
Jet τ fake rate	50%	$\pm 0.29^*$	$\pm 0.42^*$	-	± 1.07	-
Energy scale	13% ($W \rightarrow e\nu$) / 12% ($W \rightarrow \tau\nu$)	$\pm 0.28^*$	$\pm 0.23^*$	± 0.36	± 0.28	± 1.7
	7% (signal) / 13% (Z) /15% (tt)					
Pile-up re-weighting	0.5% (signal) / 0.58% (tt)	$\pm 0.01^*$	$\pm 0.01^*$	-	± 0.03	± 0.1
	1.3% (Z)	-	-	-	-	-
MC underlying event model	8%	$\pm 0.03^*$	$\pm 0.03^*$	-	-	± 2.0
MC showering model	13%	$\pm 0.05^*$	$\pm 0.05^*$	-	-	± 3.2
Luminosity	11%	$\pm 0.07^*$	$\pm 0.1^*$	-	± 0.24	± 2.7
Theoretical cross-section	5% (Z)	$\pm 0.03^*$	$\pm 0.05^*$	-	± 0.10	± 1.2
	6% ($t\bar{t}$)	$\pm 0.01^*$	$\pm 0.004^*$	-	± 0.01	-
W rescaling factor	8.7% in A, B	$\pm 0.04^*$	$\pm 0.06^*$	± 0.24	-	-
	3.1% in C, D	-	-	-	-	
Multijet est. (bkg subtraction)	-	± 0.47	± 0.58	-	-	-
Multijet est. (method systematics)	-	± 0.44	± 0.41	-	-	-
Total system.	-	± 0.65	± 0.71	± 0.43	± 1.35	± 7.9

Table 10.2: *The summary of all systematic uncertainities for the electron channel [109]. All systematic uncertainties affects the background estimation as well as the signal performance.*

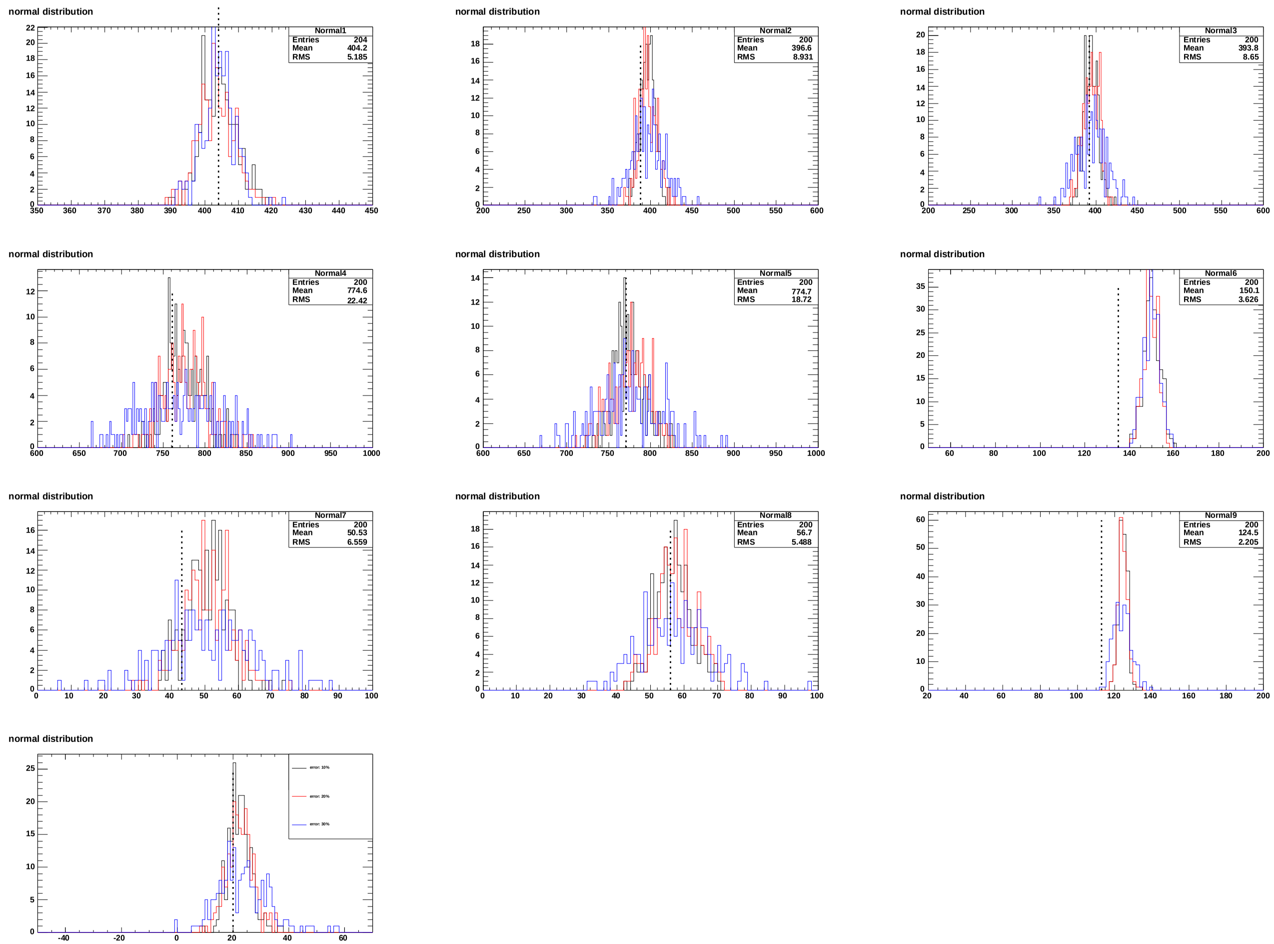

Figure 10.8: *The gaussian distribution for all 10 variables with respect to the three uncertainty levels 10%, 20% and 30%. It is visible that for the latter values the distribution smeares out. The deviation of the gauss value to the true value in the plots on the right hand side is related to the fact that because of the low statistic the relative fake rates are not the same for OS and SS. This has to be rescaled.*

List of Figures

List of Tables

Bibliography

[1] M.L. Perl et al. 1975. Phys.Rev.Lett, 35:1489.

[2] S.N. Mukherjee T. Morii, C.S. Lim. *The Physics of the Standard Model and Beyond*. 2004. World Scientific Publishing Co.

[3] H. Yukawa. 1935. Proc.Phys.Math.Soc.Japan,17:48.

[4] H. C. Paxton F. N. D. Kurie, J. R. Richardson. *The Radiations Emitted from Artificially Produced Radioactive Substances. I. The Upper Limits and Shapes of the β-Ray Spectra from Several Elements*. 1936. Physical Review 49 (5): 368381.

[5] R.P Feynman. *Theory of Fundamental Processes. Chapters 6 and 7*. 1962.

[6] S. Weinberg. *A Model of Leptons*. 1967. Phys. Rev. Lett. 19 (1967), 12641266.

[7] A. Salam. *Proc. 8th Nobel Symposium*. 1968. Almqvist and Wiksell, Stockholm.

[8] S.P. Martin. *A Supersymmetry primer*. 2006.

[9] *http://faculty.physics.tamu.edu/kamon/research/refColliders/LHC/2008_LHC_First_Beam/*.

[10] O. Bruning et al. *LHC design report. Vol I: The LHC main ring*. 2004. CERN-2004-003-V-1.

[11] ATLAS collaboration. *ATLAS detector and physics performance*. 1999. Technical report.

[12] *Axis system definitions*. 1996. ATL-GE-CERN_QAP-0204.01, CERN/QAP/204.01.

[13] The ATLAS Collaboration. *The ATLAS Experiment at the CERN Large Hadron Collider*. 2008. JINST 3 (2008) S08003.

[14] ATLAS Collaboration. *ATLAS Inner Detector: Technical Design Report, vol. 1*. 1997. CERN, ISBN 92-9083-102-2. ATLAS TDR 4, CERN/LHCC/97-16.

[15] ATLAS Collaboration. *ATLAS Inner Detector: Technical Design Report, vol. 2*. 1997. CERN, ISBN 92-9083-103-0. ATLAS TDR 5, CERN/LHCC/97-17.

[16] T. Akesson et al. *Status of Design and Construction of the Transition Radiation Tracker (TRT) for the ATLAS experiment at the LHC*. 2004. Nucl. Instrum. Meth., A522:131-145.

[17] ATLAS Collaboration. *ATLAS Calorimeter Performance, Technical Design Report, volume 1*. 1999. ATLAS TDR 14, CERN/LHCC 99-14.

[18] ATLAS Collaboration. *ATLAS Liquid Argon Calorimeter: Technical Design Report*. 1996. ISBN 92-9083-090-5. ATLAS TDR 2, CERN/LHCC/97-41.

[19] ATLAS Collaboration. *ATLAS Tile Calorimeter: Technical Design Report*. 1996. ISBN 92-9083-091-3, ATLAS TDR 2, CERN/LHCC/97-42.

[20] M. Cobal. *The ATLAS tile hadronic calorimeter*. 1998. Nucl. Phys. Proc. Suppl., 61B:77-82.

[21] ATLAS Collaboration. *ATLAS Muon Spectrometer: Technical Design Report*. 1997. ISBN 92-9083-108-1. ATLAS TDR 10, CERN/LHCC/97-22.

[22] The ATLAS collaboration. *The ATLAS Inner detector commissioning and calibration*. 2010. Eur. Phys. J. C70, 787-821, arXiv:1004.5293v2.

[23] The ATLAS collaboration. *Electron and photon reconstruction and identification in ATLAS: expected performance at high energy and results at 900 GeV*. 2010. ATLAS-CONF-2010-005.

[24] The ATLAS collaboration. *Muon reconstruction performance*. 2010. ATLAS-CONF-2010-064.

[25] The ATLAS collaboration. *Performance of the ATLAS Detector using First Collision Data*. 2010. arXiv:1005.5254v1.

[26] *Impact of the electromagnetic-inner detector inter alignment on cluster track matching quantities*. 2011. ATL-COM-PHYS-2011-246.

[27] T. Sjostrand. *Monte Carlo Generators*. hep-ph/0611247.

[28] M. A. Dobbs et al. *Les Houches guidebook to Monte Carlo generators for hadron collider physics*. hep-ph/0403045.

[29] J. B. Hansen M. Dobbs. *The HepMC C++ Monte Carlo event record for High Energy Physics*. 2001. Computer Physics Communications 134 (2001) no. 1, 41.

[30] P. Skands T. Sjostrand, S. Mrenna. *PYTHIA 6.4 physics and manual*. 2006. JHEP 05 (2006) 026,hep-ph/0603175.

[31] G. Corcella et al. *HERWIG 6: An event generator for hadron emission reactions with interfering gluons (including supersymmetric processes)*. 2001. JHEP 01 (2001) 010, hep-ph/0011363.

[32] M. Mangano et al. *ALPGEN, a generator for hard multiparton processes in hadronic collisions*. 2003. JHEP 07 (2003) 001, hep-ph/0206293.

[33] B. R. Webber S. Frixione. *Matching NLO QCD computations and parton shower simulations*. 2002. JHEP 06 (2002) 029, hep-ph/0204244.

[34] A. Dellacqua et al. *GEANT-4: An Object oriented toolkit for simulation in HEP*. CERN-DRDC-94-29.

[35] The ATLAS collaboration. *Luminosity Determination in pp Collisions at* sqrts=*7 TeV Using the ATLAS Detector at the LHC*. 2011. CERN-PH-EP-2010-069.

[36] K. S. Cranmer. *The ATLAS analysis architecture*. 2008. Nucl. Phys. Proc. Suppl. 177-178 (2008) 126.

[37] `http://root.cern.ch/drupal`.

[38] ATLAS Collaboration. *The ATLAS HLT, DAQ and DCS Technical Design Report*. 2003. ATLAS-TDR-016.

[39] The ATLAS collaboration. *Level-1 Trigger Technical Design Report*. 1998. ATLAS-TDR-012.

[40] G. Commune et al. *Steering the ATLAS High-level trigger*. 2006. ATLAS-DAQ-CONF-2006-16.

[41] *Level-1 Technical Design Report(issue 1.1)*. 1998. http://atlas.web.cern.ch/Atlasy/GROUPS/DAQTRIG/TDR/tdr.html.

[42] The ATLAS collaboration. *The ATLAS Trigger Monitoring and Operation in proton-proton collisions*. 2010. ATL-DAQ-PUB-2010-003.

[43] M. Verducci. *ATLAS conditions database experience with the LCG COOL conditions database project*. 2008. Journal of Physics: Conference Series, Volume 119, Issue 4, pp. 042031.

[44] J. Garvey et al. *Use of FPGA to identify electromagnetic clusters and isolated hadrons in the ATLAS Level-1 calorimeter trigger*. 2003. Nucl. Inst. and Meth. **A512**, 506-616.

[45] Mogens Dam for the ATLAS TDAQ Collaboration. *The ATLAS Tau Trigger*. 2010. Journal of Physics: Conference Series 219(2010)032006.

[46] ATLAS Collaboration. *Tau Leptons in Expected Performance of the ATLAS Experiment*. 2008. CERN-OPEN-2008-020, 229-259.

[47] *www-h1.desy.de/.../home/phys_poster/proton.html*.

[48] The LEP Electroweak Working Group. *Combines the Measurements of the four LEP experiments ALEPH, DELPHI, L3 and OPAL*. 2008. http://lepewwg.web.cern.ch/LEPEWWG/.

[49] P.M. Nadolsky. *Theory of W and Z boson production*. 2004. ANL-HEP-CP-04-138.

[50] W.J. Stirlinga A.D. Martin, R.G. Roberts and R.S. Thorne. *Parton Distributions and the LHC: W and Z Production*. 1999. DTP/99/64, OUTP/9931P, RAL-TR-1999-047, hep-ph/9907231.

[51] The ATLAS Collaboration. *Measurement of the transverse momentum distribution of $Z/\gamma^\star$ bosons in proton-proton collisions at $\sqrt{s} = 7\,TeV$ with the ATLAS detector.* 2011. ATLAS-STDM-2011-09-001.

[52] S.L. Glashow. 1961. Nucl. Phys. 22, S309.

[53] S. Weinberg. 1967. Phys. Rev. Lett. 19, 1264.

[54] A. Salam. 1968. Proc. 8th Nobel Symposium Stockholm, 367.

[55] G. Arnison et al. UA1 Collaboration. 1983. Phys.Lett.,B 122:103.

[56] G. Arnison et al. UA1 Collaboration. 1983. Phys.Lett.,B 126:398.

[57] M. Banner et al. UA2 Collaboration. 1983. Phys.Lett.,B 122:476.

[58] F.M. Renard A. Blondel, B.W. Lynn and C. Verzegnassi. 1998. Nucl. Phys. **B304**.

[59] L. Trentadue. *Neutrino counting.* 1989. Z Physics at LEP1, ed. Altarelli, G., Kleiss,R., and Verzegnassi, C. (CERN 89-08, Geneva).

[60] Wolfgang Mader. *Measurement of the Strangeness Spectral Function and the Mass of the Strange Quark in Hadronic τ Decays with the Opal Detector.* 2004. PhD Thesis.

[61] N. Cabibbo. *Unitary Symmetry and Leptonic Decays.* 1963. Physical Review Letters 10 (12): 531533.

[62] E. Mirkes M. Finkemeier. *Decay Rates, Structure Functions and New Physics Effects in Hadronic Tau Decays.* 1995. MADPH-95-906, HUTP-95/A030, hep-ph/9508312.

[63] M. Finkemeier R. Decker. 1994. Phys. Lett. B **334**,199.

[64] M. Davier. *Proceedings of the Third Workshop on Tau Lepton Physics (Montreux, September 1994).* 1995. Nucl. Phys. B (Proc. Suppl.) 40(1995).

[65] Y.S. Tsai. 1971. Phys. Rev. D **4**, 2821 (1971).

[66] J.J. Sakurai H.B. Thacker. 1971. Phys. Lett. B **36**, 103 (1971).

[67] S.H. Rhie F.J. Gilman. 1984. Phys. Rev. D **31**, 1066(1984).

[68] S.Tse E. Braaten, R.J. Oakes. 1990. Int. J. Mod. Phys. **A 14**, 2737 (1990).

[69] Z. Was R. Decker, E. Mirkes. 1993. Z.Phys. C **58** 445 (1993).

[70] A. Santamaria J.H. Kuehn. 1990. Z. Phys.C **48**, 445 (1990).

[71] E. Mirkes J.H. Kuehn. 1992. Z. Phys.C **56**,661 (1992).

[72] E. Mirkes J.H. Kuehn. 1992. Phys. Lett. B **286**, 281(1992).

[73] DONuT collaboration. *Final tau-neutrino results from the DONuT experiment.* 2008. PHYSICAL REVIEW D 78, 052002 (2008).

[74] N. Agafonova et al. OPERA collaboration. *OPERA catches its first tau-neutrino*. 2010. CERN Courier.

[75] I. Lawson R.J. Sobie, R.K. Keeler. *An upper limit on the tau neutrino mass from leptonic tau decays*. 1996. Z.Phys. C70, 383-385.

[76] Rev. D4, 2821. 1971. Phys. Rev.

[77] D. Decamp et al. *ALEPH Collaboration*. B265. 1991. Phys. Lett.

[78] *Identification of hadronic tau decays with ATLAS detector*. ATL-COM-PHYS-2007-066. September 30,2007. ATLAS CSC Note.

[79] The LEP Working Group for HiggsBoson Searches. *Search for the Standard Model Higgs Boson at LEP*. 2003. Phys. Lett. B565, 61.75.

[80] ATLAS Collaboration. *Tau Reconstruction and Identification Performance in ATLAS*. 2010. ATLAS-CONF-2010-086.

[81] ATLAS Collaboration. *Data-Quality Requirements and Event Cleaning for Jets and Missing Transverse Energy Reconstruction with the ATLAS Detector in Proton-Proton Collisions at a Center-of-Mass Energy of* $\sqrt{s} = 7$ *TeV*. 2010. ATLAS-CONF-2010-038 (2010).

[82] B. Aubert et al. *ATLAS Electromagnetic Liquid Argon Calorimeter Group*. 2003. Nucl. Inst. Meth. **A500** (2003) 202-231.

[83] M. Aharrouche et al. *ATLAS Electromagnetic Barrel Calorimeter*. 2006. Nucl. Inst. Meth. **A568** (2006) 601-623.

[84] ATLAS Collaboration. *Expected Performance of the ATLAS Experiment-Detector, Trigger and Physics*. 2008. CERN-OPEN-2008-020 (2008).

[85] S. Hassini et al. 2007. NIM **A572** (2007) 77-79.

[86] D. Adams et al. 2003. ATL-SOFT-2003-007(2003).

[87] Th. Lagouri et al. 2004. IEEE Trans. Nucl. Sci. **51** (2004) 3030-3033.

[88] G. Bagliesi. *Reconstruction and identification of tau decays at CMS*. 2008. Journal of Physics: Conference Series 119 (2008) 032005.

[89] The ATLAS collaboration. *Validation of the ATLAS jet energy scale uncertainties using tracks in proton-proton collisions at* $\sqrt{s}$=7 *TeV*. 2011. ATLAS-CONF-2011-067.

[90] E. Coniavitis et al. *Reconstruction, Energy Calibration, and Identification of Hadron Decays for Winter 2011*. 2011. ATL-COM-PHYS-2011-217.

[91] G. Soyez M. Cacciari, G.P. Salam. *The anti-*k_t *jet clustering algorithm*. 2008. JHEP **04** (2008) 063.

[92] ATLAS Collaboration. *Calorimeter clustering algorithms: Description and performance.* 2008. ATL-LARG-PUB-2008-002.

[93] ATLAS Collaboration. *The ATLAS Experiment at the CERN Large Hadron Collider.* 2008. JINST 3(2008) SO8003.

[94] S. Qian P. Billoir. 1992. Nucl. Instr. and Meth. **A311** (1992) 139-150.

[95] T. Speer R. Fruhwirth, K. Prokofiev, P. Vanlaer, and W. W. Waltenberger. 2003. Nucl. Instr. and Meth. **A502** (2003) 699-701.

[96] V. Kostyukhin. *VKalVrt-package for vertex reconstruction in ATLAS.* 2003. ATLAS Physics Note ATL-PHYS-2003-031.

[97] D. Cavalli M. Heldmann. *An improved tau-Identification for the ATLAS experiment.* 2006. ATL-PHYS-PUB-2006-008.

[98] T.Szymocha E. Richter-Was. *Hadronic tau identification with track based approach: the $Z \to \tau\tau$, $W \to \tau\nu$ and dijet events from DC1 data samples.* 2005. ATL-PHYS-PUB-2005-005.

[99] ATLAS Collaboration. *Cut-based Identification of Hadronic τ Decays in Early ATLAS Data.* 2010. ATL-PHYS-PUB-2010-001.

[100] ATLAS collaboration. *Tau Reconstruction and Identification Peformance in ATLAS.* 2010. ATLAS-CONF-2010-086.

[101] The ATLAS collaboration. *Tau Reconstruction and Identification Performance in ATLAS.* 2010. ATLAS-CONF-2010-086.

[102] E. Coniavitis et al. *Reconstruction, Energy Calibration, and Identification of Hadron Decays for Winter 2011.* 2011. support note.

[103] M. Wolter. *Tau identification using multivariate techniques in ATLAS.* 2009. ATL-PHYS-PROC-2009-016.

[104] N. Styles et al. P. Bechtle, A. Pingel. *Studying Tau Reconstruction and Identification Performance in Di-Jet, Three-Jet and Photon Jet Events with the ATLAS experiment.* 2011. Draft for ATLAS note.

[105] A. Straessner F. Friedrich, W. Mader. *Determination of the τ-Identification Fake Rate Using $Z(\ell\ell)$+Jets Events with the ATLAS Detector.* 2011. ATL-COM-PHYS-2011-192.

[106] M. Baak et al. *Data Quality Status Flags and Good Run Lists for Physics Analysis in ATLAS.* 2009. ATL-COM-GEN-2009-015.

[107] S. Bedikian et al. *ATLAS Tau Data Quality.* 2010. ATL-COM-GEN-2010-011.

[108] `https://atlas-datasummary.cern.ch/lumicalc`.

[109] E. Coniavitis et al. *Observation of $Z \rightarrow \tau\tau$ Decays with the ATLAS detector*. 2010. ATLCOM-CONF-2010-114.

[110] The ATLAS collaboration. *Data-Quality Requirements and Event Cleaning for Jets and Missing Transverse Energy Reconstruction with the ATLAS Detector in Proton-Proton Collisions at a Center-of-Mass Energy of $\sqrt{7}$ TeV*. 2010. ATLAS-CONF-2010-038.

[111] M. Aharrouche et al. *$W \rightarrow e\nu$ and $Z \rightarrow ee$ cross section measurement in proton-proton collisions at $\sqrt{s} = 7$ TeV with the ATLAS Detector*. 2010. ATL-COM-PHYS-2010-701.

[112] C. Issever K. Lohwasser, J. Ferrando. *On direct measurement of the W production charge asymmetry at the LHC*. 2010. JHEP 1009:079.

[113] W.J. Stirling R.S. Thorne, A.D. Martin and G. Watt. *The Effects of combined HERA and recent Tevatron $W \rightarrow \ell\ \nu$ charge asymmetry data on the MSTW PDFs*. 2010. PoS DIS2010:052.

[114] C. Boddy et al. *Measurement of $Z \rightarrow \tau\tau$ production cross-section in proton-proton collisions at $\sqrt{s} = 7$ TeV with the ATLAS detector - Support Note for lep-had channels*. 2011. ATLAS-COM-2011-xxx.

[115] The ATLAS collaboration. *Measurement of the $W \rightarrow \ell\nu and Z/\gamma^{\star} \rightarrow \ell\ell$ production cross sections in proton proton collisions at $\sqrt{7}$ TeV with the ATLAS detector*. 2010. CERN-PH-EP-2010-037.

[116] D. Froidevaux O. Arnaez. *Recommendations for electron efficiencies*. Feb. 2011. twiki from egamma working group.

[117] *Luminosity Determination using the ATLAS detector*. 2010. ATLAS-CONF-2010-060.

[118] M. Aharrouche et al. *$W \rightarrow e\nu and Z \rightarrow ee$ cross section measurement in proton-proton collisions at $\sqrt{7}$ TeV with the ATLAS Detector*. 2010. ATL-COM-PHYS-2010-701.

[119] `http://mathworld.wolfram.com/Gauss-SeidelMethod.html`.

[120] Tech. Rep. *Charged particle multiplicities in p p interactions at $s = 0.9$ and 7 TeV in a diractive limited phase-space measured with the ATLAS detector at the LHC and new PYTHIA6 tune*. 2010. ATLAS-CONF-2010-031.

[121] Tech. Rep. *Updated Luminosity Determination in pp Collisions at $\sqrt{s}$=7 TeV using the ATLAS Detector*. 2011. ATLAS-CONF-2011-011.

[122] K. Nakumara et al. *Review of particle physics, J.Phys. G37*. 2010. Particle Data Group Collaboration.

[123] Tech. Rep. *A measurement of the total $W\pm$ and $Z/\gamma^{\star}$ cross sections in the e and decay channels and of their ratios in pp collisions at $\sqrt{s} = 7$ TeV with the ATLAS detector*. 2011. ATLAS-CONF-2011-041.

[124] E.Barberio et al. *Measurment of the cross section* $\sigma \times BR(Z \rightarrow \tau\tau)$ *in the dilepton channel with the ATLAS detector: Supporting Note*. 2011. ATL-COM-PHYS-2011-XXX.

[125] The ATLAS Collaboration. *Expected performance of the ATLAS experiment*. 2008. CERN-OPEN-2008-020.

[126] The ATLAS collaboration. *Muon reconstruction efficiency in reprocessed 2010 LHC proton-proton collision data recorded with the ATLAS detector*. 2011. ATLAS-CONF-2011-063.

[127] The ATLAS Collaboration. *Measurement of the* $Z \rightarrow \ell\ell$ *production cross section in proton-proton collisions at* $\sqrt{s}$ *TeV with the ATLAS detector*. 2010. ATLAS-CONF-2010-076.

[128] P.M. Nadolsky et al. *Implications of CTEQ global analysis for collider observables*. 2008. Phsy.Rev. D78(2008)013004.

[129] Z. Was P. Golonka. *PHOTOS Monte Carlo: A precision tool for QED corrections in Z and W decays*. 2006. vol.C45.

[130] R. Decker S. Jadach, Z. Was. *The* τ *decay library TAUOLA, version 2.4*. 1993. vol.76, Comput. Phys. Commun.

[131] J. Kroseberg N. Moeser, M. Schmitz, M. Schumacher, and N. Wermes. *Estimation of* $Z \rightarrow \tau\tau$ *Background in VBF* $H \rightarrow \tau\tau$ *Searches from* $Z \rightarrow \mu\mu$ *Data using an Embedding Technique*. 2009. ATL-PHYS-INT-2009-109.

[132] R. Decker S. Jadach, Z. Was. *The* τ *decay library TAUOLA, version 2.4*. 1993. 10.1016/0010-4655(93)90061-G, 361-380.

[133] T. Schwindt. 2010. Private communication.

[134] The CMS collaboration. *Measurement of the Inclusive Z Cross Section via Decays to Tau Pairs in pp Collisions at* $\sqrt{s}$*=7 TeV*. 2011. CMS-EWK-10-013.